A SYSTEM OF MECHANICAL GENETICS WITH APPLICATIONS TO PULMONARY FIBROSIS

A Dissertation
Presented to
The Academic Faculty

By

Dwight McCoy Chambers

In Partial Fulfillment
of the Requirements for the Degree
Doctor of Philosophy in the
School of Biomedical Engineering

Emory University
and
Georgia Institute of Technology

August 2018

A SYSTEM OF MECHANICAL GENETICS WITH APPLICATIONS TO PULMONARY FIBROSIS

Approved by:

Dr. Thomas H Barker, Co-Advisor
Department of Biomedical Engineering
University of Virginia

Dr. Philip J Santangelo, Co-Advisor
Department of Biomedical Engineering
Georgia Institute of Technology

Dr. Johnna S Temenoff
Department of Biomedical Engineering
Georgia Institute of Technology

Dr. Melissa L Kemp
Department of Biomedical Engineering
Georgia Institute of Technology

Dr. Lonnie D Shea
Department of Biomedical Engineering
University of Michigan

Date Approved: May 24, 2018

One fails forward towards success.

C.S. Lewis

To my brother, Davis

To my mother, Carol

To my father, J. Richard

ACKNOWLEDGEMENTS

Many people have supported me on my journey towards scientific independence. I would like to thank my family - their unconditional support and love has been critical to any success I have enjoyed in this program. I would also like to thank my thesis committee: Tom Barker, Phil Santangelo, Melissa Kemp, Johnna Temenoff, and Lonnie Shea. This group has given me indispensable advice during the various highs and lows of my assorted projects during grad school. My co-advisors, Tom Barker and Phil Santangelo, have given me the opportunity to develop and explore my own ideas, for which I am very grateful. I would also like to acknowledge the support of numerous friends and colleagues in the Barker and Santangelo labs, at the School of Medicine at Emory, at GT generally, from MIT and from Nashville. These people have buoyed my spirit on numerous occasions during this process. Finally, I gratefully acknowledge the support and material contributions of the academic and core facility support staff at Georgia Tech and Emory who have helped me to navigate a complex research program with minimal discomfort.

TABLE OF CONTENTS

LIST OF TABLES

LIST OF FIGURES

SUMMARY

Over the past decade and a half, scientific research into pulmonary fibrosis has come full circle. The fibrotic matrix, a disorganized, stiff accumulation of extracellular proteins, has gone from being the unfortunate product of pathological fibroblast activation to being a key driver of its own accumulation through mechanical cues to the cells. Important mechanical regulation by the matrix occurs in distinct spatial domains throughout the cell (*e.g.* at the cell-ECM interface, in the mechanical machinery of the cytosol, and through the genome), which all contribute to the long-term disease phenotype. While the importance and therapeutic promise of understanding this pathologic mechanotransduction has been explored in the scientific literature, there are still no therapies to reverse pulmonary fibrosis, and life expectancy with this condition has been largely unchanged even after the advent of new medical management. The identification and demonstration of novel matrix-responsive therapies represents a new frontier in the medical approach to pulmonary fibrosis, which could directly address the disease feature (*i.e.* the matrix itself) responsible for the dyspnea and eventual asphyxiation that kills patients.

This thesis focuses on the application of genetics and nucleic acids to directly treating and to identifying novel therapeutic targets that break this deadly feedback cycle. Each Chapter of this thesis is dedicated to applying genetics to a particular domain/step in pathologic mechanotransduction: Chapter 2 demonstrates the delivery of mRNA-based therapeutics to modulate cell-ECM interactions; Chapter 3 illustrates how the fibrotic matrix perverts the cell's innate mechanosensing machinery to potentiate pathologic TGFβ-driven transcription factor biology; and, Chapter 4 explores the structure and activation of a mechanically regulated transcription factor system, the MRTF/SRF axis, to allow for the rational exploitation of mechanical genetic.

In Chapter 2, I have demonstrated the mRNA-based delivery and efficacy of two cell-tethered, conformationally sensitive fibronectin binding single chain antibody fragment

variants, H5-CD8 and H5-GPI. I have shown that H5 expression alters the focal adhesion profile of fibroblasts in a linker dependent fashion and characterized the resultant mechanotransductive phenotypes of fibroblasts expressing these variants. Furthermore I have shown that these mRNA-based therapies can be translated *in vivo* in anticipation of efficacy testing in a bleomycin model of pulmonary fibrosis in mice. In Chapter 3, I have discovered a unique mechanism by which the fibrotic matrix sensitizes cells to TGFβ transcription through stiffness-dependent inhibition of a TGFβ inhibitor, LEMD3. I have found and characterized unique, cytosolic elements of LEMD3 biology and extended these finding into *ex vivo* human tissues. Finally, in Chapter 4, I have mapped the stiffness-based translocation of MRTF with and without TGFβ treatment in initial mechanosensing by fibroblasts. I have also characterized the genomic space that activated MRTF and its cofactor SRF act over by profiling the number and sequence characteristics of CArG elements in the murine genome. Finally, I have developed the tools necessary to complete a thermodynamic survey of this system in anticipation of the construction of models to predict the stiffness-dependent behavior of therapeutic CArG-based transgenes.

These three particular, individual stories follow the path of mechanical information as it weaves from the matrix, into the cell and ultimately back into the matrix. Each Chapter suggests unique approaches to pathologic mechanosensing, and the integration of these insights and its implications for future work are discussed in the Chapter 5.

CHAPTER 1
INTRODUCTION

1.1 Overview

This thesis represents the work I undertook to understand the intersection of cellular mechano-sensing in fibrosis and genetics through 1) the therapeutic application of nucleic acids to modulating the rigidity-dependent intergin-ECM binding, 2) the mechano-biology of Transforming Growth Factor β a transcription factor relevant to pulmonary fibrosis, and 3) the organization of the murine CArGome, a set of mechanically regulated elements in the genome. This global introduction focuses on the critical clinical features of pulmonary fibrosis that motivated these works collectively and the organization of these projects inside a framework of bi-lateral cell-matrix communication. The review of the literature and necessary biological background for each Chapter is embedded in that Chapter to maintain the clarity of presentation across these diverse projects.

1.2 Pulmonary Fibrosis

1.2.1 Pulmonary Fibrosis is a Heterogeneously Presenting, Deadly Sclerosis

Pulmonary fibrosis (PF) is a progressive scarring of the lung parenchyma with a median survival-rate of 3-5 years post diagnosis and which kills 16,200 Americans each year. [1, 2] While lung transplantation is often curative, it is, itself, an overly morbid process, is unavailable to overly frail patients, and has median survival rates for single lung transplantation at 4.6 years and 6.6 years for a double organ transplant. [3] Fibrotic regions in the PF lung present heterogeneously with a general basal to apical progression, are largely collagen dominated, are significantly stiffer than healthy regions (median stiffness of 1.96 kPa and 16.52 kPa respectively), and are marked an irreversible loss of lung compliance arising

from alveolar collapse during injury. [4, 5] Interstitial fibrosis also impairs gas exchange as evidenced by decreased diffusion of hyperpolarized Xe and carbon monoxide studies in PF patients. [6] Medical management of PF is an historically fraught business with numerous failed phase III clinical trials along multiple therapeutic axes (e.g. N-acetyl cysteine, Etanercept, interferon-gamma 1b, prednisone, azathioprine, tyrosine kinase inhibitor imatinib mesylate, JNK inhibitor CC-930, anti-IL13 antibody QAX576, etc.). [7] However, in 2015, the FDA approved two agents, pirfenidone (an "anti-fibrotic" agent) and nintedanib (tyrosine kinase inhibitor affecting CTGF, FGF, PDGF) for the treatment of mild-to-moderate PF after both showed statistically significant decreases in the rate of loss of forced vital capacity ($\approx$50% reductions in annual loss). Moreover, meta-analysis of the CAPACITY and ASCEND pirfenidone trials demonstrated a reduction in trial participant mortality to all causes and to IPF-related causes not seen with nintedanib. [8, 9, 10, 11] While these drugs mark an important turning point in the management of PF, they do not offer a cure or a means to deal with crippling dyspnea present in clinically evident patients.

1.2.2 Matrix Mechanics is a Pathologic Driver in Pulmonary Fibrosis

Recent scientific and translational attention has focused on the role on the fibrotic matrix itself. In addition to being the central pathological symptom of the disease process, the fibrotic matrix appears sufficient to drive myofibroblastic differentiation and potentiates important soluble factors, like TGFβ. Liu et al. demonstrated that matrix stiffness alone was able to initiate a fibrotic program in naive fibroblasts. [12] These findings have subsequently been reproduced using 3D, acellular matrices derived from healthy and diseased human lung tissue [4]; and, mechanistically, mechanosensitive transcription factor families, like transforming growth factor β ("TGFβ"), the myocardin-related transcription factor family (commonly MRTF A/B or MKL1/2) and yes-associated protein/ transcriptional coactivator with PDZ-binding motif (YAP/TAZ) have been implicated in conveying this matrix-derived phenotype. [13, 14, 15] The fibrotic matrix, as a nexus of both

pathological cause of effect, has become a target for therapeutic intervention as recognized by NHLBI. [16] However, there are currently not many investigations into matrix-driven therapy: a recent matrix-focused clinical trial, simtuzumab, an anti-lysyl oxidase therapy, failed Phase II trials in 2016 due to a lack of efficacy. [7, 17] There are still cellular-focused, Rho/ROCK [18, 19, 20] and MRTF specific therapeutics [21] under investigation; however, these therapeutics often elicit pleiotropic effects in multiple organ systems since these kinases/transcription factors regulate basic cell processes, like motility, polarity and cell-cell junctions. [22] Because the matrix and the cell's ability to sense the mechanical cues of the matrix are so central to the pathology of fibrosis, there is a clinical need for understanding pathologic mechano-transduction to identify new potential therapeutic interventions. The Chapters of this thesis are dedicated to uncovering novel approaches to pathological mechano-transduction through genetic tools and investigation.

1.3 Conceptual Organization of This Thesis

These chapters fall neatly into two organizational frameworks - one spatial and one conceptual. Spatially, this thesis is organized "outside-in" - starting with biology of the cell-matrix interface, traversing the intra-cellular machinery that transduces biophysical signals into the biochemical language of the cell and working towards the heart of the nucleus. Conceptually, this work mirrors this spatial organization and mimics the biological feedback that exists between genetics and matrix mechanics. The cell senses mechanical forces thought ligand-matrix binding events at the cell-ECM interface (Chapter 2), which the cell then transduces into biochemical signals using a variety of tools including actin polymerization and post-translational modifications to a variety of kinases and transcription factors (Chapter 3), which filter through the particular decision matrix of the genome (Chapter 4) and become reactions that update the mechanical environment and the state of the cells as it evolves in time.

The ultimate goal of this thesis is to enable coupling of the insights and tools from each

Chapter to rationally antagonize or hijack the cell's innate mechanosensing systems to provide novel therapeutics that complement the existing clinical management for PF. In Chapter 2, I described the use of nucleic acids to modulate cell-ECM interactions by mRNA-based expression a conformationally specific single chain antibody fragment ("scFV") to fibronectin. I hypothesized that scFV expression would antagonize pathologic αVβ3 integrin tone in fibrosis and demonstrated that: (1) cell linked scFv retained their ability to bind strain-mimic fibronectin fragments; (2) that these scFVs modulated focal adhesions in a linker-dependent fashion; (3) that these changes in focal adhesion biology did not fully predict the effects of these scFVs in mechanically-driven cell spreading assays; and, (4) that these scFVs can be expressed *in vivo* out to 8 days post instillation. In Chapter 3, I explored the mechanical regulation of TGFβ biology through LEMD3, an inner nuclear membrane protein, and LEMD3's role in the substrate stiffness-driven sensitization of fibroblasts to TGFβ signaling. I hypothesized that LEMD3's known inhibition of TGFβ signaling would itself be inhibited in a cellular stress dependent fashion. I found that: (1) that LEMD3's inhibitory interactions were inversely correlated to substrate stiffness; (2) that these interactions were not dependent on cellular stress to the nucleus, but were negatively correlated to both actin polymerization and YAP/TAZ knockdown; (3) that LEMD3 interactions were throughout the cell; (4) that LEMD3 was proteolytically modified in two locations and that cytoplasmic fragments resembling endogenous LEMD3 fragments were regulated by a serine protease, possibly cathepsin G; and, (5) that biopsies from pulmonary fibrosis patients recapitulated these *in vitro* phenotypes and demonstrated extra-nuclear LEMD3 interactions. Finally, in Chapter 4, I dissected the genomic architecture of the myocardin related transcription factor family ("MRTF") and serum response factor ("SRF") axis, a mechanically regulated transcription factor family, and characterized the development of tools necessary to understand its thermodynamic structure. I hypothesized that understanding the thermodynamic landscape for MRTF/SRF would permit for the development of stiffness-specific promoter elements from a rational design perspective. In this Chapter I showed:

(1) that the translocation of MRTF to the nucleus was stiffness-dependent but largely independent of fibrosis-relevant growth factor signaling from TGFβ at short time-scale; (2) that the murine CArGome was comprised of $\approx$ 20,000 individual CArG boxes, distributed over $\approx$ 2,000 individual sites, and that RNA transcription, MRTF/SRF occupancy, and the number and quality of CArG boxes in a particular peak were all correlated with one another; (3) that decoy CArG sequences were delivered to the cell on the scale of the endogenous CArGome *in vitro*; and (4) that a broad range of CArG probes from both endogenous and synthetic designs supported SRF binding necessary for future NGS-multiplexed gel-shift experiments.

CHAPTER 2

CONTEXTUAL ANTAGONISM OF αVβ3 INTEGRIN WITH A FN-STRAIN SPECIFIC SCFV, H5

2.1 Introduction

2.1.1 Importance of Fibronectin to Pulmonary Fibrosis

Fibronectin ("FN") is a key component of the provisional matrix deposited during wound healing and in tissue regeneration/fibrosis, which helps to pattern the collagen matrix of the new tissue and bind regenerative growth factors. [23, 24] Chronic lung injury through occupational and environmental exposures are key risk factors in the development of pulmonary fibrosis [25, 26] and much of the fibrotic program is derived from wound-associated myofibroblasts, which become constitutively active. [14, 27, 28, 29, 30] Given the central role of wound healing in pulmonary fibrosis and direct experimental evidence indicating that fibronectin's and particular fibronectin splice-variants' deposition is increased in fibrotic pathology [31, 32, 33], understanding the ability of this matrix molecule to drive cellular phenotype is of translational significance.

2.1.2 Fibronectin Mechano-sensing at the Matrix-Cell Interface

Many important mechano-transductive events occur at the interface between cells and the extra-cellular matrix ("ECM") as this space is the physical connection between the cell and its environment. This introduction focuses on fibronectin and focal adhesion biology that could be exploited to alter the cell's ability to sense its mechanical environment and to antagonize stiffness-driven fibrotic phenotypes. Specifically, this section motivates the therapeutic delivery of "H5", a strained-fibronectin specific single chain antibody fragment (scFv) by mRNA to antagonize excessive αvβ3 integrin signaling.

Integrin Switch in Fibronectin Between $\alpha v\beta 3$ and $\alpha 5\beta 1$

Physical Distention of Fibronectin's Integrin Binding Domain Drives the Integrin Switch

The integrin binding domain, located in the 9^{th} and 10^{th} type III repeats of fibronectin ("III_9" and "III_{10}", respectively), is engaged by both αv and α5 integrins. [34, 35, 36, 37] While αv integrins typically only require the RGD loop present in FN's III_{10} domain, α5 integrin's affinity for FN is strongly potentiated by the PHSRN sequence in FN III_9. [35, 34] Because FN's type III repeats are not stabilized by intra-repeat disulfide bridges, the relative position between the III_9 and III_{10} domains (and the PHSRN and RGD peptide sequences) can be strained by pico-newton levels of stress provided by cellular contraction. [38, 39, 40] This physical decoupling of the III_9 and III_{10} domains allows for mechanical forces applied to FN to dictate the relative balance of αv and α5 integrin binding, the so-called "integrin-switch," which has now been verified *ex vivo* in fibrotic and developing tissues. [38, 41, 29]

Cellular Phenotypes Associated with the Integrin Switch

The use of protein mimetic or fragments of fibronectin III_9 and III_{10} provide strong *in vitro* evidence that a shift towards αvβ3 integrin engagement over $\alpha 5\beta 1$ supports mesenchymal and fibrotic phenotypes. [42, 43, 44] Epithelial cells exposed to biochemically decoupled III_9 and III_{10} domains were more likely to undergo epithelial-to-mesenchymal transformation and expressed myofibroblastic markers, like α-smooth muscle actin, than cells plated on FN with stabilized III_9 and III_{10} domains. [43, 44] In fibroblast, a fibronectin fragment lacking the $\alpha 5\beta 1$ necessary III_9 domain strongly up-regulated matrix synthesis relative to III_8-III_{10} fragments. [45] Integrin selection through unfolded fibronectin has also been shown to be important in regulating the levels of wound-healing associated growth factors like VEGF. [46] These alternations in phenotype are likely due to changes in focal adhesion composition and activity, such as focal adhesion kinase and the Src family of kinases,

that accompany the switch between αv and α5 integrins when the III_9 and III_{10} repeats are decoupled. [47] The importance of these *in vitro* findings are corroborated by cre-knockout of the αv integrin *in vivo*, which has proven to be strongly protective against fibrotic development in multiple organs, including the lungs, liver and kidneys in mice. [48]

Targeting Strained Fibronectin to Inhibit $\alpha v\beta 3$ Integrin Switching

The altered mechanics of fibrosis drive inappropriate $\alpha v\beta 3$ tone through a conformational distortion of fibronectin's III_9 and III_{10} integrin binding domains (IBDs). Targeting this altered confirmation of fibronectin may have therapeutic value through antagonizing $\alpha v\beta 3$ tone relative to $\alpha 5\beta 1$ tone. Previously, the Barker lab discovered a single chain antibody fragment (scFv) through phage display that specifically bound biochemically decoupled ("strain mimic") fibronectin IBD fragments relative to biochemically stabilized ("relaxed mimic") fibronectin IBD fragments. [49] This scFv, termed H5, has been shown to bind physically strained fibronectin preferentially both *in vitro* and *ex vivo*, and inhibits $\alpha v\beta 3$ signaling. [29] Moreover, this antibody's accumulation in the lungs was correlated with the progression and regression of a bleomycin-induced model of pulmonary fibrosis in mice relative to a control, scrambled scFv, indicating that H5 is able to recognize fibrosis associated distortions to the matrix. [49] These findings motivate the therapeutic use of H5 in experimental models of fibrosis as an antagonist to pathologic, matrix-driven $\alpha v\beta 3$ signaling.

2.1.3 Genetics as a Therapeutic Intervention at the Cell-Matrix Interface

While information from the physical environment filters through the cells and converges on the genome of the cell to drive long-term alterations in mechanical phenotypes, genetics and nucleic acids proper are not thought to play a direct role in stiffness sensing at ECM-cell interface. However, using an innovative technique pioneered by the Santangelo lab, I have chosen to deliver H5 as messenger RNA ("mRNA"), encoding membrane tethered

forms of H5, thereby demonstrating the novel use of nucleic acids to modulate mechanosensing at the cell-ECM interface. In the following sections I describe the motivation for delivering of H5 as mRNA and the motivation for the specific membrane linkers I chose to explore.

Airway Delivery of H5 mRNA

mRNA as a vehicle for therapeutic delivery of proteins or as therapy in and of itself has been demonstrated in a variety of *in vivo* application to the lung and beyond, including the treatment of anemia, asthma, and lung surfactant deficiency. [50, 51, 52, 53] These approaches different significantly from DNA- [54, 55], viral- [56, 57, 58] or recombinant protein [59] based-therapies in terms of their safety (*e.g.* no risk of genomic incorporation), immunogenicity/repeatability (*e.g.* no antibodies develop against the viral delivery vectors) and cost-effectiveness. Additionally, incorporation of modified chemical bases into the sequence of synthetic mRNAs has been shown to decrease their recognition by the innate immune system and prevent stress-granule formation, which can limit translation of exogenous genetic therapeutics. [60] Finally, using an micro-spraying technique pioneered by the Santangelo Lab, the delivery of naked mRNA in a PBS-based aerosol has been demonstrated (Personal Communication). This simple and safe formulation allows mRNA-based therapeutics to be delivered specifically to the airspace, without systemic exposure, and without the pharmacological and inflammatory complications associated with chemical/liposomal or nano-/micro-particle delivery mechanisms. [61, 62, 63]

Motivation for Thy-1-inspired GPI Linker and CD8 Peptide Linkers

The necessity for cellular translation of mRNA-based therapy by cells affords unique opportunities to use cells themselves as a solid support for therapeutic protein expression. Specifically, it restricts access of H5 to fibronectin that is necessarily accessible to cells, potentially increasing the efficacy of the therapeutic targeting as H5 is not sequestered

by cellularly inaccessible fibronectin. Additionally, tethering H5 proteins to cells avoids many of the pharmco-kinetic difficulties encountered in delivering proteins and peptides to the lungs including clearance by the muco-ciliary tract [64], absorbance and clearance by the lymphatic and systemic routes [65, 66], and sequestration and degradation by airway macrophages. [67, 68] Previous characterization of the pulmonary half life of human growth factor ($\approx$ 22kDa, similar in size to H5) found its effective half-life was $\approx$ 10.5 hours in rat lungs. [68] Tethering H5 to the surface of cells may alter these undesirable kinetics without without the need for advanced pharmacological interventions to the protein, such as Fc domain fusions [69, 70] or extensive PEG-ylation of the molecule. [71]

Furthermore, tethering H5 expression to the cells' surfaces may allow for additional functionality to be derived from the linker to the membrane itself. The glycosylphosphatidylinositol ("GPI") linker derived from Thy-1, a cell-surface glyco-protein, is of particular interest to applications in pulmonary fibrosis because of Thy-1 innate role in the development of pulmonary fibrosis and because of its role in modulating the biology of αVβ3 integrins. [72, 73, 74, 30] Specifically, the GPI-linker of Thy-1 has been shown to associate with αVβ3 integrin in the plasma membrane. This association is lost with mutation of Thy-1's RLD domain or through substitution of the GPI linker for a canonical single-pass peptide transmembrane domain from CD8's α transmembrane domain. [75] This association with αVβ3 integrin has been shown to be dependent on the GPI linker's association with cholesterol lipid rafts on the membrane's surface. [76, 77] Furthermore, the association of Thy-1's GPI linker with lipid rafts allows for Thy-1 to coordinate the composition of proteins in focal adhesions. Specifically, Thy-1 has been shown to precluster fyn, a member of the Src Family Kinases ("SFK") found in lipid rafts, within focal adhesions, modulating the relative balance of focal adhesion kinase ("FAK") and SFK signaling through integrins. [78, 79, 80, 81] The experimental contrast between CD8- and GPI-based linkers led me to incorporate these design features into my work with membrane-bound H5.

In this Chapter I present my work exploring the hypothesis that membrane-bound H5

antagonizes αVβ3 integrin signaling both through H5's innate function in binding strained fibronectin and through modulation of focal adhesion signaling, and I demonstrate the ability to deliver these therapeutic mRNA constructs *in vivo.*

2.2 Methods

2.2.1 Cell Culture, Fibronectin Fragments and Transfection Protocol

Primary human foreskin fibroblasts ("HFFs") were procured from ATCC (ATCC SCRC-1041, ATCC, Manassas, VA) and routinely cultured in DMEM (ThermoFisher, Waltham, MA) supplemented with 15% FBS and 1% penicillin/streptomycin (ThermoFisher, Waltham, MA) in 5% CO_2 at 37C in a humidified incubator to passage 13. Chinese Hampster Ovary ("CHO") cells were stably transfected to express either human αVβ3 integrin ("CHOB2") or human α5β1 integrins ("CHOK1") and previously characterized and gifted to the Barker lab. [82] These cells were routinely cultured in F-12K median (ThermoFisher, Waltham, MA) supplemented with 10% FBS and 1% penicillin/streptomycin (ThermoFisher, Waltham, MA) in a 5% CO_2 in a humidified incubator till passage 25. Rat lung fibroblasts ("RFL-6") were procured from ATCC (ATCC CCL-192, ATCC, Manassas, VA) and routinely cultured in DMEM (ThermoFisher, Waltham, MA) supplemented with 20% FBS and 1% penicillin/streptomycin (ThermoFisher, Waltham, MA) in 5% CO_2 at 37C in a humidified incubator to passage 13.

Fibronectin fragments (fibronectin's III_9 and III_10 domains) were a kind gift from Dr. Haylee Bachman. The fragments contain either a stabilizing proline mutation, which relatively fixes the domains' positions ("9*10") or a 4 glycine linker, which conformationally destabilizes the two domains ("4G"). The production and purification of these fragments are described in detail previously. [29] Fragments were stored at -80C until use and only freeze-thawed 3 times.

All cells were transfected with mRNA using Lipofectamine 2000 (ThermoFisher, Waltham, MA). Confluent or near confluent cultures of fibroblasts or CHO cells in 6 well plates

were inoculated with 250 μL of OptiMEM containing 1μg of mRNA and 2uL of Lipofectamine2000, formulated according to the manufacturer's protocol. All transfections were done in antibiotic free media or OptiMEM for at least 6 hours, at which point, the cells were washed and cultured routinely.

2.2.2 mRNA Cloning and Production

DNA encoding the mRNA constructs were codon optimized and ordered as Gene Blocks (IDT, Coralville, IA) and ligated into pMA-7 plasmid backbones using NotI/HindIII (New England Biolabs, Ipswich, MA) digestion and ligation. Sequences for these constructs were confirmed using Oligos from Table 2.2 by Sanger sequencing (Macrogen USA, Rockville, MD). Subsequent incorporation of nano-luciferase fusions into these designs was accomplished by Gibson assembly using a HiFi Assembly Kit and NEBuilder tool (New England Biolabs, Ipswich, MA) from stock nano-luciferase containing plasmids in the Santangelo Lab, originally obtained from Addgene (Cambridge, MA). Oligos for Gibson assembly are listed in Table 2.2. DNA plasmid stocks were purified using a DNA Midi Kit (Qiagen, Hilden, Germany).

Plasmids encoding mRNA constructs were linearized with Not-I HF (New England Biolabs, Ipswich, MA) overnight and PCR purified using PCR clean-up kit (Qiagen, Hilden, Germany). *In vitro* transcription was performed using a T7 mScript Kit (Cellscript, Madison WI) according to the manufacturer's instructions with the following modifications: N1-methylpseudouridine-5-triphosphate (TriLink, San Diego, CA) was used instead of uracil with equimolar concentrations of other nucleotides (ATP, CTP, GTP, also TriLink). Constructs were capped with 2-O-Methytransferase followed by enzymatic addition of a poly-A tail for 90 minutes. Finally, constructs were treated with Antarctic Phosphatase (New England Biolabs, Ipswich, MA) for 1 hour (New England Biolabs, Ipswich, MA). Intermediate and final purifications were performed using an RNeasy midi or maxi-kit (Qiagen, Hilden, MA) according to the expected yield of mRNA. After final purification, RNA was recon-

stituted in PBS, and the concentration was determined using 260nm/280nm module on a NanoDrop spectrophotometer (ThermoFisher, Waltham, MA). The mRNA was stored at -80°C until use.

2.2.3 Dose and Time Course Assay

HFFs were transfected on glass coverslips as above in antibiotic free media at doses ranging from 100ng to 1μg. All time course data cells were dosed with 1μg of mRNA. Time course cells were fixed in 4% paraformaldehyde in PBS at the appointed time post-transfection. All dose-response cells were cultured for one day and then fixed in 4% paraformaldehyde in PBS. Coverslips were then permeabilized in 0.1% Triton X-100 in PBS. Following permeabilization, the cells were blocked in 5% BSA, 5% goat serum and 5% donkey serum in PBS for one hour at room temperature. Cells were then incubated with primary anti-V5, anti-αVβ3 antibodies from Table 2.1 overnight in a 1% goat serum solution of PBS at 4°C. The following day, the coverslips were washed three times in PBS-T, and incubated for an hour at room temperature with the 488, 657 secondary antibodies listed in Table 2.1 in PBS-T, counter-stained with 1:40 AlexaFluor546 conjugated phallodin and 1:1000 Hoescht 33342 (ThermoFisher, Waltham, MA) and washed three more times for 5 minutes each in 1X PBS-T. Coverslips were then mounted to 25mm coverslips with Prolong Gold (ThermoFisher, Waltham, MA). These coverslips were sealed to a microscope slide and stored at -20°C until imaged.

Coverslips were imaged using a Axiovert 200M microscope (Carl Zeiss Microscopy, Jena, Germany) with an UltraVIEW spinning disk (PerkinElmer, Waltham, MA) and Flash 4.0v2 cMOS camera (Hamamatsu Photonics, Hamamatsu City, Japan). 40X images were collected using a 1.4NA Plan-Apochromat objective (Carl Zeiss Microscopy, Jena, Germany). Image acquisition and analysis of cell expression was performed in Volocity (PerkinElmer, Waltham, MA). Cells' expression data were exported and analyzed in Prism (Graphpad, La Jolla, CA).

2.2.4 CHO-Fibronectin Binding Assay

Clear bottom, 96 well plates were prepared by incubation at 37°C for 1 hour with one of four ligands: (1) fibronectin fragments that mimic the stabilized, mechanically relaxed integrin binding domain ("9*10"); (2) fibronectin fragments that mimic a strained, destabilized integrin binding domain ("4G"); (3) 10μg/mL human fibronectin; or (4) 1% BSA passivated surfaces. All surfaces were then washed 3 times with PBS and blocked at 4°C with 1% BSA in PBS until use. After initial characterization of cell binding to the fibronectin fragments with ligand concentrations between 250nM and 2μM, all subsequent experiments with fragments were conducted at 250nM.

Stably transfected CHO cells expressing either human αVβ3 or α5β1 integrins were harvested in 135mM potassium chloride with 1.5mM sodium citrate, spun down at 1000g for 5 minutes, and resuspended to a concentration of 200,000 cells/mL in pre-warmed, serum free media. For the standard curve, these cells were plated in a dilution series from 20,000 cells per well to 1000 cells per well in a constant volume of 100 μL in duplicate for each CHO cell line on full length fibronectin surfaces. For experimental conditions, 20,000 cells were plated in 100 μL volumes on the experimental surfaces and incubated for 20 minutes at 37°C in a 5% CO_2 incubator. The standard curve conditions were plated first and then the experimental cells were plated. All plating and subsequent washing was conducted using an 8-channel multi-well pipette to allow for minimal plating time. Following the incubation at 37°C, the standard curve cells were fixed directly in the wells through the addition of 10% glutaraldehyde in PBS. For experimental cells, the media was removed, cells were washed once with ice-cold PBS, and then fixed in 5% glutaraldehyde for 10 minutes. After fixation, wells were washed three times with PBS and then stained with 0.1% crystal violet in water for one hour. After staining, well were washed 3 times with PBS and allowed to air dry over night inverted. After drying, the remaining crystal violet was solubilized with 100μL of 10% acetic acid and the absorbance of wells was measured on a Synergy H4 with Hybrid Technology plate reader (BioTek, Winooski, VT)

plate reader using a monochromoter at 570nm. Raw absorbance values were imported into Prism (Graphpad, La Jolla, CA) for analysis. Each well's absorbance was corrected for background crystal violet staining using wells without cells plated and the final number of adherent cells was interpolated from the standard curve from that plate.

2.2.5 RFL6 Mechanotransduction Assay

RFL-6 cells were plated at a concentration of 10,000 cells/cm^2 in 6 well plates and allowed to adhere for 4 hours. After the cells had adhered, the media was exchanged for OptiMEM (ThermoFisher, Waltham, MA), and these fibroblasts were then transfected with 1μg of mRNA or vehicle alone using 2 μL of Lipofectamine2000 (ThermoFisher, Waltham, MA) in a 250 μL reaction in OptiMEM according to the manufacturer's instructions. The following day, cells were harvested in 135mM potassium chloride with 1.5mM sodium citrate, spun down at 1200g for 5 minutes and resuspended in serum free media. 3000 cells/cm^2 were plated on 1kPa and 25 kPa hydrogel surfaces (Matrigen, Brea, CA) functionalized with 10 μg/mL human fibronectin according to the manufacturer's instructions. Cells were allowed to spread on these surfaces at 37°C in a 5& CO_2 incubator for 4 hours.

After spreading, cells were washed in ice-cold PBS, fixed in 4% paraformaldehyde in PBS for 10 minutes and then permeabilized in 0.1% Triton X-100 in PBS. Following permeabilization, the cells were blocked in 5% BSA, 5% goat serum and 5% donkey serum in PBS for one hour at room temperature. Cells were then incubated with primary anti-V5 antibody from Table 2.1 overnight in a 1% goat serum solution of PBS at 4°C. The following day, the hydrogels were washed three times in PBS-T, and incubated for an hour at room temperature with the 488 secondary antibody listed in Table 2.1 in PBS-T, counter-stained with 1:40 AlexaFluor546 conjugated phallodin (ThermoFisher, Waltham, MA) and washed three more times for 5 minutes each in 1X PBS-T. Hydrogels were then mounted to 25mm coverslips with PLA Mounting Media with DAPI (Sigma, Hilden, Germany). These coverslips were sealed to a microscope slide and stored at -20°C until imaged.

Hydrogels were imaged using a Axiovert 200M microscope (Carl Zeiss Microscopy, Jena, Germany) with an UltraVIEW spinning disk (PerkinElmer, Waltham, MA) and Flash 4.0v2 cMOS camera (Hamamatsu Photonics, Hamamatsu City, Japan). 40X images were collected using a 1.4NA Plan-Apochromat objective (Carl Zeiss Microscopy, Jena, Germany). Image acquisition and analysis of cell morphology was performed in Volocity (PerkinElmer, Waltham, MA). Individual cell morphologies were exported and analyzed in Prism (Graphpad, La Jolla, CA).

2.2.6 Focal Adhesion Phosphorylation by Western Blot

HFFs were transfected in 6 well plates at confluence in antibiotic free media with 1μg of mRNA or vehicle alone using 2 μL of Lipofectamine2000 (ThermoFisher, Waltham, MA) in a 250 μL reaction in OptiMEM according to the manufacturer's instructions. After overnight incubation, cells were collected using a solution of 135mM potassium chloride and 1.5mM sodium citrate, spun at 1200g for 5 minutes and resuspended in warm serum free media. 100,000 cells were plated into 6 well plates functionalized with 10μg/mL human fibronectin in 1 mL total volume. These cells were incubated at 37°C for 30 minutes in a 5% CO_2 incubator. After incubation, the surfaces media was aspirated and washed with ice-cold PBS. The PBS was aspirated and the cells were directly lysed into 60μL of 2X loading dye supplemented with Pierce protease and phosphatase inhibitors tablets (ThermoFisher, Waltham, MA). This lysate was collected using a cell scraper and then treated with 0.3 μL of benzonuclease (ThermoFisher, Waltham, MA) for 15 minutes at room temperature with vigorous shaking. Samples were heated to 95°C for 5 minutes and 20μL of the total solution was run on a 4-12% Bis-Tris gel in 1x MES buffer and run for 70 minutes at 150V. The gel was then transferred to a nitrocellulose membrane using the XCell Blot Module (ThermoFisher, Waltham, MA) at 25V for 65 minutes. Membranes were air-dried for an hour, and blocked with 5% BSA in 1X TBS for an hour at room temperature. The blots were then incubated with primary antibodies as described in Table

2.1 in 1X TBS-T with 1% BSA for 16-24 hours at 4°C with shaking. Near-IR or HRP conjugated secondaries as described in Table 2.1 were then incubated with the blot and imaged subsequently on either an Odyssey CLx system (Licor, Lincoln, NE) Band analysis was performed using the associated Licor software and exported to Prism (Graphpad, La Jolla, CA) for analysis.

2.2.7 In vivo Delivery of mRNAs

Eight to 10-week old female BALB/c mice (Charles River Laboratories, Wilmington, MA) were house in the Physiology Research Lab in the Engineering Biosciences Building and cared for in accordance with Georgia Institute of Technology and National Institutes of Health guidelines. Food and water was provided *ad libitum.* Animals were quarantined for 6 days before any experiments were performed. All animals were euthanized with CO_2 asphyxiation. Experimental review covering this work was provided by Georgia Institute of Technology's Institutional Animal Care and Use Committee (IACUC), protocol #A17015.

For mRNA instillation, mice were anesthetized using an IP injection of 87 mg/kg ketamine and 16 mg/kg xylazine. The mice were intubated with 1.22 mm endotracheal tubing (Hallowell EMC, Pittsfield, MA) on a 45° tilt table with a surgical lamp to provide visualization of the trachea. Aerosol delivery was performed using a MicroSprayer Model 1A-1C with a High Pressure Syringe Model FMJ-250 (PennCentury, Philadelphia, PA), which was pumped using a custom Pump 11 Elite Nanomite handheld syringe pump (Harvard Apparatus, Holliston, MA). 50 μL of mRNA were delivery for each animal and total mRNA doses of V5-tagged and nano-luciferase fused mRNA constructs were 100 μg per animal and 133 μg per animal, respectively. Animals were recovered from anesthesia under a heat lamp and returned to housing until experimental sacrifice one and eight days after mRNA instillation.

2.2.8 Flow Cytometry and FACS of Single Cell Suspensions

Generation of Live/DEAD Stained, Single Cell Suspensions

Dissected lungs were washed in ice cold PBS and then digested into a single cell suspension using the Miltenyi Biotec Lung dissociation kit and protocol (Cat. # 130-095-927, Miltenyi Biotec, Auburn, CA) with the following changes: (1) the amounts of enzyme D and enzyme A were reduced by 40% to 60uL enzyme D and 9uL enzyme A per cell prep; (2) the digestive enzymes were not added until after the initial tissue crush in the gentleMACS device; and, (3) the samples were not incubated on a rotor during the digestion by enzymes A and D but were shaken vigorously at 37°C in a shaking water bath upright. After the Miltenyi digestion protocol, the suspensions were pelleted at 4°C for 10 minutes at 300g and resuspended in 3mL of red cell lysis solution (Alfa Aesar, Haverhill, MA) for 5 minutes. The reaction was quenched by addition of at least 20 mL of ice-cold PBS to each suspension. The cells were then pelleted at 4°C for 10 minutes at 300g and counted using a hemocytometer. 3 million cells were aliquoted per reaction and stained for 30 minutes at 4°C with Blue Live/DEAD fixable dye (ThermoFisher, Waltham, MA) according to the manufacturer's instructions. The cells were then pelleted at 4°C for 10 minutes at 300g.

Flow Cytometry Protocol

After pelleting the cells following Live/DEAD staining, the cells were resuspended in PBS with 2% FBS and then pelleted again at 4°C for 10 minutes at 300g. The cell pellet was resuspended in 500 μL of 2% paraformaldehyde and incubated for 10 minutes at room temperature. From this point on, the cells were routinely pelleted at 4°C for 5 minutes at 1200g. After pelleting the cells were washed once in 1mL of 2% FBS in PBS, pelleted again and stained in 200 μL of antibody solution for 30 minutes shaking at 4°C. The antibodies used, along with their relative dilutions into 2% FBS in PBS, are listed in Table 2.1. After antibody staining, the cells were pelleted and washed once in 2% FBS in PBS before

being resuspended in 250 μL and strained into flow tubes through a 70μm filter. Cells were stored on ice until run on the cytometer. Cells were analyzed using a LSRFortessa running FACSDiva software (BD, Franklin Lanes, NJ). Exported FCS files were analyzed and representative plots generated in FlowJo (BD, Franklin Lanes, NJ). Data exported from FlowJo was analyzed and graphed in Prism (Graphpad, La Jolla, CA). Compensation and gating by negative cell populations are described below.

FACS Protocol

Staining the cells in preparation for FACS is similar to the protocol used for flow cytometry with the following changes: (1) cells were not fixed after Live/DEAD staining and were instead resuspended and washed in 2% FBS in PBS; (2) all pelleting steps remained at 4°C for 10 minutes at 300g; (3) the primary antibody solution did not contain the primary V5-647 conjugate listed in Table 2.1 but did contain all the other primary antibodies; (4) during their final resuspension, the cells were resuspended in FACS buffer (1mM EDTA, 25mM HEPES at pH 7, 1% FBS in 1X PBS). Cells were stored on ice until run on a custom BD FACSAria Fusion sorter running FACSDiva software (BD, Franklin Lanes, NJ). Sorts were conducted using a "4-way purity sort" until there were at least 10,000 cells in each population. Cells were sorted into chilled FACS buffer. Exported FCS files were analyzed and representative plots generated in FlowJo (BD, Franklin Lanes, NJ). Data exported from FlowJo was analyzed and graphed in Prism (Graphpad, La Jolla, CA). Compensation and gating by negative cell populations are described below.

Compensation and Fluorescence Minus One Controls for FACS and Flow Cytometry

Antibody compensation beads were prepared using AbC Total beads according to the manufacturer's protocol (ThermoFisher, Waltham, MA). One drop of beads was incubated with 1μL of each individual primary antibody for 30 minutes at 4°C. A single drop of the kit's negative control beads was then added to each reaction, which was supplemented with 100

μL of 2% FBS in PBS. Live/DEAD compensation beads were prepared in a similar fashion using ArC beads and the associated ArC negative control beads instead of AbC beads (ThermoFisher, Waltham, MA). Fluorescence minus one ("FMO") controls were prepared from cell suspensions that were processed according to the FACS and flow cytometry staining protocols above except a single primary antibody conjugate was omitted from the antibody staining solution for each marker used in the panel.

Each cytometer's detector voltage settings were calibrated using the compensation beads to create at least a half log difference in fluorescent intensity between that bead's channel and any other detector used during the assay. A compensation matrix was generated and algorithmically validated by the cytometer's software. FMO samples were used to create the gates discriminating positive and negative cell populations for each antibody/dye.

2.2.9 nanoLuciferase Assays

In vitro nano-luciferase assay: Transfected cells were harvested from culture or from FACS and plated in a white 96-well plate microtiter plate (Corning, Corning, NY) in 100 μL volumes. Nano-luciferase assays were performed on a Synergy H4 with Hybrid Technology plate reader (BioTek, Winooski, VT) according to the manufacturer's instructions (Promega, Madison, WI) with the following modifications: 100 μL of nano-luciferase assay buffer was injected using plate reader's integrated pumps, luciferase integration times were held to 1 second, and the plate reader's detector voltages were adjusted by the software based on brightest wells to maximize the dynamic range of the assay. Raw luminescence values were exported to text files and analysis was performed in Prism (Graphpad, La Jolla, CA).

In vivo nano-luciferase assay: Lungs harvested from experimental animals were washed in ice-cold PBS and then incubated in 500 μL of a 1:40 nano-luciferase reagent in PBS (Promega, Madison, WI) in black, 12 well plates (BioTek, Winooski, VT) and imaged using an IVIS Spectrum CT (PerkinElmer, Waltham, MA). Images were acquired using

an integration time of 60 seconds and a binning factor of 8. ROIs were fitted to each well and the area and total luminescence for each ROI were exported to Prism for analysis (Graphpad, La Jolla, CA).

2.2.10 Immunofluorescence in Cyrosectioned Lung Tissue

Dissected lungs were immersed in a 3:1 by volume solution of 30% sucrose and OCT (ThermoFisher, Waltham, MA) on ice. These lungs were subjected to house vacuum for an hour before being transferred to cyromolds filled with OCT. Molds were frozen in a 2-methyl-butane bath (Sigma, St. Louis, MO) cooled with dry ice. Embedded sections were stored at -80°C until sections. 10μm sections were cut on a CyroStar NX70 cyrostat (ThermoFischer, Waltham, MA).

Following sectioning, tissue was isolated using a pap-pen, fixed for 10 minutes in 2% paraformaldehyde in 1X PBS, permeabilized for 5 minutes in 0.1% Triton X-100 in PBS and blocked in 5% BSA, 5% goat serum, and 5% donkey serum solution in 1X PBS for one hour at room temperature. Samples were incubated in primary antibody solution overnight at 4°C using the V5 antibody listed in Table 2.1 in PBS-T with 1% goat serum. Tissues were washed three times in PBS-T with 5 minute incubations before incubation for an hour at room temperature with the 488 secondary antibody listed in Table 2.1 in PBS-T, counter-stained with 1:40 AlexaFluor546 conjugated phallodin and 1:1000 Hoescht 33342 (ThermoFisher, Waltham, MA) and washed three more times for 5 minutes each in 1X PBS-T. Samples were sealed with Prolong Gold (ThermoFisher, Waltham, MA) and stored at -20°C until imaged.

Tissues were imaged using an Axiovert 200M microscope (Carl Zeiss Microscopy, Jena, Germany) with an UltraVIEW spinning disk (PerkinElmer, Waltham, MA) and Flash 4.0v2 cMOS camera (Hamamatsu Photonics, Hamamatsu City, Japan). High resolution images (40X) were collected using a 1.4NA Plan-Apochromat objective (Carl Zeiss Microscopy, Jena, Germany). Whole tissue images were created by finding an ROI to encom-

pass the entire tissue, fitting the ROI to a focus map to adjust for systemic focal bias, and then stitching individual images together using 15% overlap between individual frames. Image acquisition and analysis was performed in Volocity (PerkinElmer, Waltham, MA).

Table 2.1: Primary and Secondary Antibodies Used in this Chapter

					Application					
	Target	Clone	Host	Dye Conjugate	IF	FlowCyto	FACS	WB	Vendor	Cat #
Primary	V5	1036H	Rabbit	Alexa Fluor 647		1:50			R&D Biosystems	FAB8926R
	CD31	390	Rat	PE-CF594		1:200	1:200		Biolegend	102429
	CD45	30-F11	Rat	Brilliant Violet 711		1:500	1:500		Biolegend	103147
	CD326	G8.8	Rat	APC/Cy7		1:50	1:50		Biolegend	118217
	V5	Polyclonal	Rabbit		1:1000			1:1000	Abcam	ab9116
	pFAK	Polyclonal	Rabbit					1:1000	Invitrogen	44-624G
	pSFK	Polyclonal	Rabbit						CST	2101
	GAPDH	D-6	Mouse					1:1000	Santa Cruz	sc166545
	Integrin	LM609	Mouse		1:1000				EMD Millipore	MAB1976
Secondary	Donkey anti-Rabbit IR680	Polyclonal	Donkey	680 IR Dye				1:20000	Licor	926-68073
	Donkey anti-Mouse CW800	Polyclonal	Donkey	800 IR Dye				1:20000	Licor	926-32212
	Goat anti-Rabbit	Polyclonal	Goat	Alexa Fluor 488	1:500				Invitrogen	A-11008
	Goat anti-Mouse	Polyclonal	Goat	Alexa Fluor 647	1:500				Invitrogen	A-21245

Table 2.2: Oligos for Sequencing and Cloning Used in this Chapter

Oligo	5'-3' Sequence	Purpose	Tm	Concentration	Vendor	Cat. #
nanoLuc Adapter Forward	gctgcccccgcctccTCTCTTGATTTCCACCTTG	Gibson Assembly of H5-CD8 & Thy-1 mRNA with nanoLuc	59.7	500nM		
nanoLuc Adapter Reverse	gctGCTGCTGCTGCTCACGAG		59.7	500nM		
H5-CD8-NanoLuc Forward	ccaaggtggaaatcaagagaggaggagcgggggcagcATGGTCTTCACACTCGAAGATTTCG	H5-CD8 Specific Gibson Primers	67.6	500nM		
H5-CD8-NanoLuc Reverse	gtctcgtgagcagcagcagcagcCGCCAGAATGCGTTCGCAC		67.6	500nM		
Thy-1-NanoLuc Forward	tcagagacaaactggtcaagggaggcgggggcagcATGGTCTTCACACTCGAAGATTTCG	Thy-1 Specific Gibson Primers	67.5	500nM	IDT	Custom
Thy-1-NanoLuc Reverse	gtctcgtgagcagcagcagcagcCGCCAGAATGCGTTCGCAC		67.6	500nM		
Interior Seqeuncing Primer	TAAGCTGCTGATCTACGCTGCC	Interior Sanger Sequencing Primer for Gibson Products	60	2uM		
5' mRNA Sequencing Primer	TTTTAAGCTTTAATACGACTCACTATAGG	5' Sanger Sequencing Primer for mRNA Constructs	60	2uM		
3' mRNA Sequencing Primer	TTTTTGCGGCCGCCTTC	3' Sanger Sequencing Primer for mRNA Constructs	60	2uM		

2.3 Results

2.3.1 mRNA Constructs Expressed in a Dose-Dependent Fashion on the Surface of Fibroblasts within 4 Hours of Transfection

The kinetics and dose-dependence of surface expressed mRNA constructs were assessed by confocal microscopy. HFFs transfected with H5-mRNA constructs using Lipofectamine 2000 demonstrated clustered surface expression of H5-GPI and H5-CD8 proteins that was qualitatively distinct from the pattern of $\alpha V\beta 3$ surface expression in these cells (Figure 2.1A). Expression of mRNA constructs was linearly dose-dependent (r^2=0.9377)

with mRNA loads between 100ng and 1ug of mRNA one day after transfection (Figure 2.1B). HFFs began expressing mRNA constructs on their surface 4 hours after transfection (p=0.0106), and expression increased further during one day of culture (Figure 2.1C, p=0.0054).

2.3.2 CD8- and GPI-linked H5 Constructs Specifically Increased Adherence to Strained Fibronectin Fragments

In order to ascertain whether this surface expressed H5 protein was functional, adhesion assays using CHO cells expressing a single human integrin pair ("CHOB2" cells expressed αVβ3 while "CHOK1" cells expressed α5β1 integrins) were performed on previously established fibronectin fragments that mimic the strain or relaxed forms of the integrin binding domain of fibronectin's III_9-III_{10} repeats (Figure 2.2). [44, 43, 29, 49] Untransfected CHOK1 cells demonstrated a binding preference to relaxed-mimic fragments ("9*10") relative to strain-mimic fragments ("4G") at all fragment concentrations, though the difference was greatest at 250nM concentration. CHOB2 cells did not have a preference for strain- or relaxed-mimic fragments at any fragment concentration (Figure 2.2A&B). These data were consistent with previous literature, which found that α5β1 integrins required both the RGD motif on fibronectin's III_{10} repeat and the close juxtaposition of the PHSRN sequence on fibronectin's III_9 repeat, while αVβ3 integrins only required the RGD motif and were insensitive to PHSRN's relative position. [35, 34].

Experimentally treated CHOB2 and CHOK1 cells demonstrated greater binding to full length fibronectin coated surfaces than BSA passivated surfaces after 30 minutes in serum free media (Figure 2.2C, p=0.0141 and p=0.0058 for CHOK1 and CHOB2 binding to fibronectin relative to BSA, respectively). Overall, the expression of either H5-CD8 or H5-GPI linked proteins significantly shifted the balance of CHOK1 binding towards stain-mimic fibronectin fragments (p=0.002 and p=0.0022 for CHOK1 cells treated with CD8- and GPI-linked H5 mRNA). A similar, non-significant trend was observed in CHOB2 cells,

indicating potentially increased cellular avidity for these surfaces. These data indicated that H5 expression imparted a fibronectin strain-specific affinity to cells' interactions with their surrounding matrices.

2.3.3 H5-GPI Expression Increased Global Src Family Kinase Phosphorylation in Fibroblasts

I hypothesized that the H5-GPI linker would specifically promote pre-clustering of members of the Src Family Kinases ("SFK") to focal adhesions and increase their activity via phosphorylation, based on a previous established role for Thy-1's GPI linker. [30] To test this hypothesis and to determine if either mRNA construct had an effect on global focal adhesion signaling as measured by alterations in focal adhesion kinase ("FAK") phosphorylation, phospho-western blots on lysates from fibroblasts expressing H5-CD8 and H5-GPI linked proteins were performed (Figure 2.3). H5-GPI linked constructs demonstrated significantly increased levels of phospho-SFK relative to vehicle treated controls (Figure 2.3B, $p=0.0088$). A similar, statistically insignificant trend was observed in lysates from H5-CD8 expressing fibroblasts. Interestingly, the degree of phospho-FAK and phospho-SFK were strongly correlated to the degree of GPI-linked H5 expression in these lysates (Figure 2.3C&D, $r=0.9951$ with $p<0.0001$ and $r=0.9768$ with $p=0.0008$ for H5-GPI vs. pFAK and H5-GPI vs pSFK correlations, respectively). Similarly, less pronounced trends were present in lysates from fibroblasts transfected with H5-CD8 constructs. These correlations suggested that H5-GPI constructs, in particular, may be both pre-clustering elements of the focal adhesion complex while also modulating focal adhesion signaling globally.

2.3.4 H5-CD8 Constructs Altered the Mechanotransductive Phenotype of Thy-1 Null Fibroblasts

RFL6 mechanosensing on soft and stiff substrates through cell spreading and polarization was used to assess the phenotypic consequences of expression of H5-CD8 or H5-GPI constructs. RFL6 cell spreading and polarization had previously been shown to be

sensitive to $\alpha V\beta 3$ modulation through expression of Thy-1. [30] Surprisingly, while all cells, regardless of experimental group, showed increased cell spreading on stiff relative to soft substrate ($p<0.0001$ for all groups), H5-CD8 treated cells were significantly more spread than vehicle treated controls (Figure 2.4C, p=0.0012). Furthermore, RFL6 cells on stiff substrates trended towards being less polarized, with a significant difference observed in vehicle treated control fibroblasts (Figure 2.4B p=0.0005). These data indicated that global alternations in focal adhesion protein activation observed in Figure 2.3 may not have cleanly correlated to mechano-transductive phenotypes in fibroblasts. This discordance may have arisen specifically because H5-CD8 proteins may not have co-clustered as significantly with $\alpha V\beta 3$ integrins and thus may have provided unique binding opportunities to fibroblasts. Further experimentation examining the focal adhesion more directly will help resolve this particular discrepancy.

Additionally, the lack of polarization in RFL6 cells with increasing substrate stiffness was surprising given that cell spread area and cell polarization are usually correlated. [30, 83] Phenotypically, cells on stiffer substrates demonstrated significant actin remodeling consistent with previous literature, including the development of prominent actin stress fibers. These observations supported the conclusion that the hydrogel surfaces in these assays were differentially presenting mechanical cues to RFL6 cells. However, it remained possible for there to be differential ligand conjugation to the soft and stiff hydrogel surfaces, which could independently modulate cell polarity, resolving this apparent paradox (specifically, these results are consistent with lower fibronectin conjugation to soft hydrogels with relatively higher conjugation on stiff hydrogels). [83] Importantly, both mRNA treatments led cells towards being more polarized on stiff substrates, which is consistent with the cell spreading data.

2.3.5 H5-CD8 Constructs Expressed *In Vivo*

Flow Cytometry Did Not Detect V5-Tagged mRNA Constructs

Translation of the mRNA-based technology *in vivo* required characterization of the delivery of these constructs to the airspace. Flow cytometry is a high-throughput characterization technique suitable to assay the effective delivery and expression of V5-tagged mRNA constructs with single cell resolution and the ability to characterize the cellular tropism of mRNA expression. [84] Mice were intubated and sprayed with a PBS-mRNA solution, and their lungs, after digestion into a single cell suspension, were assayed for V5 expression one day after mRNA instillation (Figure 2.5). Pooled analysis from 3 mice with and without mRNA exposure did not reveal differential population shifts in the median fluorescent intensity of the V5 signal at any antibody concentration (Figure 2.5A). While the fluorescent intensity was linearly correlated with the concentration of the V5 antibody used for staining (r^2=0.998 and r^2=0.9721 for mRNA treated and untreated animals, respectively), indicating the expected dose-response, the slopes of these responses were not significantly different, indicating that there was not an antibody concentration dependence in the inability to separate these two populations (Figure 2.5B, p=0.2396).

All mice, regardless of mRNA treatment, stained brightly with the V5 antibody relative to unstained controls, possibly indicating a high background to the antibody's binding profile. Complicating this interpretation, however, was the observation that decreasing antibody concentration led to a bi-modal movement of cells from the positive peak to a negative peak, co-localized with unstained cells. This trend was qualitatively stronger in the mRNA untreated population. These data were most consistent with the interpretation that the V5 detection system has a relatively low affinity profile towards the V5 epitope on these cells, requiring strong electronic amplification in the cytometer's detectors to discriminate the signal - *e.g.* cells moved digitally from a "stained" to "unstained" population. The relatively low affinity of this previously characterized antibody for the V5 epitope towards

these constructs may be explained by the relative placement of the V5 epitope, between the H5 protein and the membrane linker, as this location for the epitope could have high steric hindrance associated with it, which could negatively impact surface detection by flow cytometry. [85, 86] While this digital population shift could have been indicative of effective delivery and expression of V5 to the air space, it was insufficient to determine the degree of relative expression (due to a lack of shift in the positive population) and direct detection of the V5 epitope by flow cytometry was not considered going forward.

FACS Isolated H5-Luciferase Fusion Constructs Were Inhibited by Tissue Preparation

To maintain the ability to characterize the relative cellular tropism of expression of H5 in the lungs of sprayed mice while avoiding steric/detection issues identified in the previous flow cytometry experiments, single cell preps from sprayed and unsprayed mice were sorted using a FACS scheme previously validated to isolate hematopoietic, epithelial, endothelial, and lineage negative cells. [84] Additionally, the fused V5 tag of these mRNA constructs were replaced with a nano-luciferase enzyme, which would allow for the antibody-free, enzymatically amplified detection of translated mRNAs.

This FACS work flow sorted cells into single, live cells populations before dividing them into CD45+ and CD45- groups (Figure 2.6A-D). These two subpopulations were each subsequently subdivided into CD31 and CD326 positive and negative populations. Hematopoietic (Figure 2.6E, lower left quadrant, CD45+CD31-CD326-), epithelial (Figure 2.6F, lower right quadrant, CD326+CD45-CD31-), endothelial (Figure 2.6F, upper left quadrant, CD31+CD45-CD326-), and lineage negative cell populations (Figure 2.6F, lower left quadrant, CD31-CD45-CD326-) were then isolated in a 4 way purity sort.

Characterization of the nano-luciferase system *in vitro* revealed linear, sensitive detection of mRNA expressed in HFFs down to dilutions of a hundred transfected cells (Figure 2.7A, r^2=0.9949 and r^2=0.9969 for the cell number vs luciferase response of Thy-1 and H5-CD8 constructs, respectively). Given that *in vitro* transfection is not perfectly efficient,

these data suggested that the nano-Luciferase system was able to detect 10s of transfected cells with a high signal-to-noise ratio relative to untransfected HFFs, which had a flat luciferase response to input cell number.

Following cell type isolation from FACS, individual cell populations from the right lungs of mice were analyzed using a nano-luciferase assay one day after mRNA instillation (Figure 2.6C). An independently prepared standard curve (Figure 2.7B) from *in vitro* transfected HFFs demonstrated the same linear luciferase response previously observed (Figure 2.6A), down to abundances of 100 input cells. Unfortunately, no FACS isolated population had luciferase readings within the interpolation range of the standard curve and were similar to readings from wells without any cells. There were no statistical differences in the luciferase readings in any cell population between mRNA exposed and unexposed animals except for the lineage negative ("Triple Negative") population, which had significantly higher luciferase readings in the mRNA untreated cells than in cells from either mRNA treatment ($p<0.0001$). Given the previously demonstrated sensitivity of the nano-luciferase system, I hypothesized that there may be tissue-derived inhibitors of the nano-luciferase reaction which were preventing detection of the translated proteins. This hypothesis was supported by nano-luciferase assays in which single cell suspensions of mRNA treated animals demonstrated a biphasic response to dilution in FACS buffer. Specifically, Thy-1 treated single cell suspension showed a trend towards increasing luciferase signal with increasing dilution in FACS buffer, which peaked around a ten-fold dilution and began to fall with decreasing cellular input at one hundred fold dilutions. Single cell preps from control of H5-CD8 mRNA treated animals did not show this same bi-phasic response (Figure 2.7D). Subsequently, I tested whether single cell preps from animals without exposure to nano-luciferase fused mRNA could inhibit the activity of nano-luciferase expressed *in vitro*. *In vitro* treated HFFs, which demonstrated a linear dose-response in nano-luciferase assays (Figure 2.7B), showed a clear loss of luciferase signal when mixed 1:1 by volume with cell suspensions from control animals relative to 1:1 volume dilution in FACS buffer (Figure

2.7E, p=0.0332 and p=0.0215 for H5-CD8 and Thy-1 expressing HFFs, respectively).

These data supported the conclusion that there were tissue-derived nano-luciferase inhibitors present in the single cell preparations, though the specific source of that inhibitor was unclear. One noticeable difference between individual single cell lung preps from different animals was the level of residual blood in the suspension. While red blood cells ("RBC") were lysed using osmotic treatment in the preparation of these lysates, differential levels of RBC contamination could have been present in each prep, complicating the potential downstream analysis. RBCs or RBC lysis products have not been previously shown to inhibit nano-luciferase assays and these data may contribute a unique perspective on the limitations of such studies *ex vivo*. [87]

Whole Lung Tissues Demonstrated mRNA-Dependent Luciferase Activity

While tissue digestion and processing seemed to produce a nano-luciferase inhibitor, several groups have demonstrated the use of nano-luciferase as a reporter system in intact tissues and living animals. [84] Right and left lungs, dissected from mice but otherwise intact, were assayed for nano-luciferase activity using an IVIS imager 8 days after mRNA instillation (Figure 2.8A). Kinetic measurements of the luciferase response from these tissues showed a time-invariant trend, where Thy-1 mRNA treated animals demonstrated significantly higher luciferase readings at 7 and 15 minutes relative to untreated animals' lungs (Figure 2.8B, p=0.0414 and p=0.0078 for 7 and 15 minutes, respectively). H5-CD8 mRNA sprayed animals displayed a similar trend (Figure 2.8B, p=0.2292 and p=0.1295 for 7 and 15 minutes, respectively), though one H5-CD8 sprayed animal had luciferase readings comparable to non-treated lungs. Single time-point analysis at 15 minutes of the combined left and right lung luciferase response demonstrated this trend as well (Figure 2.8C, p=0.4494 and p=0.1645 for H5 and Thy-1 luciferase activity relative to untreated lungs, respectively). The nano-luciferase assays also revealed a left-right lung expression bias, with increased expression in the left lung, in all animals (Figure 2.8D). While the

increased expression in the left lungs of mRNA treated animals could indicate delivery bias ($p=0.108$ and $p=0.14$ for left vs right luciferase activity in Thy-1 and H5-CD8 mRNA treated animals, respectively), the difference in untreated animals suggested that intrinsic mass biases between the left and right lungs need to be accounted for in future studies.

Spatial Distribution and Heterogeneity of mRNA Expression in the Lung by Immunofluorescence

In order to account for the spatial distribution of mRNA expression in the airspace, immunofluorescence on V5-tagged mRNA constructs was performed on cyrosectioned lung tissue from mRNA exposed and unexposed animals. Whole lung imaging of these tissues reveal millimeter sized variation in H5/V5 expression in mRNA treated animals (Figure 2.9A). Interestingly, certain cell populations inside the lungs of control animals demonstrated exceptionally high staining background, specifically on the luminal surfaces of structures that could plausibly be either arteries or bronchial airways. This heterogeneity in V5 staining background could have been a complicating factor which made analysis of single cell suspensions derived from these tissues difficult to assay cleanly by flow cytometry (Figure 2.5).

At higher resolution, areas of high V5 signal in mRNA exposed animals had qualitatively distinct patterns of V5 expression relative to areas of low V5 signal expression in mRNA exposed animals and to control animals' lungs. Control animals and low-expression regions of mRNA treated animals demonstrated faint V5 staining, which appeared to be colocalized with the nucleus. In contrast, high expression regions from mRNA exposed animals, demonstrated a cellular dispersed V5 signal, indicating high levels of local transfection of these tissue regions. These data demonstrated that profiling V5 expression by immunofluorescence was a tractable way to address spatial heterogeneity in the delivery and translation of mRNA to the lungs and could potentially be multiplexed with cell-type markers in the future to characterize the relative cellular tropism of mRNA transfection.

2.4 Discussion

2.4.1 αVβ3 Antagonism as a Therapy for Pulmonary Fibrosis

The ability of the fibrotic matrix to drive pathology has emerged as a frontier in the discovery for treatments of pulmonary fibrosis. [16] This new focus has been driven by the discovery of a variety of mechanisms through which the matrix and mechanical cues from it drive fibrotic pathology. These matrix-driven factors include activation of the myocardin related transcription factor family and YAP/TAZ transcription factors [12, 15, 14], potentiation of TGFβ activation [13] and cellular-sensitization [88, 89, 90, 91] (discussed further in Chapter 3 of this thesis), and alterations in integrin signaling, specifically focused on αV and α5 integrins. [30, 49, 29]

Unfortunately, this scientific enthusiasm for the matrix and mechanical signaling to cells has not translated yet into a bevy of new clinical trials to explore novel matrix-based therapeutic avenues: of the current 19 clinical trials in Phase II or Phase III for pulmonary fibrosis, only a single trial focuses on cell-ECM interactions, a monoclonal antibody therapy directed against αVβ6 integrin by Biogen Pharmaceuticals. [92] Another matrix-based therapy, simtuzumab, a monoclonal antibody against lysyl oxidase-like 2, recently failed its Phase II clinical trial after it failed to demonstrate efficacy in progression-free survival relative to placebo. [93] Other clinical trials in progress mainly focus on previous failed approaches in the setting of co-administration with pirfenidone or nintedanib, newly approved drugs for pulmonary fibrosis. [10, 9]

The ability of H5 to recognize and contextually antagonize αVβ3 integrin signaling through strained fibronectin matrices has been previously established. [29, 49] A H5-based approach differs significantly from Biogen's αVβ6 therapy in that H5's antagonism of integrin is contextual - it specifically recognizes a mechanically-activated, fibrosis-associated state of fibronectin. Indeed, in this Chapter, H5 has shown that the ability to discriminate between fibronectin strain states was preserved when H5 was attached to cells by a GPI or

CD8 peptide linker. This contextual antagonism of H5 may be especially important clinically because of the physiological role played by αV integrins in various processes like wound healing and regeneration. [94, 95, 96] Another important difference between a H5- and αVβ6-based approach is the former's ability to antagonize TGFβ activation in addition to matrix-ECM contacts. [97, 98] αV integrins have been shown to be able to mechanically activate TGFβ from matrix-bound latent complexes through binding of an RDG motif in the latent-associated peptide. [13] Previous work in characterizing the binding of H5 has established that RGD alone is not sufficient for engagement, and H5 likely recognizes a particular three-dimensional confirmation of the III_9 and III_{10} domains of fibronectin. [29, 49] These fundamental differences in the mechanisms of H5 and other matrix-focused therapies underscores the novelty of work in this area and may present an opportunity for synergistic, combination therapies in the future.

2.4.2 Role of Cell Linkers in Modulating the Function of Surface Expressed Proteins

Cell Tethering as a Modulator of Molecular Pharmacokinetics

The ability to conjugate H5 to the surface of cells is a novel approach to modulating cell-ECM interactions. [29] Tethering to cells likely changes the pharmcodynamics of H5 residency in the lung by preventing rapid clearance into the lymphatic and systemic circulation [65, 64] and by resident airway marcophages. [67, 68] Proteins of equivalent mass delivered to the airway in previous studies, like human growth factor, have demonstrated tissue life-times on the order of 10 hours in previous studies [68]. These half-lives can be extended through various engineering solutions such as PEG-ylation of the molecule, which provided PEG-lysine dendrimers tissue half-lives on the order of 1-2 days mostly by preventing them from leaching into the systemic circulation [71]. Alternatively, groups have also used Fc-fusions to proteins, which increased the therapeutic protection of IL-7 against influenza infection in mice on the order of weeks [99], but which are also associated with increased transcytosis of the proteins into the systemic circulation and directed associa-

tion with immune cells in the lung, potentially increasing off-target effects for a H5-based therapy. [69, 70] In contrast, cell surface expression of H5 affords straight-forward, cell-implemented (*i.e.* not requiring external modification and subsequent characterization of the proteins' purity and function) strategy, which intrinsically focuses the therapeutic activity of H5 on fibronectin which is cellularly accessible. Furthermore, data in this Chapter suggests that H5-nano-luciferase fusions are present in the lung 8 days after instillation, indicating a substantially improved half-life over similarly sized molecules. [68]

Cell Tethering as a Modulator of H5 Biology

The conjugation of H5 to the surface of cells also affords the opportunity to modulate H5's efficacy based on the innate biological regulation of the linker itself. Thy-1 and its GPI linker have served as a biologically-inspired template for how to link H5 to cells because of Thy-1's endogenous role in regulating mechano-transduction in fibrosis. [72, 100, 74] Specifically, Thy-1 has been shown to associate with αVβ3 integrins in a GPI and cholesterol-dependent fashion, which is lost when Thy-1 is expressed with a single-pass peptide transmembrane linker from CD8. [75, 76, 77, 30] This association is significant both because of Thy-1's ability to lock αVβ3 into a "bent", inactive conformation through cis-binding of Thy-1's RLD domain [30] and because the GPI linker pre-clusters members of the Scr Family Kinases, specifically fyn, into focal adhesions, which alters the mechanical phenotype of the cell in a Rho- and cytoskeleton-dependent fashion. [81, 78, 79, 80]

Work in this Chapter has shown that GPI-linked H5 constructs are just as effective as H5-CD8 constructs at binding strain-mimic fibronectin fragments while also significantly, and differentially to H5-CD8, increasing global phospho-SFK signaling. Interestingly, in a study of Thy-1 null fibroblast spreading on soft and stiff surfaces, H5-CD8 constructs led to increased cell spreading relative to H5-GPI and vehicle treated controls, implying that the ultimate effect on the mechano-transductive phenotype of the cells may not be fully captured by the alterations in focal adhesion biology. Indeed, the pre-clustering of H5 with

αVβ3 integrins may also modulate the kinetics of integrin-ECM interactions. Previous studies of integrin-ECM binding have found that the cell's glycocalyx creates an energy barrier due to the relative extent of this mucin-layer and integrins from the cell's surface. [101] The consequence of this energy barrier is that single binding events, which necessarily occur in regions where this energy and space barrier have been overcome, act as kinetic funnels for the subsequent binding of other integrins. [102] In this context, non-associated H5-CD8 constructs may actually serve as an unique nidus for cell-ECM interactions, apart from H5-GPI/integrin clusters, which could ultimately potentiate the ability of αVβ3 integrins to associate with the matrix. Studying the ability of H5-CD8 and H5-GPI integrins to modulate the number and size of focal adhesions in the cell as well as the ability of these H5 proteins to compete directly for matrix binding sites with integrin in pull-down assays (both described below in Future Directions) will help to directly these questions.

Finally, the use of the GPI and CD8 linkers should be considered in the context of Thy-1's regulation in inflammatory and fibrotic settings. Thy-1 expression is lost in fibrotic tissues both through epigenetic heterochromatinization of its promoter [73], and through TNFα- and IL-1-driven activation of phospholipase C, which cleaves the GPI anchor. [72] The effect of phospholipase C's activity on H5-GPI constructs in the diseased setting has not been considered here but could negatively impact the tissue residency of H5-GPI constructs and motivate the use of H5-CD8 designs. Interestingly, other groups have explored the cleavage of various GPI-linked proteins by phospholipases *in vitro* and *in vivo* and found evidence for discrimination in the enzymes' activity. [103] Understanding the protein features associated with this discrimination may afford the ability to design cleavage resistant H5-GPI constructs to avoid inflammation-driven loss of H5 from the cell's surface.

2.4.3 Role of Aerosol Spray For Delivering mRNA Therapeutics to the Lung

Direct Administration Via the Airspace Compared to Oral- or Injection-based Routes

The delivery of aerosolized mRNA without a secondary delivery scheme to the airspace is a unique method of drug delivery pioneered by the Santangelo group. Direct therapeutic administration to the lung has obvious advantages in targeting the therapy to the affected organ and avoiding systemic side-effect. The approach in this chapter differs significantly from most currently investigated therapeutics. All currently investigated therapies for pulmonary fibrosis except the small molecules TD139, an inhibitor of inflammatory signaling through galactin-3, and trepostinil, a prostacyclin, are currently administered orally or by injection. [92] Previous work by the Barker group had focused on the vascular delivery of H5 to the lung. [49, 29] This route of delivery exploits unique derangements of the vascular permeability in fibrotic regions, likely driven by local inflammation. However, the long-term accessibility to the lung through this vascular mechanisms has yet to be validated. An investigation of collagen-I PET probes, which used injection as a route to longitudinally study the progression of pulmonary fibrosis, demonstrated that efficient disease tracking was only possible in an experimental model of fibrosis that combined bleomycin with FTY720, a sphingosine-1-phosphate receptor modulator that increased vascular permeability to the lung. [104, 105] Further work with aerosolized mRNA should help to establish the direct pharmacological benefits of this particular route of administration.

Effects of Gene Therapy Carriers and Vectors In Delivery to the Airspace

Remarkably, the spraying method used in this work allows for the expression of mRNA constructs as demonstrated by immunofluorescence and nano-luciferase activity without the need for a delivery vehicle. This is extremely advantageous as delivery vehicles for gene therapy require additionally engineering controls to implement and often interact themselves with the biology of the lung. For instance, gene therapy approaches using adeno-

viral vectors have been thwarted by the presence of endogenous antibodies against the vectors themselves, raising questions about the efficacy of these treatments in adeno-virus exposed populations and the repeatability of therapeutic intervention along this route. [58] Additionally, several different cationic polymer-based approaches to gene delivery have been employed in the lung, using both synthetic and naturally derived compounds. PEI, in particular, has been used in several pre-clinical model of gene therapy to the airspace. [106, 107] Analysis of these vehicles' effects on gene regulation alone find that both PEI and naturally derived polymer systems, such as chitosan, independently increased the transcription of inflammatory genes, COX and HO-1, which may be especially disadvantageous in the setting of diseased, frail tissues. [108] Indeed, the inflammatory activity of PEI, in particular, seems critical to its ability to target genes to the lung when administered systemically. [109] Delivery of mRNA-based therapies without an additional carrier represents an important and novel method to address these current limitations.

The lack of carriers for mRNA in this system also helps reduce the pharmacological complexity of their delivery. Efficient delivery of macromolecules to the airspace is dependent on a variety of factors including the relative size, charge, and particle-particle interactions of the cargoes in an aerosol. [110] Previous studies of airway delivery have found that micron-sized particles like those generated by the microsprayer in this work are needed for efficient delivery of therapeutics to the alveolar airspace as larger particles remain entrapped in the upper airways and have difficult penetrating the mucus layer in the lung.[110] I have demonstrated that naked mRNA droplets reached the distal airspace in the immunofluorescent profiling of V5 expression in transfected lungs. This technique can be employed in future studies exploring the spatial heterogeneity of mRNA delivery to the airspace.

Mechanism of mRNA Uptake Delivered by Aerosolized Particles

How does mRNA delivered to the distal airspaces get taken up by cells and become translated? Previous work in the Santangelo lab has extensively characterized the routes of entry by exogenous mRNA to cells and found that polymer-based systems primarily employ a mixture of clathrin- and caveolin-mediated endocytosis to gain entry to the cells. [60] Interesting, additional work studying the uptake of naked and nano-particle delivered mRNA found that substrate mechanics significantly altered the endocytic route and release of mRNA in the cytoplasm. [111] These mechanistic insights will be particularly important in the delivery of therapeutics to the fibrotic lung where normal matrix mechanics have been significantly deranged. While aerosolized DNA- and mRNA-based therapeutics have been delivered to the lungs [112, 113] and the genital tract [114] in a variety of experimental models, these studies were always performed with the use of cationic polymers or viral vectors, which confounded an understanding of the aerosol itself as a potential vector for gene therapy. This lack of knowledge as to how the physical delivery of mRNA connected to the endocytosis and translation of mRNA in tissues will be an important area of future research to understand delivery of naked mRNAs by aerosols fully.

2.5 Future Directions

2.5.1 Experiments In Progress

Thy-1 Motivated Experiments

While Thy-1 has served as biological inspiration in this work through the use of its GPI linker, I have planned to use delivery of Thy-1 itself as a positive control mRNA construct in bleomycin models of fibrosis in Thy-1 null mice. The delivery of Thy-1 constructs *in vivo* has been demonstrated in this Chatper. Experiments to validate the *in vitro* functionality of Thy-1 constructs include proximity ligation assays ("PLA") to assess its association with αVβ3 integrins, and RFL-6 cell spreading assays to demonstrate Thy-1's role in mod-

ulating cellular mechanosensing. The data for both experiments have been collected, and the data are in analysis currently. Additionally, I have used Thy-1 mRNA as a negative control mRNA in the CHO fibronectin binding experiments. These experiments have also been conducted and the data are being analyzed. Work in this Chapter has demonstrated the *in vivo* delivery efforts I have undertaken to deliver Thy-1 to the lungs of mice along side H5-CD8 constructs.

H5 Motivated Experiments

Experiments to demonstrate the GPI-dependent association of H5 mRNA constructs with αVβ3 integrins by PLA have also been conducted and are currently in analysis. These experiments have been conducted in two ways: with paxillin post-staining and with V5 post-staining. Paxillin post-staining will allow me to quantify global alterations in focal adhesion number, size and placement in the cell with and without H5 expression. This data may be especially useful in understanding the effects observed in the RFL-6 cell spreading assays with H5-CD8 and H5-GPI linked constructs. PLA experiments with V5 post-staining are an important methodological control that will allow me to control for the degree of H5 expression in assessing its relative interaction frequency with αVβ3 integrins. Additionally, there are a planned set of experiments using dSTORM super-resolution microscopy to analyze the clustering of αVβ3 integrins, fibronectin and the various mRNA constructs used in this work. These experiments are in the data collection phase. Finally, a set of "focal adhesion pull down" experiments have been performed and are currently being blotted and analyzed based on methodology previous developed in the Barker lab. [30] These experiments use magnetic beads coupled to fibronectin to assess the ability of H5-CD8 and H5-GPI constructs to compete for matrix binding directly (*i.e.* does the ratio of αV and α5 integrins bound to these matrix-coated beads vary with H5-CD8 or H5-GPI treatment?) and to specifically assess the recruitment of fyn to focal adhesions. These data will help validate claims concerning the competitive antagonism of αVβ3 integrin by H5-

based constructs and validate global focal adhesion experiments already performed, which show increased SFK phosphorylation with H5-GPI treatment.

In vivo Efficacy of mRNA Constructs

Finally, the efficacy of these mRNA constructs (both Thy-1 and H5-CD8) *in vivo* needs to be assessed. The Barker lab at UVA is independently working to address bleomycin optimization in this model to ensure a robust fibrotic response, and I have prepared the materials and methods necessary to conduct these experiments once the model is in place.

2.5.2 Development of a Chimeric H5-Thy1 Construct, Thy-5

One future project inspired by this work would be the development and characterization of a chimeric Thy-1/H5 construct that fully integrates the ability of both molecules to modulate $\alpha V\beta 3$ signaling. Currently, H5-GPI construct capture one important element of Thy-1 biology - the ability of the GPI anchor to associate with $\alpha V\beta 3$ integrin and to pre-cluster focal adhesion protein. [78, 79, 80, 30] However, Thy-1 is also able to antagonize $\alpha V\beta 3$ by stabilizing the inactive, "bent" integrin conformation of the integrin through cis-binding in the membrane to Thy-1's RLD motif. [30] Incorporating the first 30 amino acids, which include the RLD domain, of Thy-1's mature sequence into the design of H5 is molecularly straight-forward; however, because the binding interface of H5 and fibronectin has not been firmly mapped beyond knowing that it is restricted to the III_9 and III_{10} domains of fibronectin, characterization of the chimeric protein will have to ensure that H5's innate ability to bind fibronectin is not compromised in the process.

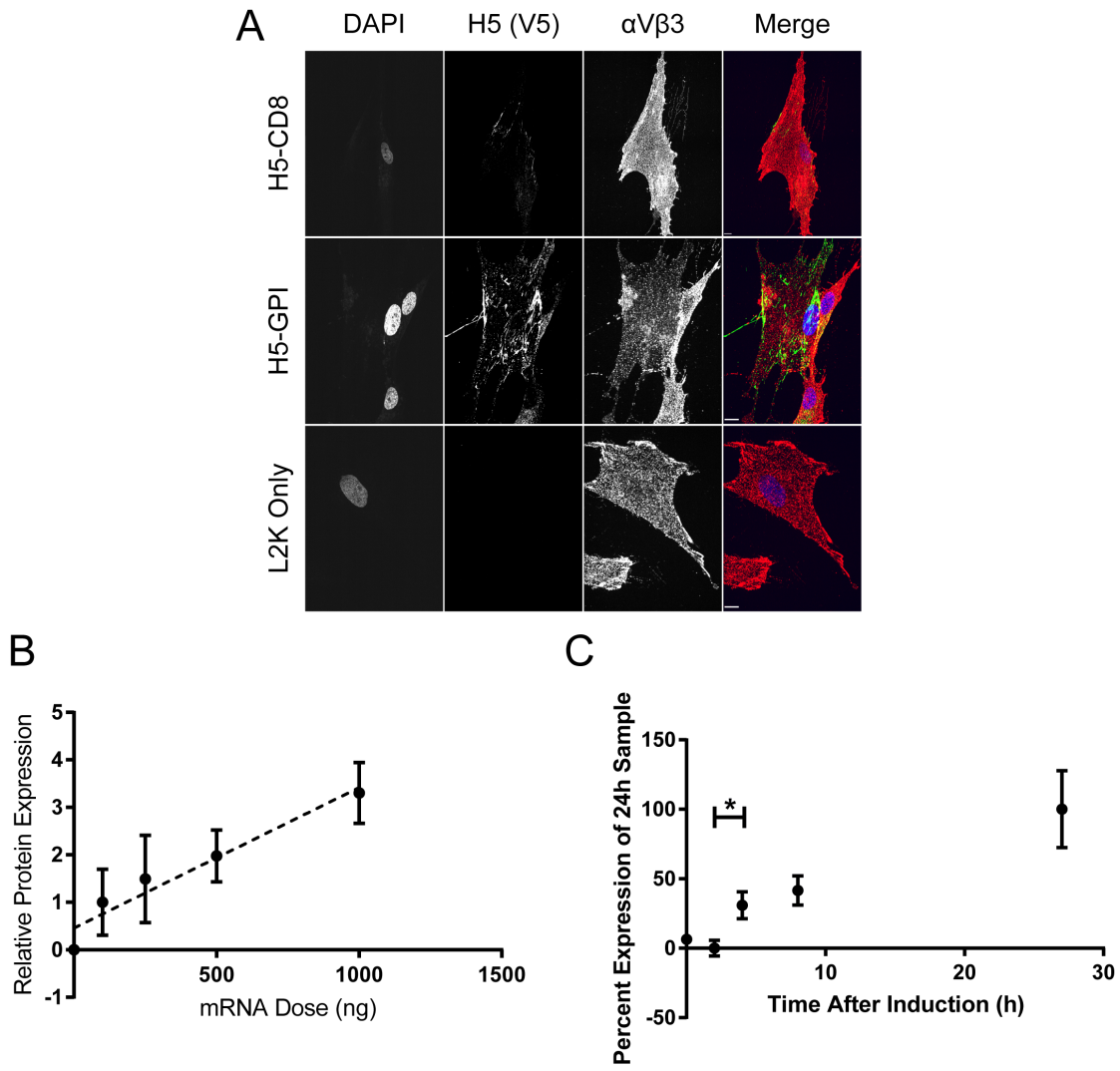

Figure 2.1: **Dose and Temporal Response of Fibroblasts to mRNA Delivered *in vitro*** A, micrographs of HFFs transfected with 500ng of CD8- or GPI-linked H5 mRNA along with vehicle treated control cells. H5 surface expression in unpermeablized cells qualitatively showed clustering of both the CD8- and GPI-linked H5 constructs, which was distinct from the punctate pattern of $\alpha V\beta 3$ staining on the cells' surfaces. B, HFFs demonstrated a linear, dose-dependent increase in surface expressed V5-tagged proteins (r^2=0.9377, linear regression) one day after transfection. C, significant increases in V5-tagged protein expression was observed as early as 4 hours post-mRNA transfection (p=0.3203 and p=0.0106 for "0 hours vs 2 hours" comparison and "2 hours vs 4 hours" comparison, respectively, ANOVA, Tukey post-test). V5-tagged protein surface expression grew significantly over the 24 hour period (p=0.0054, ANOVA, Test for trends).

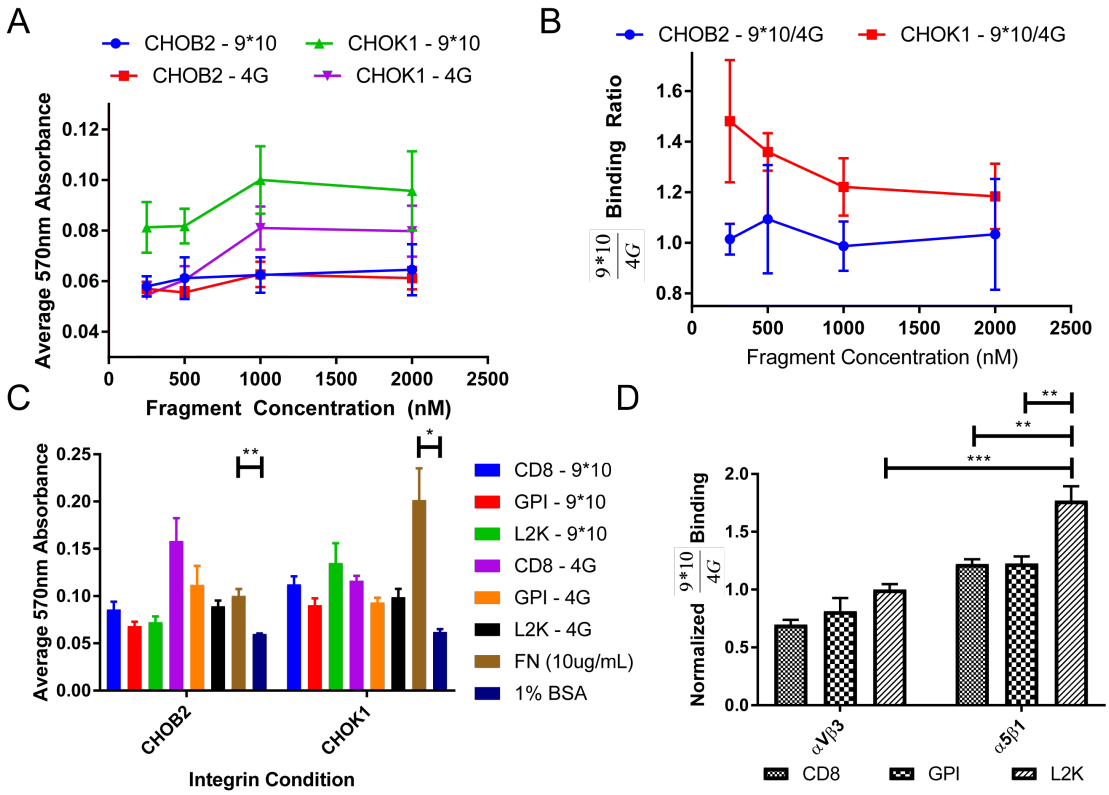

Figure 2.2: **H5 mRNAs Specifically Bound Strain Fibronectin Fragments** A, integrin null CHO cells expressing human $\alpha5\beta1$ integrins ("CHOK1" cells) adhered to "relaxed-mimic" fibronectin fragments ("9*10") preferentially to "strain-mimic" fibronectin fragments ("4G"). Integrin null CHO cells expressing human $\alpha V\beta3$ integrins ("CHOB2" cells) did not discriminate between the two fibronectin fragment types. B, quantification of fragment-concentration dependence from (A) for CHOK1 and CHOB2 cells showed the greatest difference in cell adhesion at concentrations of 250nM of fibronectin fragments. C, Raw absorbance values for CHO adhesion experiments to fibronectin fragments and control surfaces at 250nM concentrations. Both CHOK1 and CHOB2 cells adhered in greater numbers to full length human fibronectin than to BSA passivated surfaces (p=0.0141 and p=0.0058 for CHOK1 and CHOB2 relative binding, respectively, Student's t-test). Additionally, each cell line trended towards higher binding to full length fibronectin than fibronectin fragments in vehicle treated control cells. D, quantification of the relative "relaxed" to "strained" fragment binding in CHO cells demonstrated that H5 expression with either a GPI or CD8 linker significantly increased adhesion of $\alpha5\beta1$ expressing cells to "strained" fibronectin fragments (p=0.002 and p=0.0022 for CHOK1 cell adhesion ratios with CD8- or GPI-linked H5 transfection relative to vehicle treated controls, respectively, 2-way ANOVA, simple row effects with Tukey post-test). CHOB2 cells also demonstrated the same mRNA-dependent trend. Vehicle treated CHOB1 cells statistically preferred "strained" fragments for binding relative to vehicle treated CHOK1 cells (p=0.0002, Student's t-test).

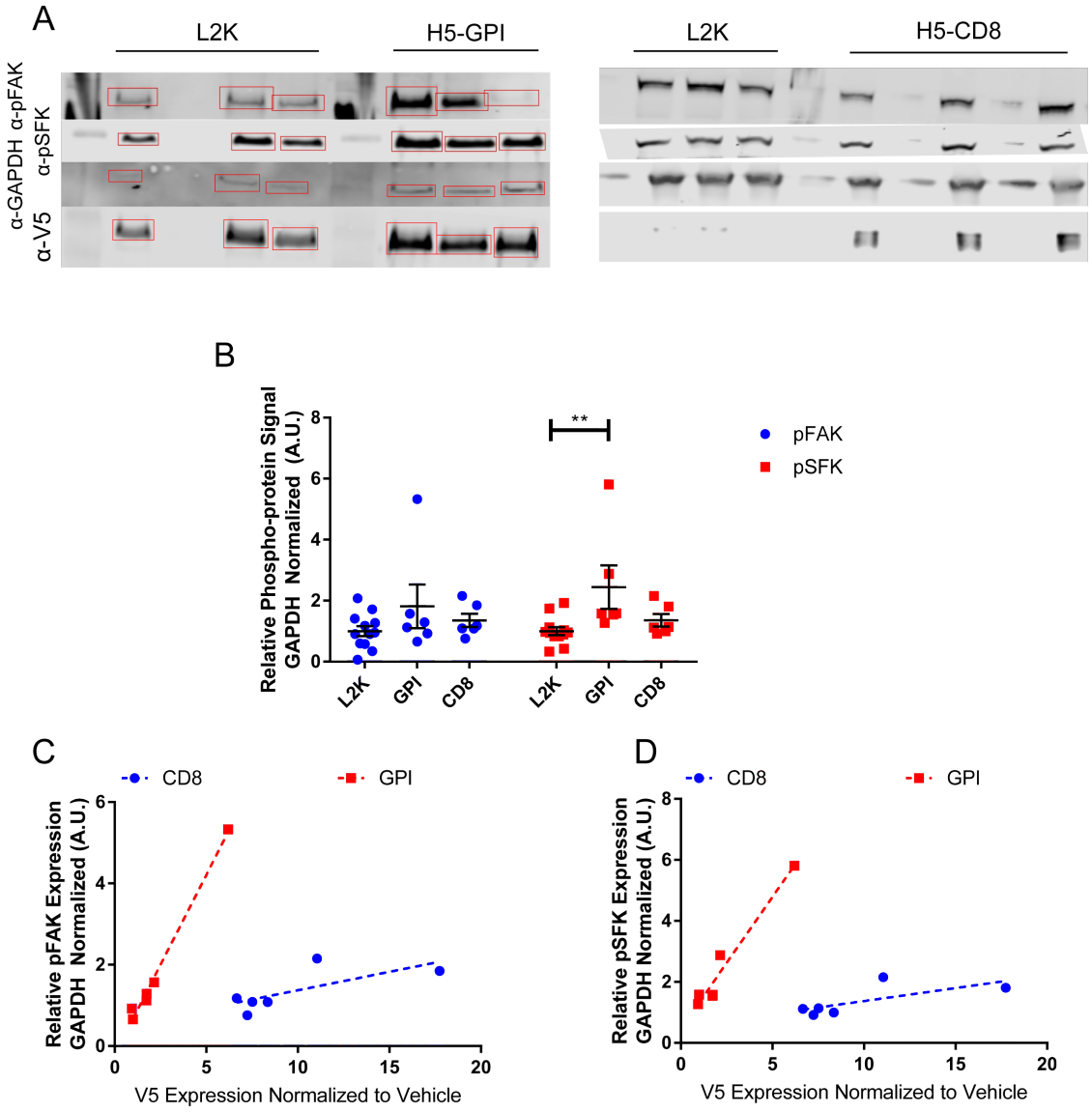

Figure 2.3: **GPI-linked H5 mRNA Increased phospho-Src Family Kinases** A, representative blot for phospho-FAK (top row), phospho-Src Family Kinases (2^{nd} row from top), GAPDH (3^{rd} row from top, and H5-V5 constructs (bottom row) from lysates transfected with H5-GPI (left column) or H5-CD8 mRNAs (right column). B, quantification of global changes in phospho-focal adhesion complex proteins normalized by GAPDH expression. H5-GPI linked lysates had significantly higher levels of phospho-Src Family Kinases (p=0.0088, 2-way ANVOA with simple row effects, Dunnett's post-test). C, phospho-FAK abundances were statistically correlated to the degree of H5/V5 expression in GPI but not CD8 expressing lysates (r=0.9951 with p<0.0001 and r=0.7154 with p=0.1099 for GPI- and CD8-linked H5 mRNA lysates, respectively, Pearson's correlation coefficient). D, phospho-SFK levels were statistically correlated to the degree of H5/V5 expression in GPI but not CD8 expressing lysates (r=0.9768 with p=0.0008 and r=0.7069 with p=0.1163 for GPI- and CD8-linked H5 mRNA lysates, respectively, Pearson's correlation coefficient).

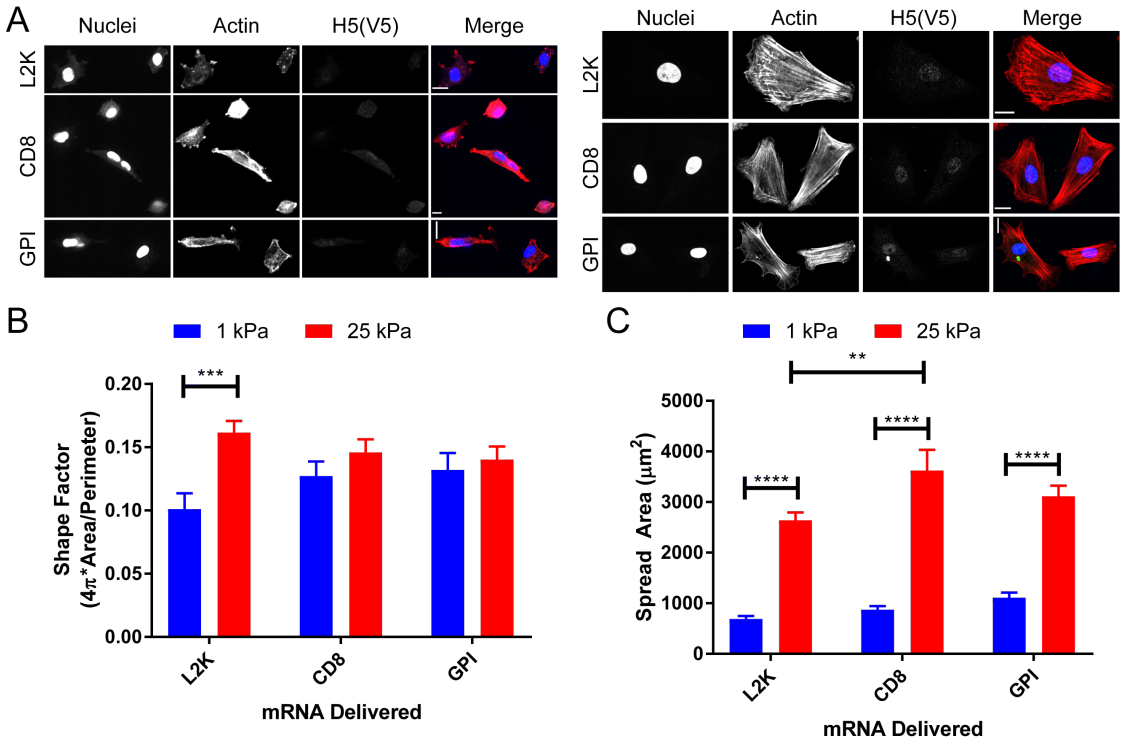

Figure 2.4: **H5-CD8 Altered the Cell-Spreading Phenotype of Thy-1 Null Fibroblasts on Stiff Substrates** A, micrographs of GPI- or CD8-linked H5 expressing RFL6 fibroblasts on soft (1kPa) or stiff (25kPa) substrates after 4 hours in serum free media. mRNA expression on stiff substrates seemed to be restricted mostly to nuclear staining. B, cell polarization on soft and stiff substrates as measured by the ratio $\frac{4\pi \times Area}{Perimeter^2}$. Vehicle treated RFL6 fibroblasts were significantly less polarized on stiff substrates relative to soft substrates after 4 hours (p=0.0005, 2-way ANOVA with Sidak's post-test). C, cell spread area as a function of substrate stiffness and mRNA treatment in RFL6 fibroblasts. All mRNA conditions had a significant increase in cell spread area between soft and stiff substrates ($p<0.0001$ for all comparisons, 2-way ANOVA with Sidak's post-test). H5-CD8 transfected cells were significantly more spread on stiff substrates than vehicle treated controls (p=0.0012, 2-way ANOVA, simple column effect, Tukey's post-test). Scale bars are 17μm.

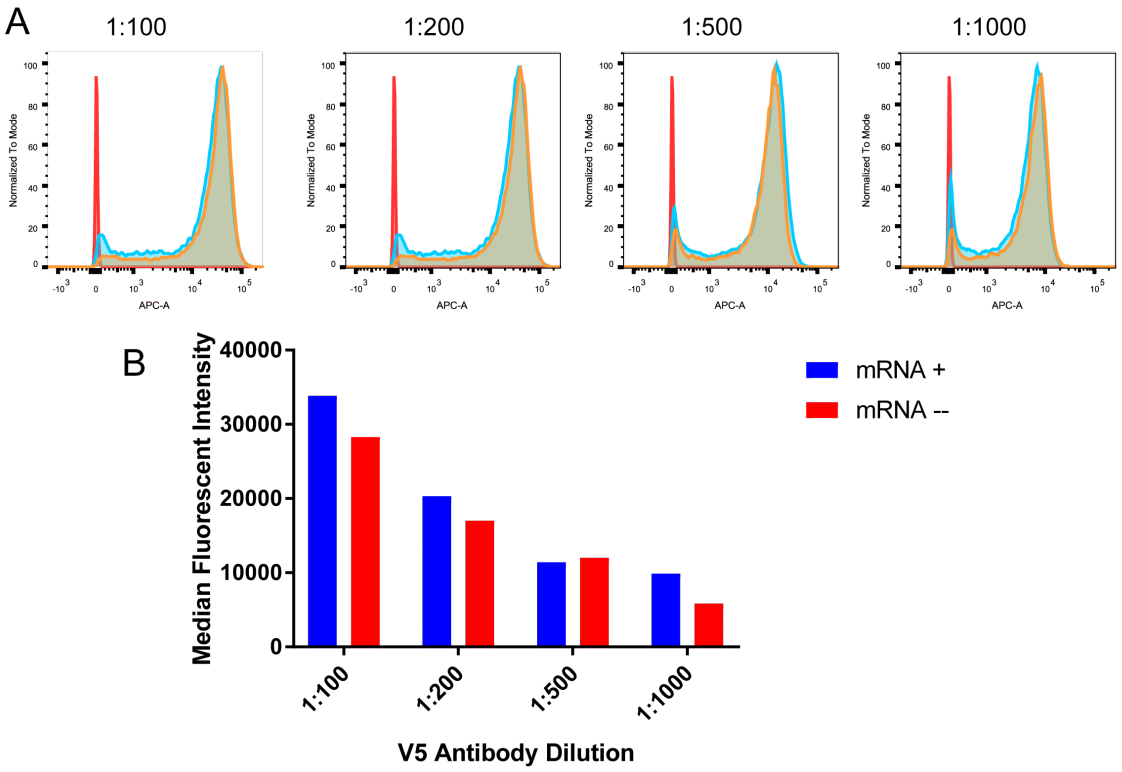

Figure 2.5: **V5 Surface Expression Was Insufficient for Identifying mRNA Transfected Cells from Single Cell Lung Preps** A, V5 antibody titration did not demonstrate statistically meaningful population shift in fluorescent intensity of mRNA exposed (yellow histograms) single cell preps relative to untreated (blue histograms) single cells preps one day after mRNA instillation. Antibody labeled cells were significantly and uniformly brighter than unlabeled cells (unlabeled cells are shown with red histograms, $p<0.0001$ for all mRNA conditions, all dilutions, 2-way ANOVA with Dunnett's post-test). B, quantification of median fluorescent intensity of various V5 antibody dilutions revealed a linear antibody dose trend ($r^2=0.998$ and $r^2=0.9721$ for mRNA exposed and mRNA untreated cell preps, respectively), which did not significantly vary in slope between mRNA-treated and untreated cell preps ($p=0.2396$).

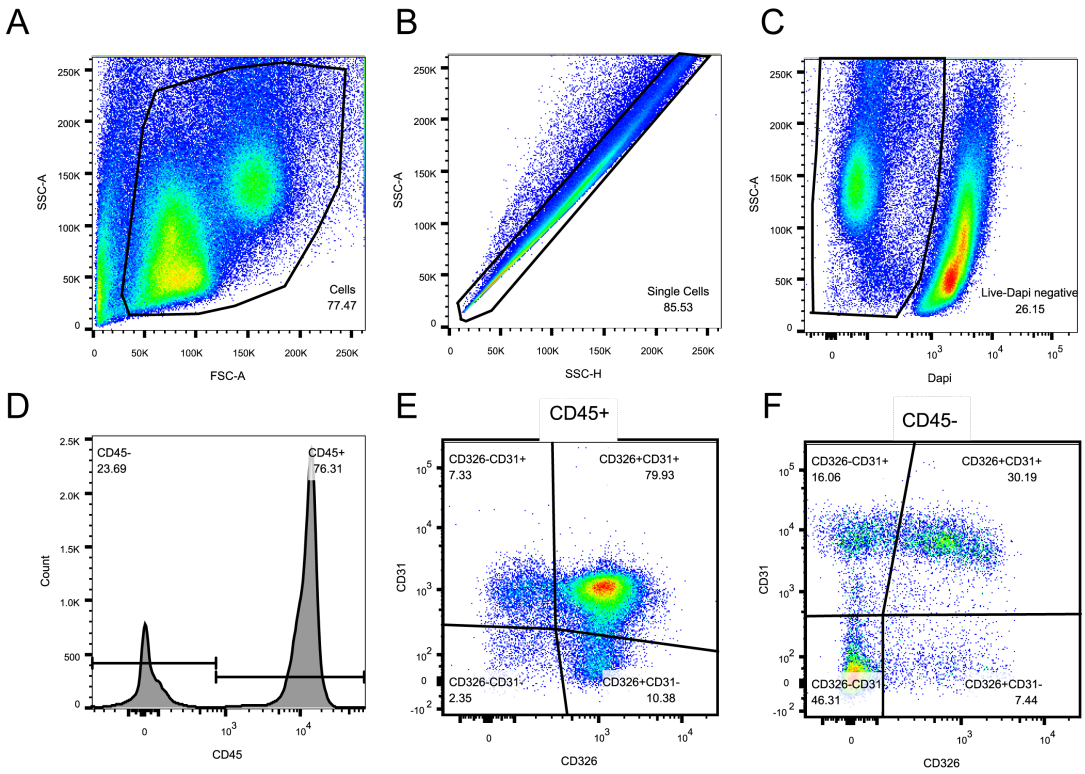

Figure 2.6: **Epithelial, Endothelial, Hematopoietic, and Lineage Negative Population Isolation by FACS** A, forward and side scatter gating identified the total population of cells by relative size and internal complexity. B, single cell populations were gated by restricting forward and side scatter area and height traces to a linear correlation. C, live cells were isolated using an amine-reactive, cell-impermanent viability dye. D, live cells were divided into CD45+ and CD45- populations, which were then subdivided in (E) and (F). E, CD45+ cells were gated on CD31 and CD326 to isolate hematopoietic lineage cells (lower left quadrant, "CD45+CD31-CD326-"). F, CD45- cells were gated on CD31 and CD326 to reveal endothelial lineage cells (upper left quadrant, "CD31+CD45-CD326-"), epithelial lineage cells (lower right quadrant, "CD326+CD31-CD45-") and lineage negative cells (lower left quadrant, "CD31-CD45-CD326-").

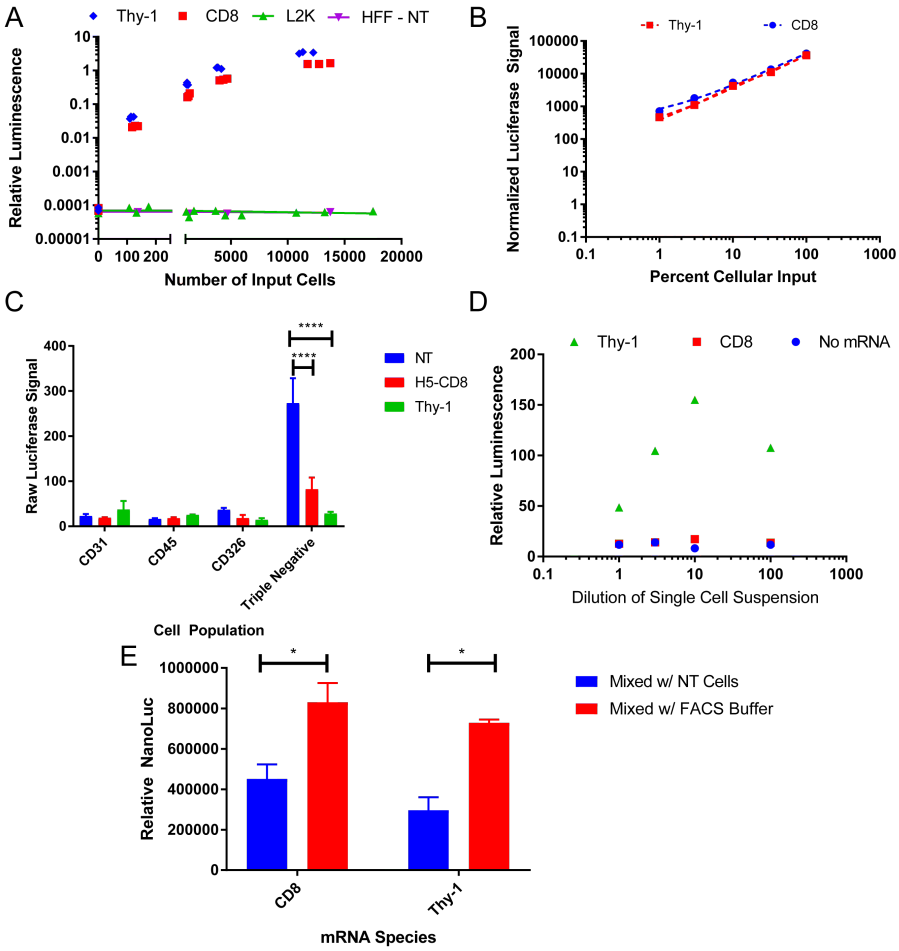

Figure 2.7: **FACS Isolation of Lung Populations Revealed Intrinsic Luciferase Inhibitor in Lung Preps** A, nanoLuciferase assays demonstrated a linear (r^2=0.9949 and r^2=0.9969 for Thy-1 and H5 transfected HFFs, respectively) and sensitive dose-response to transfected cell number. Each mRNA demonstrated a three orders of magnitude signal-to-noise ratio at the 100 cell input level, which indicated sufficient power to detect 1-10% transfected cells in isolations of thousands of cells from FACS. B, standard curve with 10,000 transfected input cells used to normalize luciferase assay results from (C). Both curves were linear over the input range (r^2=0.9988 and r^2=0.9991 for Thy-1 and H5-transfected HFFs, respectively). C, luciferase activity of endothelial ("CD31"), hematopoietic ("CD45"), epithelial ("CD326"), and lineage negative ("Triple Negative") populations from FACS. Absolute luciferase values were below range for standard curve interpolation and did not vary significantly in any cell population with or without mRNA treatment except in the lineage negative population ($p<0.0001$ for no-treatment vs. H5 or Thy-1 exposed lungs, 2-way ANOVA, Tukey post-test). D, dilution of single cell preps from Thy-1 mRNA exposed lungs in BSA buffer demonstrated a bi-phasic luciferase response with dilutions between one- and ten-fold increasing luciferase activity, which dropped with hundred-fold dilution of input suspension. No apparent change in the luciferase activity of diluted H5-treated cells was seen relative to non-treated lung preps. E, single cell suspension from non-treated lungs significantly inhibited luciferase activity from *in vitro* transfected HFFs for both H5 ($p=0.0332$, 2-way ANOVA, Sidak post-test) and Thy-1 mRNAs ($p=0.0215$, 2-way ANOVA, Sidak post-test) relative to BSA buffer.

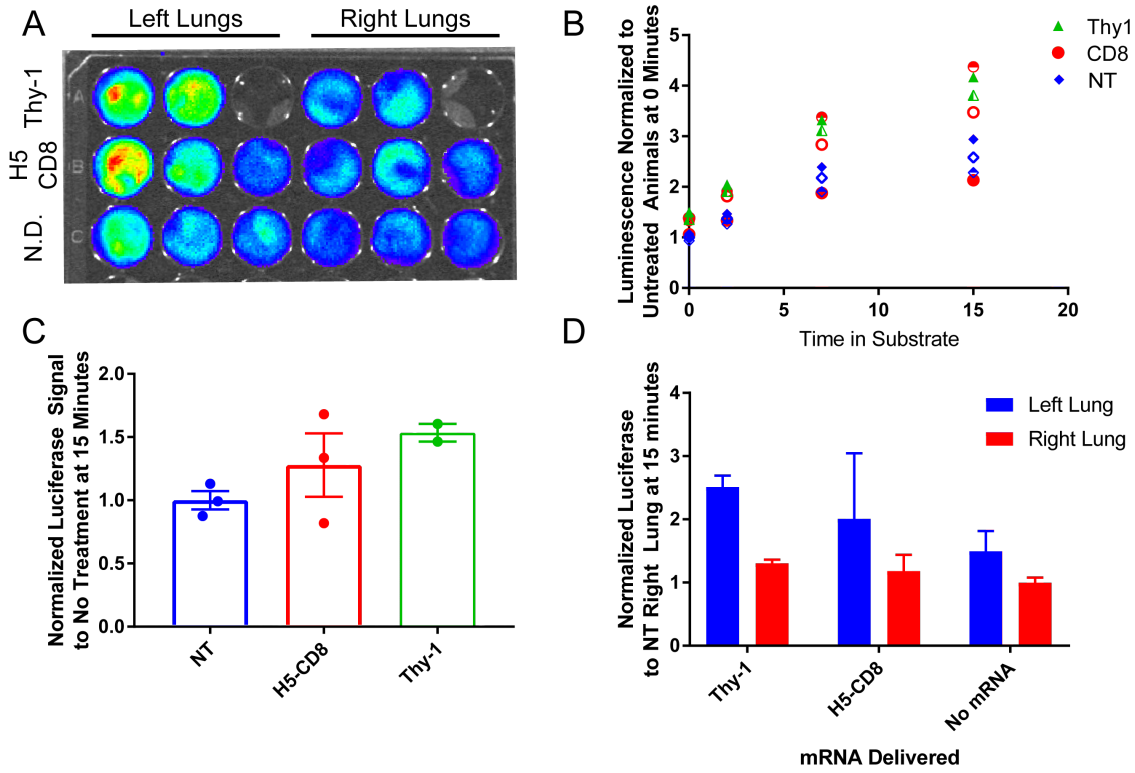

Figure 2.8: **mRNA-sprayed Lungs Demonstrated Stronger Luciferase Activity than Non-Sprayed Lungs 8 Days After mRNA Instillation** A, representative image of luciferase activity from dissected lungs from Day 8 mice. B, Luciferase kinetics of *ex vivo* right and left lungs demonstrated that Thy-1 sprayed lungs have significantly higher luciferase activity at 7 minutes and 15 minutes (p=0.0414 and p=0.0078, 2-way ANOVA, Dunnett's post-test, respectively) than non-exposed lungs. H5-sprayed lungs trended towards higher expression at those time points as well (p=0.2992 and p=0.1295, 2-way ANOVA, Dunnett's post-test, respectively) but one H5-sprayed lung did not show increased luciferase activity relative to control lungs. C, quantification of normalized luciferase activity of right and left lungs at 15 minutes trended towards higher luciferase activity in exposed lungs, relative to non-exposed lungs (p=0.4494 and p=0.1645 for H5 and Thy-1 mRNA-sprayed lungs, respectively, ANOVA with Dunnett's post-test). D, quantification of normalized luciferase activity at 15 minutes from right or left lungs demonstrated a trend toward asymmetric delivery of mRNA to the left lung (p=0.108 and p=0.14 for Thy-1 and H5-sprayed lungs, respectively, 2-way ANOVA with Holm-Sidak post-test). Difference in luciferase activity in untreated lungs could indicate intrinsic mass-bias in measurement.

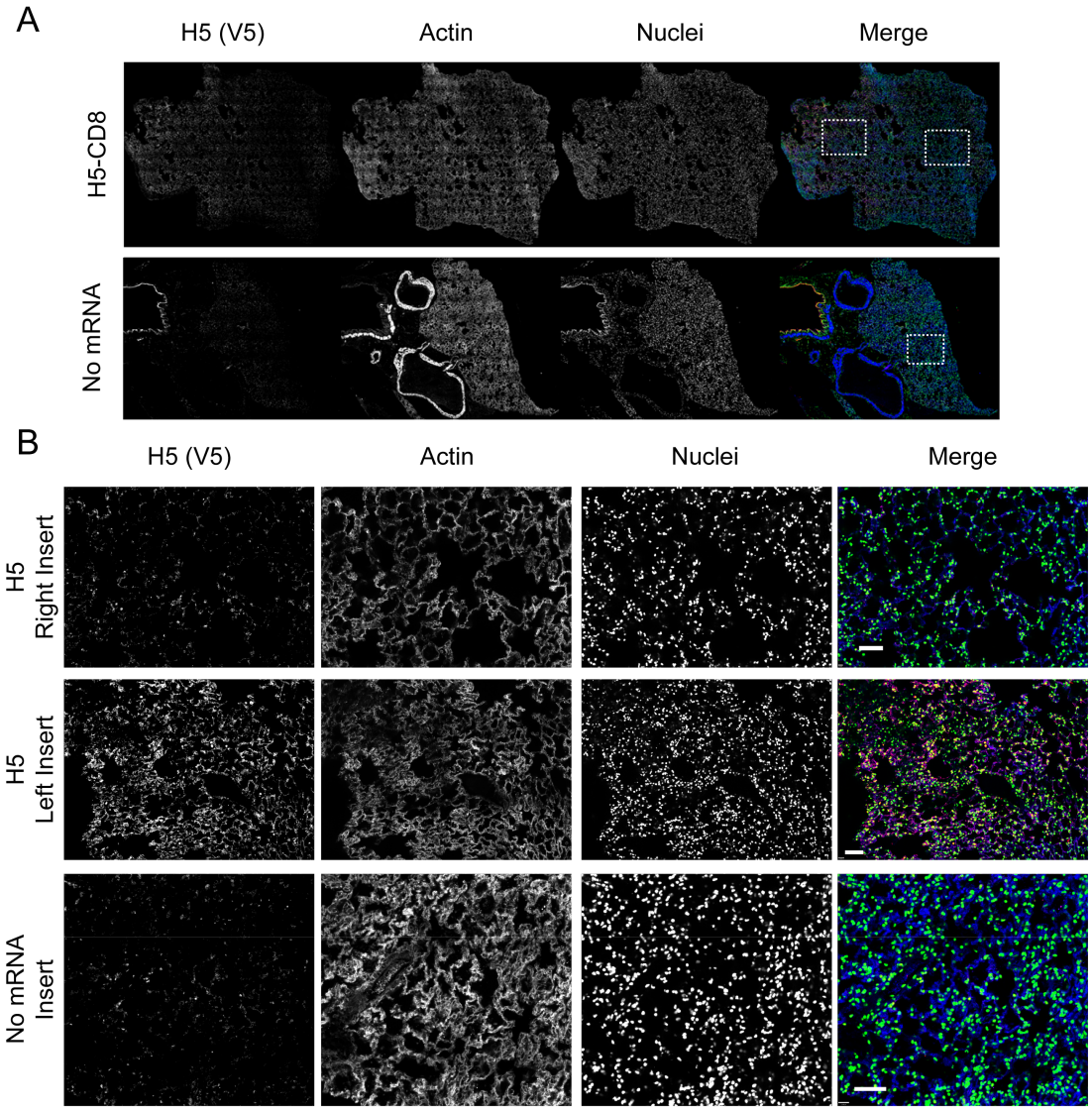

Figure 2.9: **Spatial Distribution of Aerosolized mRNA in the Lung** A, whole mount, cyrosectioned left lungs from mRNA sprayed (top row) and unsprayed (bottom row) lungs revealed heterogeneous delivery to the lung parenchyma with millimeter-scale variation in delivery. Additionally, cell-type specific, high backgrounds for the V5 antibodies were revealed in control lungs, giving insight into the potential background issues seen in whole tissue flow cytometry analysis. B, micron-scale resolution of inserts regions from (A). Heterogeneity of the delivery of aerosolized mRNA was revealed by comparing the inserts from the mRNA-exposed lung (top two rows) between high H5 protein-expressing region (middle row in (B), left insert from top row in (A)) and low or non-expressing H5 region (top row in (B), right insert from top row in (A)). These low or non-expression H5 regions (middle row) were comparable in staining to mRNA unexposed section (bottom row in (B), insert from bottom row in (A)) and demonstrate largely nuclear V5 staining. Scale bars are 50μm.

CHAPTER 3

MATRIX-STIFFNESS REGULATION OF TRANSFORMING GROWTH FACTOR-β BY INNER NUCLEAR MEMBRANE PROTEIN 3

3.1 Introduction

TGFβ in Pulmonary Fibrosis

Transforming Growth Factor β ("TGFβ") and its intra-cellular transcription factor partners, receptor-Mothers Against Decapentaplegic 2 & 3 ("Smad2/3"), are a growth factor/transcription factor system whose central role in wound healing, immunity, inflammation, fibrosis and development has long been appreciated. [115, 116, 117, 118] The connection between TGFβ and pulmonary fibrosis has been repeatedly underscored by clinical studies that show increased TGFβ protein and mRNA in fibrotic tissues and lung lavages relative to healthy tissues and secretions. [119, 120] Antagonism of TGFβ activation through inhibition or deletion of αv integrins generally [48], and αvβ6 integrins specifically [98, 121], have been shown to be protective against experimental models of pulmonary fibrosis and fibrosis in multiple other organ systems. Moreover, transgenic Smad3 knockout mice have also been shown to be protected from fibrosis. [122, 123] Interestingly, TGFβ might also contribute to pulmonary fibrosis through its suppression of the innate immune system, which allows for chronic and acute-on-chronic infections of the lung that injure the tissue and drive further fibrosis. [118, 124, 125]

Clinically, pirfenidone has led to a slowing of disease progression, potentially through antagonism of TGFβ. [10] Experimentally, pirfenidone has been shown to normalize TGFβ expression and tissue stores in multiple organ models of fibrosis. [126, 127] Pirfenidone has also been shown to inhibit TGFβ-driven myofibroblastic differentiation (*e.g.* fibroblast activation) but did not inhibit epithelial mesenchymal transition. [128]

3.1.1 Mechanical Regulation of Transforming Growth Factor β

One of the most interesting features of TGFβ signaling is that it is highly contextual, as it seemingly imparts opposite phenotypes to cells based on the context of its activity. [129, 130] Understanding the molecular basis of TGFβ signaling regulation is key not only to understanding its role in physiology and pathology, but in developing targeted, contextual therapies. Given the focus on tissue fibrosis, this introduction to TGFβ biology focuses on how micro-environmental mechanics regulates TGFβ activity both extra- and intracellularly to drive Smad2/3 transcriptional decision in the cell.

Canonical TGFβ Signaling

The canonical features of TGFβ signaling are well understood - TGFβ is a 25 kDa homodimer, which activates intracellular signaling by ligating to a Type II Transforming Growth Factor Receptor ("TβR"), which in turn forms a heterodimer of two Type II and two Type I TβRs. This ligated TβRII activates the serine/theronine kinase activity of the TβRI receptor, which ultimately drives the phosphorylation of Smad2 and Smad3 on its C-terminal S-S-X-S motif. [131, 132, 133, 134] Smad2 and Smad3, in complex with Smad4, translocate to the nucleus in a sorting nexin 9- and importin 9/β-dependent fashion and act as transcription factors and chromatin remodelers directly. [135, 129, 136, 137, 138, 139] In the nucleus, Smads2/3 can also act in concert with a variety of other transcription factors and these partners help to impart distinct transcription programs and signaling integration (*e.g.* coordinating with Wnt [140] and Akt signaling [141]). Smad2/3's nuclear residency is closely tied to its phosphorylation state, and de-phosphorlyation, through a variety of mechanisms, leads to its cytoplasmic sequestration. [142, 143]

Stiffness Driven Activation of Latent TGFβ

In tissues, TGFβ is stored in a latent complex, comprised of the latency-associated peptide ("LAP") and the latent TGFβ binding protein ("LTBP"), which physically connects to

ECM proteins, like fibronectin and its splice variants and fibrillin-1. [144, 145] These stores of TGFβ are quiescent until activated by cells or the environment, where after the newly freed TGFβ acts in a paracrine fashion. There are a variety of TGFβ activation mechanisms from the latent complex, including ROS production, low pH conditions, and proteolysis. [146, 147, 148, 149]

One additional mechanism of liberating free TGFβ from the matrix is that cells may physical pry open the latent complex through αv integrin's engagement of LAP in the latent complex. This mechanism is dependent on cellular contractility and is antagonized by function blocking αv integrin antibodies. While mechanical activation by integrin was found to be distinct from proteolytic activation of the latent complex [13], the ability of αv integrins to help coordinate MT1-MMP activity against the latent complex has also been demonstrated. [148] Genetic deletion of αv integrins or antagonism of αvβ6 particularly has been shown to be protective against fibrosis in a variety of organ systems. [98, 121, 48]

Mechanical activation of TGFβ is potentiated by the underlying stiffness of the substrate. The current physical model is that the matrix-bound latent TGFβ complexes is stress/strain-shielded by the physically connected ECM, which acts as a spring in parallel to the latent complex. In fibrotic matrices, this shielding is diminished and more physical force is transmitted to the latent complex, "popping" TGFβ out of its molecular prison. [13, 150] Because matrix stiffness is correlated both to the sensitivity of the latent complex to mechanical perturbation and to the force applied to the latent complex through cellular contractility, mechanical activation of TGFβ is particularly insidious in the fibrotic setting.

Stiffness Potentiation of Receptor-Mothers Against Decapentaplegic (rSMADs)

A number of *in vitro* studies have indicated that matrix stiffness also potentiates the cellular responses to free TGFβ. In particular, cells on increasingly stiff substrates have increased TGFβ-targeted transcription, cellular contractility and matrix synthesis when exposed to pre-activated, free TGFβ *in vitro*. [88, 89, 90, 91] These data strongly suggest that the

stiffness of the matrix imparts a "double-hit" in fibrosis - the increased stiffness not only increases the available supply of free TGFβ, but also increases cellular sensitivity to any free TGFβ.

The mechanism of this stiffness-dependent sensitivity to TGFβ signaling is unclear. It is known that TGFβ's intracellular signaling partners, Smad2/3, associate with mechanically regulated proteins like Rho-Associated Protein Kinase ("ROCK") and Yes Associated Protein/Transcriptional Co-activator with PDZ-binding motif ("YAP/TAZ"). These proteins could provide mechanically contextual cues to Smad2/3 through post-translation modifications ("PTMs") of the linker and MH1 domains of the Smads, respectively. [151, 91, 152] The PTMs by YAP/TAZ on Smad2/3 appear to influence the nuclear translocation of Smads in response to TGFβ stimulus, potentiating pro-fibrotic signaling in a model of renal fibrosis. This nuclear accumulation phenotype is particularly sensitive to small molecular antagonism of YAP by verteporfin, which indicates that YAP and TAZ may play differential roles in the mechanical regulation of Smad2/3. [91]

TGFβ also appears to acquire some of its mechano-sensitivity and to confer some of the mechanical phenotypes associated with it through association with both the myocardin-related transcription factors-A and -B (MRTF). Contrastingly, while YAP/TAZ appear to have a potentiating effect on TGFβ signaling through Smad2/3 with increasing substrate stiffness [91], Smad3 appears to impart a mechanical phenotype by inhibiting the activity of MRTF-A at baseline but not during TGFβ stimulation in the pulmonary vasculature. [153] There is also evidence that TGFβ exerts a mechanical phenotype through MRTF-A in a Smad-independent fashion, though the molecular mechanism is not known. [154]

3.1.2 Inner Nuclear Membrane Protein 3

Inner nuclear membrane protein 3 (LEMD3), or MAN1, is a double-pass integral inner nuclear membrane protein. The N- and C-terminal arms of LEMD3 are both nucleoplasmic, while the intra-transmembrane domain region lies in the peri-membrane space, be-

tween the inner and outer nuclear membranes. LEMD3 is named, in part for its LEM (LAPB2/Emerin/Man1) N-terminal domain, which is necessary for the nuclear targeting of the mature protein through a kinetic trap with the nuclear lamina. [155, 156, 157, 158, 159, 160, 161] In addition to a localizing function, the LEM domain of LEMD3 helps organize peripheral chromatin through binding with Barrier-to-Autointegration Factor (BAF) and heterochromatin protein 1 (HP1). [155, 162] The functional overlap between the LEMD3 and other LEM containing proteins, specifically emerin, is unclear and LEMD3 and emerin may have compensatory roles in nuclear organization. [157, 158, 163] Following its two transmembrane domains, LEMD3 has two annotated protein domains: the RNA recognition motif (RRM), and its MSC (MAN1-Src1 C-Terminal) domain. The MSC domain of LEMD3 has redundant chromatin/BAF binding functionality and appears to play a role in chromosomal organization during mitosis. [164] The RRM domain, discussed below, is a known Smad2/3 and Smad1 binding domain, which is necessary for LEMD3's antagonism of TGFβ superfamily signaling. [161, 165, 166, 167, 168, 169, 170, 171]

Inhibition of TGFβ Signaling by LEMD3

LEMD3 is a known inhibitor of TGFβ signaling. LEMD3 binds and inactivates the downstream transcription factor partners of both TGFβ and bone morphogenic protein (BMP), Smads 2&3 and 1&5&8, respectively. [161, 165, 166, 167, 168, 169, 170, 171] LEMD3s RNA recognition motif (RRM) domain competes with other transcription factors, such as FAST/Forkhead Box Protein H1 and Runx, for binding to Smad2/3 and promotes Smad2/3 dephosphorylation and nuclear export by acting as a coordinating scaffold for protein phosphatase, Mg^{2+}/Mn^{2+}-dependent 1α (PPM1α). [142, 166]

In humans, heterozygous loss of LEMD3 is frequently, but not always [172], associated with the development of Buschke-Ollendorf syndrome (BOS), in which patients develop some constellation of cutaneous collagenomas and elastomas (from aberrant TGFβ signaling) and osteopoikilosis (from aberrant BMP signaling), hyperostic lesions in long

bones, which can mimic osteoblastic metastatic lesions radiographically. [170, 173, 174, 175, 176, 177, 178, 179, 180, 181] Depending on the penetrance and specific genotype, heterozygous loss of LEMD3 can also be associated with more severe ECM pathologies, such as melorheostosis, a rare, progressive sclerosis frequently found in long bones that may lead to disfigurement and joint destruction. [170, 173]

Biophysical Linkages of LEMD3

In addition to its clear role in antagonizing TGFβ signaling both *in vitro* and *in vivo*, LEMD3 is retained in the inner nuclear membrane through its connection to the nuclear lamin superstructure by the activity of its N-terminal LEM domain. [156, 157, 158, 159, 160, 161] This connection, in turn, creates a direct biophysical link to the cells actin microfilament network through the nesprin-sun Linker of Nucleus and Cytoskeleton (LINC) complex, which has been shown to be necessary for the transmission of cytoplasmic and substrate derived stresses to the nucleus. [182, 183, 184] The LINC complex has been antagonized genetically using dominant negative constructs that competitively inhibit functional nesprin-actin linkages on the cytoplasmic side of the nucleus or nesprin-sun linkages in the perinuclear membrane space. These constructs allow for a functional decoupling of nuclear and cytoplasmic mechanics, without obviously compromising cell-ECM coupling and mechanics. [184]

3.1.3 Hypothesis and Summary

Given LEMD3s role in antagonizing Smad2/3 and its biophysical connection to the cells cytoskeleton, I hypothesized that LEMD3s inhibition of Smad2/3 would be reduced by cytoskeletal stress, thereby potentiating TGFβ signaling in an ECM stiffness-dependent fashion. In this thesis, dermal fibroblasts displayed ECM stiffness- and actin-dependent TGFβ responsiveness, and LEMD3 knockdown or over-expression modulated this stiffness responsiveness. This modulation was correlated to trends in Smad3 phosphorylation we ob-

served with LEMD3 over-expression or knockdown. LEMD3s interactions with Smad2/3 were negatively regulated by ECM stiffness and potentiated by disruption of the actin cytoskeleton, but these complexes were not potentiated by disruption of the LINC complex or over-expression of the LEM domain. Furthermore, knockdown of YAP or TAZ reduced Smad2/3-LEMD3 interactions by PLA and shifted the remaining interactions towards the nucleus on soft substrates. We demonstrated cytosolic interactions between LEMD3 and Smad2/3, which called into question basic assumptions about the current understanding of LEMD3's biology and its regulation of TGFβ. To understand these cytosolic events, I identified and genetically localized N- and C-terminal LEMD3 fragments, which separated LEMD3's Smad-binding RRM and lamin-binding LEM domains. I established that these fragments were created through post-translational proteolysis by a serine protease and were differentially regulated by lamin integrity. Finally, I found correlates between my *in vitro* findings and human lung tissue from idiopathic pulmonary fibrosis (IPF) and non-IPF patients. Specifically, interactions between LEMD3 and Smad2/3 demonstrated greater intra-patient/total variability in frequency and were more frequent in the cytoplasm in human lung core biopsies from IPF patients relative to non-IPF tissues. Additionally, IPF tissues had unique low-frequency LEMD3-Smad2/3 interaction regions, possibly indicative of local fibrotic disease. My work demonstrates novel aspects of LEMD3 biology as well as identifies a potential target for TGFβ antagonism relevant to fibrosis that complements current medical management.

3.2 Methods

3.2.1 Primary Fibroblast Cultures and Transfection, Human Lung Biopsies, and Other Reagents

Primary human foreskin fibroblasts (HFFs) were procured from ATCC (ATCC SCRC-1041, ATCC, Manassas, VA) and routinely cultured in DMEM (ThermoFisher, Waltham, MA) supplemented with 15% FBS and 1% penicillin/streptomycin (ThermoFisher, Waltham,

MA) in 5% CO_2 at 37C in a humified incubator to passage 13. CCL210s, a primary human pulmonary fibroblast line, were procured from ATCC (ATCC CCD-19Lu, ATCC, Manassas, VA) and routinely cultured in EMEM (ThermoFischer, Waltham, MA) supplemented with 10% FBS and 1% penicillin/streptomycin (ThermoFisher, Waltham, MA). For DNA transfections, 50,000 HFFs were resuspended in 10uL of Buffer R and electroporated using a 1700V, 20ms pulse width, 1 pulse program with 1μg DNA in a Neon transfection system (ThermoFisher, Waltham, MA). For siRNA transfections, 8,000-10,000 cells/cm^2 were treated with 25nM or 200nM siRNA with Lipofectamine2000 (ThermoFisher, Waltham, MA) according to the manufacturer's recommendations. IPF and non-IPF human lung core biopsies were generously provided by Dr. Eric White and the Lung Tissue Research Consortium (NHLBI: HHSN2682016000021). Selected cores all came from distal sections of lung parenchyma. Human subjects approval for this tissue was obtained through the University of Michigan Institutional Review Board. This study abides with the Declaration of Helsinki principles. For information on the oligos, antibodies, and uncommon chemicals used in this work, please refer to the Tables 3.1, 3.2, and 3.3 for supplier and use information.

3.2.2 Generation of Recombinant Constructs

LEMD3 Constructs

LEMD3 constructs were derived from the pSVK3-FLAG-MAN1 construct, kindly provided by Dr. Howard Worman (Addgene plasmid # 26002). [156] Site directed mutagenesis (SDM) was performed using the Q5 SDM kit (New England Biolabs, Ispwich, MA) according to their protocol, including the use of "NEB BaseChanger" applet to design primers and select PCR conditions. Primers and associated melting points for each mutagenesis are listed in Table 3.1. Constructs were confirmed with Sanger sequencing (MacrogenUSA, Rockville, MD).

DN LEM Construct

DN Kash and DN Control plasmids (pCDHEF1-MCS1-puro-mCherry-Nesprin-1αKASH and pCDH-EF1-MCS1-puro-mCherry, respectively) were kindly provided by Dr. Jan Lammerding and are described in detail in [184]. The DN LEM construct was created by Gibson Assembly of the N-terminal LEM domain cDNA from LEMD3 (without FLAG) from pSVK3-FLAG-MAN1 into the frame occupied by Nesprin-1αKASH in the pCDHEF1-MCS1-puro-mCherry-Nesprin-1αKASH construct with primers and PCR conditions as described in Table 3.1.

3.2.3 Western Blotting

For non-phospho-protein western blots

cell lysates from tissue culture plastic or from 2 or 25 kPa, 150cm Petrisoft dishes (Matrigen, Brea, CA) were either: harvested directly in 4X protein loading buffer (Licor, Lincoln, NE) supplemented with protease and phosphatase inhibitors (#A32959, ThermoFisher, Waltham, MA) according to the manufacturer's instructions; or, processed with the NE-PER compartment isolation kit (ThermoFisher, Waltham, MA) according to the manufacturer's instructions. Lysates were treated with 0.3 μL of benzonuclease (ThermoFisher, Waltham, MA) for 15 minutes at room temperature with vigorous shaking. Samples were heated to 95C for 5 minutes and run on a 4-12% Bis-Tris gel in 1x MES buffer and run for 70 minutes at 150V. The gel was then transferred to a nitrocellulose membrane using the XCell Blot Module (ThermoFisher, Waltham, MA) at 25V for 65 minutes. Membranes were air-dried for an hour, blocked with 5% non-fat milk in 1X PBS for an hour at room temperature, and then incubated with primary antibodies as described in Table 3.2 in 1X PBS-T with 1% milk for 16-24 hours at 4C. Near-IR or HRP conjugated secondaries as described in Table 3.2 were then incubated with the blot and imaged subsequently on either an Odyssey CLx system for near-IR dyes (Licor, Lincoln, NE) or a ChemiDoc MP system

(Bio-Rad, Hercules, CA) with SuperSignal West Femto reagents (ThermoFisher, Waltham, MA) for HRP secondaries according to the manufacturer's instructions. Band analysis was performed using the associated Licor or Biorad software.

For phospho-protein western blots

The procedure above was followed with the following changes: Cells were treated with 100pg/mL TGFβ 90 minutes before lysis. Membranes were incubated in and washed in buffers formulated with TBS instead of PBS. Membranes were blocked in 5% BSA in 1X TBS and all antibody incubations were done in 1% BSA in 1X TBS-T.

For recombinant LEMD3 western blots

Two samples of HFFs were prepared and electroporated as above and plated onto each plastic or hydrogel surface for 12 hours (protease inhibitor experiments) or 24 hours (LEMD3 fragment abundance and deletion mutant experiments) before harvesting.

3.2.4 qPCR

RNA was isolated from cultured cells using RNEasy Plus Mini kits (Qiagen, Hilden, Germany) according to the manufacturer's instructions. cDNA libraries were constructed using RT^2 First Strand kit (Qiagen, Hilden, Germany) according to the manufacturer's instruction. 25μL qPCR reactions were prepared using SYBR Green Master Mix (ThermoFisher, Waltham, MA) with 250nM primers, listed in Table 3.1 and 10ng input cDNA. Reactions were carried out on a StepOnePlus (ThermoFisher, Waltham, MA) for 40 cycles. Melt curves were visually inspected after each run to confirm a single, defined peak in the derivated intensity plot. Data from each run was imported into LinRegPCR, which performed baseline correction and measured PCR efficiency by amplicon group as described in [185]. The relative number of transcripts was calculated by dividing the C_q threshold by the PCR efficiency for the reaction raised to the power of C_q, the cycle number at which

the threshold is reached for a given target. For relative quantification between conditions, LEMD3 transcripts were either: normalized for each condition to the mean of two reference genes, 18S and ACTB, if the samples were all from a single stiffness condition; or, normalized to 18S alone if substrate stiffness was an experimental condition.

3.2.5 Smad-Driven Luciferase Assays

HFFs were transfected with Cignal Lenti Reporter virus (Qiagen, Hilden, Germany) with a MOI of 40 and subsequently selected using 400 ng/mL puromycin until untransduced HFFs died. Stably transfected HFFs, with or without additional LEMD3-focused genetic treatments as described above, were plated at 10,000 cells/well on a HTS plate (Matrigen, Brea, CA) containing glass surfaces and poly-acrylamide gels, which ranged in stiffness from 0.2 kPa to 50kPa, all functionalized with 10 μg/mL plasma-purified human fibronectin according to the manufacturer's instruction. Cells adhered to the surfaces for 4 hours in serum-free DMEM supplemented with 1% BSA and 1% penicillin/streptomycin. Media was then supplemented with the desired amounts of TGFβ and, when applicable, with cytoskeletal agents as described in the results. HFFs were then incubated for 16 hours at 37C before the luciferase reaction. Wells were supplemented to 2mM VivoGlo d-luciferin (Promega, Madison, WI) using an plate reader controlled auto-injector system and light production was subsequently quantified every 5 minutes for 30 minutes on a Synergy H4 plate reader (BioTek, Winooski, VT). The raw luciferase signal was the median intensity measured over this timecourse minus the intensity from luciferase-transfected cells not treated with TGFβ to account for any TGFβ elaborated and activated by the cells *in situ*. Cells were then fixed with 4% paraformaldehyde, permeabilized with 0.1% Triton X-100, and then stained with 1:10,000 Hoechst 33342 in 1X PBS for 30 minutes at room temperature (Thermo Fischer, Waltham, MA). The raw luciferase signal was then normalized to the nuclear signal, which was inside a linear standard curve form cells plated on glass and on polyacrylamide within each plate. Data for each condition was then fit to a three-parameter logistic equation using

a least-squares minimization fit in Prism (GraphPad, La Jolla, CA). For curves that did not converge with this model, individual data points are shown with the standard error of the mean to illustrate data heterogeneity. Otherwise, the trends across the maximal luciferase signal ("Top" variable from the model) or the mid-transition point observed between "Bottom" and "Top" signals ("EC50" variable from the model, called "transition point" in text), were statistically compared using an ANOVA with "Test for Trends," which restricts the hypothesis testing to a particular order of the data-sets (*e.g.* max luciferase signal as a function of increasing TGFβ dose or transition point as a function of increased LEMD3 expression). Each data point represents at least three biological replicates.

3.2.6 Proximity Ligation Assays

Ex vivo PLA

Lung biopsy samples were prepared by OCT embedding flash-frozen tissue (Tissue-Tek, Sakura Finetek, Torrance, CA) and preparing 10 μm cryosections on a CryoStar NX70 (Thermo Fisher, Waltham, MA). Sections were fixed for 10 minutes at 4C in 2% paraformaldehyde in 1x PBS. Protein-protein proximity ligation assays (PLA) were performed with antibody pairs listed in Table 3.2 as described previously in [186] with the following modifications: all primary antibody incubations were done for 16-24 hours at 4C, sections were blocked in 0.5 % Tween-20, 0.1 % Triton X-100, 0.5 % gelatin, 5 % donkey serum, 2 % bovine serum albumin (BSA), and 5 μg/mL poly dI-dC DNA in PBS, and sections were actin counter-stained with 1:40 phalloidin-488 (Thermo Fischer, Waltham, MA) for 30 minutes at room temperature following the PLA reaction using the IF protocol recommended by Sigma's PLA Resource Center. Slides were analyzed using a Axiovert 200M microscope (Carl Zeiss Microscopy, Jena, Germany) with an UltraVIEW spinning disk (PerkinElmer, Waltham, MA) and Flash 4.0v2 cMOS camera (Hamamatsu Photonics, Hamamatsu City, Japan). Low resolution images (20X) were collected using a 0.8NA Plan-Apochromat, and high resolution images (63X) were collected using a 1.4NA Plan-

Apochromat objective (Carl Zeiss Microscopy, Jena, Germany). Image acquisition and analysis was performed in Volocity (PerkinElmer, Waltham, MA). To analyze the incidence of LEMD3-Smad2/3 interactions between IPF and non-IPF biopsies at least 6 random points were chosen by Volocity in each section and registered to a serial section of the same tissue which was prepared as a no primary antibody PLA control. Tiled images with 20% overlap were acquired at 20X, covering a 628 μm by 334 μm area with z-slices acquired every 0.6 μm. The PLA signal was processed in Volocity using a consistent intensity threshold to identify PLA puncta, which were then spatially filtered by excluding PLA signal not associated with the actin or DAPI tissue-based signals. The remaining PLA signal was processed using the "Subtract" function to remove tissue autofluorescence, measured independently in an unused spectral window (615nm, width 70nm). The PLA signal was then normalized to the measured nuclear volume in the image slice. Relative PLA incidence between conditions was calculated by subtracting the normalized PLA signals between experimental and no primary antibody at each co-registered pair of points. High resolution imaging (63X) of each tissue was preformed over at least 6 randomly chosen areas, each 111 μm by 106 μm with z-slices acquired every 0.2 μm, to measure the cytosolic and nuclear PLA compartments in tissue. Signal processing was similar to the low-resolution processing described above except that the PLA signal was subdivided using the "Exclude Non-Touching" function in Volocity to measure nuclear and non-nuclear associated signal.

In vitro PLA

Protein-protein PLA was performed with antibody pairs listed in Table 3.2 as described in [186] with the following modifications: cells were plated on FN-coated glass or hydrogels (Matrigen, Brea, CA). All primary antibody incubations were performed for 16-24 hours at 4C and cells were counter-stained with 1:40 phalloidin-488 or phalloidin-546 in 1X PBS for 30 minutes at room temperature and/or further processed for IF imaging using the proce-

dure recommended in Sigma's PLA Resource Center. For all recombinant LEMD3 experiments, HFFs were electroporated as above and allowed to culture for 24 hours on 10μg/mL fibronectin coated glass or hydrogels before fixation. For LEMD3-phospho-Smad2/3 PLA assays: cells were treated 90 minutes before fixation with 100pg/mL TGFβ. For FLAG post-staining of PLA processed tissues, cells were blocked with unlabelled AffiniPure donkey anti-rabbit antibodies (Jackson ImmunoResearch, West Grove, PA) at a 1:10 dilution in 1X PBS-T at room temperature for 1 hour before further IF processing with 1:1000 rabbit anti-FLAG (#F7425, Sigma-Aldrich, Darmstadt, Germany) for 1 hour in PBS-T at room temperature. Following three washes with PBS-T for 5 minutes, each sample was stained with 1:500 goat anti-rabbit 546 in PBS-T for 1 hour at room temperature, washed again and then counter-stained as above. For V5 post-staining of PLA processed samples, cells were incubated with 1:200 647 labeled anti-V5 antibody (R&D Systems, Minneapolis, MN) diluted in PBS-T at room temperature for 1 hour before washing three times in PBS-T for 5 minutes each and then counter-stained as above. Imaging and analysis was performed as described for high-resolution *ex vivo* PLA signals except that no tissue autofluorescence signal was measured or needed to be subtracted and, when appropriate, other IF signal (e.g. FLAG) were measured in parallel. For cells on Matrigen HTS plates (Figure 3.5c&d), the confluence of cells prevented identifying individual cell boundaries. Instead, the PLA signal was quantified as the PLA volume divided by the nuclear intensity for each image. Each data point represents at least 3 unique surfaces with at least 12 cells measured per surface.

3.2.7 Atomic Force Microscopy and Cell Morphology

Experiments were conducted on an MFP-3D atomic force microscope (AFM) (Asylum Research, Santa Barbara, CA) on an inverted optical microscope (Nikon, Melville, NY). MCLT O-10 cantilevers (Bruker Nano, Camarillo, CA) were functionalized manually with 4.47μm polystyrene beads. Probes were calibrated before each experiment using a com-

bination of glass indention and thermal fluctuation measurements. Cellular and hydrogel measurements were acquired using a 2nN relative force trigger with a tip velocity of 2μm/s. Hydrogels were measured over a 400μm^2 space without cells, sampled as a 4X4 array. Young's modulus was calculated using custom scripts in MATLAB (TheMathWorks, Waltham, MA) that use a linearized Hertz approach for force-indentation measurements 40-60 nm into each surface. Cells and hydrogels were assumed to be incompressible (Poisson's ratio, ν, = 0.5). After AFM analysis, cells were fixed in 4% PFA for 10 minutes and stained with 1:40 Phalloidin-488 and 1:1000 Hoescht 33342 for 30 minutes. Cell spread area and morphology were analyzed from images taken at 63X in Volocity (as above). Each data point represents at least 3 unique surfaces with at least 10 cells per surface.

3.2.8 Mass Spectroscopy on LEMD3 Fragments

LEMD3 fragments were affinity purified from RIPA extracted lysates using FLAG (clone M2, #A2220, Sigma-Aldrich, Darmstadt, Germany) or V5 (clone V5-10, #A7345, Sigma-Aldrich, Darmstadt, Germany) affinity agarose according to the instructions of the manufacturer. Purified fragments were separated by SDS-PAGE on a 4-12% Bis-Tris gel in 1x MES buffer and visualized by SimplyBlue staining (Thermo Fischer, Waltham, MA). In gel digestion, nano-LC-MS/MS, and peptide identification was performed as previously described [187] with the following modifications. Reverse phase chromatography was performed using an in-house packed column (40 cm long X 75 μm ID X 360 OD, Dr. Maisch GmbH ReproSil-Pur 120 C18-AQ 1.9 μm beads) and a 120 min. gradient. The Raw files were searched using the Mascot algorithm (ver. 2.5.1) against a protein database constructed by combining the FASTA file for LEMD3 with a contaminant database (cRAP, downloaded 11-21-16 from http://www.thegpm.org) via Proteome Discoverer 2.1. Only peptide spectral matches with expectation value of less than 0.01 (High Confidence) were used.

Table 3.1: Oligos Used in this Chapter

Oligo Name	5'-3' Sequence	Purpose	Tm	Concentration Used	Vendor	Cat #
siLEMD1	GGAUAGAGCUGUUGACUUC	siRNA anti-LEMD3	NA	Pooled to 200nM	Dharmacon	siGENOME SMARTpool siRNA D-006306-01
siLEMD2	GAACUUCUCCAGCAAUUUA	siRNA anti-LEMD3	NA		Dharmacon	siGENOME SMARTpool siRNA D-006306-02
siLEMD3	GGAAUAAGGUGUGUUGGUU	siRNA anti-LEMD3	NA		Dharmacon	siGENOME SMARTpool siRNA D-006306-03
siLEMD4	CAAGGCAGAUGUAUGAUAU	siRNA anti-LEMD3	NA		Dharmacon	siGENOME SMARTpool siRNA D-006306-04
siYAP (pool of 4 siRNAs)	Not Disclosed	siRNA anti-YAP	NA	25nM	Dharmacon	SMARTpool siRNA M-012200-00-0005
siTAZ (pool of 3 siRNAs)	Not Disclosed	siRNA anti-TAZ	NA	25nM	Dharmacon	siGENOME SMARTpool siRNA D-016083-04-0002; D-016083-02-0002; D-016083-01-0002;
siGFP	CAAGCUGACCCUGAAGUUCUU	siRNA Control	NA	200nM	IDT	Gift From Dr. MG Finn's Lab
insV5 For	CTGCTGGGCCTGGATAGCACCTGAAAAGCTCGAGCTCGA	p.S931-Ter932insGKPIPNPLLGLDST in pSVK3-FLAG-LEMD3	68C	500nM	IDT	Custom
insV5 Rev	CGGGTTCGGAATCGGTTTGCCGGAACTTCCTTGAGAATTGG			500nM	IDT	Custom
LEM GA For	TTAAATGGATCCCCGCCACCATGGCGGCGGCA	DN LEM Construction from pCDH-EF1-MCS1-puro-KASH-mCherry	54C	500 nM	IDT	Custom
LEM GA Rev	TGCTCACCATTCGATATTTCATGTAACGCAG		52C	500 nM	IDT	Custom
mCherry GA For	GAAATATCGAATGGTGAGCAAGGGCGAG		58C	500 nM	IDT	Custom
mCherry GA Rev	ATCCTTGCGGCCGCTCAC		62C	500 nM	IDT	Custom
del294-325 For	CTGGAGACTTCAGTTCAGGGAG	p.delQ294-R325 in pSVK3-FLAG-LEMD3-V5	68C	500nM	IDT	Custom
del294-325 Rev	TCTGCTGGAGGCCACGTC			500nM	IDT	Custom
del579-647 For	TTTGTTACTGTAACTCACAG	p.delE579-A647 in pSVK3-FLAG-LEMD3-V5	57C	500nM	IDT	Custom
del579-647 Rev	TTGAACAGAAAGCGTTCTTTG			500nM	IDT	Custom
del21-668 For	CTGCGTTACATGAAATATCG	p.delM21-V668 in pSVK3-FLAG-LEMD3-V5	60C	500nM	IDT	Custom
del21-668 Rev	TTTCTCGTCCGAATTCCTG			500nM	IDT	Custom
qLEMD3 For	TTTCGACGTGCTTTTGTTACTG	RT-qPCR - Human LEMD3, Exons 6-7	60C	250nM	IDT	Hs.PT.58.38449009
qLEMD3 Rev	TGTTTCCTCCTCTTCTTTTGTCC			250nM	IDT	
q18S For	GTAACCCGTTGAACCCCATT	RT-qPCR - Human 18S	60C	250nM	IDT	Originally found in [188]
q18S Rev	CCATCCAATCGGTAGTAGCG			250nM	IDT	
qACTB For	AGGCACCAGGGCGTGAT	RT-qPCR - Human β-Actin	60C	250nM	IDT	Originally found in [189]
qACTB Rev	GCCCACATAGGAATCCTTCTGAC			250nM	IDT	

Table 3.2: Primary, Secondary and Other Antibodies Used in this Chapter

	Target	Clone	Host	Application				Vendor	Cat#
				WB	IF	PLA	Other		
Primary	LEMD3	4E1	Mouse	1:1000		1:1000 (cells), 1:100 (tissue), used with EPR19557-4 & D27F4		LsBio	LS-C114872
	V5	V5-10	Mouse	1:1000				Sigma	V8012
	V5	Polyclonal	Rabbit			1:2000, used with 18/Smad2/3		Abcam	ab9116
	647 labelled V5	1036H	Rabbit		1:200			R&D Systems	FAB8926R
	Smad2/3	18/Samd2/3	Mouse			1:2000, used with Abcam ab9116		BD Bioscience	610842
	Smad2/3	EPR19557-4	Rabbit			1:1000 (cells), 1:100 (tissue), used with 4E1		Abcam	ab202445
	phospho-Smad2/3	D27F4	Rabbit	1:1000		1:1000, used with 4E1		CST	#8828
	FLAG	Polyclonal	Rabbit	1:1000	1:1000			Sigma	F7425
	GAPDH	D-6	Mouse	1:1000				Santa Cruz	sc166545
	Lamin A/C	EPR4068	Rabbit	1:1000				Abcam	ab108922
Secondary	Goat αMouse-HRP	N/A	Goat	1:15000				Abcam	ab7023
	Goat αRabbit-HRP	N/A	Goat	1:15000				ThermoFisher	A-27036
	Donkey αRabbit-IR680	N/A	Donkey	1:20000				Licor	926-68073
	Donkey αMouse-CW800	N/A	Donkey	1:20000				Licor	926-32212
	Goat αRabbit-546	N/A	Goat		1:500			ThermoFisher	A-11010
Blocking	Donkey αRabbit	N/A	Donkey				1:10	Jackson ImmunoResearch	711-066-152

Table 3.3: Chemicals and Recombinant Proteins Used in this Chapter

Name	CAS	Working Concentration	Solvent	Use	Vendor	Cat #
Cytochalasin D	22144-77-0	2 μM	DMSO	Stablizes g-actin	Sigma	C8273
Blebbistatin	674289-55-5	2 μM	DMSO	Inhibits myosin II	Sigma	203389
Jasplakinolide	102396-24-7	100-200 nM	DMSO	Stablizes f-actin	Enzo	ALX-350-275
E-64D	88321-09-9	2-40 μM	DMSO	Irreversible cystein protease inhibitor: calpain, papain, actinidase, cathepsins B, H, and L	Sigma	E8640
E-64	66701-25-5	10-100 μM	DMSO	Irreversible cystein protease inhibitor: calpain, papain, actinidase, cathepsins B, H, and L	Sigma	E3132
DCI	51050-59-0	10-100 μM	DMSO	Irreversible serine protease / esterase inihibitor: cathepsin G, elastase, thrombin, plasmin, factor Xa & X11a, granzymes A, B, and H	Sigma	D7910
MMPi III	927827-98-3	1-20 μM	DMSO	Reversible MMP inhibitor: MMP1, MMP2, MMP3, MMP7, MMP13	Millipore	444264
MG-132	133407-82-6	10 μM	DMSO	Inhibits 26S proteosome	Sigma	M7449
Roscotine	186692-46-6	0.1-35 μM	DMSO	Inhibits cdc2/cyclin B, cdk2/cyclin A, cdk2/cyclin E, cdk5/p35	Tocris	1332
TGFβ	N/A	50-1000 pg/mL	4mM HCL with 10% BSA	Recombinant human TGF-β	R&D Systems	240-B

3.3 Results

3.3.1 Fibroblast TGFβ Responsiveness is Potentiated by ECM Stiffness and Inhibited by LEMD3 Expression

Dose-Dependent Stiffness Potentiation of TGFβ

I sought to validate that fibroblasts in our system displayed stiffness-dependent TGFβ responsiveness using primary human dermal fibroblasts (HFFs) stably transfected with a Smad-driven luciferase. First, I characterized stiffness and morphology phenotypes associated with mechanotransduction using optical microscopy and atomic force microscopy (AFM). With increasing stiffness, fibroblasts underwent cellular compliance matching (p=0.0022) and increased their cell spread surface area (p=0.1801) and polarization (p=0.0263) as seen in Figure 3.1a and Figure 3.2, respectively. Luciferase transfected HFFs showed a sigmoidal responsiveness to recombinant human TGFβ (rhTGFβ) as a function of substrate stiffness (Figure 3.1b). This stiffness potentiation was dose-dependent with increasing pg/mL doses of rhTGFβ appearing to shift the transition point of the sigmoid towards softer substrates ("soft-shift", p=0.07). Transition points in the pg/mL dose-range occurred at stiffness over a range from $\approx$ 1-4 kPa. These cells also showed the expected rhTGFβ dose-response (increasing luminescence with increasing TGFβ dose) on stiff substrates ($p<0.0001$, Figure 3.1b). Previous studies have also shown stiffness-dependent modulation of TGFβ signaling, and our work improves the resolution of these results by more finely probing the stiffness space across a range from 0.5 kPa to 50 kPa and the TGFβ dose-dependence of this effect. [88, 89, 90, 91]

LEMD3 Modulation of Fibroblasts' TGFβ-Stiffness Response

Having confirmed the TGFβ/stiffness phenotype, I tested how modulating LEMD3 alters the stiffness responsiveness of fibroblasts using Lipofectamine 2000 delivered siRNA against LEMD3 ("siLEMD3") and electroporation with pFLAG-LEMD3-V5 (LEMD3 over-

expression plasmid with N-terminal FLAG epitope tag and C-terminal V5 epitope tag). Increasing LEMD3 expression (Figure 3.3a) induced a decrease in maximal luminescence (p=0.04) and a "stiff-shift" in the stiffness response's sigmoidal transition point ($p<0.0001$, Figure 3.1c). There was a corresponding "soft-shift" in the transition point ($p<0.0001$) and increase in maximal luminescence (p=0.04) when LEMD3 expression was decreased through siRNA treatment (Figure 3.3b). There were no significant differences in either maximal luminescence or the stiffness transition point of the sigmoid model between HFFs treated with Lipofectamine2000, electroporated control HFFs ("Neon HFF"), or HFFs treated with concentration matched siRNA against GFP ("siGFP").

To connect LEMD3's TGFβ antagonism seen in Figure 3.1c to Smad2/3's activation, I investigated the effect LEMD3's modulation on Smad3 phosphorylation (Figure 3.4). 100pg/mL TGFβ treatment for 90 minutes increased the ratio of phospho-Smad3 to total Smad3 relative to untreated HFFs (p=0.0506). Treatment with either Lipofectamine 2000 or electroporation reduced the phospho-Smad3/Smad3 ratio, but treatments with 25nM and 200nM siRNA against LEMD3 increased the phospho-Smad3/Smad3 ratio relative to siRNA against GFP (p=0.1103 and p=0.0057 for 25nM and 200nM siRNA groups, respectively). Electroporation with pFLAG-LEMD3-V5 or a C-terminal fragment (pFLAG-LEMD3p.Δ21-669-V5, "CTF"), previously shown to be sufficient for Smad2/3 binding and de-phosphorylation [166, 171, 169, 168, 190], decreased the pSmad3/Smad3 ratio; however, as in Figure 3.1c, there was no difference between electroporation controls and electroporation with any LEMD3 plasmids on tissue culture plastic. The stiffness-modulation of LEMD3's inhibition of TGFβ shown here is a novel finding, but the general inhibition of TGFβ signaling [171, 161, 170, 165, 166] and Smad phosphorlation [168, 171, 169] by LEMD3 (on stiff substrates) confirmed findings from previous reports.

3.3.2 Cytoskeletal Determinants of TGFβ-Stiffness Response

To test which components of the cell's microfilament cytoskeleton control the stiffness-response of HFFs to rhTGFβ, I used chemical inhibition of the structural (cytochalasin D, a g-actin stabilizer) and contractility machinery (blebbistatin, a myosin II inhibitor). Stiffness-dependent TGFβ responses required actin polymerization but did not require cellular contractility (Figure 3.1d). Treatment with 10 μM blebbistatin (a myosin II inhibitor) did not significantly shift the transition point nor increase the maximal luminescence of cells relative to HFFs treated with rhTGFβ alone. Cells treated with 2 μM cytochalasin D showed a low, flat luminescent profile over increasing ECM stiffness, and the data did not converge to a sigmoidal model. Curiously, siRNA against LEMD3 did not rescue the cytochalasin D phenotype, though the degree of LEMD3 knockdown may not have been sufficient (Figure 3.3b). These data indicate that the actin cytoskeleton, but not cellular stress per se, is needed for stiffness-modulated TGFβ signaling.

3.3.3 LEMD3-SMAD2/3 Complexes are Inversely Correlated to Substrate Stiffness and Occur Throughout the Cell

LEMD3-Smad2/3 Interactions Are Negatively Regulated by ECM Stiffness and Invariant to TGFβ Dose

Given that LEMD3 modulated the stiffness response of fibroblasts to TGFβ, I used proximity ligation assays (PLA, methodologically reviewed in [186]) to examine the stiffness dependence of LEMD3-Smad2/3 interactions on hydrogels whose stiffness is representative of physiologic (1 kPa) and fibrotic (25kPa) lung tissue in humans. [4] LEMD3-Smad2/3 interactions were negatively correlated with substrate stiffness in both the cytoplasm and the nucleus (Figure 3.5a&b). This negative correlation was independent of rhTGFβ dosing (50pg/mL, inside the range of stiffness-responsive doses identified in 3.1b), consistent with previous findings that LEMD3-Smad2/3 interactions are phosphorylation-

independent. [171] While LEMD3-Smad2/3 interactions were unperturbed by TGFβ dosing, I explicitly tested the ability of LEMD3 to bind phospho-Smad2/3 (Figure 3.6). I found that HFFs treated with 100pg/mL TGFβ on glass had significantly higher LEMD3-phospho-Smad2/3 interactions than untreated fibroblasts (p=0.0333) and that there was a significant negative correlation between substrate stiffness and LEMD3-phospho-Smad2/3 interactions (p=0.0305). These data confirm and extend previous observations that LEMD3 can bind both phosphorylated and un-phosphorylated Smad2/3. [171]

I extended our findings by performing the PLA assay across a finer range of stiffness with both HFFs and CCL210s, an adult, pulmonary-derived fibroblast line (Figure 3.5c). Both CCL210s and HFFs showed a biphasic response to stiffness with peak values at 1 kPa. CCL210s demonstrated a greater dynamic range in response to stiffness as well as a more gradual loss of PLA interactions on progressively stiffer substrates relative to HFFs. Additionally, the abrupt loss of LEMD3-Smad2/3 interactions between 1 kPa and 4 kPa in HFFs correlated with the stiffness dependence of the luciferase signal measured in Figure 3.1b.

LEMD3-Smad2/3 Interactions Occur in the Cytosol

Provocatively, I found that approximately half ($\approx$ 50% and 42% on 1 kPa and 25 kPa surfaces, respectively, in Figure 3.5a&b) of the PLA interactions on both substrates occurred in the cytoplasm of the cells. Across a broader range of stiffness, I found that the nuclear proportion of LEMD3-Smad2/3 interactions was inversely correlated to substrate stiffness in both HFFs ($p<0.0001$) and CCL210s (p=0.0199), as seen in Figure 3.5d. Given that LEMD3 is thought to be an integral protein of the inner nuclear membrane, I validated our findings through V5-Smad2/3 PLA in cells transfected with pFLAG-LEMD3-V5 (Figure 3.5e&f). Near identical trends were observed with this independent, recombinant PLA reaction: a reduction in PLA frequency overall ($p<0.0001$), and reductions in both the cytoplasm ($p<0.0001$) and nuclear (p=0.0018) compartments with increasing substrate

stiffness. To control for the degree of recombinant LEMD3 expressed across stiffness conditions, I found a significant difference in the linear regression between PLA puncta per cell and the per-cell FLAG intensity in cells on both soft and stiff surfaces ($p<0.0001$) (Figure 3.5g). The steeper slope observed for cells on soft substrates confirmed a higher rate of LEMD3-Smad2/3 complex formation per arbitrary unit of LEMD3 expressed (as measured by the fused FLAG epitope) relative to stiff substrates.

I also validated that our PLA methodology faithfully reported on sub-cellular interactions between LEMD3 and lamin B1, a nuclear intermediate filament. $94.34\% \pm 0.005\%$ PLA interactions between LEMD3-lamin B1 were compartmentalized to the nucleus (Figure 3.7). There was not significant variation in this frequency across the biological replicates. These data indicate that our PLA methodology and analysis techniques are sensitive enough to determine the sub-cellular localization of LEMD3 interactions.

The C-terminal fragment of LEMD3 (pFLAG-LEMD3p.Δ21-669-V5, "CTF") I cloned and described earlier has been shown to be sufficient for Smad2/3 binding [169, 171, 168, 190, 166] and lacks the necessary domains for nuclear localization [156, 168, 161]. I repeated these recombinant PLA experiments between the V5 epitope and Smad2/3 with the CTF to ascertain 1) whether this fragment of LEMD3 was sufficient for generating stiffness-dependent Smad2/3 interactions; and 2) whether these fragments were uniquely localized to the cytoplasm. The CTF-expressing fibroblasts on 1 kPa hydrogels had significantly more Smad2/3 interactions overall ($p<0.0001$), in the cytoplasm ($p<0.0001$), and in the nucleus ($p=0.0082$) relative to CTF-expressing HFFs on 25kPa hydrogels (Figure 3.8a). Transfected fibroblasts on 25 kPa hydrogels had significantly more overall CTF-Smad2/3 interactions than electroporation control fibroblasts ($p=0.0227$). To control for degree of recombinant CTF expression we compared the V5 signal and the PLA interactions per cell across each group. I found that fibroblasts on 1kPa hydrogels had a steeper slope (*i.e.* more PLA per arbitrary unit of V5 expressed) than fibroblasts on 25 kPa hydrogels ($p=0.1476$, Figure 3.8b). Unexpectedly, a significant fraction ($\approx$ 40-55%, depending on stiffness) of

CTF-Smad2/3 interactions took place in the nucleus. While the N-terminus of LEMD3 up to the first transmembrane domain has been shown to be necessary for faithful localization of full length LEMD3 to the nucleus [156, 161], the CTF has an independent ability to bind both barrier-to-autointegration factor (BAF, a nuclear chromatin protein, [157]) and DNA directly [190], which may allow for some partial enrichment of the CTF in the nucleus. Overall, these V5-Smad2/3 PLA assays with recombinant LEMD3 proteins confirmed 1) the negative stiffness correlation and cytoplasmic localization of LEMD3-Smad2/3 complexes observed with endogenous protein antibodies; and 2) that the CTF is sufficient for cytoplasmic LEMD3-Smad2/3 interactions.

3.3.4 Mechanism of LEMD3-Smad2/3 Stiffness Regulation

LINC Disruption Does Not Potentiate LEMD3-Smad2/3 Interactions

We hypothesized that the frequency of LEMD3-Smad2/3 complexes would be decreased by transmission of ECM-driven cytoskeletal tension to LEMD3 through a two-part physical linkage: 1) the nesprin-sun LINC complex joining the nuclear lamina and actin cytoskeleton; and, 2) through nuclear lamina-LEMD3 couping via the LEM domain. We tested this hypothesis by disrupting the molecular linkages at either the level of the LINC complex by expressing a previously validated dominant negative nesprin construct, DN-Kash-mCherry, [184] or by disrupting LEMD3-lamin interactions by expressing a novel DN-LEM-mCherry constructs and assessing complex formation by PLA. Neither DN Kash nor DN LEM expression increased the LEMD3-Smad2/3 PLA frequency relative to mCherry-only expressing fibroblasts on glass (Figure 3.9a&b). To assess if my findings were biased by the degree of DN Kash or DN LEM expression, I correlated PLA puncta against the mCherry expression of the fusion protein per cell (Figure 3.9c). None of the Pearson's coefficients (r=-0.251 and r=-0.087 for DN Kash and DN LEM, respectively) varied significantly from 0 (p=0.0579 and p=0.43 for DN-Kash and DN-LEM, respectively), indicating that the degree of dominant-negative protein expression was not a likely explanation for my

findings. These results also corroborated findings in Figure 3.1d, where cellular contractility inhibition, through blebbistatin antagonism of myosin II, did not significantly modify the rhTGFβ stiffness-response of fibroblasts.

Actin Polymerization Negatively Regulates LEMD3-Smad2/3 Interactions

Because g-actin stabilizing agents did modify the fibroblast stiffness-response (Figure 3.1d), I examined the effect of actin polymerization on LEMD3-Smad2/3 complex formation by PLA. Actin polymerization was significantly, negatively correlated to the frequency of LEMD3-Smad2/3 complexes (Figure 3.9d-f). Fibroblasts on glass treated with 2 μM cytochalasin D for 90 minutes demonstrated an increase in the total frequency of LEMD3-Smad2/3 complexes overall (p=0.0089). The frequency of LEMD3-Smad2/3 complexes also increased in the cytosolic (p=0.0871) and nuclear compartments (p=0.5657). Conversely, f-actin stabilization through jasplakinolide treatment for 2 hours on 1 kPa hydrogels demonstrated a dose-dependent decrease in LEMD3-Smad2/3 interactions ($p<0.0001$ for vehicle/DMSO treated cells vs both 100nM and 200nM jasplakinolide, and p=0.0312 for 100nM vs 200nM jasplakinolide treatment, Figure 3.9f). Significant reductions in LEMD3-Smad2/3 complex formation were observed in both the cytoplasm ($p<0.0001$ for DMSO treated cells vs. both 100nM and 200nM jasplakinolide) and in the nucleus (p=0.0466 for DMSO treated cells vs. 100nM jasplakinolide and p=0.002 for DMSO treated cells vs. 200nM jasplakinolide). Considered with the results in Figure 3.1a and Figure 3.2, showing increased cell spreading, polarization and stiffness as a function of substrate stiffness, these data suggested that actin polymerization in response to substrate stiffness helps coordinate the LEMD3-dependent stiffness response of cells to TGFβ.

YAP/TAZ Knockdown Disrupts LEMD3-Smad2/3 Interactions

Neither LEMD3 nor Smad2/3 are known to bind actin directly, so I considered that other actin-regulated, mechano-sensitive transcription factors might mediate this cytoskeletal

effect. Yes-associated protein and Transcriptional Coactivator with PDZ-binding motif (YAP/TAZ) are shuttled between the cytosol and nucleus in an actin-LATS1/2 dependent fashion. [191, 15, 192] Moreover, YAP/TAZ bind Smad2/3 and have been shown to be necessary for nuclear accumulation of Smad2/3 in response to TGFβ stimulus. [91, 152, 193, 194] TAZ, in particular, has been shown to bind to the MH1 domain of Smad2. [152]

I assessed the effect of YAP or TAZ knockdown by siRNA on LEMD3-Smad2/3 interactions by PLA on 1 kPa hydrogels in HFFs (Figure 3.10). siRNA against YAP ("siYAP") reduced the interaction rate by 69.5% $\pm$ 2.4% (Figure 3.10b, $<$0.0001) while siRNA against TAZ ("siTAZ") reduced the interactions by 46.9% $\pm$ 5.6% (Figure 3.10b, p=0.0005). While there was a significantly greater reduction of interactions with siYAP relative to siTAZ (Figure 3.10b, p=0.0094), siYAP treatment was also more effective in knocking down YAP expression relative to siTAZ knocking down TAZ expression (Figure 3.10e, $\approx$ 85% and $\approx$ 72% reductions, respectively).

Treatment with either siYAP or siTAZ shifted the remaining LEMD3-Smad2/3 interactions towards the nucleus (Figure 3.10c). siYAP treated HFFs had an increased nuclear PLA fraction of 11.4% $\pm$ 2.9% relative to vehicle treated HFFs (p=0.0039), while siTAZ treated cells had an increased nuclear PLA fraction of 8.4% $\pm$ 3% (p=0.0716) relative to vehicle HFFs. These data together suggest that YAP and TAZ positively cooperatively regulate LEMD3's binding to Smad2/3 but only in the cytosol, implicating phosphorylated, quiescent YAP/TAZ in regulating LEMD3-Smad2/3 interactions.

3.3.5 LEMD3 Fragments are Generated by a Serine Protease and Differentially Regulated by the Integrity of the Nuclear Lamina

Mass Spectroscopy and Genetic Perturbation of LEMD3 Fragments

I observed cytosolic LEMD3-Smad2/3 interactions with PLA antibody pairs against the native protein and against either the full length recombinant LEMD3 protein or a C-terminal fragment of LEMD3, each expressing a V5 epitope tag. An $\approx$ 50 kDa LEMD3 frag-

ment was also isolated from the cytosol in fractionated cell western blots using antibodies against the native protein (Figure 3.11b). Additionally, these cytosolic interactions seemed to be stiffness-regulated given their negative correlation with actin polymerization (Figure 3.9d-e). To understand how LEMD3 could interact with Smad2/3 in the cytosol, I performed mass spectroscopy on lysates from cells transfected with pFLAG-LEMD3-V5 constructs (Figure 3.12a). Results from a FLAG-purified 60 kDa fragment showed two transitions in the peptide spectral matches to LEMD3's primary sequence - first at p.294-325 and second at p.579-647 (these protein coordinates are offset by 20 amino acids inserted with the N-terminal FLAG tag in the pFLAG-LEMD3-V5 construct from the native protein sequence). The primary sequence relationship between these two regions and other known domains of LEMD3 are shown in Figure 3.12b. Deletion mutants (pFLAG-LEMD3p.Δ294-325-V5 & pFLAG-LEMD3p.Δ579-647-V5) exploring these two regions showed differential fragment presentation in western blots which probed either the N-terminal FLAG tag or C-terminal V5 tag of the recombinant protein (Figure 3.12c). Specifically, pFLAG-LEMD3p.Δ294-325-V5 lysates lacked the 60kDa FLAG fragment (the FLAG fragment at $<$50 kDa was also missing but was not consistently found in all blots) and the 46kDa V5 fragment. Suggestively, the 46kDa V5 fragment was similar in size to a cytoplasmically localized fragment of LEMD3 using a native antibody (Figure 3.11b). The pFLAG-LEMD3p.Δ579-647-V5 lysates did not appear to change the FLAG fragment presentation but did eliminate V5 fragments at 60kDa and 85kDa. These genetic data suggested that the protein was modified in at least two regions, one in the nucleoplasm (Δ294-325) and one in the peri-nuclear membrane space (Δ579-647). Moreover, all the V5/C-terminal fragments identified by my genetic mutations contained the CTF used in Figures 3.4 and 3.8, indicating that they are sufficient for binding Smad2/3 in a stiffness-dependent fashion and binding Smad2/3 in the cytoplasm.

Proteolytic Degradation of LEMD3

Following the observation of cytoplasmic interactions with an intron-less LEMD3 cDNA construct, I hypothesized that these fragments were generated proteolytically. I used western blots to determine the effects of several broad-spectrum protease inhibitors against cysteine (E64 & E64d), serine (3,4 dichloroisocoumarin, DCI) and matrix metallo-proteinases (MMP inhibitor III - MMPi) as seen in Figure 3.12d&e. From fragments controlled by the Δ294-325 region, the 60kDa FLAG fragment was reduced relative to the full length protein in cells treated with DCI (p=0.0153), a known inhibitor of cathepsin G, elastase, thrombin, plasmin, factors Xa & X11a, and granzymes A, B and H. [195] This fragment was also reduced when cells were treated with MG-132 (p=0.0238), an inhibitor of the 26S proteosome complex, an important regulator of overall protein homeostasis and particularly critical for degrading ubitquinated proteins (reviewed recently in [196]). These same trends were observed for the 46kDa V5 fragment (DCI: $p<0.0001$; MG-132: p=0.0238), which is also controlled by the Δ294-325 region. Monash University's PROSPER (Protease specificity Prediction Server as described in [197]) predicted only a single serine protease, cathepsin G, cleaving between p.V275-L276 (native protein coordinates, score=1.14) in pFLAG-LEMD3p.Δ294-325-V5's deletion region. Using a more selective cathepsin G inhibitor, I found a significant reduction in the 60 kDa FLAG fragment (p=0.0075) but no significant trend with the 46 kDa V5 fragment. From the Δ579-647 region, the 60 kDa V5 fragment was not significantly modified by any protease inhibitor treatments explored here. Surprisingly, the 85 kDa fragment was only potentiated by MMPi (p=0.0004) and E64d (p=0.0044) treatment. These fragment data together suggested that a serine protease, possibly cathepsin G, operates in the Δ294-325-V5 region, with a distinct mechanism of fragment generation occurring in the Δ579-647 region.

Because pFLAG-LEMD3p.Δ579-647-V5's deletion region lies in the peri-nuclear membrane space, I hypothesized that this location might only be susceptible to degradation during mitosis. Because LEMD3's localization is controlled necessarily by its association with the nuclear lamina through its LEM domain [161, 165, 158, 159, 160], I chose roscovitine, a selective inhibitor of cdk1, which prevents cell cycle progression in part by preventing lamin phosphorylation and disassembly. [198] Surprisingly, roscovitine only modulated fragments associated with pFLAG-LEMD3p.Δ294-325-V5 - significantly reducing the generation of the 60kDa FLAG fragment ($p=0.0051$) and significantly increasing the generation of the 46kDa fragment ($p<0.0001$).

Finally, Figure 3.5d showed that LEMD3-Smad2/3 interactions shifted towards the cytoplasm with increasing substrate stiffness. I tested whether this shift was driven by alterations in C-terminal LEMD3 fragment abundances as a function of substrate stiffness with western blots assaying HFFs transfected with pFLAG-LEMD3-V5 (Figure 3.13a&b). After 24 hours, cells grown on 1 kPa and 25 kPa hydrogels each had decreased proportions of full length LEMD3 relative to fibroblasts cultured on tissue culture plastic ($p=0.0062$ and $p=0.0031$ for TC vs. 1 kPa and TC vs. 25 kPa, respectively). Lysates from 1 kPa and 25 kPa hydrogels had similar abundances of the 85 kDa and 60 kDa fragments, though the 45 kDa fragment was almost twice as abundant on 25kPa hydrogels as on 1 kPa hydrogels ($p=0.5196$). I also found that full length native LEMD3's abundance was not modulated significantly by culture on 1 kPa or 25 kPa surfaces (Figure 3.14a) and that LEMD3's mRNA expression level was also invariant to culture on these surfaces (Figure 3.14b).

3.3.6 LEMD3-SMAD2/3 Complexes are More Cytosolic and Their Frequencies are More Varied in IPF Biopsies than non-IPF Biopsies

Subcellular Localization of Smad2/3-LEMD3 Interactions

I sought to validate our *in vitro* findings in human lung core biopsies from six patients (three with and three without IPF). IPF patients had significantly more cytosolic LEMD3-Smad2/3 interactions than non-IPF patients (p=0.0307, Figure 3.15a&c). These data are compelling because they connect the cytoplasmic PLA localization trend seen with increasing stiffness in *in vitro* in Figure 3.5d and the pattern observed in fibrotic relative to non-fibrotic human tissue *ex vivo*. Additionally, these data directly demonstrated that extra-nuclear LEMD3-Smad2/3 interactions occur in human lung tissue, which I also discovered in Figure 3.5, indicating that extra-nuclear LEMD3 is not an artifact of *in vitro* culture.

Interaction Frequency Ex Vivo

Patients with IPF also had a slightly higher median frequency of LEMD3-Smad2/3 interactions relative to patients without IPF (Figure 3.15d, p=0.5783). However, while each non-IPF patient had a fairly consistent LEMD3-Smad2/3 interaction "set-point," IPF patients displayed a higher degree of intra-patient heterogeneity across their sampled tissue regions (67% vs. 30% average coefficient of variance for IPF and non-IPF patients, respectively). Overall, the whole IPF data set had a higher degree of kurtosis (4.765 vs. -0.1391 for IPF and non-IPF patients, respectively), indicating that more of the LEMD3-Smad2/3 variance in IPF tissue comes from extreme deviations in interaction frequency. In particular, $\approx 22\%$ of tissue regions in IPF patients had uniquely low LEMD3-Smad2/3 interaction rates ($<25\%$ the mean interaction frequency), which was not observed in non-IPF tissue. Previous micro-mechanical investigations of IPF tissue revealed a high degree of spatial heterogeneity to tissue stiffness in IPF lungs. [4] My findings were consistent with the interpretation that spatially heterogeneous regions of fibrosis in the IPF tissue created both

increased variability in the LEMD3-Samd2/3 interaction rate and regions of locally lower LEMD3-Smad2/3 interactions. These data in aggregate suggested that LEMD3 regulation of TGFβ through Smad2/3 is locally diminished in IPF tissue relative to non-IPF tissue and that LEMD3's role was not confined to the nucleus in human tissue.

3.4 Discussion

3.4.1 Relevance of LEMD3 to Pulmonary Fibrosis

The medical management of fibrotic diseases, such as pulmonary fibrosis, has enjoyed recent success with the approval of pirfenidone, an anti-fibrotic agent, and nintedanib, an inhibitor of multiple tyrosine kinase receptors after years of failed clinical trials with a variety of other agents including anti-inflammatory and anti-oxidant drugs. [199, 10, 200, 9] Subsequent study of the mechanisms of pirfenidone has shown that pirfenidone antagonizes fibrotic progression in part by inhibiting the synthesis of TGFβ [126, 127], which is preferentially activated in fibrotic matrices. [13, 150] While pirfenidone may successfully decrease the supply of TGFβ available in fibrotic pathology, my findings and others' findings indicate that the fibrotic matrix also potentiates cellular responses (*e.g.* synthesis of extracellular matrix and increased cellular contractility) to remaining TGFβ. [88, 89, 90, 91] I focused on the role of LEMD3 in this matrix-driven sensitization and a graphical summary of our working model for LEMD3-Smad2/3 stiffness-driven interactions is shown in Figure 3.16. We showed *in vitro* that LEMD3 over-expression antagonized TGFβ-driven transcription and "stiff-shifts the responsiveness of these fibroblasts to TGFβ while LEMD3 knockdown by siRNA "soft-shifts" the mechanical response to TGFβ and potentiates TGFβ signaling. I also showed *in vitro* that LEMD3-Smad2/3 interactions are inhibited and cytoplasmically shifted with increasing substrate stiffness and actin polymerization. *Ex vivo*, I identified these same phenotypic correlates in IPF biopsies relative to non-IPF tissue: IPF tissue had a pronounced cytoplasmic shift in PLA subcellular localization; and, $\approx$ 22% of IPF tissue regions had a unique reduction in LEMD3-Smad2/3 interactions relative

to non-IPF tissue and a higher degree of variation in the LEMD3-Smad2/3 interaction rate across various tissue regions, both in individual patients and overall. These low interaction regions in IPF are not likely attributable to changes in overall LEMD3 abundance in pathology. My data, and others, showed that full length LEMD3 was not regulated by ECM stiffness at the mRNA or protein level *in vitro* for endogenous LEMD3 (Figure 3.14) or for recombinant LEMD3 (Figure 3.13). [12, 15] Moreover, IPF patients do not show evidence of altered LEMD3 transcription in either microarray or NGS sequencing of IPF and control patients. [201, 202, 203]

Supporting my discovery of LEMD3-Smad2/3 cytoplasmic interactions, I have discovered here that LEMD3 was post-translationally cleaved at two sites and have implicated serine proteases (possibly cathepsin G) in the generation of C-terminal fragments that lack the necessary LEM domain for nuclear targeting. [204, 156, 157] I have also shown that a C-terminal fragment of LEMD3 bound Smad2/3 throughout the cell. However, the underlying mechanism for a cytoplasmic shift in LEMD3-Smad2/3 interactions with increasing substrate stiffness *in vitro* and in IPF patient *ex vivo* is not clear. *In vivo*, there is strong evidence for an altered and generally more active serine [205], cysteine [206, 207], and matrix metallo-proteinases [208, 209, 210, 211, 212] landscape in IPF tissue, though much of the attention has focused on extra-cellular proteolysis. This more pronounced proteolytic environment could contribute to the cytoplasmic shift seen in IPF patients in our study. *In vitro*, I found that stiffness representative of scarred tissue in IPF (25 kPa) and physiologic lung tissue (1 kPa) produced statistically similar abundances of all the LEMD3 fragments I identified (Figure 3.13). However, the 46 kDa fragment was nearly twice as abundant on 25 kPa matrices, prompting a need for further investigation. Overall, I have demonstrated that LEMD3 sits at an promising intersection of mechanical and biochemical cues in pulmonary fibrosis and LEMD3 expression may be a promising adjunctive avenue for addressing fibrosis-driven cellular sensitivity to TGFβ in combination with pirfenidone.

3.4.2 Mechanism of Stiffness Regulation of LEMD3

My original hypothesis for the stiffness regulation of LEMD3-Smad2/3 complexes was that LEMD3s affinity for Smad2/3 would be negatively regulated by biophysical stress from the actin network transmitted to LEMD3 through the LINC-lamina-LEM set of complexes. However, this hypothesis requires critical re-evaluation in light of our discovery of cytosolic LEMD3 fragments that bind Smad2/3 and the apparent lack of efficacy of cytosol-nuclear and lamin-LEM disrupting constructs (DN-Kash and DN-LEM) in increasing LEMD3-Smad2/3 complex formation in the nucleus. I have also observed that LEMD3-Smad2/3 complexes are negatively correlated to actin polymerization. However, it is not obvious how actin polymerization itself would directly modulate LEMD3-Smad2/3 complex formation given that neither LEMD3 nor Smad2/3 have a known direct association with actin. One parsimonious explanation would be that LEMD3 competes for Smad2/3 binding with other actin-regulated proteins, namely, yes-associated protein (YAP)/transcriptional coactivator with PDZ-binding motif (TAZ). I have shown directly that LEMD3's binding of Smad2/3 is negatively regulated by knockdown of either YAP or TAZ. Interestingly, YAP/TAZ and LEMD3 appear to bind different domains of Smad2/3. TAZ has been shown to bind to the MH1 domain of Smad2 [152], while yeast two-hybrid assays indicate that LEMD3 binds to the MH2 domain of both Smad2 and Smad3 [161]. While it is unclear how YAP/TAZ regulate LEMD3 binding to Smad, YAP/TAZ have been shown to negatively regulate the Smad binding of forkhead box protein H1 (FOXH1), which competes for binding to Smad2/3's MH2 domain with LEMD3 in embryonic stem cell CHIP assays [213, 166], indicating that YAP/TAZ can regulate MH2 domain binding proteins.

While these data strongly indicate a role for YAP/TAZ in modulating LEMD3's ability to bind Smad2/3 in an actin polymerization-dependent fashion, other actin-associated proteins should also be considered. Rho-associated protein kinase (ROCK) has also been shown to bind Smad2/3. [151] In particular, ROCK inhibition has been shown to modulate phosphorylation in Smad3s linker region (Ser203, Ser207, Ser212) [151] and could

be an important alternative hypothesis for the stiffness-dependence of LEMD3-Smad2/3 interactions.

3.4.3 LEMD3 in Buschke-Ollendorff Syndrome

LEMD3 is directly implicated in the development of Buschke-Ollendorff syndrome (BOS) with and without melorheostosis. My findings that LEMD3 was post-translationally processed proteolytically and has cytosolic forms raises new questions regarding the pathogenesis of BOS. Many of the identified BOS patients possess nonsense or splice-site mutations which eliminate the Smad-binding C-terminal end of LEMD3. [170, 173, 174, 175, 176, 177, 178, 179, 180] Promisingly, there are a five mis-sense mutations of unknown clinical significance associated with BOS in NCBIs ClinVar database, which are associated with one of the two deletion mutants (p.Δ294-325 and p.Δ579-647) identified in this study.[1] [214] These mis-sense mutations suggest that alterations to the fragment controlling regions of LEMD3 might play a role in the development of BOS. Additionally, our finding that LEMD3 was processed by a serine protease and the 26S proteosome might suggest additional targets/mechanisms in individuals with BOS who lack mutations in LEMD3. [181]

3.4.4 Insights into Biology of Integral Nuclear Membrane Proteins

Finally, I have characterized several N- and C-terminal LEMD3 fragments and demonstrated their varying sensitivities to: 1) genetic perturbation through deletion mutants; 2) serine (DCI), cathepsin G and 26S proteosome (MG-132) inhibitors; 3) lamin integrity/disassembly through cdk1 inhibition; and 4) substrate stiffness. One particular pair of fragments, the 60 kDa N-terminal FLAG and 46 kDa C-terminal V5 fragments, are particularly interesting because they are both sensitive to the same mutation region (p.Δ294-325), both fragments' abundance is reduced with respect to DCI and MG-132 treatment, and they plausibly sum

[1] SCV000332734.2, SCV000341129.2, SCV000380866.2, SCV000380877.2, SCV000380879.2, SCV000380878.2

to the mass of full length LEMD3. However, these two fragments are differentially regulated by integrity of the lamin network (following inhibition of cdk1 by roscovitine) and by cathepsin G inhibition, making it less likely that these fragments are generated in a concerted proteolytic reaction. Additionally, I do not have a straight-forward explanation for the position of our deletion mutations and the fragments' sizes they seemingly control. It is not possible to directly align our western blot fragment data and mass spec data because of the unknown distributions of post-translational modifications in LEMD3; however, the fragments' relative masses controlled by either deletion mutant do not logically correspond with expected size of products from cleavage in those areas.

This is, to my knowledge, the first report of an integral, inner nuclear membrane protein processed proteolytically into cytosolic forms. However, my observations fit a broader pattern of a more locationally dispersed role for nuclear envelope integral proteins. Several integral members of the nuclear membrane have alternative splice forms that both include and omit their trans-membrane domain(s), including nesprin, lamina-associated polypeptide 2, (LAP2), torsin-1a-interacting protein 1 (LAP1), and nurim. [215, 216, 217, 218] Moreover, some localized elements of the nuclear envelope have been found dispersed throughout the cytosol based on the cellular context. For example, nesprins, structural elements of the outer nuclear membrane that link the cytoskeleton and nucleus are restricted to the nuclear envelop in myoblasts but are not in differentiated myotubes [219, 220], and certain nesprin isoforms are also de-compartmentalized during muscle regeneration in Duchenne muscular dystrophy. [220] In addition, alternatively spliced, KASH-less nesprins, which lack the nuclear envelope anchoring domain, KASH, have recently been linked to a variety of cytosolic locations, including focal adhesions and actin stress fibers [215], Golgi bodies, [221] and RNA-processing bodies. [222, 223] My findings expand on the observed mechanisms that regulate the localization of nuclear envelope proteins in the cell.

3.5 Future Directions

3.5.1 LEMD3 as a Novel IPF Theraputic

The ability of LEMD3 over-expression to "stiff-shift" the stiffness potentiation of fibroblasts to TGFβ signaling indicates that it is a viable avenue for addressing an unmet clinical need in fibrosis. While pirfenidone has been shown to reduce the matrix stores of TGFβ [127, 126], it has not been shown to reduce cellular sensitivity to any remaining TGFβ. Clinically, pirfenidone has been shown to reduce the rate of loss of functional lung capacity but only has a modest mortality benefit ($\approx$ months of life extension). [10, 8] The ability to address stiffness-dependent TGFβ sensitization through LEMD3 over-expression may be an important synergistic treatment.

The work in this thesis indicates some important design considerations for the therapeutic expression of LEMD3 in the lung. First, LEMD3 is a relatively large, double-pass molecule with a theoretical molecular weight of 100 kDa. My work with a consensus LEMD3 C-terminal fragment ("CTF") indicates that smaller fragments ($\approx$ 33 kDa) of LEMD3 are just as effective as full length LEMD3 in dephosphorylating Smad3. Moreover, this CTF also recapitulates the same stiffness-dependent binding phenotype as full-length LEMD3 and, interestingly, this CTF may retain some degree of nuclear targeting through its MSC domain. These findings indicate that the majority of LEMD3's primary sequence is dispensable for its function as a TGFβ inhibitor, but how much more of the CTF could be trimmed and still retain this essential function is an open question. The annotated Smad-binding domain of LEMD3 is comprised of the last 213 amino acids on the C-terminal end and LEMD3's binding of Smad1 can be completely abrogated by point mutations at L703-I704 and Y835-V836. [171] Unfortunately, no similar, point-mutant mapping exists for Smad2/3 binding to LEMD3. Finding this "minimal LEMD3" may be important in optimizing the ability to deliver it to the lung and in preventing the engagement of other biological processes (*e.g.* chromatin binding, cell cycle regulation, nuclear lamina structure),

which LEMD3 has been shown to perform.

3.5.2 LEMD3 as a Biochemical Clutch Between YAP/TAZ and TGFβ

Understanding the regulation of LEMD3-Smad2/3 interaction by YAP/TAZ is of translational and scientific importance. YAP/TAZ have previously been shown to be necessary for Smad2/3 translocation to the nucleus and contribute to the progression of fibrosis in multiple organ systems. [152, 15] My work adds an important and contrasting view of YAP/TAZ's role in Smad/fibrosis biology - namely, that YAP/TAZ help coordinate an inhibitor of Smad2/3.

Resolving this apparent discrepancy might reveal additional therapeutic potential to LEMD3-based approaches to fibrosis. My current hypothesis is that only phosphorylated, inactive YAP/TAZ help to promote LEMD3-Smad2/3 interactions through direct binding to Smad's MH1 domain. If correct, it would be extremely intriguing to see if LEMD3 over-expression has a reciprocal effect on YAP/TAZ-Smad2/3 interactions (*i.e.* does LEMD3 over-expression stabilize the cytosolic interactions between YAP/TAZ and Smad2/3?). By understanding this mechanism more fully, we may learn that LEMD3 is not only antagonizing TGFβ-dependent signaling but also matrix-derived stiffness signaling, which has been shown to be important to fibrosis. [15]

Important question to answer about this mechanism would be:

- How does YAP/TAZ knockdown change the stiffness profile of LEMD3-Smad2/3 interactions? Is the actin polyermiztion phenotype for LEMD3-Smad2/3 interactions observed here dependent on YAP/TAZ expression? Is this a global or stiffness-responsive inhibition? This question could be addressed by repeating PLA experiments from this paper in YAP/TAZ knockdown (siRNA) and over-expression *in vitro* systems.

- Is YAP/TAZ binding to the MH1 domain important for modulating LEMD3-Smad2/3 interactions or do PTMs in the MH1 domain confer this effect independent of YAP or

TAZ actually being bound to Smad2/3? Experimentally, generating Smad2/3 recombinant mutants (deletion of Smad2/3's MH1 domain versus point mutation of known PTMs sites in Smad 2/3) for PLA-based assayes could answer whether these binding events or PTMs modulate the ability of LEMD3 to associate with Smad2/3.

- Does YAP/TAZ's phosphorylation state influence the potentiation of LEMD3-Smad2/3 binding? Generation of YAP/TAZ point mutants that cannot be phosphorylated and/or inhibition of LATS1/2 could help address this particular question.

- Does LEMD3 expression modulate the interaction frequency of YAP/TAZ and Smad2/3? If so, does LEMD3 expression modulate the translocation of YAP/TAZ to the nucleus as a function of substrate stiffness and does that change the abundance of YAP/TAZ associated transcripts? These questions could also be answered using a combination of RT-qPCR, immunofluorescence, fractionated cell western blotting and PLA.

- Is the YAP/TAZ regulation of LEMD3-Smad2/3 binding recapitulated *in vitro*? Fortunately, conditional YAP, TAZ, and YAP/TAZ floxed mice all exist and tissue PLA approaches used in this paper could be adapted to answer this question directly. [224, 225, 226]

3.5.3 LEMD3 as a Novel mRNA Binding Protein

The discovery of a cytosolic role for LEMD3 and its previously annotated RNA-recognition motif raise the intriguing possibility that LEMD3 or LEMD3 fragments are novel RNA regulatory proteins, much like recently identified nesprin splice variants. [222, 223] Currently there is no clear understanding of transcriptional changes that accompany LEMD3 expression modulation. Understanding what, if any, mRNA species are affected by LEMD3 knockdown or over-expression would be a a critical first step in identifying potential targets for post-transcriptional regulation. Given that LEMD3 does antagonize TGFβ and BMP signaling, it would be important to determine if any unique mRNAs outside those signal-

ing families are modulated by LEMD3 expression. Alternatively, the use of CLIP-based assays could be employed to directly explore the role of LEMD3 in mRNA binding. If LEMD3 is found to be an RNA binding protein, then the connection between some of the novel LEMD3 biology identified in this thesis (*e.g.* LEMD3 fragmentation and proteolysis) would be intriguing avenues to explore and connect.

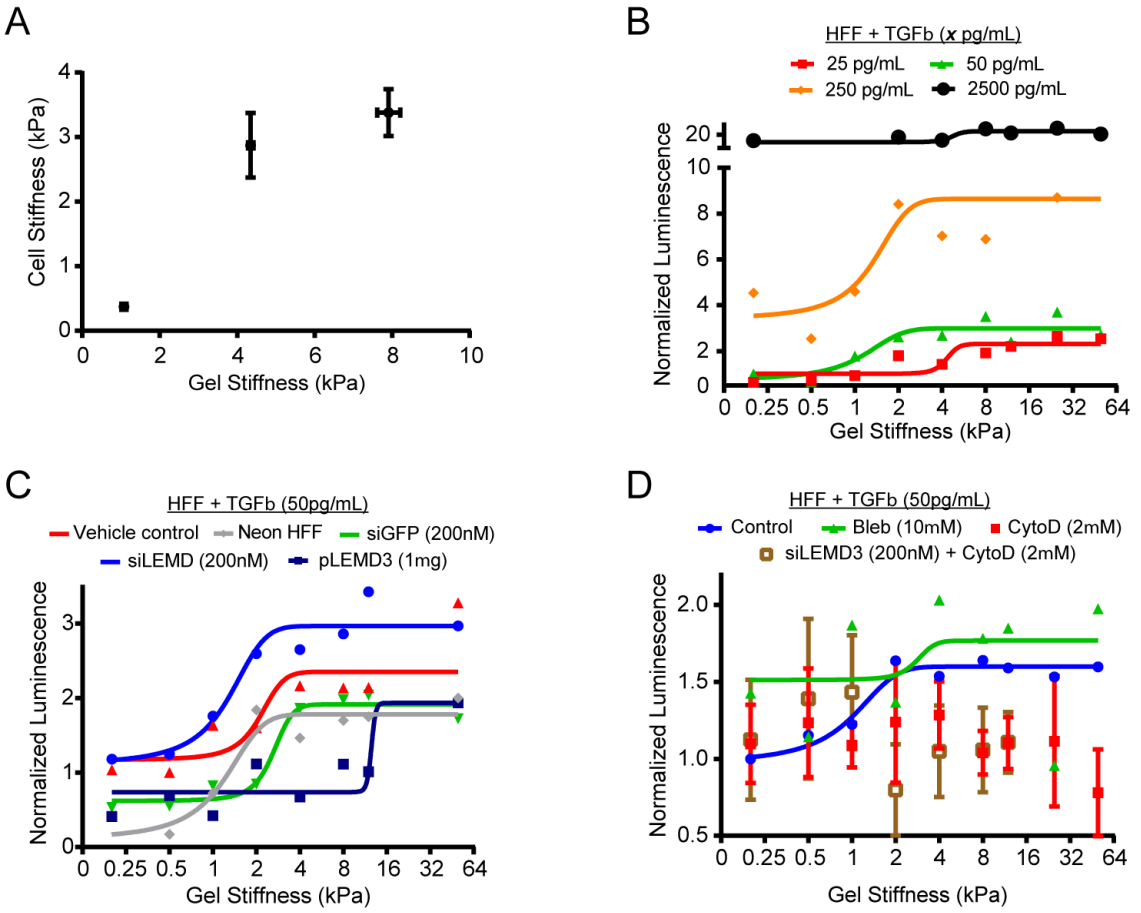

Figure 3.1: **LEMD3 modifies the stiffness response of fibroblasts to activated TGFβ.** A, fibroblasts demonstrate mechano-sensitivity to ECM stiffness through cytoskeletal compliance matching as measured by AFM on increasingly stiff matrices (p=0.001). B, fibroblasts stably transfected with Smad-responsive luciferase demonstrate a dose-dependent, stiffness modulation of their TGFβ responsiveness. Increasing doses of TGF β are associated with a softer sigmoidal inflection point (p=0.07) and cells demonstrate a dose-response to TGFβ on stiff surfaces (p<0.0001). C, LEMD3 expression is correlated with a stiffer transition point in TGFβ-stiffness responsiveness (p<0.0001) and with decreased luminescence (p=0.04). D, cytoskeletal depolymerization, but not myosin II inhibition, is associated with a decreased and flattened luminescent response of fibroblasts to TGFβ. LEMD3 KD does not rescue actin-depolymerization phenotype. Treatments with cytochalasin D did not converge to a sigmoidal model and the data are represented by the mean with standard error of the mean to convey the heterogenity of the results. All cell stiffness/morphology phenotypes and stiffness model parameters were statistically analyzed using an ANOVA - Test for Trends analysis.

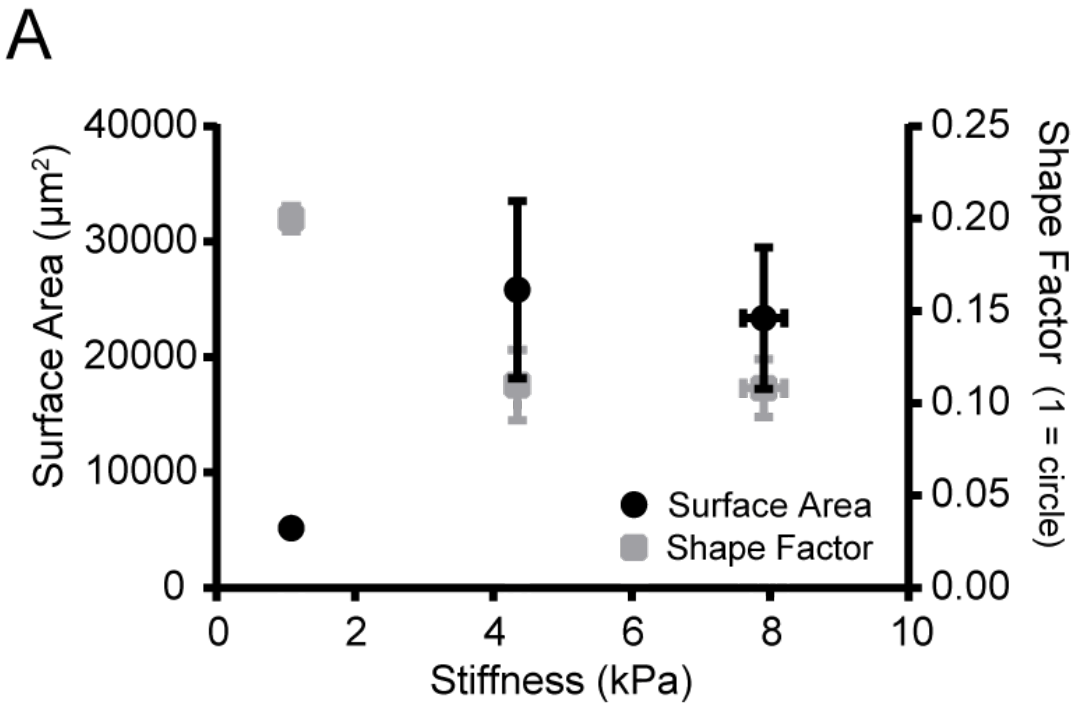

Figure 3.2: **Fibroblasts spread and polarize in response to substrate stiffness** A, fibroblasts demonstrate mechano-sensitivity to ECM stiffness as demonstrated by increased cell spreading (p=0.1801, ANOVA - Test for Trends) and polarization (p=0.0263, ANOVA - Test for Trends).

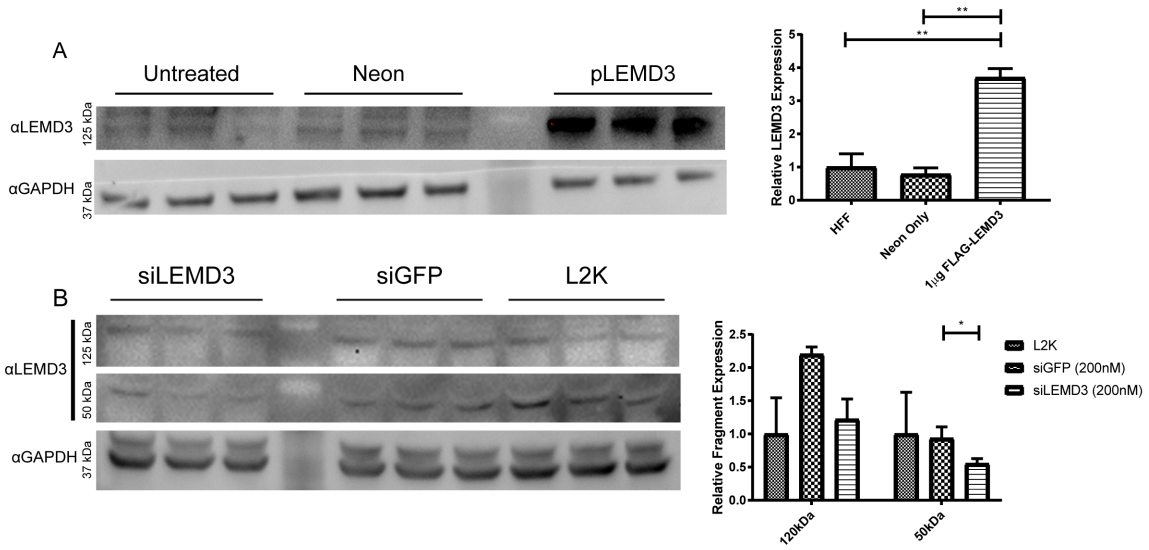

Figure 3.3: **Over-expression and knockdown of LEMD3 using pFLAG-LEMD3-V5 and siRNA.** A and B, representative western blots and quantification from plasmid over-expression (A) and siRNA knockdown experiments (B). pFLAG-LEMD3-V5 electroporation significantly increases full length LEMD3 (p=0.0018 for HFF vs. 1 μg pFLAG-LEMD3-V5, p=0.0012 for Neon Only vs. 1 μg pFLAG-LEMD3-V5, ANOVA with Tukey post-test). siLEMD3 delivered by Lipofectamine 2000 (L2K) significantly decreases LEMD3 expression relative to siGFP control (p=0.0248, Student's T-test).

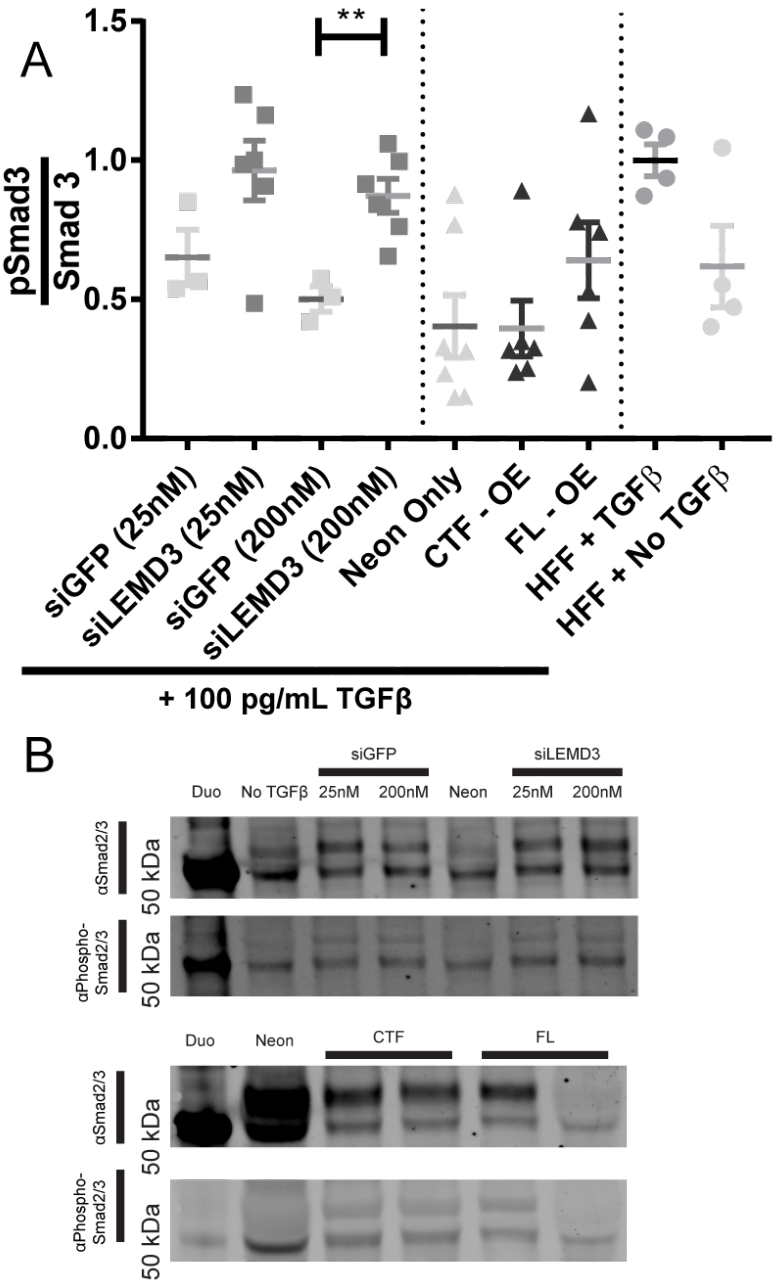

Figure 3.4: **LEMD3 negatively regulates Smad3 phosphorylation.** A, Phospho-Smad3 to Smad3 ratios were measured by western blot in HFFs on tissue culture plastic. HFFs treated with 100 pg/mL TGFβ for 90 minutes had an increased pSmad3/Smad3 ratio relative to untreated fibroblasts (p=0.0506). HFFs treated with 100 pg/mL TGFβ and 25nM or 200nM siRNA against LEMD3 ("siLEMD3") had a higher pSmad3/Smad3 ratio than cells treated with a concentration matched siRNA against GFP ("siGFP"; p=0.1103 and p=0.0057 for 25nM and 200nM, respectively, Student's T-test). TGFβ dosed HFFs electroporated with pFLAG-LEMD3-V5 ("FL-OE") or pFLAG-LEMD3p.Δ21-669-V5 ("CTF-OE") had diminished pSmad3/Smad3 ratios relative to TGFβ treated HFFs (p=0.0124 and p=0.2116 for CTF-OE and FL-OE, respectively) but were not statistically different from the electroporation-only ("Neon Only") control. B, representative blots for Smad2/3 and phospho-Smad2/3. Smad3 is the lower band at $\approx$ 50 kDa.

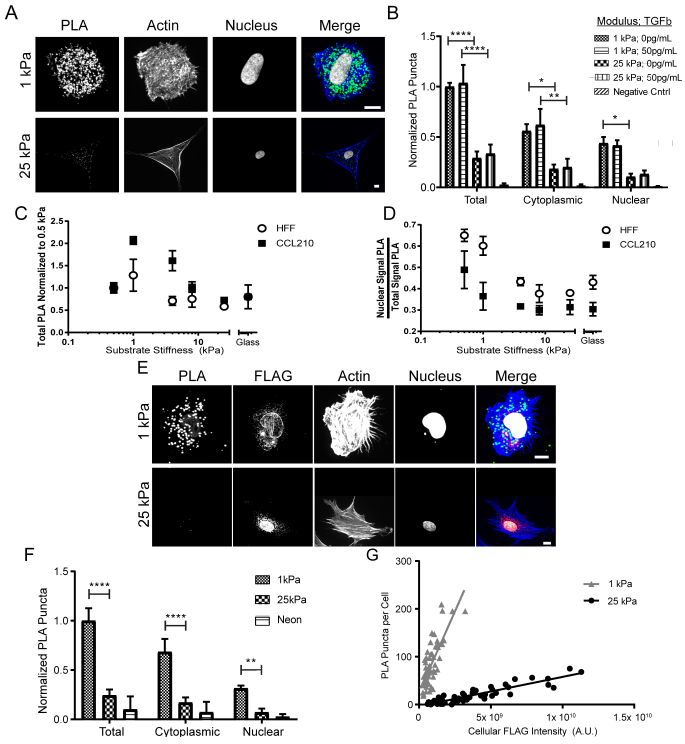

Figure 3.5: **LEMD3-Smad2/3 interactions are inversely correlated to substrate stiffness and occur in the nucleus and cytoplasm.** A, micrographs of LEMD3-Smad2/3 PLA interactions on soft (top row, 1 kPa) and stiff (bottom row, 25 kPa) matrices (PLA in green, f-actin in blue, nucleus in white). B, quantification of PLA interactions grouped by substrate stiffness and by TGFβ dose. Total LEMD3-Smad2/3 interactions are negatively correlated to substrate stiffness ($p<0.0001$ for 1 kPa vs 25 kPa for both 0 pg/mL and 50 pg/mL TGFβ) but are not correlated to TGFβ dose. Cytoplasmic ($p=0.0164$ for 0 pg/mL TGFβ, $p=0.0087$ for 50 pg/mL TGFβ) and nuclear compartment ($p = 0.0428$ for 0 pg/mL TGFβ, $p=0.1228$ for 50 pg/mL TGFβ) interactions are also negatively correlated to substrate stiffness. C, total HFFs and CCL210s LEMD3-Smad2/3 interactions by PLA normalized to 0.5 kPa on surfaces with stiffness of 0.5, 1, 4, 8, 25 kPa and glass. Each fibroblast population shows a biphasic trend, centered around a peak of LEMD3-Smad2/3 interactions at 1kPa. CCL210 demonstrate greater dynamic range in interaction frequency and a slower loss of interactions on stiffer substrates than HFFs. D, subcellular location of LEMD3-Smad2/3 PLA interactions in HFFs and CCL210s from (C). Each cell line demonstrates a cytoplasmic shift in location with increasing substrate stiffness ($p<0.0001$ and $p=0.0199$ for HFFs and CCL210s, respectively; ANOVA - Test for trend). E, micrographs of V5-Smad2/3 PLA interactions with pFLAG-LEMD3-V5 on soft (top row) and stiff (bottom row) matrices (PLA in green, f-actin in blue, FLAG in red, nucleus in white). F, V5-Smad2/3 PLA interactions are also negatively correlated with substrate stiffness (for 1 kPa vs 25 kPa: Total PLA - $p<0.0001$, Cytoplasmic PLA - $p<0.0001$, Nuclear PLA - $p=0.0018$) and also occur in the cytoplasm. G, V5-Smad2/3 PLA interactions are significantly higher on soft substrates independent of the degree of pFLAG-LEMD3-V5 expression (difference in linear regression slopes - $p<0.0001$). All PLA groups were statistically compared using a 2-way ANOVA with Tukey post-test unless noted. All scale bars are 10 μm.

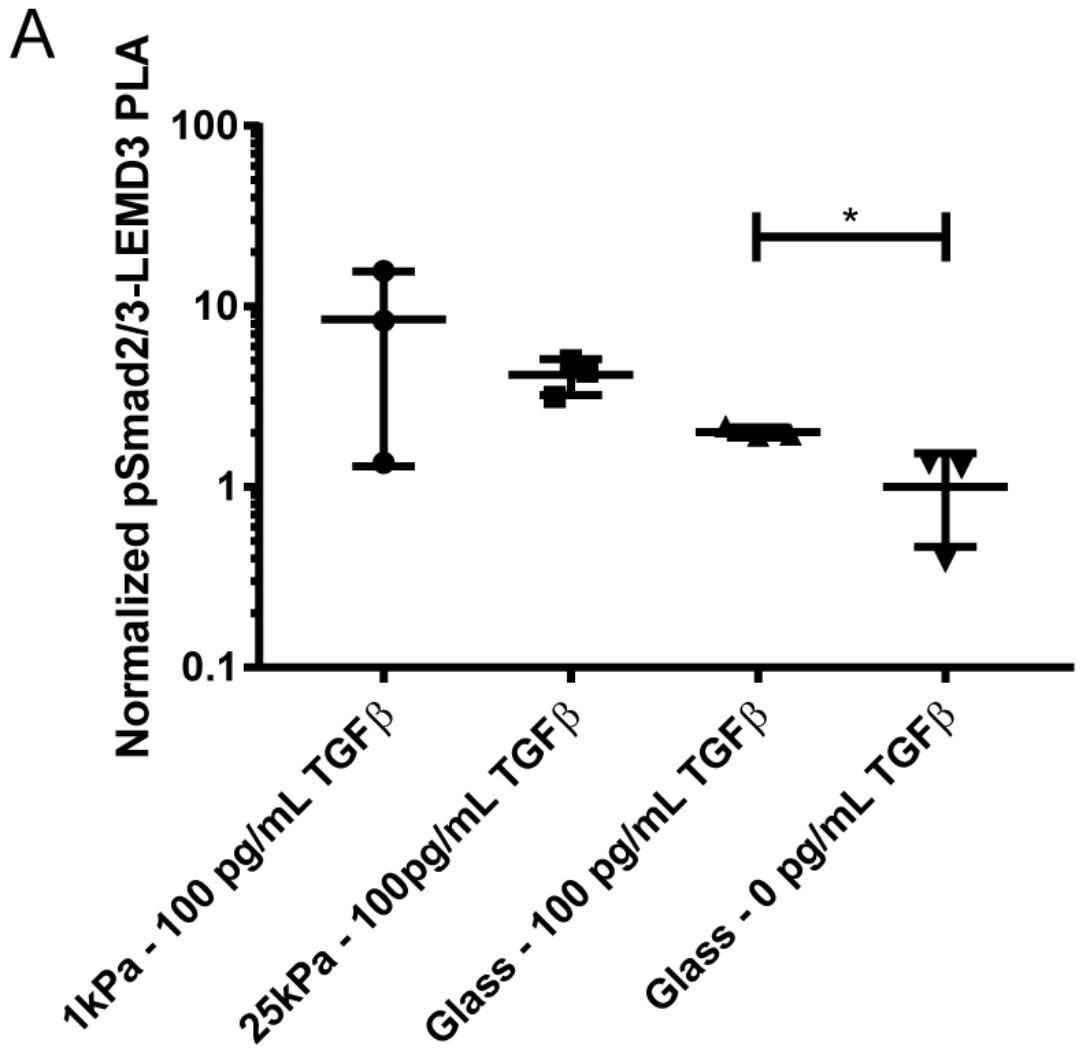

Figure 3.6: **LEMD3 binds phospho-Smad2/3 in a stiffness-dependent fashion.** PLA interactions between phospho-Smad2/3 and LEMD3, normalized to HFFs on glass without TGFβ treatment, are stiffness- and TGFβ dose-dependent. Fibroblasts on glass treated with 100 pg/mL TGFβ have significantly more LEMD3-phospho-Smad2/3 interactions than cells without TGFβ treatment. (p=0.0333, Student's T-test). There is also a significant decrease in interactions with increasing stiffness (p=0.0305, ANOVA-Test for trends).

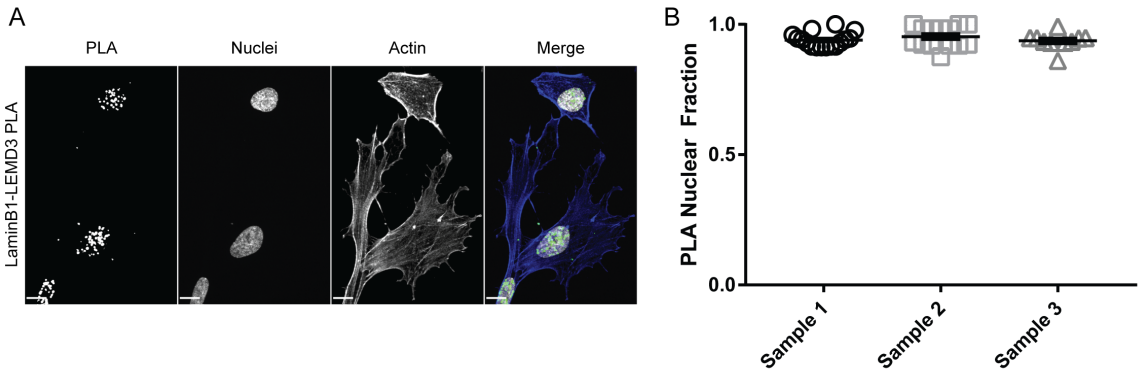

Figure 3.7: **Lamin B1-LEMD3 PLA interactions are compartmentalized to the nucleus.** To assess whether PLA and our analysis methods could localize interactions to particular subcellular compartments, we performed PLA between lamin B1, an integral element of the nuclear lamina, and LEMD3 on glass. A, micrographs of PLA interactions between lamin B1 and LEMD3. B, quantification of the subcellular (nuclear) localization of these interactions per cell. Across all biological replicates, $94.34 \pm 0.005\%$ of all lamin B1-LEMD3 interactions were compartmentalized to the nucleus. There were no significant deviations in nuclear PLA frequency across groups (all inter-group comparisons $p \geq 0.48$, ANOVA).

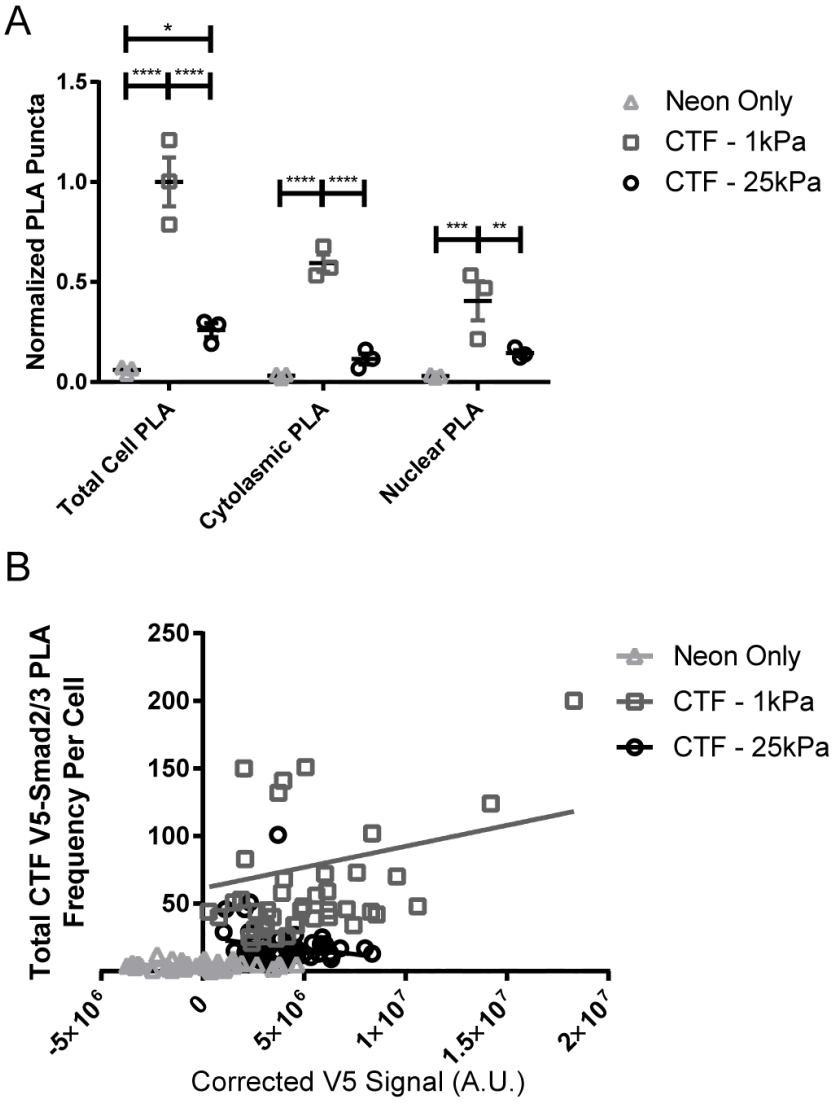

Figure 3.8: **The C-terminal end of LEMD3 is sufficient for binding Smad2/3 in a stiffness-dependent fashion.** A, PLA interactions between the V5 tag of a C-terminal fragment ("CTF") of LEMD3 (pFLAG-LEMD3p.Δ21-669-V5) and Smad2/3, normalized to the total interactions observed on 1 kPa hydrogels. HFFs on 1 kPa hydrogels have significantly more interactions overall ($p<0.0001$), in the cytosol ($p<0.0001$), and in the nucleus ($p=0.0082$) relative to fibroblasts on 25 kPa hydrogels. All transfected cells had more PLA interactions than electroporation-only ("Neon") populations ($p<0.0001$ and $p<0.0227$ for 1 kPa and 25 kPa hydrogels, respectively). B, the higher V5-Smad2/3 PLA frequencies observed in fibroblasts on 1 kPa hydrogels is independent of the degree of V5 expression. The slopes of individual cells' PLA vs. V5 staining intensity were higher for cells on 1 kPa hydrogels than on 25 kPa hydrogels ($p=0.1476$, difference in slopes). All PLA groups were statistically compared using a 2-way ANOVA with Tukey post-test unless noted.

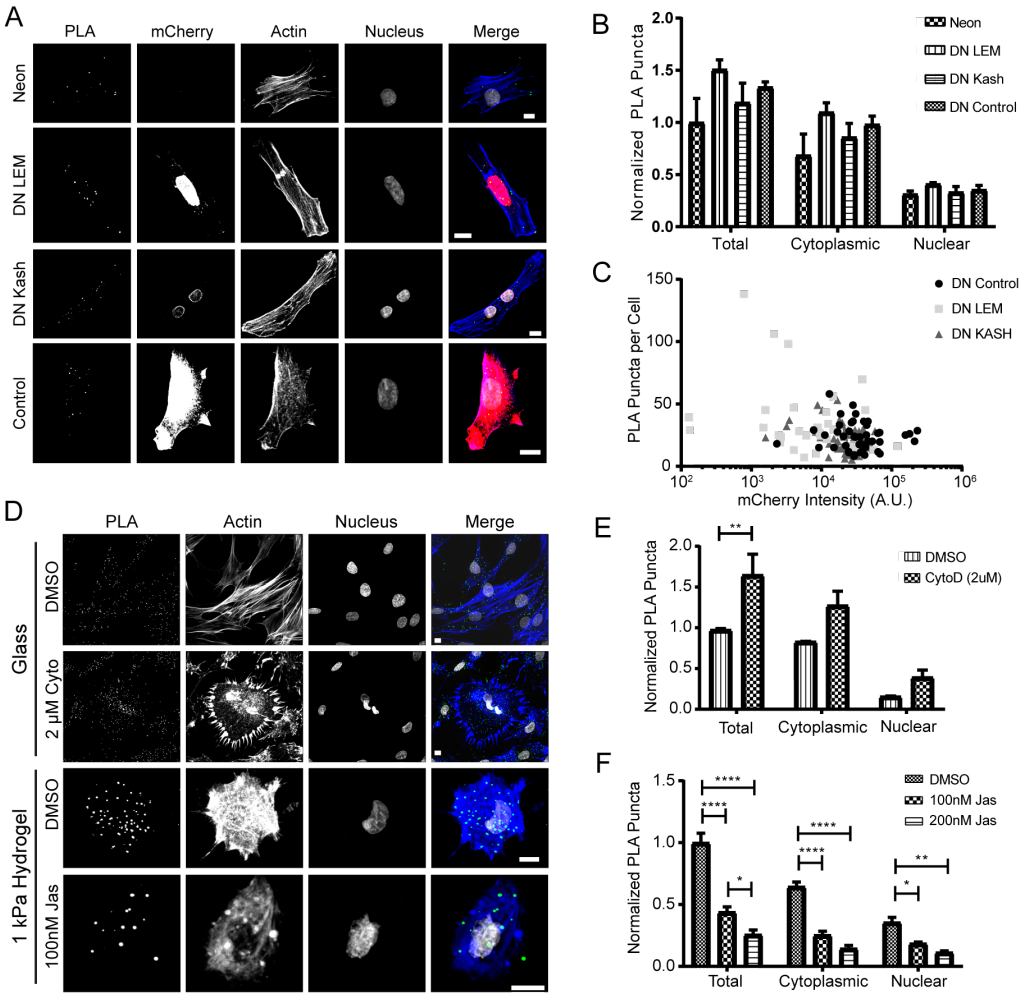

Figure 3.9: **LEMD3-Smad2/3 interactions are negatively associated with actin polymerization but not nucleus-cytoplasm coupling or LEMD3-lamin coupling.** A, micrographs of LEMD3-Smad2/3 PLA in electroporated cells (top row), mCherry-DN LEM expressing cells (2^{nd} row), mCherry-DN Kash expressing cells (3^{rd} row), or mCherry only expressing cells (bottom row), all on glass (PLA in green, f-actin in blue, mCherry in red, nucleus in white). B, no significant differences in PLA frequency are seen in the nucleus or cytoplasm of cells expressing either DN LEM or DN Kash relative to mCherry control cells. C, no correlation between DN LEM or DN Kash expression and PLA frequency in transfected cells. D, micrographs of LEMD3-Smad2/3 PLA in cells treated with cytochalasin D (top rows, g-actin stabilizer) on glass or jasplakinolide (bottom rows, f-actin stabilizer) on 1 kPa gels (PLA in green, f-actin in blue, nucleus in white). E, cytochalasin D treatment significantly increases the total frequency (p=0.0089) of PLA interactions per cell on glass. F, jasplakinolide ("Jas") treatment significantly decreases the total frequency of LEMD3-Smad2/3 interactions in a dose-dependent fashion ($p<0.0001$ for DMSO vs. 100nM Jas or 200nM Jas, p=0.0312 for 100nM Jas vs. 200nM Jas), and decreases the cytoplasmic ($p<0.0001$ for DMSO vs. 100nM Jas or 200nM Jas) and nuclear frequencies (p=0.002 for DMSO vs. 200nM Jas, p=0.0466 for DMSO vs. 100nM Jas) of LEMD3-Smad2/3 interactions on 1 kPa surfaces. All groups were statistically compared using a 2-way ANOVA with Tukey post-test. All scale bars are 10 μm.

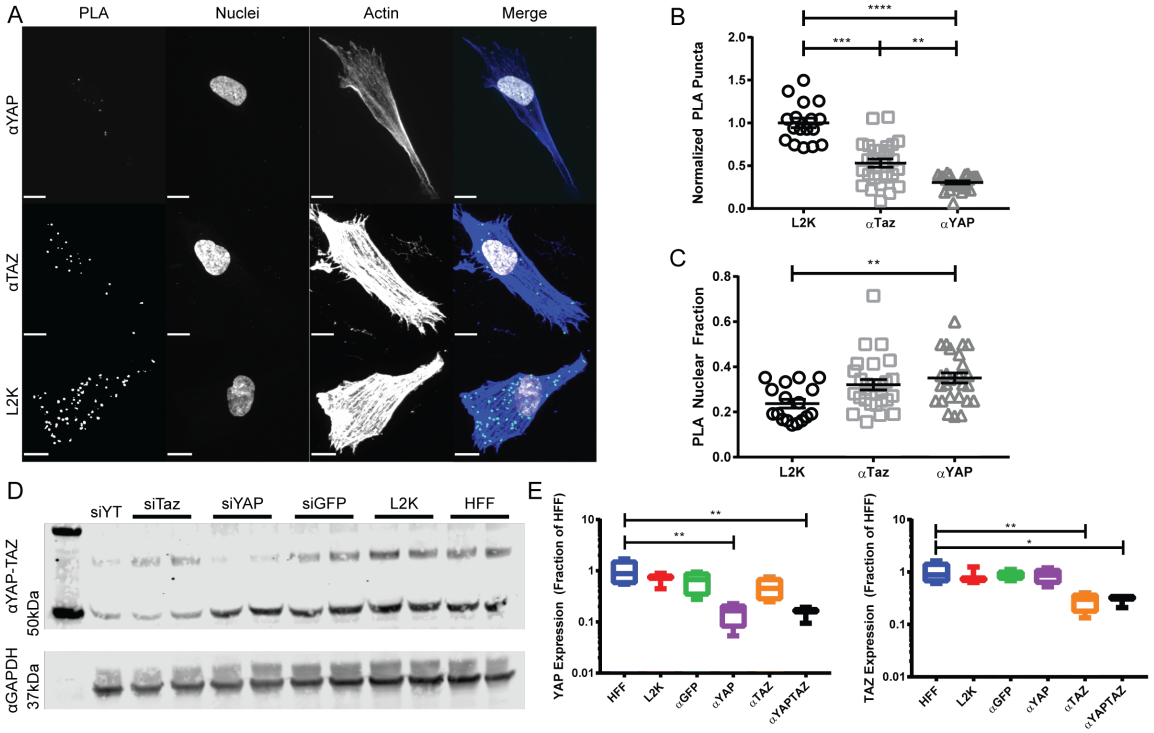

Figure 3.10: **YAP and TAZ KDs by siRNA antagonize LEMD3-Smad2/3 interactions and shift interactions towards the nucleus.** A, representative micrographs of LEMD3-Smad2/3 PLA interactions in HFFs on 1 kPa fibronectin hydrogels treated with 25nM siRNA against YAP ("siYAP", top row), 25nM siRNA against TAZ ("siTAZ", middle row), or L2K vehicle treatment ("L2K", bottom row). B, quantification of PLA puncta per cell, normalized to L2K condition, from at least two biological replicates per group. Significant loss of LEMD3-Smad2/3 interactions are observed with either siTAZ (p=0.0005) or siYAP (p<0.0001) treatment. SiTAZ treated samples also had significantly more LEMD3-Smad2/3 interactions than siYAP samples (p=0.0094). C, loss of YAP (siYAP, p=0.0039) or TAZ (siTAZ, p=0.0716) shifted remaining LEMD3-Smad2/3 interactions towards the nucleus. All comparisons made using Kruskal-Wallis test with Dunn's test for multiple comparisons. D, representative western blots demonstrated YAP and TAZ KD by siRNA using GAPDH as a loading control. E, quantification of YAP (left graph) and TAZ (right graph) KD by siRNA from (D). Treatment with 25nM siYAP or 25nM siYAP and 25nM siTAZ ("siYAPTAZ") significantly reduced YAP levels relative to untreated HFFs (siYAP p=0.0044, siYAPTAZ p=0.008). Similarly, 25nM siTAZ or 25nM siYAPTAZ reduced levels of TAZ (siTAZ p=0.0081, siYAPTAZ p=0.0145). No significant reductions in either protein are observed with vehicle alone (L2K), or siRNA against GFP ("siGFP"). All testing done using ANOVA with Dunnett's multiple comparison correction. All scale bars are 10μm.

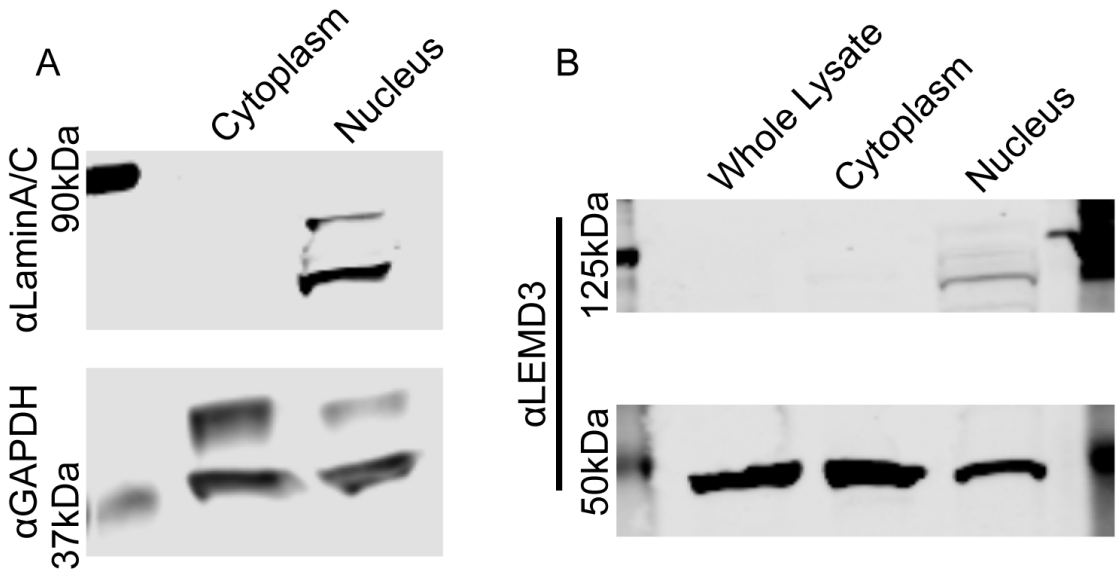

Figure 3.11: **Full length LEMD3 is localized to the nucleus, but a 46kDa fragment is localized to the cytoplasm.** A, representative western blots of cytosolic (GAPDH) and nuclear (LaminA/C) compartment markers from a fractionated lysate are shown. Cytosolic markers are observed in the nucleus but no nuclear markers are observed in the cytosol. B, LEMD3 western blot on whole cell lysate or enriched lysates for the cytoplasmic or nuclear fractions. An $\approx$ 50 kDa native LEMD3 fragment is found in the cytoplasm and possibly the nucleus, while full length LEMD3 is only found in the nucleus.

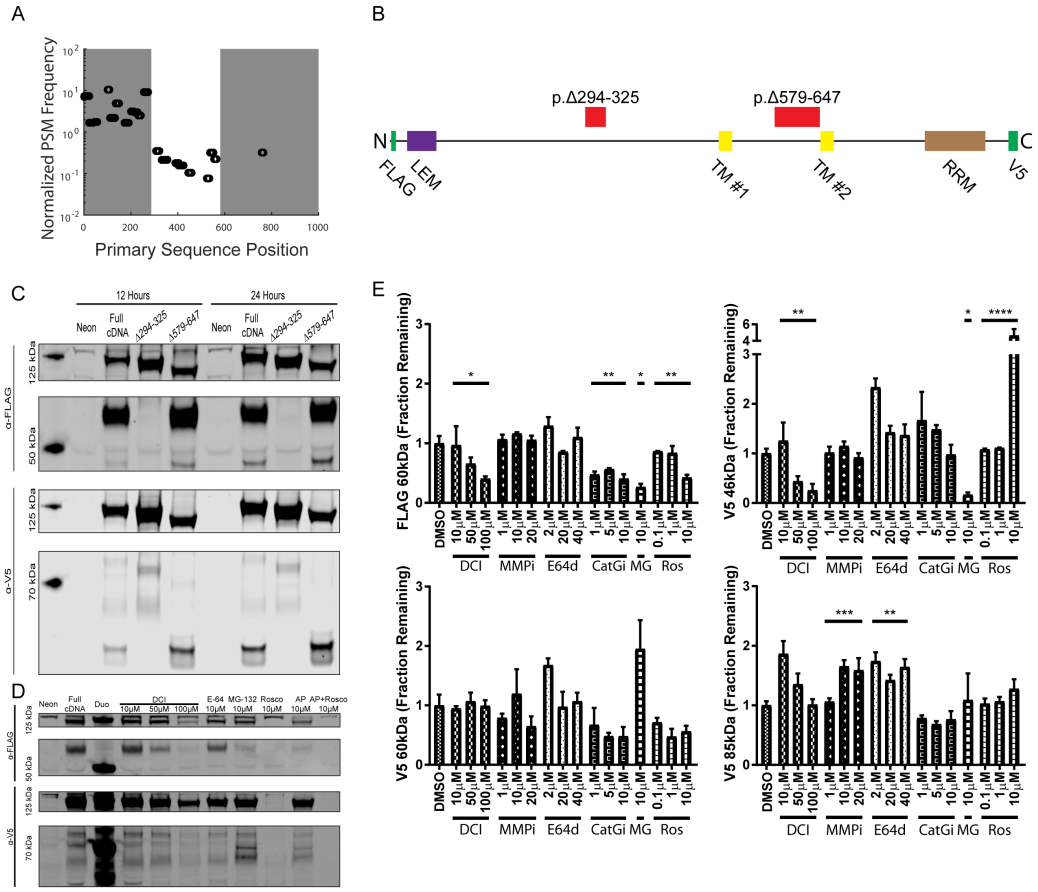

Figure 3.12: **LEMD3 is proteolytically modified by a serine protease.** A, Peptide spectral matches (PSMs) were normalized from a 60kDa FLAG fragment of LEMD3 by PSM frequencies measured in full length LEMD3. Normalized PSM frequency revealed three distinct zones: over-enriched (left shaded region), under-enriched (unshaded region), and absent (right shaded region). B, LEMD3 cartoon showing relative position of the two deletion mutants and known protein domains: LEM, transmemebrane (TMs 1&2), and RRM domains, and FLAG and V5 epitope tags. C, western blots from full length and each deletion mutant using N-terminal FLAG tag (top two blots) and C-terminal V5 tag (bottom two blots) at 12 and 24 hours after electroporation. FLAG blots consistently produce a 60 kDa fragment, while V5 blots produce 85 kDa, 60kDa, and 46 kDa fragments. D, representative western blots for protease and cell cycle inhibitor experiments using N-terminal FLAG tag (top two blots) and C-terminal V5 tag (bottom two blots). E, quantification of blots from (D), showing that 60 kDa FLAG fragment is significantly reduced relative to the full-length protein when cells are treated with DCI ($p=0.0153$), MG-132 ($p=0.0238$), Cathepsin-G inhibitor ($p=0.0075$), or roscovitine ($p=0.0051$). V5-tagged 46 kDa fragment are similar in that DCI ($p<0.0001$) and MG-132 ($p=0.0238$) treatments decrease its abundance, but dissimilar in that roscovitine increases its abundance ($p<0.0001$). V5-tagged 85kDa fragment is increased with MMP inhibitor treatment ($p=0.0004$) and E64D treatment ($p=0.0044$). All treatment groups, except MG-132, were tested statistically using ANOVA - Test for Trends with a correction for multiple hypotheses using a False Discovery Rate (FDR) of $\alpha=0.05$. MG-132 was compared to DMSO treated lysates with a Mann-Whitney test and then also corrected using the FDR approach above.

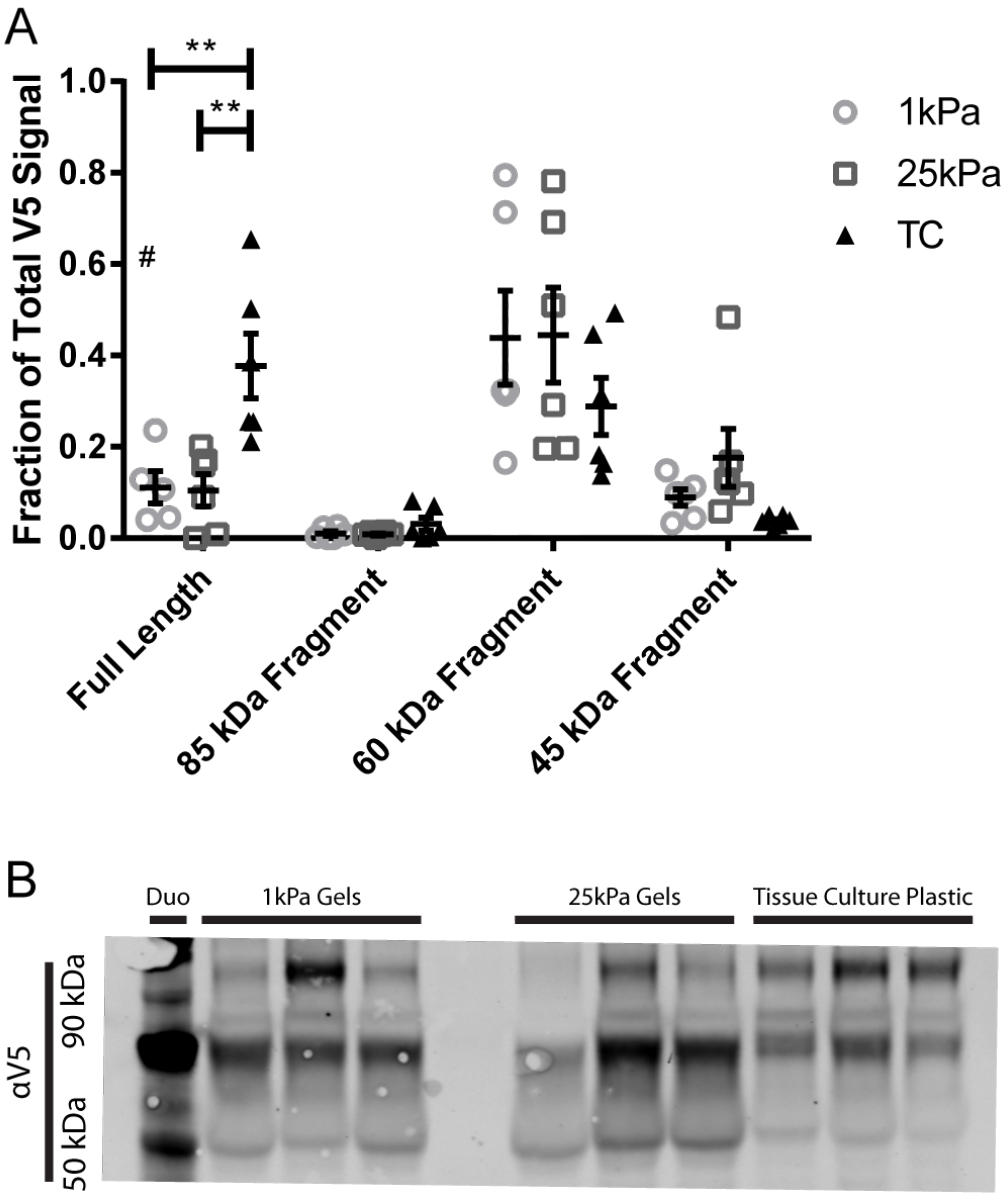

Figure 3.13: **LEMD3 C-terminal fragments are not significantly differentially abundant in HFFs cultured on 1 and 25 kPa hydrogels.** A, Fibroblasts transfected with pFLAG-LEMD3-V5 were assayed by western blot for the relative abundance (fraction of total V5 signal in that lane) of the full length protein or of the 85 kDa, 60 kDa, or 45 kDa fragments after 24 hours on 1 kPa, 25 kPa hydrogels or tissue culture plastic. Fibroblasts cultured on 1 kPa and 25 kPa hydrogels have significantly less full length LEMD3 than cells cultured on tissue culture plastic (p=0.0062 and p=0.0031 for 1 kPa and 25 kPa hydrogels, respectively) but do not vary significantly in the abundance of any identified fragment. Cells on 25 kPa hydrogels have nearly twice as much of the 45 kDa fragment than cells from 1 kPa hydrogels (p=0.5196). B, representative blots of the experimental lysates. All stiffness in a given protein mass group were statistically compared using ANOVA with Tukey post-test. Data point represented by "#" in Full Length, 1 kPa was determined to be an outlier (Grubb's method, α=0.05) and is plotted for completeness but excluded from analysis.

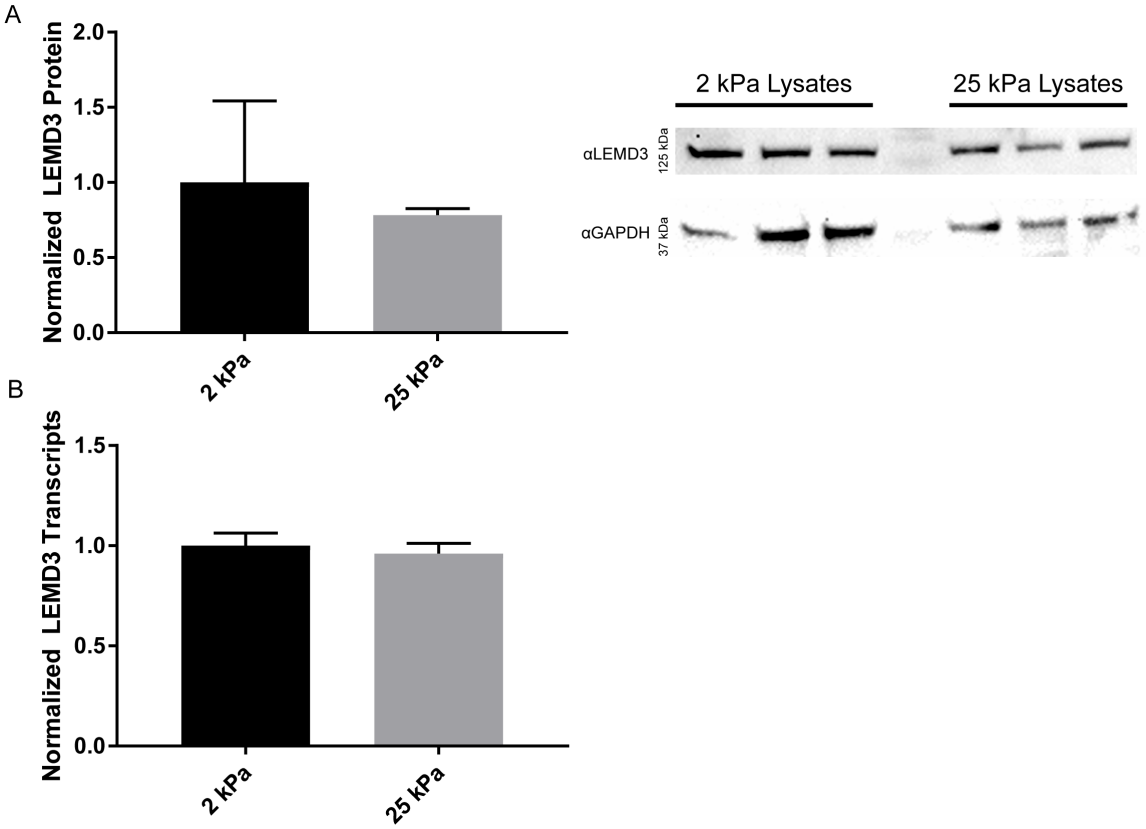

Figure 3.14: **LEMD3 is not directly regulated by substrate stiffness at the mRNA or protein level.** A, representative western blots and quantification of LEMD3 protein from soft (2 kPa) and stiff (25 kPa) hydrogels using GAPDH as a loading control. No significant difference is observed between stiffness conditions. B, LEMD3 mRNA quantification from cells on soft (2 kPa) or stiff (25 kPa) hydrogels using 18S as a house-keeping gene. No significant difference is observed between stiffness conditions.

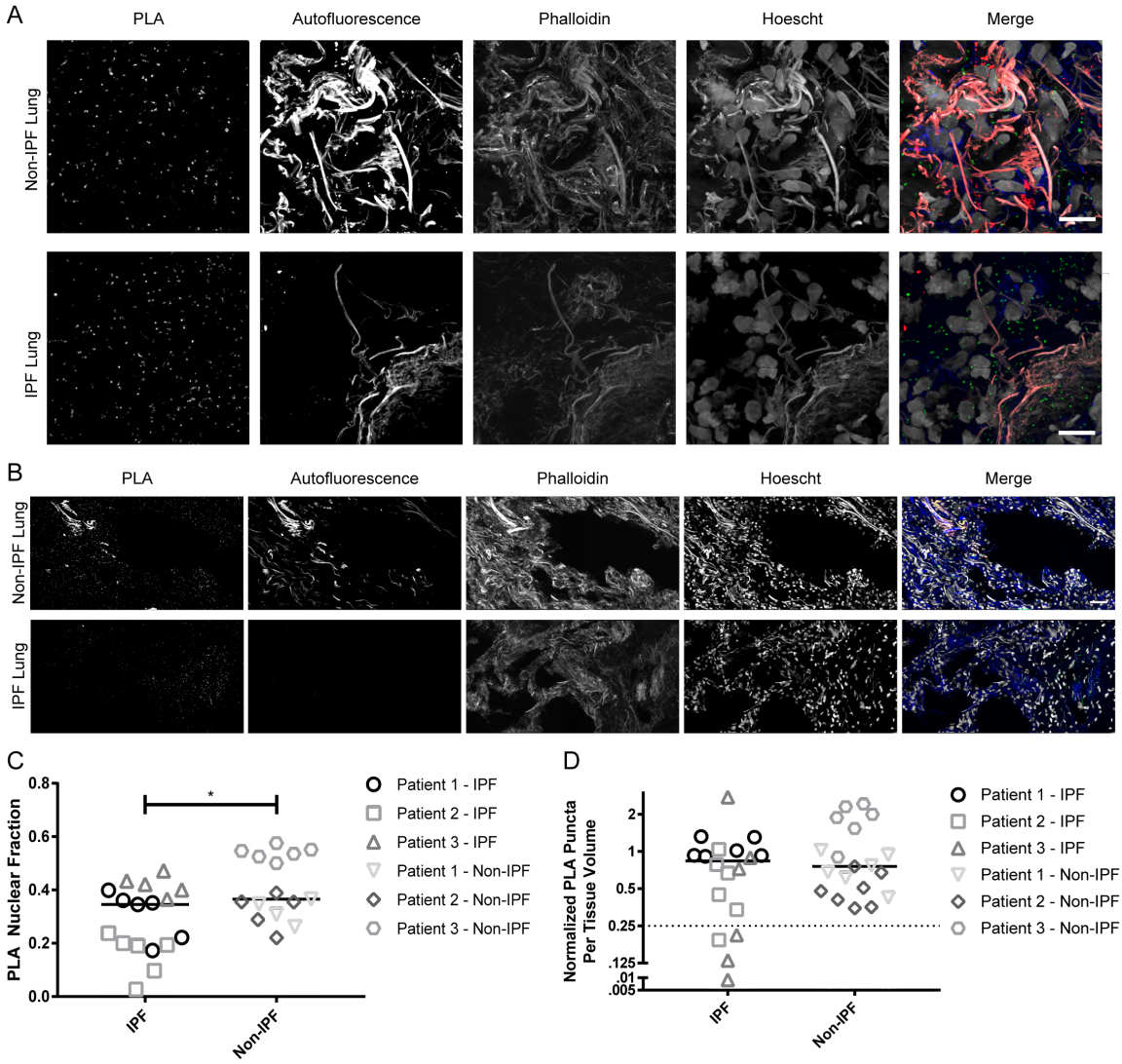

Figure 3.15: **LEMD3-Smad2/3 PLA interactions are more cytoplasmic and more varied in frequency in IPF vs. non-IPF human lung tissue.** A and B, LEMD3-Smad2/3 PLA frequency imaged at high-magnification (63X) (A) and low-magnification (20X) (B) in non-IPF (top row) and IPF (bottom row) tissue (PLA in green, f-actin in blue, autofluorescence in red, nuclei in white). C, quantification of sub-cellular localization of LEMD3-Smad2/3 PLA events from (A) showing cytoplasmic shift in PLA interactions in IPF patients (p=0.0307, Mann-Whitney test), mirroring *in vitro* trends seen in Figure 3.5c. D, quantification of total LEMD3-Smad2/3 PLA frequency from (B) showing similar frequency of interactions between IPF and non-IPF patients (p=0.5783, Mann-Whitney test). IPF tissue had a higher intra-patient variability (Coeff. of Variance = 67% and 30% for IPF and non-IPF patients, respectively) and more extreme dispersion overall (kurtosis = 4.765 and -0.1391 for IPF and non-IPF patients, respectively). 22% of IPF tissue areas sampled formed a unique low-interaction "tail" (<25% of the mean IPF interaction frequency, denoted by dotted line), which is absent in non-IPF tissues. All scale bars are 10 μM. Bars in (C) and (D) represent grand medians.

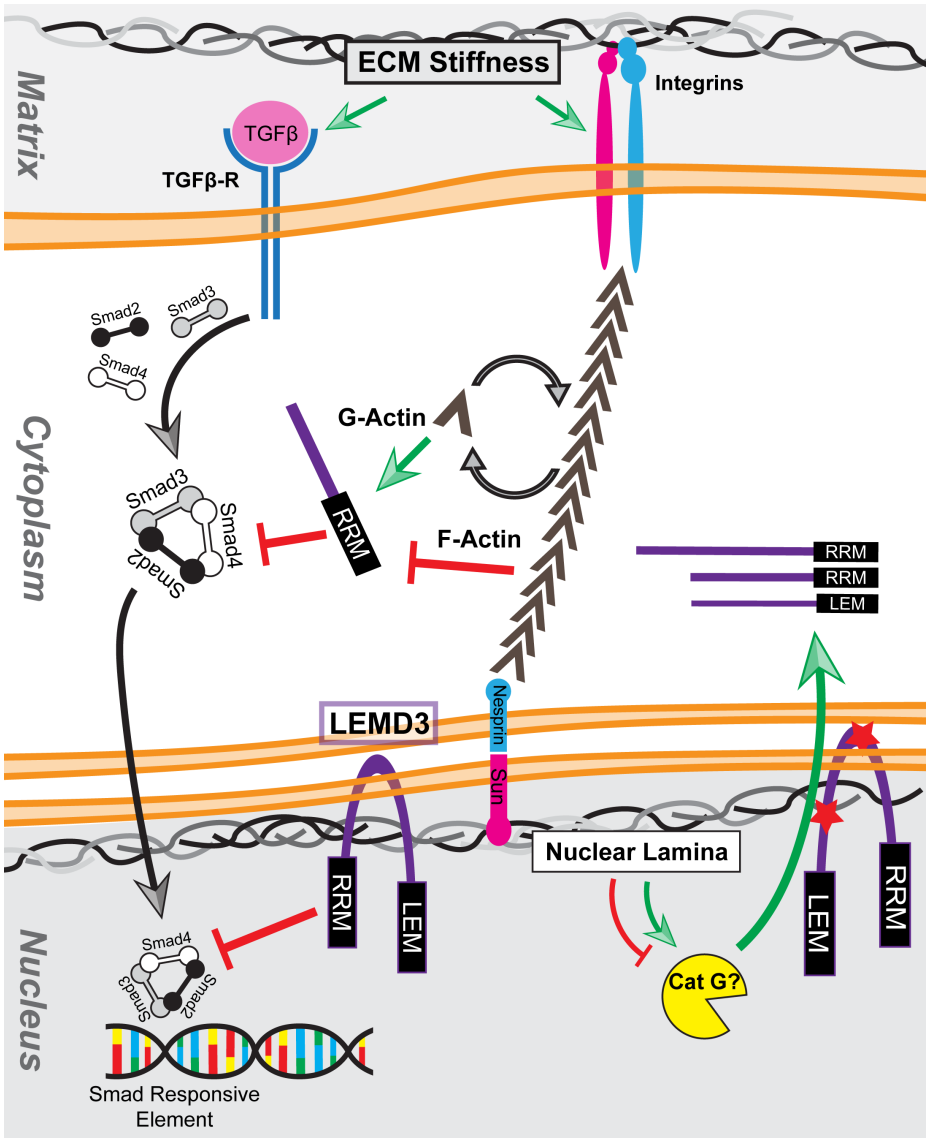

Figure 3.16: **Summary Cartoon** Mechanical cues from the extracellular matrix potentiate TGFβ activation, which forms and translocates Smad2/3/4 complexes to Smad Response Elements in the nucleus. LEMD3 antagonizes this TGFβ/Smad2/3 signaling by complexing with Smad2/3 both in the nucleus and in the cytosol and shifts the mechanical response of cells to TGFβ. Cytosolic LEMD3 fragments are post-translationally generated at two sites, which separate the nuclear localizing LEM domain and the Smad2/3 interacting RRM domain. Processing at the nucleoplasmic site (bottom red star) generates a LEM- and RRM-containing fragment, which is inhibited by serine protease inhibitors, but has differential responses to lamin phosphorylation inhibitors. Both nuclear and cytosolic LEMD3-Smad2/3 complexes are inhibited by actin polymerization, which is driven by mechanical cues from the matrix, thereby connecting ECM mechanics to inhibition of an inhibitor of Smad2/3. Inhibitory interactions are shown with red block-end arrows while activating signals are denoted with green arrows. Black arrows indicate translocation. Abbreviations: Cat G: Cathepsin G; RRM: RNA Recognition Motif; LEM: Lap2b-Emerin-MAN1 domain; TGFβ-R: TGFβ receptor.

CHAPTER 4
TOOLS TO DISSECT THE THERMODYNAMIC LANDSCAPE OF THE MURINE CARGOME

4.1 Introduction

4.1.1 Biophysically Targeting Disease and *in vivo* Stiffness Reporting

Alterations to tissue stiffness prompt a variety of temporal responses from cells. Many of the short-term changes to a cell's phenotypes are post-translationally regulated (*e.g.* increased actin polymerization and contractility [14, 227], alterations to endocytosis and intracellular transport [111], *etc.*). These short-term phenotypes, in turn, help to regulate and are frequently reinforced by genetic programs that feedback into the mechanosensory machinery of the cells and the matrix itself. [228, 12] These genetic programs drive many of the long-term phenotypic changes (*e.g.* matrix metabolism [229, 230], cellular differentiation [14], etc.) that arise from altered matrix stiffness. Provocatively, understanding how mechanical information is filtered through the genome by measuring the stiffness-response of key transcription factor families and charting the energy landscape in which those transcription factor families operate over is important for two reasons: 1) it should allow for the rational design of genetic therapies that selectively harness the cell's intrinsic mechanosensing potential, using stiffness as a stimulating cue for modular therapy; and, 2) it could provide a basis for therapeutic antagonism of gene sets that are specifically activated in fibrosis.

A proof-of-concept study exploring the ability of stiffness-driven transgenes to biophysically target metastatic breast cancer in the lung has recently been published. [231] This work exploited 8x TEAD box driven transgenes, which are YAP/TAZ responsive, to drive the therapeutic expression of a pro-drug converting enzyme from *ex vivo* modified mes-

enchymal stem cells (MSCs). While their *in vivo* data did not show a theraputic benefit of the stiffness-driven transgene relative to constitutively active expression of the converting enzyme in MSCs, their *in vitro* data demonstrated a clear proof-of-concept: genetic expression using their system was driven in a stiffness-dependent fashion with marked increases in transcription above 10kPa and was dependent on the intact focal adhesion and cytoskeletal activities of the cell. This demonstration is highly motivating to the work presented in this chapter because it begs the question as to how mechanically regulated systems could be designed rationally for specific stiffness performance criteria.

Here, I hypothesized that the stiffness-responsivity of mechanically-regulated transgenic promoters is based on the relative position of that promoter within the endogenous energy landscape of the particular response element and the sensitivity of the system to mechanical activation. I focused my efforts on understanding the mechanical activation and the underlying genetic structure of a model, stiffness-regulated transcription factor system and on developing the tools necessary to make a unique measurement of its energy landscape.

4.1.2 Mechanically Sensitive Transcription Factor Systems

While there are a variety of mechano-sensitive transcription factor families, I have focused on the activity of the myocardin related transcription factors ("MRTFs") and serum response factor ("SRF") as a model mechanical system because a detailed understanding of their mechanical regulation is already known and because of the relative simplicity of their transcriptional activities. Following an introduction to the relevant biology of MRTF/SRF, there is an overview of other mechanically sensitive transcription factor families that motivate my choice of MRTF/SRF as a model mechanical-genetic system.

Myocardin Related Transcription Factors

The myocardin related transcription factors A and B ("MRTF-A/MKL-1" and "MRTF-B/MKL-2") are actin sensitive transcription factors that regulate a variety of extracellular matrix components and mechno-sensing machinery of the cell primarily through co-activation of serum response factor (SRF). [232, 233, 228] These proteins are structurally similar to myocardin, a transcription factor largely restricted to the smooth muscle and the cardiovascular lineage [127], and the MRTFs are found near ubiquitously throughout the body in many cell types, including fibroblasts. [234, 228]

Mechanical Regulation of MRTF-A and MRTF-B

The activities of the MRTFs are controlled through their cytoplasm-nuclear shuttling. In the cytosol, the MRTFs are bound and sequestered by g-actin. When the pool of free g-actin drops during its polymerization to f-actin, MRTFs' RPEL domain, which contains cryptic nuclear localization sequences, is uncovered, allowing for rapid nuclear translation in an importin-α/β dependent fashion. [233, 232, 235, 236, 237, 238] Once inside the nucleus, nuclear export is regulated in a similar fashion - nuclear g-actin binds the MRTFs and promotes their export to the cytoplasm. [239, 240] Only the nuclear compartments of the MRTFs are transcriptionally relevant, acting as a necessary co-factor for SRF. [228]

The intimate connection between actin polymerization and substrate stiffness, mediated by both Rho GTPases and formins, means that the nuclear localization of the MRTFs is tightly correlated to the underlying substrate stiffness. [233, 241] However, this correlation between localization and substrate stiffness can be modified by post-translational phosphorylation of the MRTFs in a Rho- and serum/ERK-dependent fashion. While Rho-phosphorylation generally inhibits the association of the MRTFs with nuclear actin (promoting nuclear residency), MRTF phosphorylation by ERK has site specific effects - it can both prevent g-actin-MRTF binding and promote nuclear export by increasing MRTF's affinity for g-actin. [242, 235] Additionally, the substrate-stiffness dependence of this

process can be diminished by growth factor stimulation, which independently drives the assembly of the actin cytoskeleton. [228, 14]

The CArGome and Transcriptional Activity of MRTF-A and MRTF-B

In the nucleus, MRTFs act as the co-activator of SRF and drives transcription at DNA response elements called CArG boxes, which have a canonical sequence of 5'-CC(A/T)$_6$GG-3'. [243, 244, 245, 228] While SRF is able to be co-activated at 83 genetic loci in the murine genome in a tertinary complex factor family-dependent fashion, the MRTFs control the activation of SRF at over 2295 genetic loci and are the dominant co-activators of SRF. Moreover, SRF is co-precipitated at over 95% of all MRTFs' loci and acts as the main transcription factor partner for the MRTFs. [228] Genomically, while MRTF-A and B appear to co-regulate many of the same loci, MRTF-B seems to have a larger independent set of target loci relative to MRTF-A. CHIP seq studies of MRTF A and B reveal that they co-precipitate at 1320 genomic loci while MRTF A has 75 unique loci not found with MRTF-B, which has 1021 unique genetic loci. [228] Functionally, however, MRTF-A and B appear to play redundant roles in the development of the cardiovascular system, implying a strongly similar role for each in the regulation of SRF. [246]

The murine CArGome has been extensively characterized by CHIP-seq studies. It is formed by over 2000 distinct SRF-MRTF regulated loci and regulates hundreds of genes. [228] While the thermodynamic affinity of SRF with and without the MRTFs has been reported for some "classic" CArG boxes (*e.g.* the CArG elements in the ACTA2 and cFOS promoters), the energy landscape of the CArGome in rodents and humans remains largely uncharacterized. [228, 247, 248]

Many of the genes in the CArGome feed directly back into the cell's mechano-sensing machinery and into the matrix itself. [228] Top ontological genetic categories of MRTF-SRF targets for regulation are: cytoskeleton, actin cytoskeleton, focal adhesion, embryonic development, actomyosin, vasculature development, contractile fiber part, vesicle-

mediated transport, cell projection, hypertropic cardiomyopathy, and cell junctions. "Matrix organization" and "wound healing" ontological categories are also present in the SRF-MRTFs gene set. [228] This system-level data complements findings from reports that examine smaller, more disease focused genetic targets of MRTF/SRF. [229, 230, 14] These data imply that MRTF/SRF is not only as mechano-sensitive but is part of an innate biological feedback loop between cells and their mechanical environment.

Other Mechanically Sensitive Transcription Factor Families

Yes Associated Protein/Transcriptional Co-activator with PDZ-binding motif

Yes Associated Protein/Transcriptional Co-activator with PDZ-binding motif ("YAP/TAZ") are conserved transcription factors from the *Drosophila melanogaster* Hippo pathway, which regulate cell/tissue growth. They have been found to be mechano-sensitive transcription factors implicated in the development of fibrosis in multiple organ systems. [15, 91] Mechanically, YAP/TAZ are also regulated by actin: f-actin inhibits LATS1/2, which phosphorylates YAP/TAZ. Phosphorylated YAP/TAZ is retained in the cytosol, while unphosphorylated YAP/TAZ is able to translocate to the nucleus. While YAP/TAZ are regulated through a similar, actin-dependent modulation of their nuclear transport, YAP/TAZ's regulation by actin is more complex than MRTFs' regulation. YAP/TAZ's regulatory scheme integrates cues from g-coupled protein receptors, Wnt signaling pathways, and adherens junctions to lead to a net (inactivating) phosphorylation state. Phosphorylated or quiesced YAP/TAZ is also subject to degradation through a 14-3-3 protein mediated complex, a feature not observed in cytosolic MRTF biology. [192, 249, 250, 191]

Like the MRTFs, YAP/TAZ are co-activators and do not directly bind DNA. In contrast to the MRTFs, YAP/TAZ are more promiscuous co-activators of other transcription factors, including TEAD2, TEAD1, TEAD3, TEAD4, Smad2/3, RUNX, p73, and ErbB4 cytoplasmic domain. [251, 252] While there is near equivalent CHIP-seq information about the architectural features of the YAP/TAZ genomic space [253, 254], the lack of specificity for

a single co-activator makes it conceptually more difficult to understand the activity of YAP and TAZ on a systems-based level.

Transforming Growth Factor β

TGFβ signaling is mechanically regulated both intra-cellularly and extra-cellularly. The activation of TGFβ by cellular contractility is potentiated by substrate stiffness, which allows for efficient transmission of force to the latent TGFβ complex and subsequent release of TGFβ from the matrix. [13, 150] There is also strong *in vitro* evidence that cellular phenotypes in response to TGFβ are potentiated by substrate stiffness. [88, 89, 90, 91] Further work exploring the intra-cellular regulation of TGFβ signaling is discussed at length in Chapter 3 of this thesis.

TGFβ appears to acquire some of its mechano-sensitivity and to confer some mechanical phenotypes associated with it through physical interactions with both MRTFs and YAP/TAZ. YAP/TAZ appear to have a potentiating effect on TGFβ signaling through Smad2/3 - increasing substrate stiffness extends the nuclear residence of Smad2/3 in a YAP/TAZ-dependent fashion. [91].

The effects of TGFβ signaling on MRTF biology focus on two distinct mechanisms: (1) a RhoA/ROCK-dependent modulation of the cytoskeleton, which controls MRTF localization; and, (2) a Smad-dependent modulation of MRTF localization and transcription through protein-protein interactions in the nucleus. For Smad-based regulation of MRTF, Smad3 appears to impart a mechanical phenotype by inhibiting the activity of MRTF-A at baseline, but not during TGFβ stimulation in the pulmonary vasculature. [153] There is also evidence that TGFβ exerts a mechanical phenotype through MRTF-A in a Smad-independent fashion. [154] TGFβ has also been shown to drive the polymerization of the actin cytoskeleton in a RhoA/ROCK dependent fashion, driving epithelial-to-mesenchymal transformation and the transcription of pathologic genes like α-smooth muscle actin ("αSMA"). [255, 256, 257, 258, 259]. TGFβ also appears to negatively modulate

cadherin-based cell-cell contacts, which help promote MRTF translocation in epithelial cells. [258, 259]

4.2 Methods

4.2.1 Cell Culture and Transfection

Primary human foreskin fibroblasts (HFFs) were procured from ATCC (ATCC SCRC-1041, ATCC, Manassas, VA) and routinely cultured in DMEM (ThermoFisher, Waltham, MA) supplemented with 15% FBS and 1% penicillin/streptomycin (ThermoFisher, Waltham, MA) in 5% CO_2 at 37C in a humified incubator to passage 13. Human embryonic kidney cell lines were procured from ATCC (ATCC CRL-3216, ATCC, Manassas, VA) and routinely cultured as above except with a 10% concentration of FBS, until passage 20. For CArG sink delivery, 500,000 HFFs were resuspended in 100μL of Normal Human Dermal Fibroblast buffer with supplement and DNA CArG probes and electroporated using program U-023 in an Amaxa Nucleofector system according to the manufacturer's instructions (Lonza, Walkersville, MD). Alternatively, adherent, near confluent HFFs in 6 well plates were incubated with CArG Probes resuspended in Lipofectamine 3000 using 1μL P3000 reagent and 1.5μL Lipofectamine 3000 reagent per well according to the manufacturer's protocol for at least 6 hours. HEK cells were also transfected with 2μg of pCGN-SRF (Addgene, Cambridge, MA [260]) using Lipofectamine 3000 as above.

4.2.2 MRTF Translocation by Immunofluorescence

HFFs were plated in serum free media supplemented with 1% BSA in High-Throughput Screening plates (Matrigen, Brea, CA), containing glass and stiffness-defined hydrogel substrates, which were functionalized with 10μg/mL human fibronectin at a concentration of 2000 cells/cm^2. Cells were allowed to spread and mechanotransduce for 4 hours. Any additional treatments indicated (50pg/mL TGFβ, 50pg/mL TGFβ with 10μM Y-27632,) were added during the last 90 minutes of culture. Cells were then fixed in 4% paraformalde-

hyde in 1X PBS for 10 minutes, permeablized with 0.1% Triton X-100 in 1X PBS for 5 minutes, and blocked for 60 minutes with 5% donkey and goat sera in 1X PBS. Cells were incubated overnight with primary antibodies as indicated in Table 4.1 in PBS-T. After washing, cells were incubated with secondary antibodies as indicated in Table 4.1, washed again, and then counterstained with 1:1000 Hoescht 33342 and 1:40 Phalloidin-488 (ThermoFisher, Waltham, MA) and mounted with SlowFade Diamond (ThermoFisher, Waltham, MA). Imaging was performed with a Axiovert 200M microscope (Carl Zeiss Microscopy, Jena, Germany) with an UltraVIEW spinning disk (PerkinElmer, Waltham, MA) and Flash 4.0v2 cMOS camera (Hamamatsu Photonics, Hamamatsu City, Japan) using a 1.4NA Plan-Apochromat 63X objective (Carl Zeiss Microscopy, Jena, Germany). Data analysis and image acquisition were performed using Volocity (Perkin Elmer, Waltham, MA). Recombinant human TGFβ was procured commercially (R&D Biosystems, Minneapolis, MN) while Y-27632 was a kind gift from Dr. Andres Garcia.

4.2.3 Fuzznuc Analysis of CHIP-Seq Data from Ensault *et al.* (2014)

Sequence data for CHIP-seq loci was obtained in FASTA format from UCSDs Genome Viewer toolbox using BED genomic coordinates specified in Ensault *et al.* (2014). These sequences were analyzed using the EMBOSS suites fuzznuc program with an input sequence of "C-C-W-W-W-W-W-W-G-G" to determine the number(s) and quality/qualities (consensus, single and double mismatch) of CArG boxes present in the peaks. Custom Matlab (TheMathWorks, Waltham, MA) scripts were used to extract the peak and peak features associated with genes annotated in Ensault *et al.* (2014). Statistical analysis and data representation was performed in Prism (Graphpad, La Jolla, CA).

4.2.4 DNA Decoy Probe Construction and Labeling

Probe Construction or Purchase

Probe sequences are listed in the Appendix B of this thesis. All probes were order commercially (Integrated DNA Technologies, Coralville, IA) except for synthetic, Biobrick derived 120 bp elements, which were cloned using restriction digest into the pSB1A3 vector (iGEM Consortium, Boston, MA) and subsequently PCR amplified using Phusion polymerase according to manufacturer's instructions (New England Biolabs, Ipswich, MA) with VF2 and VR oligos from Table 4.2 and purified using PCR Cleanup Kits (Qiagen, Hilden, Germany). Probes purchased from IDT incorporated a 5' amine modified thymidine with a 6 carbon spacer for subsequent dye labeling. All commercially ordered probes were hybridized in siRNA Resuspension Buffer (ThermoFisher, Waltham, MA) according to the manufacturer's protocol for siRNA hybridization.

Probe Labeling

Probes were labeled with a fluorescent intercalating dye for flow cytometry experiments and covalently for sub-cellular localization experiments. For labeling with an intercalating dye, probes were incubated for 30 minutes at room temperature with a 1:1000 solution of SYBR Safe (ThermoFisher, Waltham, MA). Unconjugated dye was removed by spin filtration using a 30kDa Amicon Ultra centrifugation filter (Sigma, Darmstadt, Germany) according the manufacturer's instructions. Covalent labeling with a monovalent Cy3b-NHS-ester (GE Healthcare, Little Chalfont, United Kingdom) to the 5' amine modified thymidines on IDT probes was accomplished by resuspending the Cy3b ester in DMSO and incubating it with probes at a 1:10 molar excess overnight, in a 0.1M sodium bicarbonate buffer. Unconjugated dye was spin filtration using the 30kDa Amicon Ultra centrifugation filters as above.

4.2.5 RT-qPCR and qPCR

qPCR for Decoy Delivery

HFFs were electroporated with 140 fmol - 1.4 pmol of synthetic, 120bp double-stranded αSMA CArG probes as above and allowed to recover in warm media for one hour. DNA probes were then extracted from the cell using a modified Hirt extraction with subsequent purification in Miniprep columns according to the procotol from [261]. The extracted probes were assayed by qPCR with SYBR Green on a Step One Plus instrument (Applied Biosystems, Foster City, CA) using primers VF2 and VR from Table 4.2 according to the manufacturer's instructions in quadruplicate. Quadruplicate doses ranging by an order of magnitude from 100pg to 1fg were prepared and used as input template for standard curve generation and run on the same plate as experimental samples. Derivative melt curves were visually checked for single product peak. Raw amplification data were imported into LinRegPCR (Heart Failure Research Center, Amsterdam, The Netherlands) where they were baseline and efficiency corrected using linear regions of amplification for each amplicon. Absolute levels of probes per cells were calculated using the standard curve to impute the total number of probes delivered and dividing by the number of input cells. Statistical analysis and data representation was performed in Prism (Graphpad, La Jolla, CA).

RT-qPCR for Endogenous Genes

HFFs were electroporated with 1.4-3.1 pmol of synthetic, 120bp double-stranded αSMA or cFOS CArG probes as above and allowed to recover in warm media with full or low (1%) for one hour. RNA was then extracted using an RNEasy kit and cDNA was prepared using a RT^2 First Strand cDNA kit according to the manufacturer's protocol (Qiagen, Hilden, Germany). RT-qPCR was performed using a Step One Plus instrument with SYBR-Green chemistry and qPCR primers for GAPDH, XIAP, and Bcl-2 as described in Table 4.2 according to recommendation from the manufacturer (Applied Biosystems, Foster City, CA)

in technical quadruplicate. Derivative melt curves were visually checked for single product peak. Raw amplification data was imported into LinRegPCR (Heart Failure Research Center, Amsterdam, The Netherlands) where it was baseline and efficiency corrected using linear regions of amplification for each amplicon. $\Delta\Delta$CT values were calculated by normalizing apoptosis relevant gene N_0's to GAPDH and then normalizing to electroporation only control cells. Statistical analysis and data representation was performed in Prism (Graphpad, La Jolla, CA).

4.2.6 SRF Gel Shift Assays

EMSA assays were performed as described previously in [228]. Briefly, 20μL reactions with Cy3b labeled probes were incubated with either 2μg of recombinant human SRF (Origene, Rockville, MD), 2μL of pCGN-SRF over-expressing HEK lysate, or no SRF source, in 1mM EDTA, 10mM Tris HCl 7.9, 50mM NaCl, 50ug/mL BSA, 5mM spermidine, 5% Ficoll 400, 0.5% (w/v) bromophenol blue with freshly added 3mM DTT and 25μg/mL poly dIdC for 30 minutes at 37C. Samples were then mixed with 6X gel loading dye without SDS (New England Biolabs, Ipswich, MA) and loaded on a 10% TBE gel in 1X TBE and run at 100V at 4C until the gel front reached the end of the gel. The gel was post-stained with 1:10000 GelGreen (Biotium, Freemont, CA) for one hour at room temperature and imaged on ChemiDoc MP system (Bio-Rad, Hercules, CA) with a Cy3 (probe) and a FITC filter (ladder).

Table 4.1: Antibodies Used in this Chapter

	Target	Clone	Host	Concentration	Vendor	Cat. Number
Primary	SRF	G-20	Rabbit	1:1000	Santa Cruz	sc-335 (discontinuted)
	MRTF-A	Polyclonal	Rabbit	1:1000	Sigma	HPA030782
	Smad2/3	Clone18	Mouse	1:1000	BD Biosciences	610842
Secondaries	Goat αRabbit 546	Polyclonal	Goat	1:500	ThermoFisher	A-11035
	Goat αMouse 647	Polyclonal	Goat	1:500	ThermoFisher	A-21236

Table 4.2: Oligos Used in this Chapter

Oligo Name	5'-3' Sequence	Purpose	Tm	Concentration	Vendor	Cat. Number
VF2	TGCCACCTGACGTCTAAGAA	Amplificaiton and qPCR of Synthetic, 120bp CArG Probes	60	250-500nM	IDT	iGEM Primers
VR	ATTACCGCCTTTGAGTGAGC		60	250-500nM		
GAPDH For	ACCCACTCCTCCACCTTTGA	qPCR Housekeeping Gene	60	250nM	IDT	Originally From [262]
GAPDH Rev	CTGTTGCTGTAGCCAAATTCGT		60	250nM		
XIAP For	Sequence Undisclosed	RT-qPCR - SRF Competitive Antagonism	60	250nM	IDT	Hs.PT.56a.24292268
XIAP Rev			60	250nM		
Bcl2 For			60	250nM		Hs.PT.56a.654557.g
Bcl2 Rev			60	250nM		

4.3 Results

4.3.1 Substrate Rigidity Translocates MRTF to the Nucleus with Peak Responsivity Over 8kPa

In order to map the initial stiffness-response of fibroblasts' translocation of MRTF to the nucleus as a function of substrate stiffness, HFFs were plated on poly-acrylamide hydrogel surfaces functionalized with human fibronectin and assayed for MRTF localization by immunofluorescence. Because other fibrosis-relevant growth factors, like TGFβ, have been shown to modulate the activity of MRTF in a ROCK-dependent fashion [255, 256, 258, 257, 259], MRTFs' translocation was also examined with 50pg/mL TGFβ treatment and with 50pg/mL TGFβ and 10μM Y-27632 treatment. Pharmacological treatment of fibroblasts with 2μM latruculin B ("LatB"), a g-actin stabilizing agent and nuclear MRTF antagonist, demonstrated statistically significant alterations in fibroblast morphology and actin-polymerization. Cell volumes were decreased (Figure 4.1B-upper left, p=0.035, p=0.074, p$<$0.0001 for LatB vs. 0pg/mL TGFβ, vs. 50pg/mL TGFβ, and vs. 50pg/mL TGFβ + 10μM Y-27632, respectively) as were nuclear volumes (Figure 4.1B-upper right, p=0.0177, p=0.1215, p$<$0.0001 for LatB vs. 0pg/mL TGFβ, vs. 50pg/mL TGFβ, and vs. 50pg/mL TGFβ + 10μM Y-27632, respectively). Importantly, these changes in cell morphology tracked with a decreased accumulation of MRTF in the nucleus of cells with LatB treatment (Figure 4.1B-lower right, p=0.0089, p=0.0166, p=0.3615 for LatB vs. 0pg/mL TGFβ, vs. 50pg/mL TGFβ, and vs. 50pg/mL TGFβ + 10μM Y-27632, respectively), indicating

that the assay detected actin-polymerization dependent changes in MRTF localization.

TGFβ treatment with or without 10μM Y-27632 also significantly increased the nuclear residence of Smad2/3 (Figure 4.1B-lower-left, $p<0.0001$ for any TGFβ treatment relative to TGFβ untreated fibroblasts at any stiffness, except p=0.586 between 50pg/mL TGFβ treated and untreated fibroblasts at 8kPa), indicating the activity of the TGFβ treatments across all stiffness conditions. There were no significant differences in Smad2/3 translocation as a function of Y-27632 treatment at any stiffness (Figure 4.1B-lower left).

MRTF was imported into the nucleus in a stiffness-dependent fashion in all treatment conditions (Figure 4.1B-lower-right, $p<0.0001$ for all groups). TGFβ and Y-27632 untreated fibroblasts demonstrated maximal sensitivity to substrate stiffness between 8 kPa and 25 kPa with comparatively little stiffness-response between 0.5 kPa and 2kPa. Interestingly, the treatment of fibroblasts with TGFβ or with TGFβ and Y-27632 did not consistently modify the stiffness-responsive translocation of the MRTFs in HFFs. Qualitatively, it appeared that TGFβ treatment shifted the mechanical sensitivity of the MRTF-translocation phenotype to softer substrates and that this effect was rescued by ROCK inhibition by Y-27632 treatment. These data collectively indicated that TGFβ treatment with or without Y-27632 treatment did not significantly modulate the initial mechanical MRTF phenotype of fibroblasts.

4.3.2 The Murine CArGome is Primarily Organized into Single Binding Domains Comprised of 4-14, High Quality CArG Boxes

In order to understand the transcriptional activity of MRTFs/SRF after mechanical activation, the murine CArGome was architecturally characterized using publicly available CHIP-seq and RNA-seq data from 3T3 fibroblasts. [228] SRF and MRTF localization to CHIP peaks annotated to various genes were correlated to mRNA levels for those same genes with or without serum stimulus as an activating cue for MRTF (Figure 4.2A). There was a statistically significant correlation between SRF (Figure 4.2A-i), MRTF-A (Figure

4.2A-ii) and MRTF-B (Figure 4.2A-iii) residence at a given CHIP peak and transcription of the annotated gene both with and without serum stimulation (SRF: r=0.1361 and r=0.1940, $p<0.0001$ for low and high serum, respectively; MRTF-A: r=0.08515 and r=0.1953 with p=0.0004 and $p<0.0001$ for low and high serum, respectively; MRTF-B: r=0.1085 and r=0.2172, $p<0.0001$ for low and high serum, respectively). While the increase in the correlation coefficient between SRF and RNA with higher serum concentrations could indicate the activation of SRF by MRTF by serum stimulation, the increase in the correlation between MRTF-A and MRTF-B and RNA with serum stimulation was less clear. Nevertheless, the correlations between transcription factor residency and gene transcription was an important proof-of-concept finding that validates further exploration of MRTF/SRF as a driver of mechanical transcription.

In order to ascertain the number of SRF-binding regions associated with a given gene, a histogram of CHIP-seq peaks per annotated gene was computed, revealing that the vast majority of genes were regulated by a single SRF CHIP-seq peak, with $\approx 95\%$ of all annotated genes regulated by one or two SRF peaks (Figure 4.2A-iv). Additionally, there was a strong, positive correlation between the number of CHIP-seq peaks for a particular gene and the residence of SRF at that particular gene (Figure 4.2A-v, r=.4901, $p<0.0001$). These data demonstrated two important features of the CArGome: first, that individual genes were often associated with a single SRF binding domain; and second, that there was a positive association between SRF binding regions and SRF residency at a particular gene.

While characterization of the CArGome at the level of individual CHIP-seq peaks was important in validating MRTF/SRF as a potential model system for mechanical transcription generally, characterization of the number and quality (*i.e.* the inferred binding affinity of the CArG box for SRF based on sequence homology to a canonical CArG box) was performed to build a full architectural picture at the level of individual SRF binding elements inside these CHIP-seq peaks. From a *fuzznuc*-based analysis of all identified SRF CHIP-seq peaks, individual CHIP peaks were found to contain an average of 8 ± 4 CArG

boxes, with a few peaks containing over 30 individual CArG boxes (Figure 4.2B-i, the analysis searched for CArG boxes with up to two sequence mis-matches to the canonical sequence). There was a statistically significant positive correlation between the number of CArG boxes contained in an individual CHIP-seq peak and the residence of SRF at that particular peak, averaged across serum stimulating conditions (r=0.222, $p<0.0001$). Additionally, there was a negative correlation between the degree of mis-match of the highest quality CArG box in a peak and the residency of SRF at those peaks (Figure 4.2B-ii, r=-0.2850, $p<0.0001$). The decision to not explore CArG boxes past a double mis-match was further validated by these data, which indicated that only 7 CHIP-seq peaks did not contain a double mis-match or higher quality CArG box. Together, these data indicated that CArG box frequency and quality both contributed to the ability of an individual SRF-binding domain to recruit SRF. Finally, these data provided a baseline assessment of the features of the CArG boxes in the murine genome that could be used for a first-pass design of CArG-based promoter elements.

4.3.3 Decoy CArG Sinks Can Be Delivered on the Scale of the Endogenous CArGome

In order to construct a steady state, statistical mechanics-based model of the endogenous CArGome to predict mechanically-driven transcription, thermodynamic measurements of the endogenous CArGome will be required. While the tools to make cell-free measurements of individual CArG box affinity for SRF have been established using an NGS-based high-throughput EMSA approach ("Spec-Seq") [263], the ability to perturb the affinity landscape of the CArGome *in vitro* had not yet been developed. The delivery of double-stranded, linear DNA elements containing CArG boxes ("CArG probes" or "CArG sinks") derived from the αSMA or cFOS promoters was characterized to ascertain the feasibility of genomic-scale perturbations to the CArG landscape. DNA loads of 1.4 pmol of CArG sinks, delivered to cells by electroporation, produced $\approx$ 25,000 CArG sinks per cells as measured by absolute qPCR, which is on the scale of the endogenous $\approx$ 20,000 murine

CArG boxes. The delivery of CArG probes to the cell was dose-dependent with 140 fmol loads of CArG boxes delivering significantly fewer ($\approx$ 10X fewer) CArG boxes per cell (Figure 4.3A-iii, p=0.0053). Additionally, delivery of SYBR-labeled CArG sinks to cells was assayed by flow cytometry both to characterize the relative delivery of CArG probes per cell and to assess the ability to isolate fibroblasts with a specific intracellular load of CArG sinks in future assays (Figure 4.3B-i&ii). Delivery of CArG sinks displayed a dose-dependent shift in the median fluorescent intensity of individual cells (Figure 4.3B-iii, $p<0.0001$), which correlated with the qPCR assayed number of probes per cell (Figure 4.3B-iv, r=0.9823, p=0.0005).

Because nuclear CArG sinks were required for competitive antagonism of SRF binding, the sub-cellular localization of these CArG probes was assayed using confocal microscopy (Figure 4.3C) across two delivery methods: electroporation and cationic lipid delivery (Lipofectamine3000). Electroporation was statistically more efficient in delivering nuclear CArG sinks than Lipofectamine3000 (Figure 4.3D-i&iii, $p<0.0001$) though Lipofectamine was capable of delivering statistically more CArG sinks to fibroblasts both in the nucleus and in the cytoplasm (Figure 4.3D-ii, $p<0.0001$ for both compartments). These data indicate that $\approx$ 50% of CArG sinks delivered to cells by electroporation ended up in the nucleus, creating effective CArG sink loads on the same order of magnitude as the endogenous murine CArGome. Additionally, these data indicated the feasibility of multiple modes of delivery of CArG sinks to cells *in vitro* for future experiments.

4.3.4 CArG Sinks Do Not Modulate the Localization of SRF Nor Antangonize SRF Transcription on Short Time Scales

In addition to their use as thermodynamic modulators of the CArGome, CArG sinks could competitively antagonize SRF-transcription relevant to fibrosis. [14, 264] SRF transcription could be perturbed either by either mis-localizing SRF to the cytoplasm or through competitive antagonism of the sinks against the endogenous CArGome for SRF binding.

The subcellular localization of SRF with and without CArG box delivery was assayed using confocal microscopy (Figure 4.4A). Delivery of 1.4pmol loads of cFOS CArG boxes by electroporation did not induce a shift in the subcellular localization of SRF relative to electroporation only controls (Figure 4.4B).

The ability of CArG sinks to perturb SRF transcription of fibrosis relevant SRF transcripts one hour after delivery was assayed by RT-qPCR based on previous RT-qPCR experimental setups with serum stimulation. [228] CArG sinks of varying dose and varying CArG box composition did not antagonize SRF transcription relative to CArG boxes with a purine-pyrimidine substitution ("anti-CArG" sink). These data indicated that CArG box delivery did not perturb the endogenous biological localization of SRF and was insufficient at short time scales and at pmol loads of probe to antagonize SRF transcription.

4.3.5 Characterization of CArG Box Probe Design for SRF-Dependent Shift Assays

The ability to assay the thermodynamic landscape of the CArGome up to double mis-match CArG boxes, in a cell-free system required the development of probes suitable for SRF shift assays. I have characterized both naturally derived (Figure 4.5A, lanes 4-9 and Figure 4.5B, lanes 3-4 and 7-8) and synthetically derived CArG probes (Figure 4.5A, lanes 2-3), CArG probes with lengths between $\approx$120-400 bp (Figure 4.5A), and CArG probes with a single CArG box or multiple CArG boxes per probe. Probes of various length from synthetic or naturally derived sequences were all capable of binding SRF from over-expression HEK lysates (Figure 4.5A). While several of these probes (Figure 4.5A, lanes 2-3, 6-7) contained multiple consensus or mis-matched CArG boxes, no higher molecular shifts were detected from additional SRF binding, most likely because the gel lacked spatial resolution to see those multiple binding events. The integrity of the CArG box was necessary for SRF gel shifts (Figure 4.5B). Anti-CArG probes, 120 bp probes containing a purine-pyrimidine swap in the CArG box, were incapable of producing a shift when incubated with recombinant human SRF (Figure 4.5B, lane 6), while CArG probes based on the cFos or αSMA

promoter were capable of SRF-shifting. These data indicated that there was a broad tolerance of the SRF gel shift assay to design parameters of the CArG box probes used and that the assay was specific both for the presence of SRF and for the integrity of the CArG sequence in the probe.

4.4 Discussion

4.4.1 Relevance to the Design of Mechanically Driven Transgenes

The characterization of the CArGome is translationally significant in terms of providing the basis for a mechanistic understanding of how SRF-based stiffness promoters may function and in informing the design of those promoters. The results in this Chapter demonstrated the feasibility of such promoters by demonstrating correlations between the CArG number and character in SRF CHIP-seq peaks and the recruitment of SRF to those peaks and by demonstrating the correlation between SRF/MRTF occupancy at a particular genetic locus and transcription of that gene. Additionally, these results suggested initial starting designs based on the distribution of 8 ± 4 CArG box per SRF peak found through out the genome. Additionally, there may be data features of the CArGome that could be further considered to help drive the development of CArGome based promoters, including characterizing the inter-CArG box sequence spacing within peaks to optimize multiple SRF binding events, and characterizing the quality composition of the CArG boxes in terms of percentages of canonical, one and two mis-match boxes for deeper insight into the quality landscape of the CArGome absent direct thermodynamic measurement. Finally, it may be useful to screen for common sequence motifs in the interstitial sequences between CArG boxes to identify other potential transcription factors that may be acting in concert with MRTF/SRF at endogenous promoters. Identification and purposeful elimination of these sequences may be useful in improving the specificity of synthetic promoter elements for MRTF/SRF signaling. There are a number of computational techniques dedicated to the *de novo* discovery of such motifs from CHIP-seq data [265, 266, 267] as well as open-source datasets of

position-weighted matrices for known transcription factors binding sites, which could be queried directly. [268]

The characterization of the CArGome may also contribute to the use of SRF-based transgenes as reporters of cellular state beyond stiffness reporting / stiffness-targeting. Other groups have used the α-SMA CArG-based promoter as a reporter of cell state, specifically targeting myofibroblasts [269] and osteoblastic differentiation in stem cells. [270] The ability to rationally fine tune the response of these cell-state reporters by modulating their CArG box composition could be useful in identifying subpopulations of differentiating cells or in improving the specificity or sensitivity of the reporters to a particular cellular state.

The characterization of MRTF's translocation to the nucleus as a function of substrate stiffness is also significant in terms of helping to predict the performance of CArG-based transgenes. The greatest shift in MRTF localization occurred between stiffness of 8 and 25 kPa, which aligns well with pathological stiffness regimes in micro-mechanical characterization of lung biopsies from patients with pulmonary fibrosis. [4] While this sensitivity might be useful in targeting pathology that is well separated from physiologic stiffness, as in fibrosis, it indicates targeting stiffness states under 8 kPa (for other biological purposes than therapeutic targeting of fibrosis) may be uniquely difficult and require more advanced synthetic biology constructs, such as the use of bandpass terminator elements [271] or interlaced high and low pass genetic regulatory schemes. [272, 273]

How do the results of this Chapter inform the choice of transcription factor family for the construction of stiffness-driven transgenes? To date, a YAP/TAZ/TEAD box system has been demonstrated as the only proof-of-concept stiffness-driven therapy with a focus on treating metastatic disease in the lung. [231] Interestingly, there are some similarities between that approach and the MRTF-based system explored here. Specifically, the peak responsiveness of MRTF to stiffness over 8 kPa indicates that MRTF based transgenes may perform similarly *in vitro* to YAP/TAZ-based TEAD box reporters, which demonstrated

peak *in vitro* responsiveness over 10 kPa. [231] While there are no *a priori* reasons to assume that the mechanical responses of MRTF and YAP/TAZ would be similar or different, there may be reasons to suspect that the *in vivo* translation of these *in vitro* observations may be different for MRTF and YAP/TAZ. These differences are likely to arise from the relative balance of other inputs, beyond the stiffness-mediated mechanisms, to nuclear translocation for these two transcription factor systems. While MRTF is not wholly regulated by actin polymerization (*e.g.* MRTF can be phosphorylated in an ERK-dependent fashion, which modifies its affinity to bind g-actin [242, 235]), YAP/TAZ appear to receive a greater balance of non-stiffness mediated inputs into their biology. This is likely reflective of their dual role as a mechanical sensor and as a regulator of tissue/organ growth via the Hippo pathway, as Wnt signaling, g-coupled protein receptor activation, and adherens biology can direct the translocation of YAP/TAZ via its phosphorylation state. [192, 249, 250, 191]

Finally, conceptually, the CArGome is uniquely amenable to the analyses performed in this chapter because of the unique molecular monogamy that exists between the mechanically regulated and necessary co-activator, MRTF, and the direct transcription factor, SRF. [228] In comparison, YAP and TAZ appear to have coordinated but distinct transcriptional profiles that necessarily intersect with several other DNA-binding transcription factors. This would require a similar energy landscape profiling for each partnered transcription factor, including TEAD1-4, Smad2/3, Runx, ErbB4 cytoplasmic domain, and p73, leading to a significant increase in complexity of the model system. [251, 252]

4.4.2 MRTF Mechanobiology and Intersections with TGFβ Signaling

This chapter has reported on the stiffness-dependent translocation of MRTF to the nucleus and the effects of TGFβ signaling on this translocation. The stiffness-mediated translocation of MRTFs has been well reported in the literature [232, 233, 239, 240, 235], and, indeed, makes MRTF/SRF an ideal model system for studying mechanical genetics; how-

ever, this Chapter has expanded on those previous observations both by increasing the stiffness-resolution of those measurements and, more importantly, by focusing on the role of TGFβ signaling to modify this responsiveness in a ROCK-dependent fashion in the initial mechanosensing of fibroblasts. Given the demonstrated experimental and clinical importance of TGFβ signaling in fibrotic pathology [10, 119, 120, 274, 123] and the Smad-dependent and -independent [153, 154, 255, 256, 258, 259] intersections between TGFβ signaling and MRTF biology, understanding this connection is likely relevant to understanding/predicting the behavior of CArG based transgenes in the setting of fibrotic pathology.

Contrary to initial expectation based on the available literature and the result of modeling based on that literature by the Saucerman Lab at UVA, treatment with TGFβ or TGFβ and a ROCK inhibitor, Y-27632, did not have consistent effects on modulating the MRTF-stiffness phenotype of fibroblasts. However, there are several important differences between my findings and the reported literature, which may indicate a possible resolution of this discrepancy. Many of the reports focusing on the connection of TGFβ signaling to MRTF through RhoA/ROCK examine cells at extremely long time-scales (24-48 hours) relative to the transcription activity of TGFβ and to the time-scale used in this Chapter (4 hours). Indeed, an increase in αSMA translation is usually interpreted as activity of alternation to MRTF/SRF biology in these systems. [256, 258, 259] My focus on relatively short time scales is motivated by the dynamic activity of the cytoskeleton in response to substrate mechanical cues during cell spreading, which in turn control the localization of MRTF. [241, 14] Additionally, these long time-scales make it difficult to distinguish between activity by TGFβ signaling *through* the actin cytoskeleton and activity *on* the actin cytoskeleton as it relates to the dynamics of MRTFs' localization. [258, 257, 259] Furthermore, many of these other studies employ active TGFβ concentration on the order of ng/mL, which is above the physiologic range for many organs, like the liver, and is an order(s) of magnitude greater than the 50pg/mL dose used in this chapter. [275] One interpretation of these

observations is that there may be some signaling threshold for TGFβ to directly act on the cytoskeleton in order to drive TGFβ translocation. Finally, many other groups are specifically interested in TGFβ's ability to drive epithelial-to-mesenchymal transformation and focus on epithelial cell population from various organs. [257, 256, 259] Given the basic cytoskeletal and adherens junctions differences between these two cell types [276] and the role of Wnt signaling [258] and cell-cell contacts [259] in the mechanisms proposed by these groups, it is possible that different biological mechanisms are at play between fibroblasts and epithelial cells. In short, there are important kinetic, dose and cell-type selection biases between this work and the literature that may account for the seeming discrepancy in MRTF translocation as a function of TGFβ dose.

Given the lack of effect of 50pg/mL TGFβ doses alone to modulate MRTF sub-cellular localization, it is not surprising that Y-27632 treatment with TGFβ stimulation did not have a clear statistical effect on modulating the TGFβ associated phenotype. This finding is generally consistent with a report from the literature, which studied the effect of Y-27632 dosing alone on MRTF translocation at a similar dose (10μM) and at relatively short time-scales (12 hours) in aortic vascular endothelial cells. [277] This report found no effect on MRTF translocation from Y-27632 dosing without a concomitant increase in ERK-driven phosphorylation of MRTF, which modulates its affinity for g-actin. [242, 235] Fibroblasts in my system were plated in serum free media to maximize the effects of mechanical signaling relative to soluble signaling on the cytoskeleton and are consistent with this literature.

4.4.3 Impact of Mechanical Memory on Stiffness-Driven Transcription

The conceptual framework for organizing this thesis posits that the genome not only drives transcriptional changes in response to mechanical stimuli but also evolves the state of the cell in time to further stimulus. There is clear evidence that stiffness imparts an epigenetic "memory" on the genome. Numerous groups have shown that fibroblasts cultured on either

soft or stiff environments have phenotypic hysteresis when transitioning to a new mechanical environment. The phenotypes explored are of direct relevance to fibrosis: myofiborblastic differentiation, activation of latent TGFβ, and cellular proliferation and contractility [278] - as well as other pathologies, like cancer: metastatic potential, cell growth.[279]

The exact mechanism(s) of this mechanical memory is not clear. There is evidence that persistent miRNA signaling through the MRTFs is critical to maintaining the mechanical memory of mesenchymal stem cells, though the generality of this phenotype is unclear since mesenchymal stem cells have a unique chromatin architecture due to their stem-ness. [280] Other groups have found that persistent YAP signaling is critical to retaining memory in epithelial cells undergoing collective or individual migration. [251] YAP in combination with Runx signaling also appears to be critically regulated by substrate stiffness and imparts a memory phenotype in stem cells. [281] Some proposed mechanisms are not directly related to substrate stiffness as the inciting cue, *per se*, but are the consequence of other micro-environmental cues that converge on mechano-sensing pathways. The inflammation-driven epigenetic hetero-chromatinization of the Thy-1 promoter by histone deacetylases is an example of how biochemical stimuli can impart a distinct mechanical phenotype independent of changes to the actual matrix mechanical properties. [100, 282] While the science around mechanical memory continues to evolve, considerations of how CArG-based stiffness promoters interacts with the genome will have to contend with the environmental memory imparted by previous culture and tissue conditions, specifically as these epigenetic echoes converge on MRTF/SRF biology. [280]

4.5 Future Directions

4.5.1 Development of Statistical Mechanics-Based Model for Stiffness-Driven Transcription

The work in this Chapter has contributed to the development of logic-based differential equation model of MRTF/SRF biology, where individual interactions are modeled using normalized Hill functions with AND/OR logic gates, in collaboration with the Saucerman

Group at UVA. This modeling allows for an understanding of how a MRTF/SRF/promoter system may evolve in time. Currently the model focuses on the activation of MRTF by mechanical cues and by TGFβ signaling. Important next steps in the development of this model would be to link the architectural features of the CArGome into the down-stream activity of MRTF/SRF to understand how they are transcriptionally titrated. The use of statistical mechanics to model the steady state activity of transcription factors has been demonstrated experimentally [283] and the theoretical framework for various promoter architectures [284] and for coupled promoter architectures [285] have been previously established.

A critical feature of these models are thermodynamic affinities for the various promoter elements in the system. Thankfully, future work on this project is well positioned to survey the thermodynamics of the CArGome in a cell free system by employing the experimental conditions found in this Chapter for CArG-SRF gel shift assays. The ability to profile thousands of binding sequences for a given DNA-transcription factor pair has been demonstrated by previous characterization of the lac operon and its various permutations, and this approach is directly amenable to studying CArG degeneracies out to double mis-match CArG boxes. [263] One important experimental condition to optimize before constructing the necessary NGS libraries would be to optimize the CArG-SRF shift assay to incorporate MRTF-A and MRTF-B into the complex since there is evidence that MRTFs can cooperatively regulate the affinity of SRF for CArG boxes. [228, 247]

4.5.2 Development of Second Generation CArG Sinks for Thermodynamic Measurements and SRF Antagonism

In order to improve the effective delivery and the stability of CArG sinks both for thermodynamic measurements described above and for possible direct therapeutic action by competitive antagonism of SRF-endogenous genomic interactions, a second generation of the CArG sink should be developed. Important design considerations would be the incor-

poration of a nuclear localization sequence to increase the effective delivery of these boxes. NLS sequences have been profiled from viral, pro- and eukaryotic systems and there are demonstrations of their effectiveness in increasing DNA delivery to the nucleus with multiple delivery systems. [286, 287, 288, 289]

Interestingly, one of the few negative reports on the use of NLS sequences to delivery DNA efficiently to the nucleus focused on the delivery of short, linear double-stranded DNA elements. This group found that the effect of the NLS was overwhelmed by the aggressive activity of nucleases on the 3' end of their fragments. [290] This observations supports findings in this Chapter as CArG sinks, delivered on the order of the endogenous CArGome, did not antagonize fibrosis-relevant SRF transcripts. One possible solution to this problem is to incorporate modified nucleic acids into the 3' and 5' ends of the probes to render them resistant to nuclease activity. In particular, the use of peptide nucleic acids (nucleic acids with a peptide backbone instead of a phospho-diester backbone) to stabilize competitive DNA sinks against NK-κ-B signaling has been reported and could be directly incorporated into the probes used in this Chapter. [291, 292]

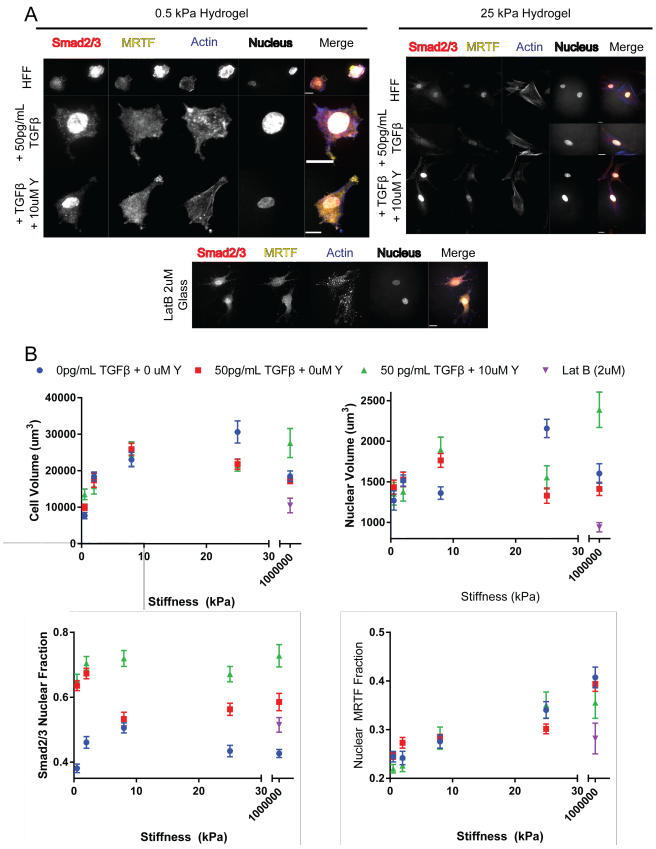

Figure 4.1: **Translocation of MRTF to the Nucleus at 4 Hours is Driven by Substrate Stiffness but Not Modulated Consistently by TGFβ Treatment or ROCK Inhibition.** A, Representative micrographs of fibroblasts on soft, physiologic-representative (0.5 kPa) hydrogels, on stiff, fibrotic-representative (25kPa) hydrogels, and on glass. Cells on glass were treated with Latruculin B. MRTF and Smad2/3 subcellular localization was probed by immunofluorescence in the presence or absence of 50pg/mL TGFβ or 50pg/mL TGFβ and 10μM Y-27632. B, Quantification of cellular volume (top right), nuclear volume (top left), nuclear MRTF fraction (bottom right), and nuclear Smad2/3 fraction (bottom left). Treatment of the cells with 2μM Latruculin B produced a reduction in measured cell volume (p=0.035, p=0.074, p<0.0001 for Latruculin B vs. 0pg/mL TGFβ, vs. 50pg/mL TGFβ, and vs. 50pg/mL TGFβ + 10μM Y-27632, respectively, ANOVA - Tukey post-test), a reduction in measured nuclear volume (p=0.0177, p=0.1215, p<0.0001 for Latruculin B vs. 0pg/mL TGFβ, vs. 50pg/mL TGFβ, and vs. 50pg/mL TGFβ + 10μM Y-27632, respectively, ANOVA - Tukey post-test), and a reduction in nuclear MRTF (p=0.0089, p=0.0166, p=0.3615 for Latruculin B vs. 0pg/mL TGFβ, vs. 50pg/mL TGFβ, and vs. 50pg/mL TGFβ + 10μM Y-27632, respectively, ANOVA - Tukey post-test). TGFβ treatment was associated with statistically increased nuclear localization of Smad2/3 (p<0.0001 for any TGFβ treatment relative to TGFβ untreated fibroblasts at any stiffness, except between 50pg/mL TGFβ treated and untreated fibroblasts at 8kPa, two-way ANOVA, simple column effect, Tukey post-test). Stiffness was associated with increased nuclear MRTF in all treatment conditions (p<0.0001 for all groups, ANOVA - Test for trends); additionally, treatment with TGFβ or TGFβ and Y-27632 did not produce consistent, statistically significant alterations in MRTF nuclear localization. All scale bars are 18μm.

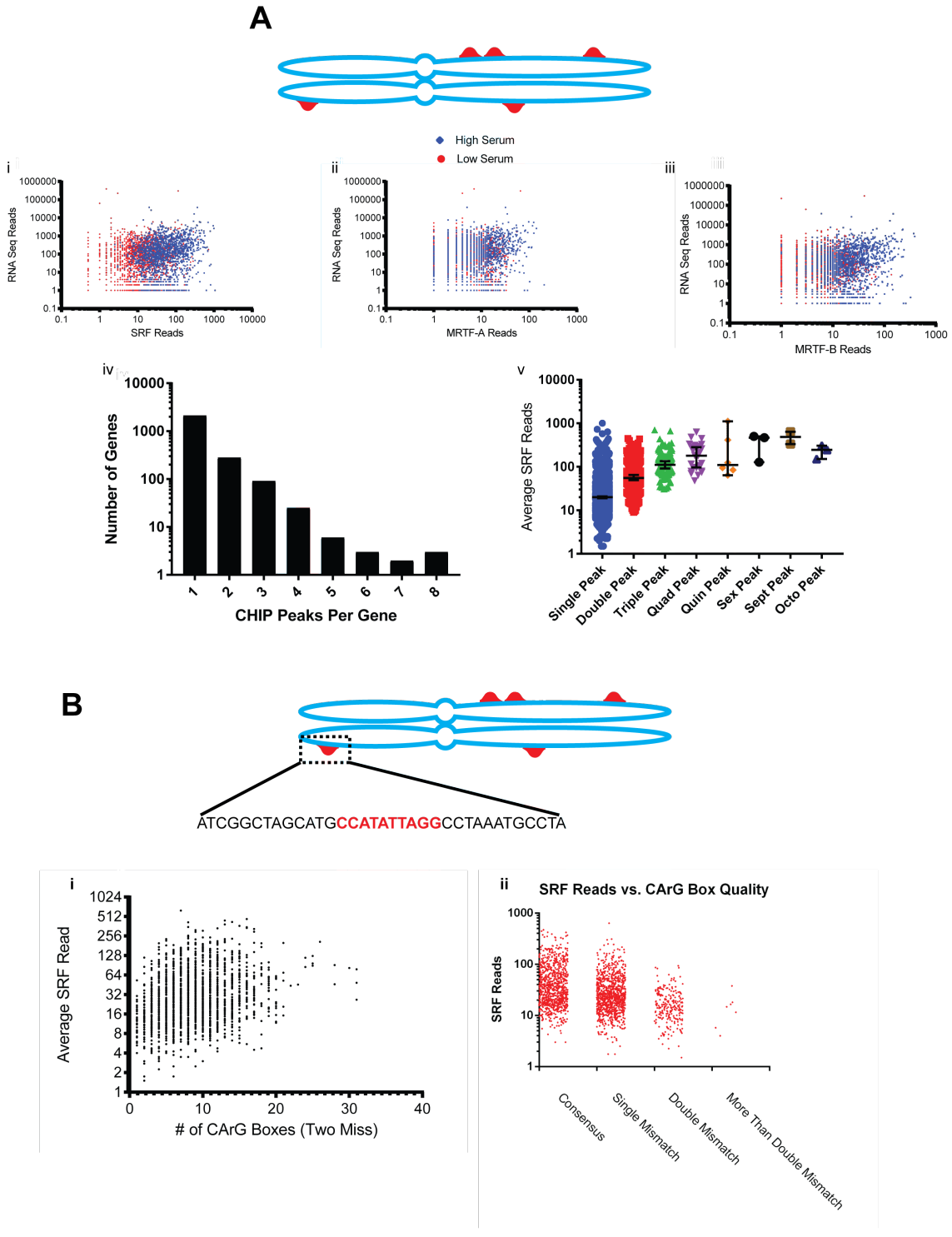

Figure 4.2: Caption continued on next page.

Figure 4.2: **CHIP-peak and Sequence Based Characterization of the Endogenous Murine CArGome** A, Summary of CHIP-peak/gene level data from Esnault *et al.* (2014) motivating the potential for SRF-MRTF based stiffness-driven transgenes. Panel i-iii) Correlation plots of SRF (i), MRTF-A (ii), and MRTF-B (iii) occupancy at a given CHIP-seq peak and the RNA reads associated with the annotated gene(s) of that peak in low serum (0.2%) and high serum (15%), cultured fibroblasts. There was a statistically significant correlation between SRF and RNA reads (r=0.1361 and r=0.1940, $p<0.0001$ for low and high serum, respectively, Pearson's correlation), MRTF-A and RNA reads (r=0.08515 and r=0.1953 with p=0.0004 and $p<0.0001$ for low and high serum, respectively, Pearson's correlation) and MRTF-B (r=0.1085 and r=0.2172, $p<0.0001$ for low and high serum, respectively, Pearson's correlation). Panel iv) Frequency distribution of SRF peaks against annotated genes demonstrated that $\approx 95\%$ of all endogenous genes were associated with two or fewer independent SRF peaks. Panel v) Correlation between the number of SRF peaks associated with a given gene and the occupancy of SRF at those particular loci demonstrated that increasing numbers of independent SRF peaks statistically increased the relative abundance of SRF occupancy at a given gene (r=0.4901, $p<0.0001$, Pearson's correlation). B, Individual CArG box identification and characterization by number and quality in Esnault *et al.* (2014) CHIP-seq SRF peaks. Panel i) Frequency distribution of individual CArG elements (up to double mismatch CArG boxes were analyzed) demonstrated that the average number of CArG box elements per SRF peak was 8 ± 4, with some SRF peaks containing over 30 individual CArG boxes. There was a statistically significant correlation between CArG box number in a CHIP-seq peak and SRF residency at that peak averaged across serum conditions (r=0.222, $p<0.0001$, Pearson's correlation). Panel ii) Decreasing quality, as indicated by number of mismatches from the canonical CArG box sequence, of the highest quality CArG box in a given SRF peak was significantly inversely correlated with occupancy of SRF in that CHIP-seq peak (r=-0.2850, $p<0.0001$, Pearson's correlation) . Collectively, the annotation of CArG box number and characterization of box quality up to two mismatches (and beyond) described the thermodynamic architecture of the murine CArGome as only 7 SRF CHIP peaks lack at least a double mismatch CArG box.

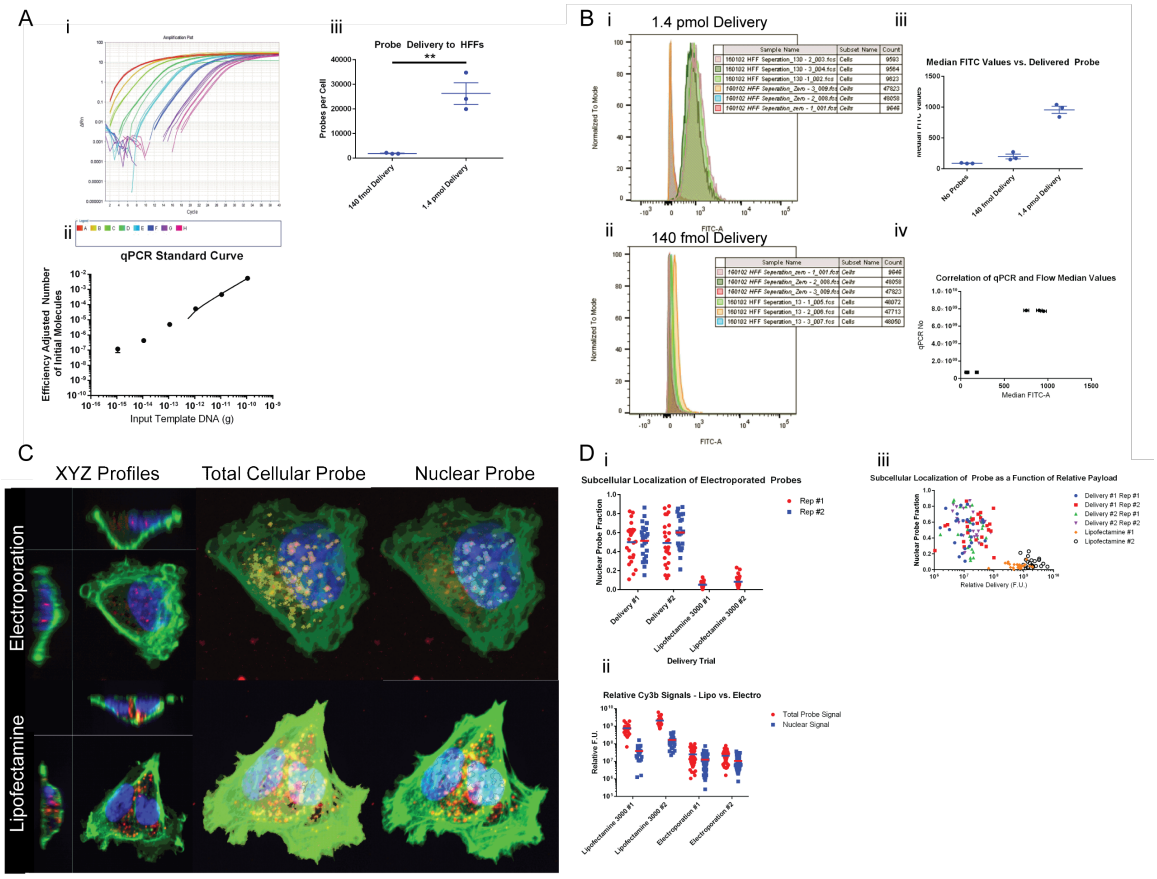

Figure 4.3: Caption continued on next page.

Figure 4.3: **Characterization of the Delivery of CArG Probes by Electroporation and Lipofectamine by Absolute qPCR, Flow Cytometry, and Confocal Microscopy** A, picomole loads of CArG sinks delivered CArG sink copies per cell on the order of magnitude of the endogenous CArGome. Panel i) Representative qPCR amplification traces for the quantification of probe delivery to cells. Panel ii) Standard curve of known input CArG box load demonstrating the linearity of the measurement over multiple orders of magnitude (r^2=0.9975). Panel iii) Delivery of 1.4 pmol of an 120 bp double stranded CArG sink by electroporation to fibroblasts delivered $\approx$ 25,000 CArG sinks per cell, which is slightly greater than the $\approx$ 20,000 CArG boxes present in the endogenous murine CArGome. There was a statistically significant increase in CArG box delivery per cell with increasing input CArG box load (p = 0.0053, Student's T-Test). B, relative quantification of CArG boxes probes by flow cytometry correlated strongly with qPCR derived results with single cell resolution. Panels i and ii) Normalized flow histograms showed a single population shift in the median fluorescent signal per cell in fibroblasts electroporated with 1.4 pmol (Panel i) or 140 fmol (Panel ii) of labeled CArG sinks. Panel iii) Quantification of the shift in per-cell median fluorescence as a function of CArG box load demonstrated a statistically significant increase in fluorescence with increasing CArG box load ($p<0.0001$, ANOVA - Test for Trends). Panel iv) Flow cytometry and qPCR quantification of delivered CArG probes were significantly correlated (r = 0.9823 with p = 0.0005, Pearson's correlation). C, representative confocal micrographs demonstrating the subcellular compartmentalization of CArG sinks delivered by electroporation (top row) or Lipofectamine3000 (bottom row). The XY/XZ/YZ profile are shown in the right column, while the middle and left columns highlight the cellularly constrained probe and the nuclearly localized probe, respectively. D, quantification of subcellular delivery of CArG probes by electroporation or Lipofectamine3000. Panel i) Relative nuclear delivery of CArG probes demonstrated that electroporation was more efficient in delivering nuclearly localized probes than Lipofectamine ($p<0.0001$, Student's T-Test). Panel ii) Lipofectamine delivered greater abundances of cellular and nuclear probes ($p<0.0001$ for both total and nuclear probes, Student's T-test) than electroporation based on relative quantification of probe fluorescent signal. Panel iii) Scatter plot of nuclear probe signal versus total probe signal per cell demonstrated greater efficiency of electroporation based delivery of CArG probes relative to Lipofectamine.

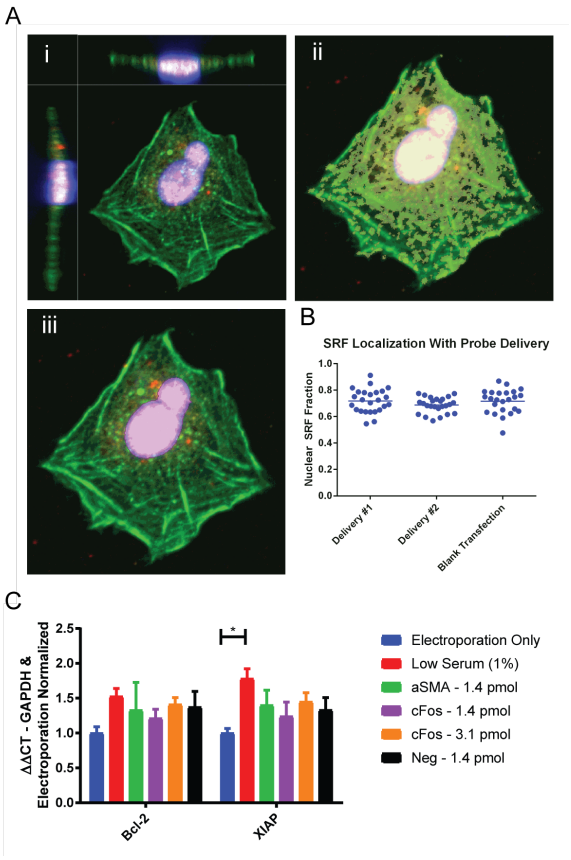

Figure 4.4: **CArG Sink Delivery by Electroporation Did Not Alter the Subcellular Localization of SRF Nor Antagonized SRF Transcripts Relevant to Pulmonary Fibrosis** A, Representative confocal microscopy images demonstrating the subcellular localization of SRF after delivery of a 120 bp double stranded, linear probe containing a CArG box based on the murine cFOS promoter. Panel i) Confocal images presented in XY/YZ/XZ planes. Panel ii) Algorithmic detection of SRF based masked by the actin cytoskeleton and nucleus. Panel iii) Algorithmic detection of nuclearly restricted SRF using a nuclear mask. B, Quantification of SRF localization following 1.4pmol of a 120 bp cFOS CArG probe relative to blank electroporation. There was no statistical difference or trend between the localization of SRF in cells with and without CArG probe delivery ($p = 0.98$ for Delivery 1 vs. Blank and $p = 0.3523$ for Delivery 2 vs. Blank, ANOVA with Dunnett's post test). C, CArG sinks of varying dose and CArG box quality did not significantly vary the transcription of disease relevant genes relative to "anti-CArG" (CArG boxes with a purine/pyrimidines substitution) sinks. cFos CArG boxes were 120 bp double stranded, linear probe containing a CArG box based on the murine cFOS promoter, while αSMA probes were analogously based on the αSMA promoter, centered on the CArG-B box. All electroporated conditions were plated in 15% serum. There was a statically significant decrease in XIAP transcripts in electroporation only control fibroblasts relative to fibroblasts in 1% serum ($p = 0.0364$, ANOVA with Dunnett's post-test), indicating that electroporation itself may have a confounding effect on SRF transcription at short time-scales.

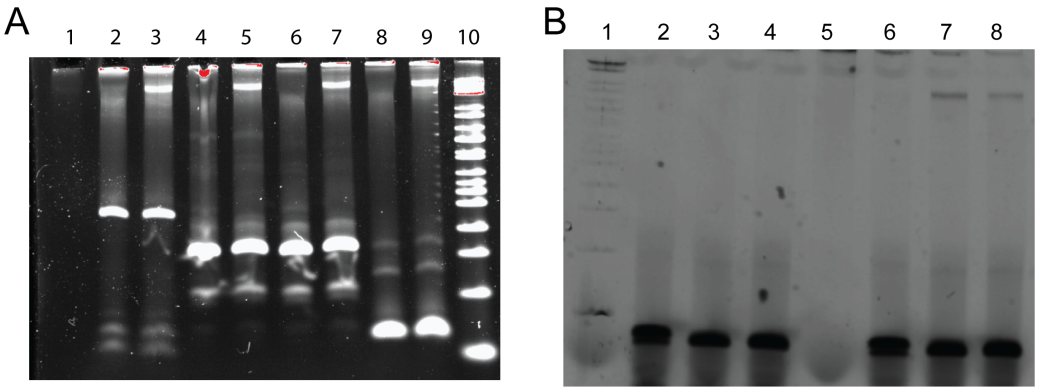

Figure 4.5: **Synthetic or Naturally-Derived Probe Shift in EMSA was Dependent on CArG Integrity and SRF** A, Synthetic and naturally-derived Cy3b-labelled CArG box probes only demonstrated a mobility shift in the presence of HEK lystate enriched for SRF. Lanes 2, 4, 6, and 8 did not contain any HEK lysate while lanes 3, 5, 7, and 9 contained HFFs transfected with pCN-SRF. Lanes 2 and 3 use a $\approx$ 430 bp double stranded, linear sequence containing 16 CArG boxes designed synthetically. Lanes 4 and 5 contained a 300bp double stranded, linear sequence containing CArG boxes from the murine cFOS promoter, centered on the CArG box, while lanes 6 and 7 contained analogously constructed probes centered on the αSMA CArG-B box. Lanes 8 and 9 contained a 120 bp double stranded, linear sequence containing the CArG box from the cFOS promoter, centered on the CArG box. Lane 1 was blank while Lane 10 was the DNA ladder. Gel shifts were observed with all synthetic and naturally-derived probes, at all probe lengths between $\approx$ 100-400 bp and with canonical and single mis-match CArG elements. No multiple binding events were detected. B, Probe shift was specific to the integrity of the probe's CArG box. Lanes 2-4 did not contain 2μg recombinant human SRF while lanes 5-8 did. Lanes 2 and 6 contained an 120 bp double stranded, linear "anti-CArG" probe wherein the purines and pyrimidines from the murine cFOS promoter's CArG box have been swapped. The surround sequences remained unmodified. Lanes 3 and 7 contained a 120 bp double stranded, linear CArG probe based on the murine αSMA promoter and centered on the CArG-B box. Lanes 4 and 8 contained a 120 bp double stranded, linear CArG probe based on the murine cFOS promoter and centered on its CArG box. Lane 5 contained SRF alone and Lane 1 was the DNA ladder. These results demonstrated the specificity of the gel-shift response to the integrity of the probe's CArG box.

CHAPTER 5
CONCLUSION

This thesis has explored the ability of genetics and nucleic acids to intervene and understand mechanotransduction and its pathologic consequences in pulmonary fibrosis. These investigations follow the path of information from the surface of cells, through the mechanotranductory machinery of the cells, and finally in the genome itself. Each chapter has summarized the implication of my findings with a focus on the state of the literature most relevant to that particular project, and I have proposed future work specific to each of those projects there. Here, I present interesting intersections between each of the projects and explore their implications for proposed future work. Finally, I have summarized the state of each project at the time of this thesis.

5.1 Future Work Inspired by Connections Between Chapters

5.1.1 Therapeutic Expression of C-Terminal LEMD3 Fragment by mRNA

In Chapter 3, I conclude by hypothesizing that C-terminal fragments of LEMD3 would be of complementary clinical use to existing pulmonary fibrosis medical management, specifically pirfenidone. This complementarity is motivated by the observations that pirfenidone limits TGFβ synthesis and matrix deposition [127, 126] while LEMD3 de-sensitizes cells to TGFβ signaling in a stiffness-dependent fashion as shown in Chapter 3. How best to achieve the therapeutic translation of LEMD3 as an intracellular protein therapy remains an open question. Literature from Chapter 2 reviews and highlights the challenges of delivering protein therapy to the lung, specifically in achieving delivery formulations sufficient to reach the full extent of the airspace [110] and highlights engineering strategies to maintain therapeutic concentrations of the delivered cargo. [67, 64, 65, 68, 66, 69, 70] The use

of mRNA to delivery pro-therapeutic transcripts of H5 and Thy-1 constructs in Chapter 2 provides a novel approach to solve this problem. The delivery of the C-terminal fragment as mRNA should be modularly adaptable with the techniques characterized and developed in Chapter 2 since these mRNA cargoes are seemingly equivalent in terms of length/size and composition. Future work in this area should focus directly on the therapeutic efficacy of C-terminal fragments of LEMD3 in bleomycin models of fibrosis.

5.1.2 Understanding Mechanotransductive Feedback After Thy-1 or H5 Expression with MRTF Translocation Models

In Chapter 4, time-variant model of MRTF translocation to the nucleus as a function of substrate stiffness were expanded to include the short-term effects of TGFβ signaling, connecting the work between Chapters 3 and 4. These models should be extended to incorporate the mechanical effects of cell-ECM interactions through integrin modulation motivated in Chapter 2. Thy-1, in particular, may be an especially compelling and important node in these models since Thy-1 is an endogenous protein, whose loss is associated with the development of fibrosis in humans [72, 80], and whose mechanism of action converges on the cytoskeleton through focal adhesion and Rho kinase modulation. [78, 79, 81, 30] Moreover, the ability to modulate Thy-1 expression, summarized in the conclusion of Chapter 2, would provide important tools to test this model and its conclusions. The development of a more complete model of MRTF translocation could be especially beneficial in its eventual application to fibrosis where the mechanical machinery of the cell is perturbed, specifically through loss of Thy-1. [73, 72]

5.1.3 mRNA-Based Stiffness Sensors

The use of promoter elements to drive stiffness expression has been demonstrated in a proof-of-concept fashion by others using a YAP/TAZ/TEAD box system in a model of metastatic disease in the lung. [231] In Chapter 4, I've characterized the genomic architec-

ture and tools necessary to permit rational design of similar promoter elements based on MRTF/SRF biology. Interestingly, the general biological system of control for both transcription factor systems is the same - stiffness, through the actin cytoskeleton, regulates the sub-cellular compartmentalization of the activating transcription factor. [192, 249, 250, 191, 233, 241, 242, 235] A novel synthesis of the approaches from Chapters 2 and 4 would be to develop mRNA-based stiffness sensors, which could potentially have complementary stiffness-sensitivity relative to DNA-based stiffness sensors. I hypothesize that therapeutic mRNA conjugated to the RPEL domains of MRTF (MRTF's actin-sensitive nuclear localization domains) would be localized to the nucleus in an actin-polymerization, stiffness-dependent fashion. Since mRNA's translational potential is controlled by its access to ribosomes outside the nucleus, this translocation would theoretically be an inactivating, rather than potentiating event. The consequences of this switch from stiffness-activation to stiffness-quiescence would be an ability to drive stiffness-dependent translation *specifically on soft substrates*, which from the model of MRTF translocation developed in Chapter 4, may be difficult to uniquely target using DNA-based approaches. Additionally the use of mRNA based therapeutics may lower the regulatory burden of future clinical translation since mRNA-based therapies do not have the same safety concerns as DNA based therapeutics. [55, 54] The RPEL domains and their interaction with actin have been previously crystallized [236], giving strong *a priori* guidance as to how to design the necessary protein domains that would control this translocation. Moreover, biologically-inspired mRNA-protein conjugation strategies through the MS2 phage coat protein have been previously developed and characterized. [293] Future work in this area should focus on a proof-of-concept demonstration of this mechanism and the ability to titrate the translocation of mRNA by modulating the copy number of the conjugated RPEL domains and in exploring point mutations in the nuclear localization and actin binding domains of RPEL.

5.2 Current State of Projects

Considerable work has occurred in each Chapter - the state of each project is briefly summarized below:

- Chapter 2: Contextual Antagonism of αVβ3 Integrin with a FN-Strain Specific scFv, H5: *In vitro* work demonstrating the surface expression and efficacy of the GPI and CD8 linked H5 mRNA constructs is complete. Colocalization with αVβ3 by PLA and confocal microscopy is underway as is a parallel experiment analyzing these clustering events using dSTORM super-resolution microscopy. Additionally, the modulation of focal adhesion number and location relative to cell centroid by these H5 constructs has been experimentally completed and the PLA images are being analyzed. The effects of these linkers on the global phosphorylation state of key focal adhesion molecules (FAK and the Src family of kinases) are complete. Focal adhesion pulldowns to assay specific competition between H5 and αVβ3 as well as fyn localization are underway. I have performed morphological mechanotransduction experiments to characterize the net effect of H5 expression to fibroblasts' mechanosensitivity. These experiments have been completed.

  Parallel experiments to validate the expression of a positive control mRNA expressing Thy-1 are also underway. The use of PLA to validate Thy-1's association with αVβ3 have been completed and are in analysis. Additionally focal adhesion western blotting experiments similar to those with H5 constructs have also been performed and are in analysis.

  In vivo, I have validated the expression of these constructs out to day 8 in healthy mice and developed the techniques and mRNA constructs necessary for rapid assessment of mRNA expression in a bleomycin model of fibrosis.

- Chapter 3: Matrix-Stiffness Regulation of Transforming Growth Factor-β by Inner Nuclear Membrane Protein 3: This project has been submitted to the *Journal of*

Biological Chemistry and has come back from review twice. After our first round of review, we were left with only one reviewer with concerns, which we have addressed experimentally. These experiments have been conducted but not yet analyzed. After analysis, the paper will be re-written and re-submitted.

- Chapter 4: Tools to Dissect the Thermodynamic Landscape of the Murine CArGome: The characterization of the transfer function between substrate stiffness and MRTF is complete. Modeling the evolution of the stiffness response through MRTF with the Saucerman Group at UVA is underway with the first generation of the model completed and in preparation for a manuscript. The characterization of the CArGome architecturally is complete. Experimentally, we are ready to conduct NGS SpecSeq experiments to characterize the CArG-SRF interactions and further optimization to assay CArG-SRF-MRTF complexes are planned for work at UVA. A second generation of CArG sinks with NLS and peptide nucleic acids have been planned and their efficacy, in terms of competing with the endogenous genome for SRF, needs to be assayed.

Appendices

APPENDIX A

CHAPTER 2: SEQUENCES FOR THERAPUTIC MRNA

These sequence contains the ORF for each of the mRNA used in Chapter 2. The V5 tag or nanoLuc enzymes attached to each mRNA are separately annotated. The protein translations are provided. Each sequence is housed in a pMA-7 vector (ThermoFischer Scientific, Waltham, MA).

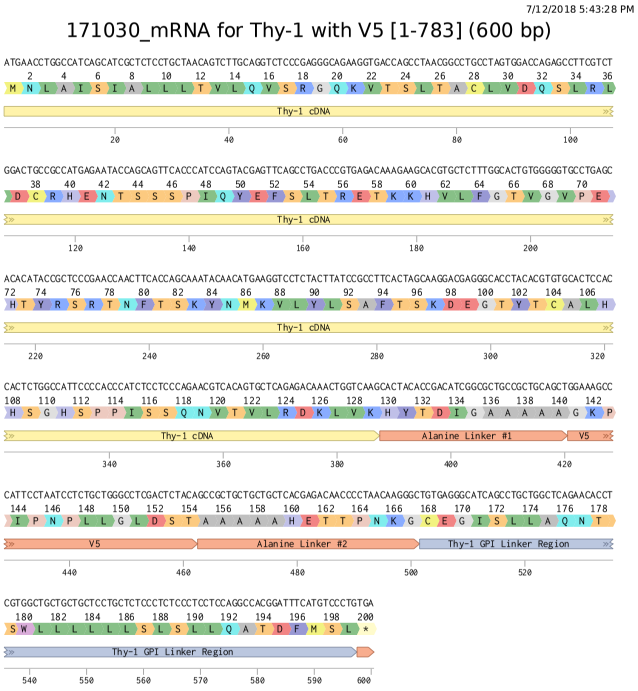

Figure A.1: **Thy-1 with C-terminal V5 epitope Tag**

Figure A.2: **Thy-1 with C-terminal nanoLuc Enzyme**

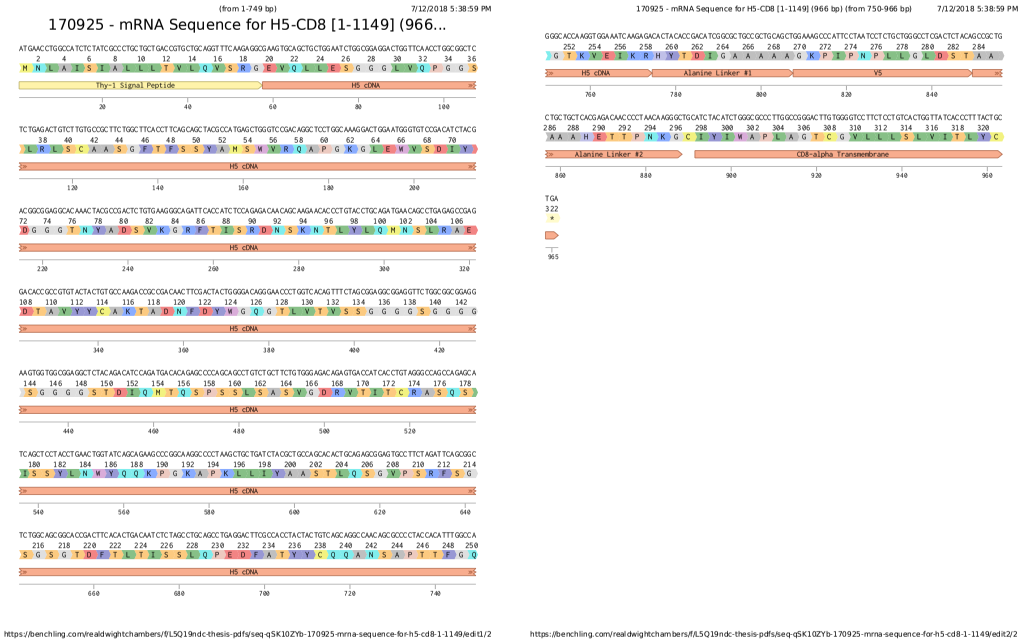

Figure A.3: **H5 scFv with C-terminal V5 epitope tag and truncated CD8 transmembrane domain**

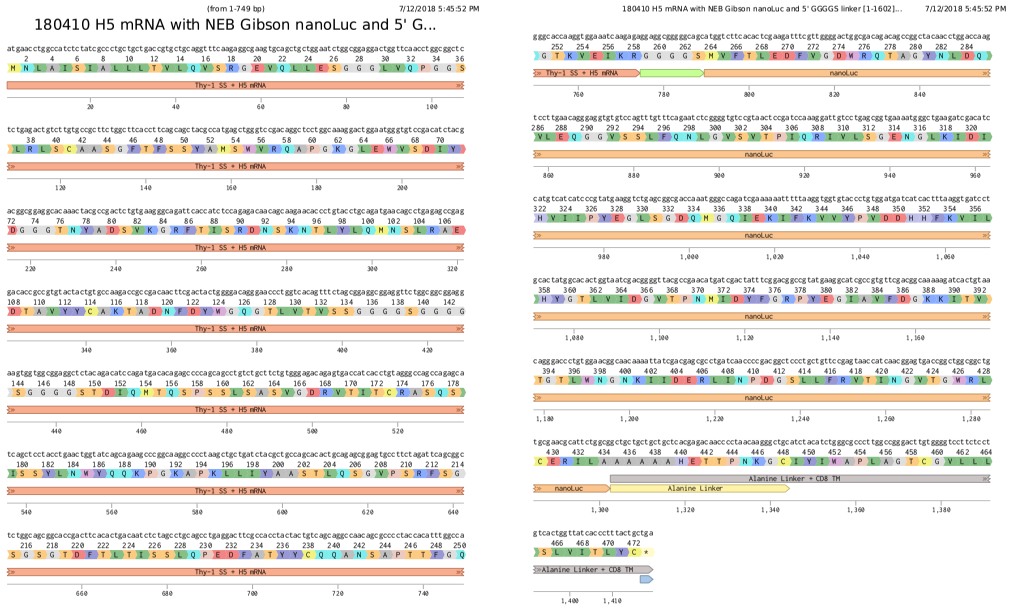

Figure A.4: **H5 scFv with C-terminal nanoLuc enzyme and truncated CD8 transmembrane domain**

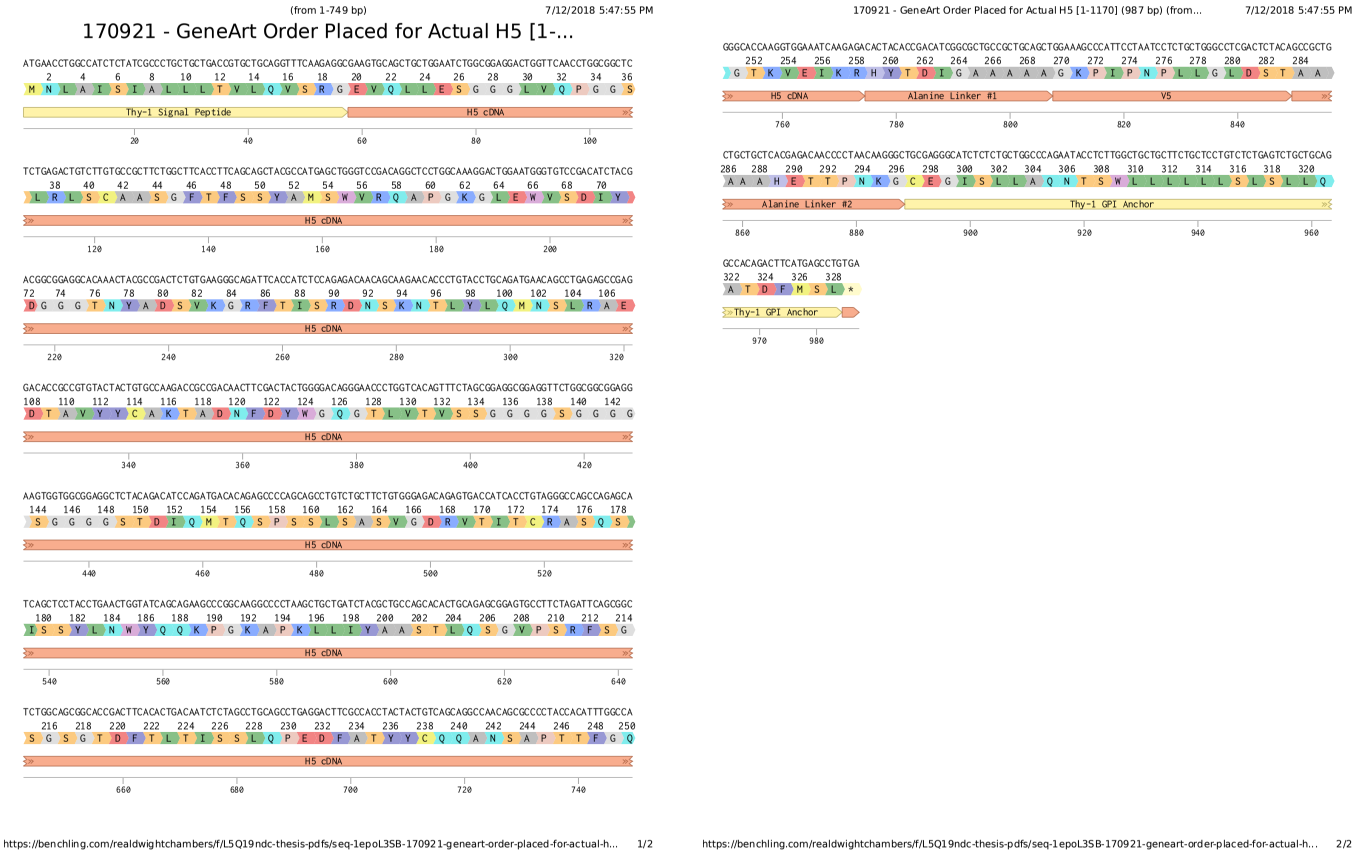

Figure A.5: **H5 scFv with C-terminal V5 epitope tag and Thy-1-based GPI linker**

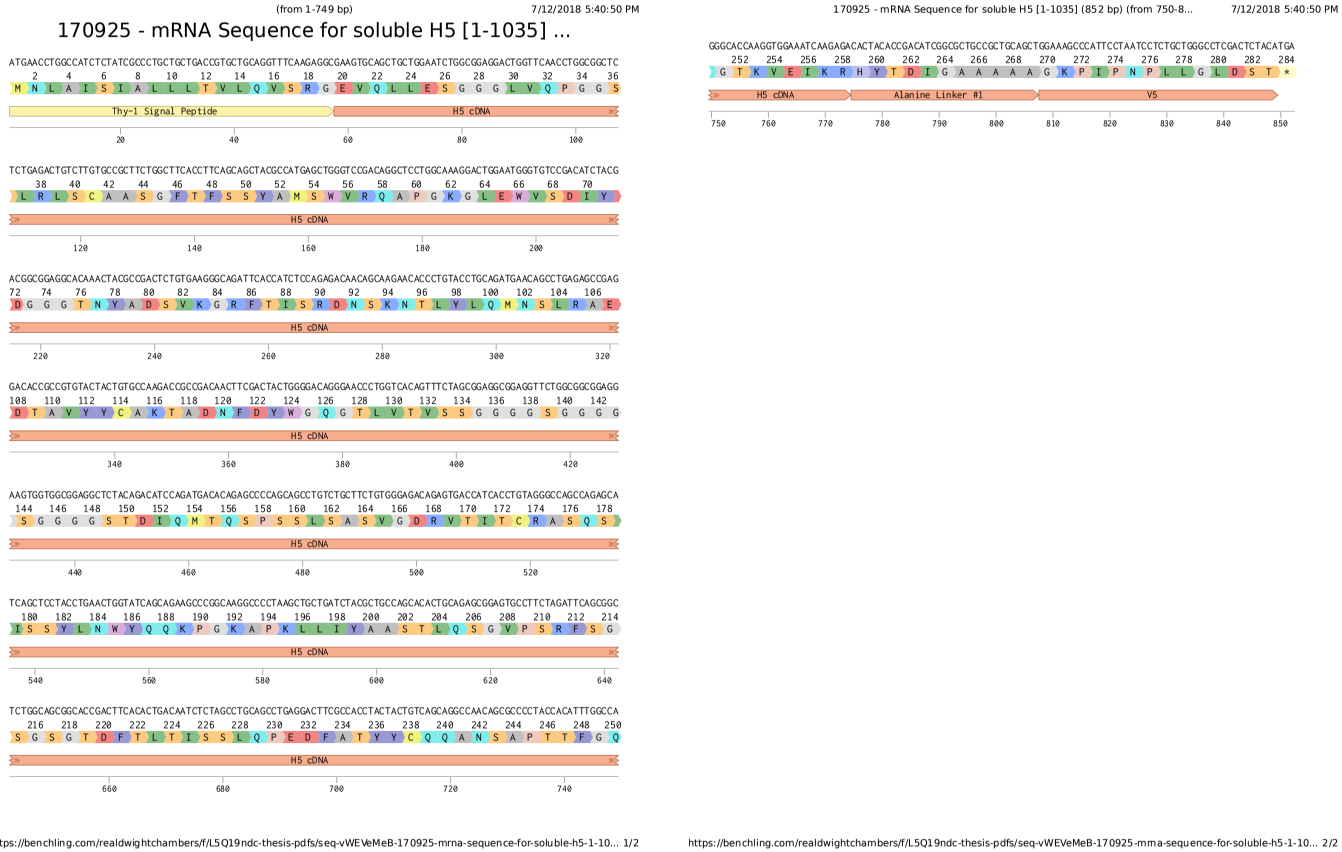

Figure A.6: **Soluble H5 scFv with C-terminal V5 epitope tag**

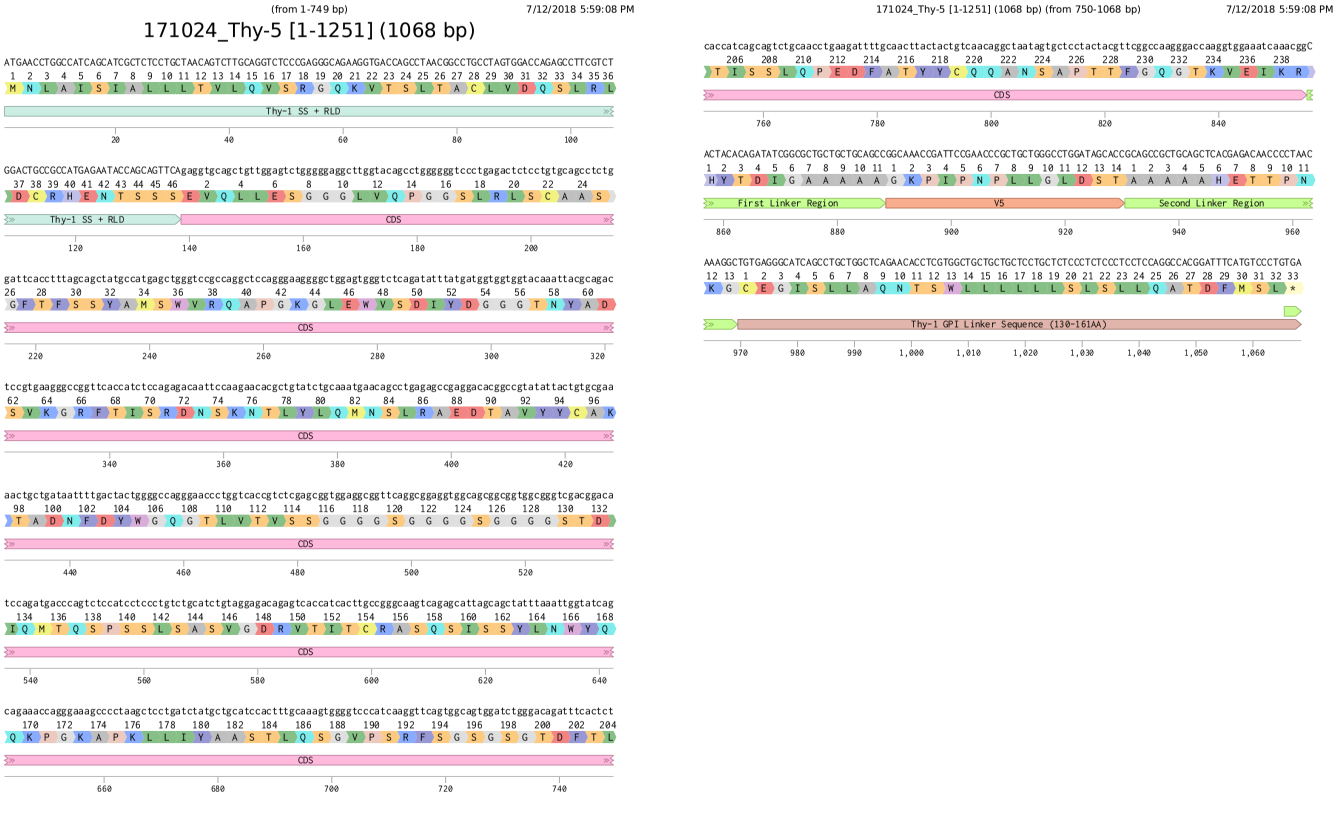

Figure A.7: **"Thy-5": H5 scFv with N-Terminal Thy-1 RLE domain and C-terminal V5 epitope tag with Thy-1 GPI Linker**

APPENDIX B

CHAPTER 4: SEQUENCES FOR CARG BOX PROBES

These are the sequences for the synthetic and naturally derived CArG box element used in Chapter 4. Each CArG box element present is annotated, though other features useful in cloning are also annotated.

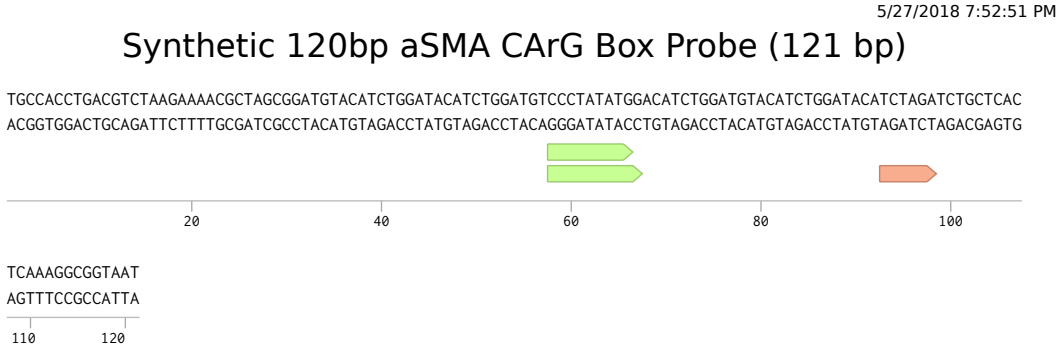

Figure B.1: **Biobrick Derived 120bp CArG Box Probe with a single αSMA-derived CArG Element**

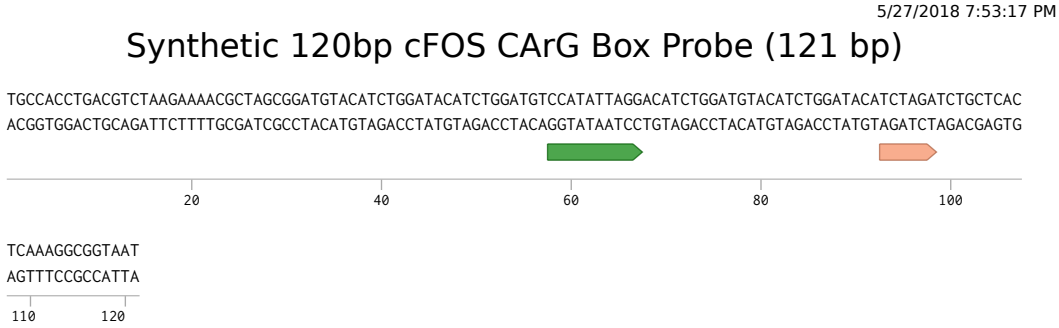

Figure B.2: **Biobrick Derived 120bp CArG Box Probe with a single cFOS-derived CArG Element**

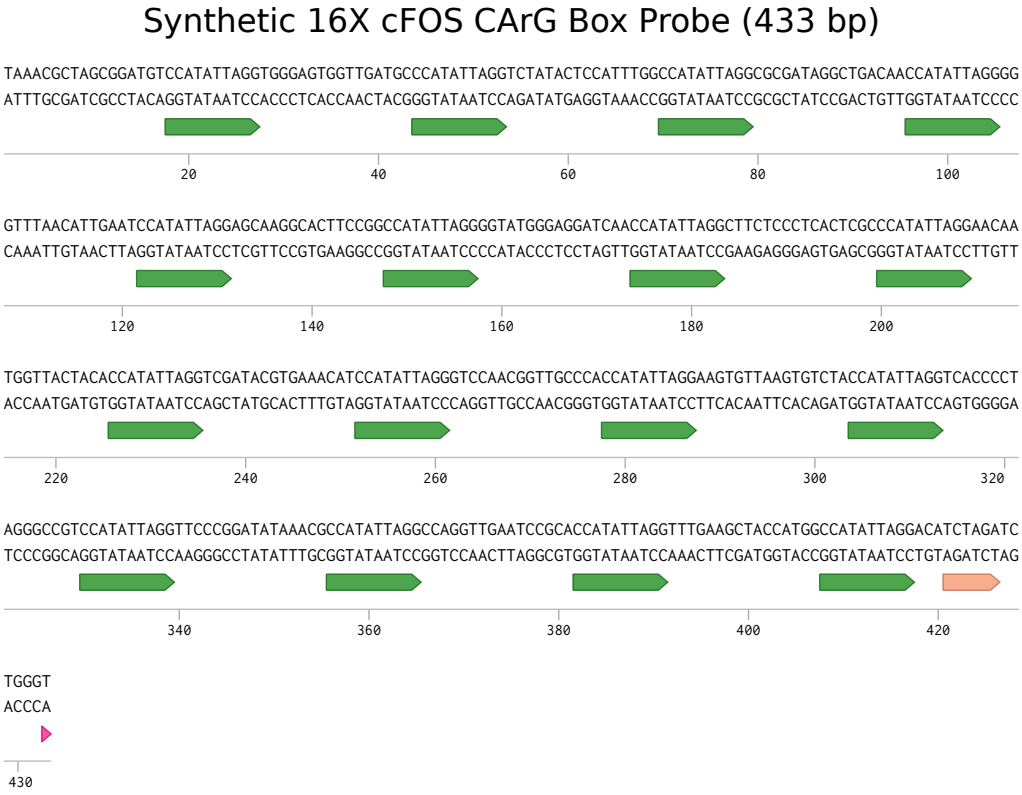

Figure B.3: **Synthetically Designed 430bp CArG Box Probe with 16 repeats of a cFOS-derived CArG Element. These interstitial sequences were generated randomly but screened for CArG boxes.**

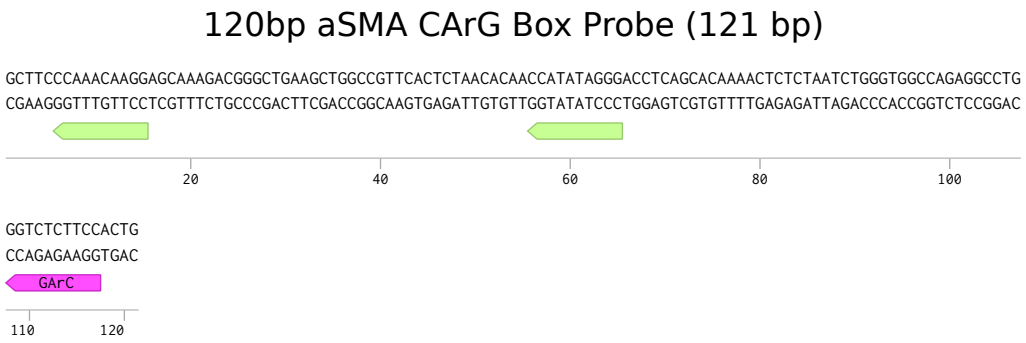

Figure B.4: **120bp CArG Box Probe from the murine αSMA promoter, centered on the CArG-B box**

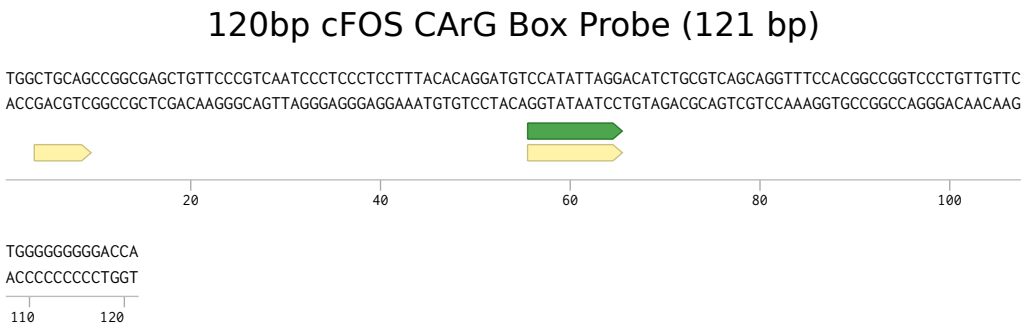

Figure B.5: **120bp CArG Box Probe from the murine cFOS promoter, centered on the CArG box**

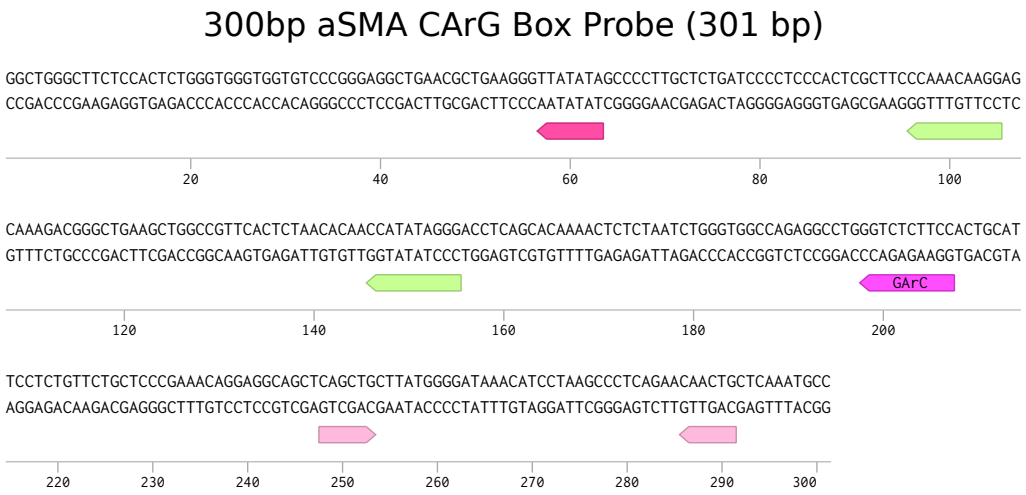

Figure B.6: **300bp CArG Box Probe from the murine αSMA promoter, centered on the CArG-B box**

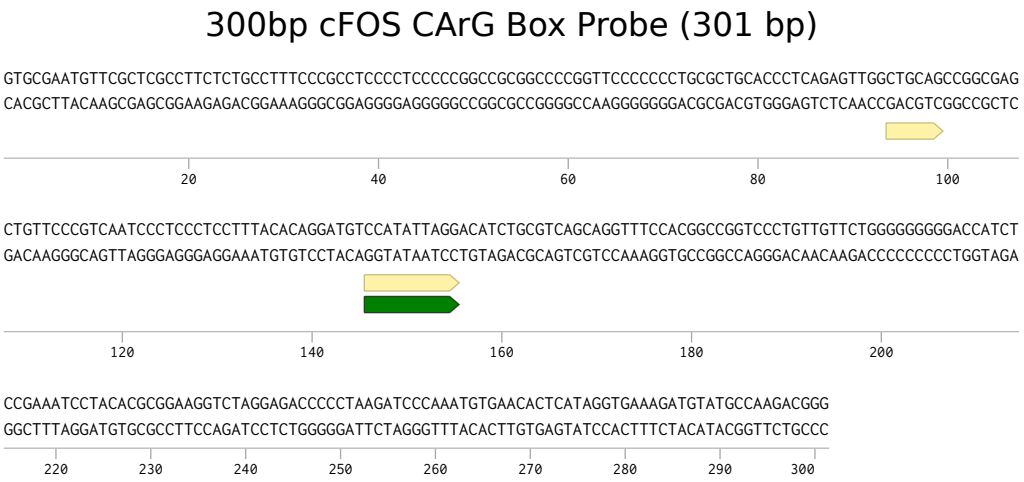

Figure B.7: **300bp CArG Box Probe from the murine cFOS promoter, centered on the CArG box**

REFERENCES

[1] "American thoracic society. idiopathic pulmonary fibrosis: Diagnosis and treatment. international consensus statement. american thoracic society (ats), and the european respiratory society (ers)," *Am J Respir Crit Care Med*, vol. 161, no. 2 Pt 1, pp. 646–64, 2000.

[2] A. L. Olson, J. J. Swigris, D. C. Lezotte, J. M. Norris, C. G. Wilson, and K. K. Brown, "Mortality from pulmonary fibrosis increased in the united states from 1992 to 2003," *Am J Respir Crit Care Med*, vol. 176, no. 3, pp. 277–84, 2007.

[3] B. I. National Heart Lung. (2013).

[4] A. J. Booth, R. Hadley, A. M. Cornett, A. A. Dreffs, S. A. Matthes, J. L. Tsui, K. Weiss, J. C. Horowitz, V. F. Fiore, T. H. Barker, B. B. Moore, F. J. Martinez, L. E. Niklason, and E. S. White, "Acellular normal and fibrotic human lung matrices as a culture system for in vitro investigation," *American Journal of Respiratory and Critical Care Medicine*, vol. 186, no. 9, pp. 866–876, 2012, PMID: 22936357. eprint: https://doi.org/10.1164/rccm.201204-0754OC.

[5] D. Lutz, A. Gazdhar, E. Lopez-Rodriguez, C. Ruppert, P. Mahavadi, A. Gunther, W. Klepetko, J. H. Bates, B. Smith, T. Geiser, M. Ochs, and L. Knudsen, "Alveolar derecruitment and collapse induration as crucial mechanisms in lung injury and fibrosis," *Am J Respir Cell Mol Biol*, vol. 52, no. 2, pp. 232–43, 2015.

[6] S. S. Kaushik, M. S. Freeman, S. W. Yoon, M. G. Liljeroth, J. V. Stiles, J. E. Roos, W. Foster, C. R. Rackley, H. P. McAdams, and B. Driehuys, "Measuring diffusion limitation with a perfusion-limited gas–hyperpolarized 129xe gas-transfer spectroscopy in patients with idiopathic pulmonary fibrosis," *J Appl Physiol (1985)*, vol. 117, no. 6, pp. 577–85, 2014.

[7] N. Ahluwalia, B. S. Shea, and A. M. Tager, "New therapeutic targets in idiopathic pulmonary fibrosis. aiming to rein in runaway wound-healing responses," *Am J Respir Crit Care Med*, vol. 190, no. 8, pp. 867–78, 2014.

[8] P. W. Noble, C. Albera, W. Z. Bradford, U. Costabel, M. K. Glassberg, D. Kardatzke, J. King T. E., L. Lancaster, S. A. Sahn, J. Szwarcberg, D. Valeyre, R. M. du Bois, and C. S. Group, "Pirfenidone in patients with idiopathic pulmonary fibrosis (capacity): Two randomised trials," *Lancet*, vol. 377, no. 9779, pp. 1760–9, 2011.

[9] L. Richeldi, R. M. du Bois, G. Raghu, A. Azuma, K. K. Brown, U. Costabel, V. Cottin, K. R. Flaherty, D. M. Hansell, Y. Inoue, D. S. Kim, M. Kolb, A. G. Nichol-

son, P. W. Noble, M. Selman, H. Taniguchi, M. Brun, F. Le Maulf, M. Girard, S. Stowasser, R. Schlenker-Herceg, B. Disse, H. R. Collard, and I. T. Investigators, "Efficacy and safety of nintedanib in idiopathic pulmonary fibrosis," *N Engl J Med*, vol. 370, no. 22, pp. 2071–82, 2014.

[10] J. King T. E., W. Z. Bradford, S. Castro-Bernardini, E. A. Fagan, I. Glaspole, M. K. Glassberg, E. Gorina, P. M. Hopkins, D. Kardatzke, L. Lancaster, D. J. Lederer, S. D. Nathan, C. A. Pereira, S. A. Sahn, R. Sussman, J. J. Swigris, P. W. Noble, and A. S. Group, "A phase 3 trial of pirfenidone in patients with idiopathic pulmonary fibrosis," *N Engl J Med*, vol. 370, no. 22, pp. 2083–92, 2014.

[11] D. J. Lederer, W. Z. Bradford, E. A. Fagan, I. Glaspole, M. K. Glassberg, K. F. Glasscock, D. Kardatzke, J. King T. E., L. H. Lancaster, S. D. Nathan, C. A. Pereira, S. A. Sahn, J. J. Swigris, and P. W. Noble, "Sensitivity analyses of the change in fvc in a phase 3 trial of pirfenidone for idiopathic pulmonary fibrosis," *Chest*, vol. 148, no. 1, pp. 196–201, 2015.

[12] F. Liu, J. D. Mih, B. S. Shea, A. T. Kho, A. S. Sharif, A. M. Tager, and D. J. Tschumperlin, "Feedback amplification of fibrosis through matrix stiffening and cox-2 suppression," *J Cell Biol*, vol. 190, no. 4, pp. 693–706, 2010.

[13] P. J. Wipff, D. B. Rifkin, J. J. Meister, and B. Hinz, "Myofibroblast contraction activates latent tgf-beta1 from the extracellular matrix," *J Cell Biol*, vol. 179, no. 6, pp. 1311–23, 2007.

[14] X. Huang, N. Yang, V. F. Fiore, T. H. Barker, Y. Sun, S. W. Morris, Q. Ding, V. J. Thannickal, and Y. Zhou, "Matrix stiffness-induced myofibroblast differentiation is mediated by intrinsic mechanotransduction," *Am J Respir Cell Mol Biol*, vol. 47, no. 3, pp. 340–8, 2012.

[15] F. Liu, D. Lagares, K. M. Choi, L. Stopfer, A. Marinkovic, V. Vrbanac, C. K. Probst, S. E. Hiemer, T. H. Sisson, J. C. Horowitz, I. O. Rosas, L. E. Fredenburgh, C. Feghali-Bostwick, X. Varelas, A. M. Tager, and D. J. Tschumperlin, "Mechanosignaling through yap and taz drives fibroblast activation and fibrosis," *Am J Physiol Lung Cell Mol Physiol*, vol. 308, no. 4, pp. L344–57, 2015.

[16] V. J. Thannickal, C. A. Henke, J. C. Horowitz, P. W. Noble, J. Roman, P. J. Sime, Y. Zhou, R. G. Wells, E. S. White, and D. J. Tschumperlin, "Matrix biology of idiopathic pulmonary fibrosis: A workshop report of the national heart, lung, and blood institute," *Am J Pathol*, vol. 184, no. 6, pp. 1643–51, 2014.

[17] ClinicalTrials.gov. (2011).

[18] Y. Shimizu, K. Dobashi, K. Iizuka, T. Horie, K. Suzuki, H. Tukagoshi, T. Nakazawa, Y. Nakazato, and M. Mori, "Contribution of small gtpase rho and its target protein

rock in a murine model of lung fibrosis," *Am J Respir Crit Care Med*, vol. 163, no. 1, pp. 210–7, 2001.

[19] Y. Zhou, X. Huang, L. Hecker, D. Kurundkar, A. Kurundkar, H. Liu, T. H. Jin, L. Desai, K. Bernard, and V. J. Thannickal, "Inhibition of mechanosensitive signaling in myofibroblasts ameliorates experimental pulmonary fibrosis," *J Clin Invest*, vol. 123, no. 3, pp. 1096–108, 2013.

[20] C. Jiang, H. Huang, J. Liu, Y. Wang, Z. Lu, and Z. Xu, "Fasudil, a rho-kinase inhibitor, attenuates bleomycin-induced pulmonary fibrosis in mice," *Int J Mol Sci*, vol. 13, no. 7, pp. 8293–307, 2012.

[21] T. H. Sisson, I. O. Ajayi, N. Subbotina, A. E. Dodi, E. S. Rodansky, L. N. Chibucos, K. K. Kim, V. G. Keshamouni, E. S. White, Y. Zhou, P. D. Higgins, S. D. Larsen, R. R. Neubig, and J. C. Horowitz, "Inhibition of myocardin-related transcription factor/serum response factor signaling decreases lung fibrosis and promotes mesenchymal cell apoptosis," *Am J Pathol*, 2015.

[22] M. Amano, M. Nakayama, and K. Kaibuchi, "Rho-kinase/rock: A key regulator of the cytoskeleton and cell polarity," *Cytoskeleton (Hoboken)*, vol. 67, no. 9, pp. 545–54, 2010.

[23] R. Pankov and K. M. Yamada, "Fibronectin at a glance," *J Cell Sci*, vol. 115, no. Pt 20, pp. 3861–3, 2002.

[24] J. A. McDonald, D. G. Kelley, and T. J. Broekelmann, "Role of fibronectin in collagen deposition: Fab' to the gelatin-binding domain of fibronectin inhibits both fibronectin and collagen organization in fibroblast extracellular matrix," *J Cell Biol*, vol. 92, no. 2, pp. 485–92, 1982.

[25] K. C. Meyer, "Pulmonary fibrosis, part i: Epidemiology, pathogenesis, and diagnosis," *Expert Rev Respir Med*, vol. 11, no. 5, pp. 343–359, 2017.

[26] A. Betensley, R. Sharif, and D. Karamichos, "A systematic review of the role of dysfunctional wound healing in the pathogenesis and treatment of idiopathic pulmonary fibrosis," *J Clin Med*, vol. 6, no. 1, 2016.

[27] S. O. Rahaman, L. M. Grove, S. Paruchuri, B. D. Southern, S. Abraham, K. A. Niese, R. G. Scheraga, S. Ghosh, C. K. Thodeti, D. X. Zhang, M. M. Moran, W. R. Schilling, D. J. Tschumperlin, and M. A. Olman, "Trpv4 mediates myofibroblast differentiation and pulmonary fibrosis in mice," *Journal of Clinical Investigation*, vol. 124, no. 12, pp. 5225–5238, 2014.

[28] J. Kach, N. Sandbo, N. Sethakorn, J. Williams, E. B. Reed, J. La, X. Y. Tian, S. D. Brain, K. Rajendran, R. Krishnan, A. I. Sperling, K. Birukov, and N. O. Dulin,

"Regulation of myofibroblast differentiation and bleomycin-induced pulmonary fibrosis by adrenomedullin," *American Journal of Physiology-Lung Cellular and Molecular Physiology*, vol. 304, no. 11, pp. L757–L764, 2013.

[29] L. Cao, J. Nicosia, J. Larouche, Y. Zhang, H. Bachman, A. C. Brown, L. Holmgren, and T. H. Barker, "Detection of an integrin-binding mechanoswitch within fibronectin during tissue formation and fibrosis," *ACS Nano*, vol. 11, no. 7, pp. 7110–7117, 2017.

[30] V. F. Fiore, P. W. Strane, A. V. Bryksin, E. S. White, J. S. Hagood, and T. H. Barker, "Conformational coupling of integrin and thy-1 regulates fyn priming and fibroblast mechanotransduction," *J Cell Biol*, vol. 211, no. 1, pp. 173–90, 2015.

[31] F. Klingberg, G. Chau, M. Walraven, S. Boo, A. Koehler, M. L. Chow, A. L. Olsen, M. Im, M. Lodyga, R. G. Wells, E. S. White, and B. Hinz, "The fibronectin ed-a domain enhances recruitment of latent tgf-beta-binding protein-1 to the fibroblast matrix," *J Cell Sci*, vol. 131, no. 5, 2018.

[32] S. Mukherjee, W. Sheng, R. Sun, and L. J. Janssen, "Ca(2+)/calmodulin-dependent protein kinase iibeta and iidelta mediate tgfbeta-induced transduction of fibronectin and collagen in human pulmonary fibroblasts," *Am J Physiol Lung Cell Mol Physiol*, vol. 312, no. 4, pp. L510–L519, 2017.

[33] E. E. Torr, C. R. Ngam, K. Bernau, B. Tomasini-Johansson, B. Acton, and N. Sandbo, "Myofibroblasts exhibit enhanced fibronectin assembly that is intrinsic to their contractile phenotype," *J Biol Chem*, vol. 290, no. 11, pp. 6951–61, 2015.

[34] A. P. Mould, J. A. Askari, S. Aota, K. M. Yamada, A. Irie, Y. Takada, H. J. Mardon, and M. J. Humphries, "Defining the topology of integrin alpha5beta1-fibronectin interactions using inhibitory anti-alpha5 and anti-beta1 monoclonal antibodies. evidence that the synergy sequence of fibronectin is recognized by the amino-terminal repeats of the alpha5 subunit," *J Biol Chem*, vol. 272, no. 28, pp. 17 283–92, 1997.

[35] H. J. Mardon and K. E. Grant, "The role of the ninth and tenth type iii domains of human fibronectin in cell adhesion," *FEBS Lett*, vol. 340, no. 3, pp. 197–201, 1994.

[36] M. Pierschbacher, E. G. Hayman, and E. Ruoslahti, "Synthetic peptide with cell attachment activity of fibronectin," *Proc Natl Acad Sci U S A*, vol. 80, no. 5, pp. 1224–7, 1983.

[37] M. D. Pierschbacher and E. Ruoslahti, "Cell attachment activity of fibronectin can be duplicated by small synthetic fragments of the molecule," *Nature*, vol. 309, no. 5963, pp. 30–3, 1984.

[38] A. Krammer, H. Lu, B. Isralewitz, K. Schulten, and V. Vogel, "Forced unfolding of the fibronectin type iii module reveals a tensile molecular recognition switch," *Proc Natl Acad Sci U S A*, vol. 96, no. 4, pp. 1351–6, 1999.

[39] G. Baneyx, L. Baugh, and V. Vogel, "Fibronectin extension and unfolding within cell matrix fibrils controlled by cytoskeletal tension," *Proc Natl Acad Sci U S A*, vol. 99, no. 8, pp. 5139–43, 2002.

[40] A. F. Oberhauser, C. Badilla-Fernandez, M. Carrion-Vazquez, and J. M. Fernandez, "The mechanical hierarchies of fibronectin observed with single-molecule afm," *J Mol Biol*, vol. 319, no. 2, pp. 433–47, 2002.

[41] J. C. Friedland, M. H. Lee, and D. Boettiger, "Mechanically activated integrin switch controls alpha5beta1 function," *Science*, vol. 323, no. 5914, pp. 642–4, 2009.

[42] A. C. Brown, J. A. Rowe, and T. H. Barker, "Guiding epithelial cell phenotypes with engineered integrin-specific recombinant fibronectin fragments," *Tissue Eng Part A*, vol. 17, no. 1-2, pp. 139–50, 2011.

[43] M. C. Markowski, A. C. Brown, and T. H. Barker, "Directing epithelial to mesenchymal transition through engineered microenvironments displaying orthogonal adhesive and mechanical cues," *J Biomed Mater Res A*, vol. 100, no. 8, pp. 2119–27, 2012.

[44] A. C. Brown, V. F. Fiore, T. A. Sulchek, and T. H. Barker, "Physical and chemical microenvironmental cues orthogonally control the degree and duration of fibrosis-associated epithelial-to-mesenchymal transitions," *J Pathol*, vol. 229, no. 1, pp. 25–35, 2013.

[45] D. C. Roy and D. C. Hocking, "Recombinant fibronectin matrix mimetics specify integrin adhesion and extracellular matrix assembly," *Tissue Eng Part A*, vol. 19, no. 3-4, pp. 558–70, 2013.

[46] A. M. Wan, E. M. Chandler, M. Madhavan, D. W. Infanger, C. K. Ober, D. Gourdon, G. G. Malliaras, and C. Fischbach, "Fibronectin conformation regulates the proangiogenic capability of tumor-associated adipogenic stromal cells," *Biochim Biophys Acta*, vol. 1830, no. 9, pp. 4314–20, 2013.

[47] B. G. Keselowsky, D. M. Collard, and A. J. Garcia, "Surface chemistry modulates focal adhesion composition and signaling through changes in integrin binding," *Biomaterials*, vol. 25, no. 28, pp. 5947–54, 2004.

[48] N. C. Henderson, T. D. Arnold, Y. Katamura, M. M. Giacomini, J. D. Rodriguez, J. H. McCarty, A. Pellicoro, E. Raschperger, C. Betsholtz, P. G. Ruminski, D. W.

Griggs, M. J. Prinsen, J. J. Maher, J. P. Iredale, A. Lacy-Hulbert, R. H. Adams, and D. Sheppard, "Targeting of alphav integrin identifies a core molecular pathway that regulates fibrosis in several organs," *Nat Med*, vol. 19, no. 12, pp. 1617–24, 2013.

[49] L. Cao, M. K. Zeller, V. F. Fiore, P. Strane, H. Bermudez, and T. H. Barker, "Phage-based molecular probes that discriminate force-induced structural states of fibronectin in vivo," *Proc Natl Acad Sci U S A*, vol. 109, no. 19, pp. 7251–6, 2012.

[50] M. S. Kormann, G. Hasenpusch, M. K. Aneja, G. Nica, A. W. Flemmer, S. Herber-Jonat, M. Huppmann, L. E. Mays, M. Illenyi, A. Schams, M. Griese, I. Bittmann, R. Handgretinger, D. Hartl, J. Rosenecker, and C. Rudolph, "Expression of therapeutic proteins after delivery of chemically modified mrna in mice," *Nat Biotechnol*, vol. 29, no. 2, pp. 154–7, 2011.

[51] J. Probst, B. Weide, B. Scheel, B. J. Pichler, I. Hoerr, H. G. Rammensee, and S. Pascolo, "Spontaneous cellular uptake of exogenous messenger rna in vivo is nucleic acid-specific, saturable and ion dependent," *Gene Ther*, vol. 14, no. 15, pp. 1175–80, 2007.

[52] L. E. Mays, S. Ammon-Treiber, B. Mothes, M. Alkhaled, J. Rottenberger, E. S. Muller-Hermelink, M. Grimm, M. Mezger, S. Beer-Hammer, E. von Stebut, N. Rieber, B. Nurnberg, M. Schwab, R. Handgretinger, M. Idzko, D. Hartl, and M. S. Kormann, "Modified foxp3 mrna protects against asthma through an il-10-dependent mechanism," *J Clin Invest*, vol. 123, no. 3, pp. 1216–28, 2013.

[53] A. J. Mahiny, A. Dewerth, L. E. Mays, M. Alkhaled, B. Mothes, E. Malaeksefat, B. Loretz, J. Rottenberger, D. M. Brosch, P. Reautschnig, P. Surapolchai, F. Zeyer, A. Schams, M. Carevic, M. Bakele, M. Griese, M. Schwab, B. Nurnberg, S. Beer-Hammer, R. Handgretinger, D. Hartl, C. M. Lehr, and M. S. Kormann, "In vivo genome editing using nuclease-encoding mrna corrects sp-b deficiency," *Nat Biotechnol*, vol. 33, no. 6, pp. 584–6, 2015.

[54] S. Manam, B. J. Ledwith, A. B. Barnum, P. J. Troilo, C. J. Pauley, L. B. Harper, n. Griffiths T. G., Z. Niu, L. Denisova, T. T. Follmer, S. J. Pacchione, Z. Wang, C. M. Beare, W. J. Bagdon, and W. W. Nichols, "Plasmid dna vaccines: Tissue distribution and effects of dna sequence, adjuvants and delivery method on integration into host dna," *Intervirology*, vol. 43, no. 4-6, pp. 273–81, 2000.

[55] B. J. Ledwith, S. Manam, P. J. Troilo, A. B. Barnum, C. J. Pauley, n. Griffiths T. G., L. B. Harper, C. M. Beare, W. J. Bagdon, and W. W. Nichols, "Plasmid dna vaccines: Investigation of integration into host cellular dna following intramuscular injection in mice," *Intervirology*, vol. 43, no. 4-6, pp. 258–72, 2000.

[56] J. Lin, R. Calcedo, L. H. Vandenberghe, P. Bell, S. Somanathan, and J. M. Wilson, "A new genetic vaccine platform based on an adeno-associated virus isolated from a rhesus macaque," *J Virol*, vol. 83, no. 24, pp. 12 738–50, 2009.

[57] V. Cottard, C. Valvason, G. Falgarone, D. Lutomski, M. C. Boissier, and N. Bessis, "Immune response against gene therapy vectors: Influence of synovial fluid on adeno-associated virus mediated gene transfer to chondrocytes," *J Clin Immunol*, vol. 24, no. 2, pp. 162–9, 2004.

[58] C. S. Peden, C. Burger, N. Muzyczka, and R. J. Mandel, "Circulating anti-wild-type adeno-associated virus type 2 (aav2) antibodies inhibit recombinant aav2 (raav2)-mediated, but not raav5-mediated, gene transfer in the brain," *J Virol*, vol. 78, no. 12, pp. 6344–59, 2004.

[59] T. Schlake, A. Thess, M. Fotin-Mleczek, and K. J. Kallen, "Developing mrna-vaccine technologies," *RNA Biol*, vol. 9, no. 11, pp. 1319–30, 2012.

[60] J. L. Kirschman, S. Bhosle, D. Vanover, E. L. Blanchard, K. H. Loomis, C. Zurla, K. Murray, B. C. Lam, and P. J. Santangelo, "Characterizing exogenous mrna delivery, trafficking, cytoplasmic release and rna-protein correlations at the level of single cells," *Nucleic Acids Res*, vol. 45, no. 12, e113, 2017.

[61] A. N. Uduehi, U. Stammberger, B. Kubisa, M. Gugger, T. A. Buehler, and R. A. Schmid, "Effects of linear polyethylenimine and polyethylenimine/dna on lung function after airway instillation to rat lungs," *Mol Ther*, vol. 4, no. 1, pp. 52–7, 2001.

[62] V. F. Fiore, M. C. Lofton, S. Roser-Page, S. C. Yang, J. Roman, N. Murthy, and T. H. Barker, "Polyketal microparticles for therapeutic delivery to the lung," *Biomaterials*, vol. 31, no. 5, pp. 810–7, 2010.

[63] Y. C. Huang, A. Vieira, K. L. Huang, M. K. Yeh, and C. H. Chiang, "Pulmonary inflammation caused by chitosan microparticles," *J Biomed Mater Res A*, vol. 75, no. 2, pp. 283–7, 2005.

[64] J. C. Hogg, "Response of the lung to inhaled particles," *Med J Aust*, vol. 142, no. 13, pp. 675–8, 1985.

[65] J. S. Patton, C. S. Fishburn, and J. G. Weers, "The lungs as a portal of entry for systemic drug delivery," *Proc Am Thorac Soc*, vol. 1, no. 4, pp. 338–44, 2004.

[66] J. Brown R. A. and L. S. Schanker, "Absorption of aerosolized drugs from the rat lung," *Drug Metab Dispos*, vol. 11, no. 4, pp. 355–60, 1983.

[67] C. Lombry, D. A. Edwards, V. Preat, and R. Vanbever, "Alveolar macrophages are a primary barrier to pulmonary absorption of macromolecules," *Am J Physiol Lung Cell Mol Physiol*, vol. 286, no. 5, pp. L1002–8, 2004.

[68] J. S. Patton, J. G. McCabe, S. E. Hansen, and A. L. Daugherty, "Absorption of human growth hormone from the rat lung," *Biotechnol Ther*, vol. 1, no. 3, pp. 213–28, 1989.

[69] J. A. Dumont, S. C. Low, R. T. Peters, and A. J. Bitonti, "Monomeric fc fusions: Impact on pharmacokinetic and biological activity of protein therapeutics," *BioDrugs*, vol. 20, no. 3, pp. 151–60, 2006.

[70] A. Sokolowska-Wedzina, G. Chodaczek, J. Chudzian, A. Borek, M. Zakrzewska, and J. Otlewski, "High-affinity internalizing human scfv-fc antibody for targeting fgfr1-overexpressing lung cancer," *Mol Cancer Res*, vol. 15, no. 8, pp. 1040–1050, 2017.

[71] G. M. Ryan, L. M. Kaminskas, B. D. Kelly, D. J. Owen, M. P. McIntosh, and C. J. Porter, "Pulmonary administration of pegylated polylysine dendrimers: Absorption from the lung versus retention within the lung is highly size-dependent," *Mol Pharm*, vol. 10, no. 8, pp. 2986–95, 2013.

[72] J. S. Hagood, P. Prabhakaran, P. Kumbla, L. Salazar, M. W. MacEwen, T. H. Barker, L. A. Ortiz, T. Schoeb, G. P. Siegal, C. B. Alexander, A. Pardo, and M. Selman, "Loss of fibroblast thy-1 expression correlates with lung fibrogenesis," *Am J Pathol*, vol. 167, no. 2, pp. 365–79, 2005.

[73] Y. Y. Sanders, A. Pardo, M. Selman, G. J. Nuovo, T. O. Tollefsbol, G. P. Siegal, and J. S. Hagood, "Thy-1 promoter hypermethylation: A novel epigenetic pathogenic mechanism in pulmonary fibrosis," *Am J Respir Cell Mol Biol*, vol. 39, no. 5, pp. 610–8, 2008.

[74] V. Sueblinvong, D. C. Neujahr, S. T. Mills, S. Roser-Page, J. D. Ritzenthaler, D. Guidot, M. Rojas, and J. Roman, "Predisposition for disrepair in the aged lung," *Am J Med Sci*, vol. 344, no. 1, pp. 41–51, 2012.

[75] M. C. Tiveron, M. Nosten-Bertrand, H. Jani, D. Garnett, E. M. Hirst, F. Grosveld, and R. J. Morris, "The mode of anchorage to the cell surface determines both the function and the membrane location of thy-1 glycoprotein," *J Cell Sci*, vol. 107 (Pt 7), pp. 1783–96, 1994.

[76] I. Stefanova, V. Horejsi, I. J. Ansotegui, W. Knapp, and H. Stockinger, "Gpi-anchored cell-surface molecules complexed to protein tyrosine kinases," *Science*, vol. 254, no. 5034, pp. 1016–9, 1991.

[77] L. Draberova and P. Draber, "Thy-1 glycoprotein and src-like protein-tyrosine kinase p53/p56lyn are associated in large detergent-resistant complexes in rat basophilic leukemia cells," *Proc Natl Acad Sci U S A*, vol. 90, no. 8, pp. 3611–5, 1993.

[78] T. H. Barker, H. E. Grenett, M. W. MacEwen, S. G. Tilden, G. M. Fuller, J. Settleman, A. Woods, J. Murphy-Ullrich, and J. S. Hagood, "Thy-1 regulates fibroblast focal adhesions, cytoskeletal organization and migration through modulation of p190 rhogap and rho gtpase activity," *Exp Cell Res*, vol. 295, no. 2, pp. 488–96, 2004.

[79] T. H. Barker, M. A. Pallero, M. W. MacEwen, S. G. Tilden, A. Woods, J. E. Murphy-Ullrich, and J. S. Hagood, "Thrombospondin-1-induced focal adhesion disassembly in fibroblasts requires thy-1 surface expression, lipid raft integrity, and src activation," *J Biol Chem*, vol. 279, no. 22, pp. 23 510–6, 2004.

[80] T. H. Barker and J. S. Hagood, "Getting a grip on thy-1 signaling," *Biochim Biophys Acta*, vol. 1793, no. 5, pp. 921–3, 2009.

[81] T. A. Rege, M. A. Pallero, C. Gomez, H. E. Grenett, J. E. Murphy-Ullrich, and J. S. Hagood, "Thy-1, via its gpi anchor, modulates src family kinase and focal adhesion kinase phosphorylation and subcellular localization, and fibroblast migration, in response to thrombospondin-1/hep i," *Exp Cell Res*, vol. 312, no. 19, pp. 3752–67, 2006.

[82] K. L. Schornberg, C. J. Shoemaker, D. Dube, M. Y. Abshire, S. E. Delos, A. H. Bouton, and J. M. White, "Alpha5beta1-integrin controls ebolavirus entry by regulating endosomal cathepsins," *Proc Natl Acad Sci U S A*, vol. 106, no. 19, pp. 8003–8, 2009.

[83] A. Engler, L. Bacakova, C. Newman, A. Hategan, M. Griffin, and D. Discher, "Substrate compliance versus ligand density in cell on gel responses," *Biophys J*, vol. 86, no. 1 Pt 1, pp. 617–28, 2004.

[84] B. D. Singer, J. R. Mock, F. R. D'Alessio, N. R. Aggarwal, P. Mandke, L. Johnston, and M. Damarla, "Flow-cytometric method for simultaneous analysis of mouse lung epithelial, endothelial, and hematopoietic lineage cells," *Am J Physiol Lung Cell Mol Physiol*, vol. 310, no. 9, pp. L796–801, 2016.

[85] W. G. Telford, M. W. Moss, J. P. Morseman, and F. C. Allnutt, "Cyanobacterial stabilized phycobilisomes as fluorochromes for extracellular antigen detection by flow cytometry," *J Immunol Methods*, vol. 254, no. 1-2, pp. 13–30, 2001.

[86] M. Wang, M. Misakian, H. J. He, P. Bajcsy, F. Abbasi, J. M. Davis, K. D. Cole, I. V. Turko, and L. Wang, "Quantifying cd4 receptor protein in two human cd4+

lymphocyte preparations for quantitative flow cytometry," *Clin Proteomics*, vol. 11, no. 1, p. 43, 2014.

[87] D. S. Auld and J. Inglese, "Interferences with luciferase reporter enzymes," in *Assay Guidance Manual*, G. S. Sittampalam, N. P. Coussens, K. Brimacombe, A. Grossman, M. Arkin, D. Auld, C. Austin, J. Baell, B. Bejcek, T. D. Y. Chung, J. L. Dahlin, V. Devanaryan, T. L. Foley, M. Glicksman, M. D. Hall, J. V. Hass, J. Inglese, P. W. Iversen, S. D. Kahl, S. C. Kales, M. Lal-Nag, Z. Li, J. McGee, O. McManus, T. Riss, J. Trask O. J., J. R. Weidner, M. Xia, and X. Xu, Eds. Bethesda (MD), 2004.

[88] A. L. Olsen, S. A. Bloomer, E. P. Chan, M. D. Gaca, P. C. Georges, B. Sackey, M. Uemura, P. A. Janmey, and R. G. Wells, "Hepatic stellate cells require a stiff environment for myofibroblastic differentiation," *Am J Physiol Gastrointest Liver Physiol*, vol. 301, no. 1, G110–8, 2011.

[89] J. S. Park, J. S. Chu, A. D. Tsou, R. Diop, Z. Tang, A. Wang, and S. Li, "The effect of matrix stiffness on the differentiation of mesenchymal stem cells in response to tgf-beta," *Biomaterials*, vol. 32, no. 16, pp. 3921–30, 2011.

[90] Y. Shi, Y. Dong, Y. Duan, X. Jiang, C. Chen, and L. Deng, "Substrate stiffness influences tgf-beta1-induced differentiation of bronchial fibroblasts into myofibroblasts in airway remodeling," *Mol Med Rep*, vol. 7, no. 2, pp. 419–24, 2013.

[91] S. G. Szeto, M. Narimatsu, M. Lu, X. He, A. M. Sidiqi, M. F. Tolosa, L. Chan, K. De Freitas, J. F. Bialik, S. Majumder, S. Boo, B. Hinz, Q. Dan, A. Advani, R. John, J. L. Wrana, A. Kapus, and D. A. Yuen, "Yap/taz are mechanoregulators of tgf-beta-smad signaling and renal fibrogenesis," *J Am Soc Nephrol*, vol. 27, no. 10, pp. 3117–3128, 2016.

[92] S. Aryal and S. D. Nathan, "An update on emerging drugs for the treatment of idiopathic pulmonary fibrosis," *Expert Opin Emerg Drugs*, pp. 1–14, 2018.

[93] G. Raghu, K. K. Brown, H. R. Collard, V. Cottin, K. F. Gibson, R. J. Kaner, D. J. Lederer, F. J. Martinez, P. W. Noble, J. W. Song, A. U. Wells, T. P. Whelan, W. Wuyts, E. Moreau, S. D. Patterson, V. Smith, S. Bayly, J. W. Chien, Q. Gong, J. J. Zhang, and T. G. O'Riordan, "Efficacy of simtuzumab versus placebo in patients with idiopathic pulmonary fibrosis: A randomised, double-blind, controlled, phase 2 trial," *Lancet Respir Med*, vol. 5, no. 1, pp. 22–32, 2017.

[94] G. Zambruno, P. C. Marchisio, A. Marconi, C. Vaschieri, A. Melchiori, A. Giannetti, and M. De Luca, "Transforming growth factor-beta 1 modulates beta 1 and beta 5 integrin receptors and induces the de novo expression of the alpha v beta 6 heterodimer in normal human keratinocytes: Implications for wound healing," *J Cell Biol*, vol. 129, no. 3, pp. 853–65, 1995.

[95] M. E. Almeida, K. S. Monteiro, E. E. Kato, S. C. Sampaio, T. T. Braga, N. O. Camara, M. L. Lamers, and M. F. Santos, "Hyperglycemia reduces integrin subunits alpha v and alpha 5 on the surface of dermal fibroblasts contributing to deficient migration," *Mol Cell Biochem*, vol. 421, no. 1-2, pp. 19–28, 2016.

[96] E. K. Duperret, C. A. Natale, C. Monteleon, A. Dahal, and T. W. Ridky, "The integrin alphav-tgfbeta signaling axis is necessary for epidermal proliferation during cutaneous wound healing," *Cell Cycle*, vol. 15, no. 15, pp. 2077–86, 2016.

[97] G. Saini, J. Porte, P. H. Weinreb, S. M. Violette, W. A. Wallace, T. M. McKeever, and G. Jenkins, "Alphavbeta6 integrin may be a potential prognostic biomarker in interstitial lung disease," *Eur Respir J*, vol. 46, no. 2, pp. 486–94, 2015.

[98] G. S. Horan, S. Wood, V. Ona, D. J. Li, M. E. Lukashev, P. H. Weinreb, K. J. Simon, K. Hahm, N. E. Allaire, N. J. Rinaldi, J. Goyal, C. A. Feghali-Bostwick, E. L. Matteson, C. O'Hara, R. Lafyatis, G. S. Davis, X. Huang, D. Sheppard, and S. M. Violette, "Partial inhibition of integrin alpha(v)beta6 prevents pulmonary fibrosis without exacerbating inflammation," *Am J Respir Crit Care Med*, vol. 177, no. 1, pp. 56–65, 2008.

[99] M. C. Kang, D. H. Choi, Y. W. Choi, S. J. Park, H. Namkoong, K. S. Park, S. S. Ahn, C. D. Surh, S. W. Yoon, D. J. Kim, J. A. Choi, Y. Park, Y. C. Sung, and S. W. Lee, "Intranasal introduction of fc-fused interleukin-7 provides long-lasting prophylaxis against lethal influenza virus infection," *J Virol*, vol. 90, no. 5, pp. 2273–84, 2015.

[100] Y. Y. Sanders, T. O. Tollefsbol, B. M. Varisco, and J. S. Hagood, "Epigenetic regulation of thy-1 by histone deacetylase inhibitor in rat lung fibroblasts," *Am J Respir Cell Mol Biol*, vol. 45, no. 1, pp. 16–23, 2011.

[101] M. J. Paszek, C. C. DuFort, O. Rossier, R. Bainer, J. K. Mouw, K. Godula, J. E. Hudak, J. N. Lakins, A. C. Wijekoon, L. Cassereau, M. G. Rubashkin, M. J. Magbanua, K. S. Thorn, M. W. Davidson, H. S. Rugo, J. W. Park, D. A. Hammer, G. Giannone, C. R. Bertozzi, and V. M. Weaver, "The cancer glycocalyx mechanically primes integrin-mediated growth and survival," *Nature*, vol. 511, no. 7509, pp. 319–25, 2014.

[102] M. J. Paszek, D. Boettiger, V. M. Weaver, and D. A. Hammer, "Integrin clustering is driven by mechanical resistance from the glycocalyx and the substrate," *PLoS Comput Biol*, vol. 5, no. 12, e1000604, 2009.

[103] A. Muller, C. Kloppel, M. Smith-Valentine, J. Van Houten, and M. Simon, "Selective and programmed cleavage of gpi-anchored proteins from the surface membrane by phospholipase c," *Biochim Biophys Acta*, vol. 1818, no. 1, pp. 117–24, 2012.

[104] B. S. Shea, S. F. Brooks, B. A. Fontaine, J. Chun, A. D. Luster, and A. M. Tager, "Prolonged exposure to sphingosine 1-phosphate receptor-1 agonists exacerbates vascular leak, fibrosis, and mortality after lung injury," *Am J Respir Cell Mol Biol*, vol. 43, no. 6, pp. 662–73, 2010.

[105] P. Desogere, L. F. Tapias, L. P. Hariri, N. J. Rotile, T. A. Rietz, C. K. Probst, F. Blasi, H. Day, M. Mino-Kenudson, P. Weinreb, S. M. Violette, B. C. Fuchs, A. M. Tager, M. Lanuti, and P. Caravan, "Type i collagen-targeted pet probe for pulmonary fibrosis detection and staging in preclinical models," *Sci Transl Med*, vol. 9, no. 384, 2017.

[106] C. L. Densmore, F. M. Orson, B. Xu, B. M. Kinsey, J. C. Waldrep, P. Hua, B. Bhogal, and V. Knight, "Aerosol delivery of robust polyethyleneimine-dna complexes for gene therapy and genetic immunization," *Mol Ther*, vol. 1, no. 2, pp. 180–8, 2000.

[107] M. Koping-Hoggard, I. Tubulekas, H. Guan, K. Edwards, M. Nilsson, K. M. Varum, and P. Artursson, "Chitosan as a nonviral gene delivery system. structure-property relationships and characteristics compared with polyethylenimine in vitro and after lung administration in vivo," *Gene Ther*, vol. 8, no. 14, pp. 1108–21, 2001.

[108] K. Regnstrom, E. G. Ragnarsson, M. Fryknas, M. Koping-Hoggard, and P. Artursson, "Gene expression profiles in mouse lung tissue after administration of two cationic polymers used for nonviral gene delivery," *Pharm Res*, vol. 23, no. 3, pp. 475–82, 2006.

[109] P. Chollet, M. C. Favrot, A. Hurbin, and J. L. Coll, "Side-effects of a systemic injection of linear polyethylenimine-dna complexes," *J Gene Med*, vol. 4, no. 1, pp. 84–91, 2002.

[110] J. S. Patton and P. R. Byron, "Inhaling medicines: Delivering drugs to the body through the lungs," *Nat Rev Drug Discov*, vol. 6, no. 1, pp. 67–74, 2007.

[111] S. M. Bhosle, K. H. Loomis, J. L. Kirschman, E. L. Blanchard, D. A. Vanover, C. Zurla, D. Habrant, D. Edwards, P. Baumhof, B. Pitard, and P. J. Santangelo, "Unifying in vitro and in vivo ivt mrna expression discrepancies in skeletal muscle via mechanotransduction," *Biomaterials*, vol. 159, pp. 189–203, 2018.

[112] S. M. Johler, J. Rejman, S. Guan, and J. Rosenecker, "Nebulisation of ivt mrna complexes for intrapulmonary administration," *PLoS One*, vol. 10, no. 9, e0137504, 2015.

[113] S. H. Hong, S. J. Park, S. Lee, C. S. Cho, and M. H. Cho, "Aerosol gene delivery using viral vectors and cationic carriers for in vivo lung cancer therapy," *Expert Opin Drug Deliv*, vol. 12, no. 6, pp. 977–91, 2015.

[114] K. Remaut, E. De Clercq, O. Andries, K. Rombouts, M. Van Gils, L. Cicchelero, I. Vandenbussche, S. Van Praet, J. M. Benito, J. M. Fernandez, N. Sanders, and D. Vanrompay, "Aerosolized non-viral nucleic acid delivery in the vaginal tract of pigs," *Pharm Res*, vol. 33, no. 2, pp. 384–94, 2016.

[115] M. Zeisberg and R. Kalluri, "Cellular mechanisms of tissue fibrosis. 1. common and organ-specific mechanisms associated with tissue fibrosis," *Am J Physiol Cell Physiol*, vol. 304, no. 3, pp. C216–25, 2013.

[116] M. Morikawa, R. Derynck, and K. Miyazono, "Tgf-beta and the tgf-beta family: Context-dependent roles in cell and tissue physiology," *Cold Spring Harb Perspect Biol*, vol. 8, no. 5, 2016.

[117] K. L. Walton, K. E. Johnson, and C. A. Harrison, "Targeting tgf-beta mediated smad signaling for the prevention of fibrosis," *Front Pharmacol*, vol. 8, p. 461, 2017.

[118] A. B. Kulkarni, C. G. Huh, D. Becker, A. Geiser, M. Lyght, K. C. Flanders, A. B. Roberts, M. B. Sporn, J. M. Ward, and S. Karlsson, "Transforming growth factor beta 1 null mutation in mice causes excessive inflammatory response and early death," *Proc Natl Acad Sci U S A*, vol. 90, no. 2, pp. 770–4, 1993.

[119] R. Aghanouri, M. Ghanei, J. Aslani, H. Keivani-Amine, F. Rastegar, and A. Karkhane, "Fibrogenic cytokine levels in bronchoalveolar lavage aspirates 15 years after exposure to sulfur mustard," *Am J Physiol Lung Cell Mol Physiol*, vol. 287, no. 6, pp. L1160–4, 2004.

[120] A. Bergeron, P. Soler, M. Kambouchner, P. Loiseau, B. Milleron, D. Valeyre, A. J. Hance, and A. Tazi, "Cytokine profiles in idiopathic pulmonary fibrosis suggest an important role for tgf-beta and il-10," *Eur Respir J*, vol. 22, no. 1, pp. 69–76, 2003.

[121] K. Puthawala, N. Hadjiangelis, S. C. Jacoby, E. Bayongan, Z. Zhao, Z. Yang, M. L. Devitt, G. S. Horan, P. H. Weinreb, M. E. Lukashev, S. M. Violette, K. S. Grant, C. Colarossi, S. C. Formenti, and J. S. Munger, "Inhibition of integrin alpha(v)beta6, an activator of latent transforming growth factor-beta, prevents radiation-induced lung fibrosis," *Am J Respir Crit Care Med*, vol. 177, no. 1, pp. 82–90, 2008.

[122] J. Zhao, W. Shi, Y. L. Wang, H. Chen, J. Bringas P., M. B. Datto, J. P. Frederick, X. F. Wang, and D. Warburton, "Smad3 deficiency attenuates bleomycin-induced pulmonary fibrosis in mice," *Am J Physiol Lung Cell Mol Physiol*, vol. 282, no. 3, pp. L585–93, 2002.

[123] D. Warburton, W. Shi, and B. Xu, "Tgf-beta-smad3 signaling in emphysema and pulmonary fibrosis: An epigenetic aberration of normal development?" *Am J Physiol Lung Cell Mol Physiol*, vol. 304, no. 2, pp. L83–5, 2013.

[124] B. J. Thomas, M. Lindsay, H. Dagher, N. J. Freezer, D. Li, R. Ghildyal, and P. G. Bardin, "Transforming growth factor-beta enhances rhinovirus infection by diminishing early innate responses," *Am J Respir Cell Mol Biol*, vol. 41, no. 3, pp. 339–47, 2009.

[125] T. R. McMillan, B. B. Moore, J. B. Weinberg, K. M. Vannella, W. B. Fields, P. J. Christensen, L. F. van Dyk, and G. B. Toews, "Exacerbation of established pulmonary fibrosis in a murine model by gammaherpesvirus," *Am J Respir Crit Care Med*, vol. 177, no. 7, pp. 771–80, 2008.

[126] T. Stahnke, B. S. Kowtharapu, O. Stachs, K. P. Schmitz, J. Wurm, A. Wree, R. F. Guthoff, and M. Hovakimyan, "Suppression of tgf-beta pathway by pirfenidone decreases extracellular matrix deposition in ocular fibroblasts in vitro," *PLoS One*, vol. 12, no. 2, e0172592, 2017.

[127] J. Du, K. Paz, R. Flynn, A. Vulic, T. M. Robinson, K. E. Lineburg, K. A. Alexander, J. Meng, S. Roy, A. Panoskaltsis-Mortari, M. Loschi, G. R. Hill, J. S. Serody, I. Maillard, D. Miklos, J. Koreth, C. S. Cutler, J. H. Antin, J. Ritz, K. P. MacDonald, T. W. Schacker, L. Luznik, and B. R. Blazar, "Pirfenidone ameliorates murine chronic gvhd through inhibition of macrophage infiltration and tgf-beta production," *Blood*, vol. 129, no. 18, pp. 2570–2580, 2017.

[128] M. Molina-Molina, C. Machahua-Huamani, V. Vicens-Zygmunt, R. Llatjos, I. Escobar, E. Sala-Llinas, P. Luburich-Hernaiz, J. Dorca, and A. Montes-Worboys, "Anti-fibrotic effects of pirfenidone and rapamycin in primary ipf fibroblasts and human alveolar epithelial cells," *BMC Pulm Med*, vol. 18, no. 1, p. 63, 2018.

[129] J. Massague, "Tgfbeta signalling in context," *Nat Rev Mol Cell Biol*, vol. 13, no. 10, pp. 616–30, 2012.

[130] C. H. Heldin, M. Landstrom, and A. Moustakas, "Mechanism of tgf-beta signaling to growth arrest, apoptosis, and epithelial-mesenchymal transition," *Curr Opin Cell Biol*, vol. 21, no. 2, pp. 166–76, 2009.

[131] J. Massague, "Tgfbeta signaling: Receptors, transducers, and mad proteins," *Cell*, vol. 85, no. 7, pp. 947–50, 1996.

[132] J. Massague, J. Andres, L. Attisano, S. Cheifetz, F. Lopez-Casillas, M. Ohtsuki, and J. L. Wrana, "Tgf-beta receptors," *Mol Reprod Dev*, vol. 32, no. 2, pp. 99–104, 1992.

[133] J. L. Wrana, L. Attisano, J. Carcamo, A. Zentella, J. Doody, M. Laiho, X. F. Wang, and J. Massague, "Tgf beta signals through a heteromeric protein kinase receptor complex," *Cell*, vol. 71, no. 6, pp. 1003–14, 1992.

[134] R. A. Anders and E. B. Leof, "Chimeric granulocyte/macrophage colony-stimulating factor/transforming growth factor-beta (tgf-beta) receptors define a model system for investigating the role of homomeric and heteromeric receptors in tgf-beta signaling," *J Biol Chem*, vol. 271, no. 36, pp. 21 758–66, 1996.

[135] X. H. Feng and R. Derynck, "Specificity and versatility in tgf-beta signaling through smads," *Annu Rev Cell Dev Biol*, vol. 21, pp. 659–93, 2005.

[136] B. Hinz, "Formation and function of the myofibroblast during tissue repair," *J Invest Dermatol*, vol. 127, no. 3, pp. 526–37, 2007.

[137] G. Thillainadesan, J. M. Chitilian, M. Isovic, J. N. Ablack, J. S. Mymryk, M. Tini, and J. Torchia, "Tgf-beta-dependent active demethylation and expression of the p15ink4b tumor suppressor are impaired by the znf217/corest complex," *Mol Cell*, vol. 46, no. 5, pp. 636–49, 2012.

[138] C. S. Hill, "Nucleocytoplasmic shuttling of smad proteins," *Cell Res*, vol. 19, no. 1, pp. 36–46, 2009.

[139] J. H. Kang, M. Y. Jung, X. Yin, M. Andrianifahanana, D. M. Hernandez, and E. B. Leof, "Cell-penetrating peptides selectively targeting smad3 inhibit profibrotic tgf-beta signaling," *J Clin Invest*, vol. 127, no. 7, pp. 2541–2554, 2017.

[140] E. Labbe, A. Letamendia, and L. Attisano, "Association of smads with lymphoid enhancer binding factor 1/t cell-specific factor mediates cooperative signaling by the transforming growth factor-beta and wnt pathways," *Proc Natl Acad Sci U S A*, vol. 97, no. 15, pp. 8358–63, 2000.

[141] J. Seoane, H. V. Le, L. Shen, S. A. Anderson, and J. Massague, "Integration of smad and forkhead pathways in the control of neuroepithelial and glioblastoma cell proliferation," *Cell*, vol. 117, no. 2, pp. 211–23, 2004.

[142] X. Lin, X. Duan, Y.-Y. Liang, Y. Su, K. H. Wrighton, J. Long, M. Hu, C. M. Davis, J. Wang, F. C. Brunicardi, Y. Shi, Y.-G. Chen, A. Meng, and X.-H. Feng, "Ppm1a functions as a smad phosphatase to terminate tgf-beta signaling," *Cell*, vol. 125, no. 5, pp. 915–928, 2006.

[143] J. Yu, L. Pan, X. Qin, H. Chen, Y. Xu, Y. Chen, and H. Tang, "Mtmr4 attenuates transforming growth factor beta (tgfbeta) signaling by dephosphorylating r-smads in endosomes," *J Biol Chem*, vol. 285, no. 11, pp. 8454–62, 2010.

[144] C. Unsold, M. Hyytiainen, L. Bruckner-Tuderman, and J. Keski-Oja, "Latent tgf-beta binding protein ltbp-1 contains three potential extracellular matrix interacting domains," *J Cell Sci*, vol. 114, no. Pt 1, pp. 187–197, 2001.

[145] K. Koli, M. Hyytiainen, M. J. Ryynanen, and J. Keski-Oja, "Sequential deposition of latent tgf-beta binding proteins (ltbps) during formation of the extracellular matrix in human lung fibroblasts," *Exp Cell Res*, vol. 310, no. 2, pp. 370–82, 2005.

[146] R. M. Lyons, J. Keski-Oja, and H. L. Moses, "Proteolytic activation of latent transforming growth factor-beta from fibroblast-conditioned medium," *J Cell Biol*, vol. 106, no. 5, pp. 1659–65, 1988.

[147] M. H. Barcellos-Hoff and T. A. Dix, "Redox-mediated activation of latent transforming growth factor-beta 1," *Mol Endocrinol*, vol. 10, no. 9, pp. 1077–83, 1996.

[148] D. Mu, S. Cambier, L. Fjellbirkeland, J. L. Baron, J. S. Munger, H. Kawakatsu, D. Sheppard, V. C. Broaddus, and S. L. Nishimura, "The integrin alpha(v)beta8 mediates epithelial homeostasis through mt1-mmp-dependent activation of tgf-beta1," *J Cell Biol*, vol. 157, no. 3, pp. 493–507, 2002.

[149] G. Ge and D. S. Greenspan, "Bmp1 controls tgfbeta1 activation via cleavage of latent tgfbeta-binding protein," *J Cell Biol*, vol. 175, no. 1, pp. 111–20, 2006.

[150] F. Klingberg, M. L. Chow, A. Koehler, S. Boo, L. Buscemi, T. M. Quinn, M. Costell, B. A. Alman, E. Genot, and B. Hinz, "Prestress in the extracellular matrix sensitizes latent tgf-beta1 for activation," *J Cell Biol*, vol. 207, no. 2, pp. 283–97, 2014.

[151] A. K. Kamaraju and A. B. Roberts, "Role of rho/rock and p38 map kinase pathways in transforming growth factor-beta-mediated smad-dependent growth inhibition of human breast carcinoma cells in vivo," *J Biol Chem*, vol. 280, no. 2, pp. 1024–36, 2005.

[152] X. Varelas, R. Sakuma, P. Samavarchi-Tehrani, R. Peerani, B. M. Rao, J. Dembowy, M. B. Yaffe, P. W. Zandstra, and J. L. Wrana, "Taz controls smad nucleocytoplasmic shuttling and regulates human embryonic stem-cell self-renewal," *Nat Cell Biol*, vol. 10, no. 7, pp. 837–48, 2008.

[153] D. Zabini, E. Granton, Y. Hu, M. Z. Miranda, U. Weichelt, S. Breuils Bonnet, S. Bonnet, N. W. Morrell, K. A. Connelly, S. Provencher, B. Ghanim, W. Klepetko, A. Olschewski, A. Kapus, and W. M. Kuebler, "Loss of smad3 promotes vascular remodeling in pulmonary arterial hypertension via mrtf disinhibition," *Am J Respir Crit Care Med*, vol. 197, no. 2, pp. 244–260, 2018.

[154] M. Z. Miranda, J. F. Bialik, P. Speight, Q. Dan, T. Yeung, K. Szaszi, S. F. Pedersen, and A. Kapus, "Tgf-beta1 regulates the expression and transcriptional activity of taz protein via a smad3-independent, myocardin-related transcription factor-mediated mechanism," *J Biol Chem*, vol. 292, no. 36, pp. 14 902–14 920, 2017.

[155] R. A. Elkhatib, M. Paci, R. Boissier, G. Longepied, Y. Auguste, V. Achard, P. Bourgeois, N. Levy, N. Branger, M. J. Mitchell, and C. Metzler-Guillemain, "Lem-domain proteins are lost during human spermiogenesis but baf and baf-l persist," *Reproduction*, vol. 154, no. 4, pp. 387–401, 2017.

[156] W. Wu, F. Lin, and H. J. Worman, "Intracellular trafficking of man1, an integral protein of the nuclear envelope inner membrane," *J Cell Sci*, vol. 115, no. Pt 7, pp. 1361–71, 2002.

[157] M. Mansharamani and K. L. Wilson, "Direct binding of nuclear membrane protein man1 to emerin in vitro and two modes of binding to barrier-to-autointegration factor," *J Biol Chem*, vol. 280, no. 14, pp. 13 863–70, 2005.

[158] J. Liu, K. K. Lee, M. Segura-Totten, E. Neufeld, K. L. Wilson, and Y. Gruenbaum, "Man1 and emerin have overlapping function(s) essential for chromosome segregation and cell division in caenorhabditis elegans," *Proceedings of the National Academy of Sciences of the United States of America*, vol. 100, no. 8, pp. 4598–4603, 2003.

[159] C. stlund, T. Sullivan, C. L. Stewart, and H. J. Worman, "Dependence of diffusional mobility of integral inner nuclear membrane proteins on a-type lamins," *Biochemistry*, vol. 45, no. 5, pp. 1374–1382, 2006.

[160] N. Wagner, B. Kagermeier, S. Loserth, and G. Krohne, "The drosophila melanogaster lem-domain protein man1," *European Journal of Cell Biology*, vol. 85, no. 2, pp. 91–105, 2006.

[161] F. Lin, J. M. Morrison, W. Wu, and H. J. Worman, "Man1, an integral protein of the inner nuclear membrane, binds smad2 and smad3 and antagonizes transforming growth factor-beta signaling," *Hum Mol Genet*, vol. 14, no. 3, pp. 437–45, 2005.

[162] A. Brachner and R. Foisner, "Evolvement of lem proteins as chromatin tethers at the nuclear periphery," *Biochem Soc Trans*, vol. 39, no. 6, pp. 1735–41, 2011.

[163] M. Reil and M. C. Dabauvalle, "Essential roles of lem-domain protein man1 during organogenesis in xenopus laevis and overlapping functions of emerin," *Eur J Cell Biol*, vol. 92, no. 8-9, pp. 280–94, 2013.

[164] S. Braun and R. R. Barrales, "Beyond tethering and the lem domain: Mscellaneous functions of the inner nuclear membrane lem2," *Nucleus*, vol. 7, no. 6, pp. 523–531, 2016.

[165] E. Konde, B. Bourgeois, C. Tellier-Lebegue, W. Wu, J. Perez, S. Caputo, W. Attanda, S. Gasparini, J. B. Charbonnier, B. Gilquin, H. J. Worman, and S. Zinn-Justin, "Structural analysis of the smad2-man1 interaction that regulates transform-

ing growth factor-beta signaling at the inner nuclear membrane," *Biochemistry*, vol. 49, no. 37, pp. 8020–32, 2010.

[166] B. Bourgeois, B. Gilquin, C. Tellier-Lebegue, C. Ostlund, W. Wu, J. Perez, P. El Hage, F. Lallemand, H. J. Worman, and S. Zinn-Justin, "Inhibition of tgf-beta signaling at the nuclear envelope: Characterization of interactions between man1, smad2 and smad3, and ppm1a," *Sci Signal*, vol. 6, no. 280, ra49, 2013.

[167] S. Bermeo, A. Al-Saedi, M. Kassem, C. Vidal, and G. Duque, "The role of the nuclear envelope protein man1 in mesenchymal stem cell differentiation," *J Cell Biochem*, vol. 118, no. 12, pp. 4425–4435, 2017.

[168] S.-I. Osada, S.-y. Ohmori, and M. Taira, "Xman1, an inner nuclear membrane protein, antagonizes bmp signaling by interacting with smad1 in xenopus embryos," *Development*, vol. 130, no. 9, pp. 1783–1794, 2003. eprint: `http://dev.biologists.org/content/130/9/1783.full.pdf`.

[169] G. P. Raju, N. Dimova, P. S. Klein, and H. C. Huang, "Sane, a novel lem domain protein, regulates bone morphogenetic protein signaling through interaction with smad1," *J Biol Chem*, vol. 278, no. 1, pp. 428–37, 2003.

[170] J. Hellemans, O. Preobrazhenska, A. Willaert, P. Debeer, P. C. Verdonk, T. Costa, K. Janssens, B. Menten, N. Van Roy, S. J. Vermeulen, R. Savarirayan, W. Van Hul, F. Vanhoenacker, D. Huylebroeck, A. De Paepe, J. M. Naeyaert, J. Vandesompele, F. Speleman, K. Verschueren, P. J. Coucke, and G. R. Mortier, "Loss-of-function mutations in lemd3 result in osteopoikilosis, buschke-ollendorff syndrome and melorheostosis," *Nat Genet*, vol. 36, no. 11, pp. 1213–8, 2004.

[171] D. Pan, L. D. Estevez-Salmeron, S. L. Stroschein, X. Zhu, J. He, S. Zhou, and K. Luo, "The integral inner nuclear membrane protein man1 physically interacts with the r-smad proteins to repress signaling by the transforming growth factor-beta superfamily of cytokines," *J Biol Chem*, vol. 280, no. 16, pp. 15 992–6001, 2005.

[172] M. Yadegari, M. P. Whyte, S. Mumm, R. G. Phelps, A. Shanske, W. G. Totty, and S. R. Cohen, "Buschke-ollendorff syndrome: Absence of lemd3 mutation in an affected family," *Arch Dermatol*, vol. 146, no. 1, pp. 63–8, 2010.

[173] A. R. Couto, J. Bruges-Armas, C. A. Peach, K. Chapman, M. A. Brown, B. P. Wordsworth, and Y. Zhang, "A novel lemd3 mutation common to patients with osteopoikilosis with and without melorheostosis," *Calcif Tissue Int*, vol. 81, no. 2, pp. 81–4, 2007.

[174] V. Pope, L. Dupuis, P. Kannu, R. Mendoza-Londono, D. Sajic, J. So, G. Yoon, and I. Lara-Corrales, "Buschke-ollendorff syndrome: A novel case series and systematic review," *Br J Dermatol*, vol. 174, no. 4, pp. 723–9, 2016.

[175] J. K. Gass, J. Hellemans, G. Mortier, M. Griffiths, and N. P. Burrows, "Buschke-ollendorff syndrome: A manifestation of a heterozygous nonsense mutation in the lemd3 gene," *J Am Acad Dermatol*, vol. 58, no. 5 Suppl 1, S103–4, 2008.

[176] M. Yuste-Chaves, J. Canueto, A. Santos-Briz, S. Ciria, R. Gonzalez-Sarmiento, and P. Unamuno, "Buschke-ollendorff syndrome with striking phenotypic variation resulting from a novel c.2203c¿t nonsense mutation in lemd3," *Pediatr Dermatol*, vol. 28, no. 4, pp. 447–50, 2011.

[177] B. Burger, D. Hershkovitz, M. Indelman, M. Kovac, J. Galambos, P. Haeusermann, E. Sprecher, and P. H. Itin, "Buschke-ollendorff syndrome in a three-generation family: Influence of a novel lemd3 mutation to tropoelastin expression," *Eur J Dermatol*, vol. 20, no. 6, pp. 693–7, 2010.

[178] A. Korekawa, H. Nakano, Y. Toyomaki, N. Takiyoshi, D. Rokunohe, E. Akasaka, K. Nakajima, and D. Sawamura, "Buschke-ollendorff syndrome associated with hypertrophic scar formation: A possible role for lemd3 mutation," *Br J Dermatol*, vol. 166, no. 4, pp. 900–3, 2012.

[179] D. Gutierrez, K. D. Cooper, A. L. Mitchell, and H. I. Cohn, "Novel somatic mutation in lemd3 splice site results in buschke-ollendorff syndrome with polyostotic melorheostosis and osteopoikilosis," *Pediatr Dermatol*, vol. 32, no. 5, e219–20, 2015.

[180] J. Kratzsch, D. Mitter, M. Ziemer, J. Kohlhase, and H. Voth, "Identification of a novel point mutation in the lemd3 gene in an infant with buschke-ollendorff syndrome," *JAMA Dermatol*, vol. 152, no. 7, pp. 844–5, 2016.

[181] A. Condorelli, N. Musso, L. Scuderi, D. F. Condorelli, V. Barresi, and R. De Pasquale, "Juvenile elastoma without germline mutations in lemd3 gene: A case of buschke-ollendorff syndrome?" *Pediatr Dermatol*, vol. 34, no. 6, e345–e346, 2017.

[182] D. A. Starr and M. Han, "Role of anc-1 in tethering nuclei to the actin cytoskeleton," *Science*, vol. 298, no. 5592, pp. 406–9, 2002.

[183] V. C. Padmakumar, T. Libotte, W. Lu, H. Zaim, S. Abraham, A. A. Noegel, J. Gotzmann, R. Foisner, and I. Karakesisoglou, "The inner nuclear membrane protein sun1 mediates the anchorage of nesprin-2 to the nuclear envelope," *J Cell Sci*, vol. 118, no. Pt 15, pp. 3419–30, 2005.

[184] M. L. Lombardi, D. E. Jaalouk, C. M. Shanahan, B. Burke, K. J. Roux, and J. Lammerding, "The interaction between nesprins and sun proteins at the nuclear envelope is critical for force transmission between the nucleus and cytoskeleton," *J Biol Chem*, vol. 286, no. 30, pp. 26 743–53, 2011.

[185] J. M. Ruijter, P. Lorenz, J. M. Tuomi, M. Hecker, and M. J. B. van den Hoff, "Fluorescent-increase kinetics of different fluorescent reporters used for qpcr depend on monitoring chemistry, targeted sequence, type of dna input and pcr efficiency," *Mikrochim Acta*, vol. 181, no. 13-14, pp. 1689–96, 2014.

[186] C. Zurla, J. Jung, E. L. Blanchard, and P. J. Santangelo, "A novel method to quantify rna–protein interactions in situ using fmtrip and proximity ligation," in *Enhancer RNAs: Methods and Protocols*, U. A. Ørom, Ed. New York, NY: Springer New York, 2017, pp. 155–170, ISBN: 978-1-4939-4035-6.

[187] T. E. Rinker, B. D. Philbrick, M. H. Hettiaratchi, D. M. Smalley, T. C. McDevitt, and J. S. Temenoff, "Microparticle-mediated sequestration of cell-secreted proteins to modulate chondrocytic differentiation," *Acta Biomater*, 2017.

[188] H.-W. Rho, B.-C. Lee, E.-S. Choi, I.-J. Choi, Y.-S. Lee, and S.-H. Goh, "Identification of valid reference genes for gene expression studies of human stomach cancer by reverse transcription-qpcr," *BMC Cancer*, vol. 10, no. 1, p. 240, 2010.

[189] L. G. Gardinassi, G. R. Garcia, C. H. N. Costa, V. Costa Silva, and I. K. F. de Miranda Santos, "Blood transcriptional profiling reveals immunological signatures of distinct states of infection of humans with leishmania infantum," *PLOS Neglected Tropical Diseases*, vol. 10, no. 11, pp. 1–24, Nov. 2016.

[190] S. Caputo, J. Couprie, I. Duband-Goulet, E. Konde, F. Lin, S. Braud, M. Gondry, B. Gilquin, H. J. Worman, and S. Zinn-Justin, "The carboxyl-terminal nucleoplasmic region of man1 exhibits a dna binding winged helix domain," *J Biol Chem*, vol. 281, no. 26, pp. 18 208–15, 2006.

[191] T. Panciera, L. Azzolin, M. Cordenonsi, and S. Piccolo, "Mechanobiology of yap and taz in physiology and disease," *Nat Rev Mol Cell Biol*, vol. 18, no. 12, pp. 758–770, 2017.

[192] S. Dupont, "Role of yap/taz in cell-matrix adhesion-mediated signalling and mechanotransduction," *Exp Cell Res*, vol. 343, no. 1, pp. 42–53, 2016.

[193] R. Samarakoon, S. P. Higgins, C. E. Higgins, and P. J. Higgins, "Tgf-beta1-induced plasminogen activator inhibitor-1 expression in vascular smooth muscle cells requires pp60(c-src)/egfr(y845) and rho/rock signaling," *J Mol Cell Cardiol*, vol. 44, no. 3, pp. 527–38, 2008.

[194] K. Grannas, L. Arngarden, P. Lonn, M. Mazurkiewicz, A. Blokzijl, A. Zieba, and O. Soderberg, "Crosstalk between hippo and tgfbeta: Subcellular localization of yap/taz/smad complexes," *J Mol Biol*, vol. 427, no. 21, pp. 3407–15, 2015.

[195] J. W. Harper, K. Hemmi, and J. C. Powers, "Reaction of serine proteases with substituted isocoumarins: Discovery of 3,4-dichloroisocoumarin, a new general mechanism based serine protease inhibitor," *Biochemistry*, vol. 24, no. 8, pp. 1831–1841, 1985, PMID: 3893537. eprint: http://dx.doi.org/10.1021/bi00329a005.

[196] G. A. Collins and A. L. Goldberg, "The logic of the 26s proteasome," *Cell*, vol. 169, no. 5, pp. 792 –806, 2017.

[197] J. Song, H. Tan, A. J. Perry, T. Akutsu, G. I. Webb, J. C. Whisstock, and R. N. Pike, "Prosper: An integrated feature-based tool for predicting protease substrate cleavage sites," *PLOS ONE*, vol. 7, no. 11, pp. 1–23, Nov. 2012.

[198] M. Peter, J. Nakagawa, M. Dore, J. Labb, and E. Nigg, "In vitro disassembly of the nuclear lamina and m phase-specific phosphorylation of lamins by cdc2 kinase," *Cell*, vol. 61, no. 4, pp. 591 –602, 1990.

[199] M. G. Jones, S. Fletcher, and L. Richeldi, "Idiopathic pulmonary fibrosis: Recent trials and current drug therapy," *Respiration*, vol. 86, no. 5, pp. 353–63, 2013.

[200] C. Vancheri, M. Kreuter, L. Richeldi, C. J. Ryerson, D. Valeyre, J. C. Grutters, S. Wiebe, W. Stansen, M. Quaresma, S. Stowasser, W. A. Wuyts, and I. t. investigators, "Nintedanib with add-on pirfenidone in idiopathic pulmonary fibrosis: Results of the injourney trial," *Am J Respir Crit Care Med*, 2017.

[201] Y. Wang, J. Yella, J. Chen, F. X. McCormack, S. K. Madala, and A. G. Jegga, "Unsupervised gene expression analyses identify ipf-severity correlated signatures, associated genes and biomarkers," *BMC Pulm Med*, vol. 17, no. 1, p. 133, 2017.

[202] D. J. DePianto, S. Chandriani, A. R. Abbas, G. Jia, E. N. N'Diaye, P. Caplazi, S. E. Kauder, S. Biswas, S. K. Karnik, C. Ha, Z. Modrusan, M. A. Matthay, J. Kukreja, H. R. Collard, J. G. Egen, P. J. Wolters, and J. R. Arron, "Heterogeneous gene expression signatures correspond to distinct lung pathologies and biomarkers of disease severity in idiopathic pulmonary fibrosis," *Thorax*, vol. 70, no. 1, pp. 48–56, 2015. eprint: http://thorax.bmj.com/content/70/1/48.full.pdf.

[203] T. Nance, K. S. Smith, V. Anaya, R. Richardson, L. Ho, M. Pala, S. Mostafavi, A. Battle, C. Feghali-Bostwick, G. Rosen, and S. B. Montgomery, "Transcriptome analysis reveals differential splicing events in ipf lung tissue," *PLOS ONE*, vol. 9, no. 3, pp. 1–15, Mar. 2014.

[204] F Lin, D. L. Blake, I Callebaut, I. S. Skerjanc, L Holmer, M. W. McBurney, M Paulin-Levasseur, and H. J. Worman, "Man1, an inner nuclear membrane protein that shares the lem domain with lamina-associated polypeptide 2 and emerin.," *Journal of biological chemistry.*, vol. 275, no. 7, pp. 4840–4847,

[205] J. H. Kristensen, M. A. Karsdal, J. M. B. Sand, N. Willumsen, C. Diefenbach, B. Svensson, P. Hgglund, and D. J. Oersnes-Leeming, "Serological assessment of neutrophil elastase activity on elastin during lung ecm remodeling," *BMC Pulm Med*, vol. 15, 2015.

[206] F. Bhling, C. Rcken, F. Brasch, R. Hartig, Y. Yasuda, P. Saftig, D. Brmme, and T. Welte, "Pivotal role of cathepsin k in lung fibrosis," *Am J Pathol*, vol. 164, no. 6, pp. 2203–16, 2004.

[207] M. Srivastava, K. Steinwede, R. Kiviranta, J. Morko, H. G. Hoymann, F. Lnger, F. Buhling, T. Welte, and U. A. Maus, "Overexpression of cathepsin k in mice decreases collagen deposition and lung resistance in response to bleomycin-induced pulmonary fibrosis," *Respir Res*, vol. 9, no. 1, p. 54, 2008.

[208] Y. Fukuda, M. Ishizaki, S. Kudoh, M. Kitaichi, and N. Yamanaka, "Localization of matrix metalloproteinases-1, -2, and -9 and tissue inhibitor of metalloproteinase-2 in interstitial lung diseases," *Lab Invest*, vol. 78, no. 6, pp. 687–98, 1998.

[209] D. C. Radisky, D. D. Levy, L. E. Littlepage, H. Liu, C. M. Nelson, J. E. Fata, D. Leake, E. L. Godden, D. G. Albertson, M. A. Nieto, Z. Werb, and M. J. Bissell, "Rac1b and reactive oxygen species mediate mmp-3-induced emt and genomic instability," *Nature*, vol. 436, no. 7047, pp. 123–7, 2005.

[210] C. M. Yamashita, L. Dolgonos, R. L. Zemans, S. K. Young, J. Robertson, N. Briones, T. Suzuki, M. N. Campbell, J. Gauldie, D. C. Radisky, D. W. H. Riches, G. Yu, N. Kaminski, C. A. G. McCulloch, and G. P. Downey, "Matrix metalloproteinase 3 is a mediator of pulmonary fibrosis," *Am J Pathol*, vol. 179, no. 4, pp. 1733–45, 2011.

[211] E. Garca-Prieto, A. Gonzlez-Lpez, S. Cabrera, A. Astudillo, A. Gutirrez-Fernndez, M. Fanjul-Fernandez, E. Batalla-Sols, X. S. Puente, A. Fueyo, C. Lpez-Otn, and G. M. Albaiceta, "Resistance to bleomycin-induced lung fibrosis in mmp-8 deficient mice is mediated by interleukin-10," *PLoS One*, vol. 5, no. 10, 2010.

[212] F. Zuo, N. Kaminski, E. Eugui, J. Allard, Z. Yakhini, A. Ben-Dor, L. Lollini, D. Morris, Y. Kim, B. DeLustro, D. Sheppard, A. Pardo, M. Selman, and R. A. Heller, "Gene expression analysis reveals matrilysin as a key regulator of pulmonary fibrosis in mice and humans," *Proc Natl Acad Sci U S A*, vol. 99, no. 9, pp. 6292–7, 2002.

[213] T. A. Beyer, A. Weiss, Y. Khomchuk, K. Huang, A. A. Ogunjimi, X. Varelas, and J. L. Wrana, "Switch enhancers interpret tgf-beta and hippo signaling to control cell fate in human embryonic stem cells," *Cell Rep*, vol. 5, no. 6, pp. 1611–24, 2013.

[214] M. J. Landrum, J. M. Lee, M. Benson, G. Brown, C. Chao, S. Chitipiralla, B. Gu, J. Hart, D. Hoffman, J. Hoover, W. Jang, K. Katz, M. Ovetsky, G. Riley, A. Sethi, R. Tully, R. Villamarin-Salomon, W. Rubinstein, and D. R. Maglott, "Clinvar: Public archive of interpretations of clinically relevant variants," *Nucleic Acids Res*, vol. 44, no. D1, pp. D862–8, 2016.

[215] D. Rajgor, J. A. Mellad, F. Autore, Q. Zhang, and C. M. Shanahan, "Multiple novel nesprin-1 and nesprin-2 variants act as versatile tissue-specific intracellular scaffolds," *PLoS One*, vol. 7, no. 7, e40098, 2012.

[216] M. Santos, S. C. Domingues, P. Costa, T. Muller, S. Galozzi, K. Marcus, E. F. da Cruz e Silva, O. A. da Cruz e Silva, and S. Rebelo, "Identification of a novel human lap1 isoform that is regulated by protein phosphorylation," *PLoS One*, vol. 9, no. 12, e113732, 2014.

[217] F. Abascal, M. L. Tress, and A. Valencia, "Alternative splicing and co-option of transposable elements: The case of tmpo/lap2alpha and znf451 in mammals," *Bioinformatics*, vol. 31, no. 14, pp. 2257–61, 2015.

[218] W. Zhang, T. Bai, S. Zhang, S. Xu, H. Chen, and C. Li, "Isoforms of the nuclear envelope protein nurim are differentially expressed during heart development in mice," *Gene*, vol. 627, pp. 123–128, 2017.

[219] Q. Zhang, J. N. Skepper, F. Yang, J. D. Davies, L. Hegyi, R. G. Roberts, P. L. Weissberg, J. A. Ellis, and C. M. Shanahan, "Nesprins: A novel family of spectrin-repeat-containing proteins that localize to the nuclear membrane in multiple tissues," *J Cell Sci*, vol. 114, no. Pt 24, pp. 4485–98, 2001.

[220] I. Holt, N. T. Duong, Q. Zhang, T. Lam le, C. A. Sewry, K. Mamchaoui, C. M. Shanahan, and G. E. Morris, "Specific localization of nesprin-1-alpha2, the short isoform of nesprin-1 with a kash domain, in developing, fetal and regenerating muscle, using a new monoclonal antibody," *BMC Cell Biol*, vol. 17, no. 1, p. 26, 2016.

[221] Y. Kobayashi, Y. Katanosaka, Y. Iwata, M. Matsuoka, M. Shigekawa, and S. Wakabayashi, "Identification and characterization of gsrp-56, a novel golgi-localized spectrin repeat-containing protein," *Exp Cell Res*, vol. 312, no. 16, pp. 3152–64, 2006.

[222] D. Rajgor, J. A. Mellad, D. Soong, J. B. Rattner, M. J. Fritzler, and C. M. Shanahan, "Mammalian microtubule p-body dynamics are mediated by nesprin-1," *J Cell Biol*, vol. 205, no. 4, pp. 457–75, 2014.

[223] D. Rajgor, J. G. Hanley, and C. M. Shanahan, "Identification of novel nesprin-1 binding partners and cytoplasmic matrin-3 in processing bodies," *Mol Biol Cell*, vol. 27, no. 24, pp. 3894–3902, 2016.

[224] A. Reginensi, R. P. Scott, A. Gregorieff, M. Bagherie-Lachidan, C. Chung, D. S. Lim, T. Pawson, J. Wrana, and H. McNeill, "Yap- and cdc42-dependent nephrogenesis and morphogenesis during mouse kidney development," *PLoS Genet*, vol. 9, no. 3, e1003380, 2013.

[225] A. Mitani, T. Nagase, K. Fukuchi, H. Aburatani, R. Makita, and H. Kurihara, "Transcriptional coactivator with pdz-binding motif is essential for normal alveolarization in mice," *Am J Respir Crit Care Med*, vol. 180, no. 4, pp. 326–38, 2009.

[226] N. Zhang, H. Bai, K. K. David, J. Dong, Y. Zheng, J. Cai, M. Giovannini, P. Liu, R. A. Anders, and D. Pan, "The merlin/nf2 tumor suppressor functions through the yap oncoprotein to regulate tissue homeostasis in mammals," *Dev Cell*, vol. 19, no. 1, pp. 27–38, 2010.

[227] J. P. Califano and C. A. Reinhart-King, "Substrate stiffness and cell area predict cellular traction stresses in single cells and cells in contact," *Cell Mol Bioeng*, vol. 3, no. 1, pp. 68–75, 2010.

[228] C. Esnault, A. Stewart, F. Gualdrini, P. East, S. Horswell, N. Matthews, and R. Treisman, "Rho-actin signaling to the mrtf coactivators dominates the immediate transcriptional response to serum in fibroblasts," *Genes Dev*, vol. 28, no. 9, pp. 943–58, 2014.

[229] L. S. Velasquez, L. B. Sutherland, Z. Liu, F. Grinnell, K. E. Kamm, J. W. Schneider, E. N. Olson, and E. M. Small, "Activation of mrtf-a-dependent gene expression with a small molecule promotes myofibroblast differentiation and wound healing," *Proc Natl Acad Sci U S A*, vol. 110, no. 42, pp. 16 850–5, 2013.

[230] L. L. Luchsinger, C. A. Patenaude, B. D. Smith, and M. D. Layne, "Myocardin-related transcription factor-a complexes activate type i collagen expression in lung fibroblasts," *J Biol Chem*, vol. 286, no. 51, pp. 44 116–25, 2011.

[231] L. Liu, S. X. Zhang, W. Liao, H. P. Farhoodi, C. W. Wong, C. C. Chen, A. I. Segaliny, J. V. Chacko, L. P. Nguyen, M. Lu, G. Polovin, E. J. Pone, T. L. Downing, D. A. Lawson, M. A. Digman, and W. Zhao, "Mechanoresponsive stem cells to target cancer metastases through biophysical cues," *Sci Transl Med*, vol. 9, no. 400, 2017.

[232] F. Miralles, G. Posern, A. I. Zaromytidou, and R. Treisman, "Actin dynamics control srf activity by regulation of its coactivator mal," *Cell*, vol. 113, no. 3, pp. 329–42, 2003.

[233] C. S. Hill, J. Wynne, and R. Treisman, "The rho family gtpases rhoa, rac1, and cdc42hs regulate transcriptional activation by srf," *Cell*, vol. 81, no. 7, pp. 1159–70, 1995.

[234] M. Uhlen, L. Fagerberg, B. M. Hallstrom, C. Lindskog, P. Oksvold, A. Mardinoglu, A. Sivertsson, C. Kampf, E. Sjostedt, A. Asplund, I. Olsson, K. Edlund, E. Lundberg, S. Navani, C. A. Szigyarto, J. Odeberg, D. Djureinovic, J. O. Takanen, S. Hober, T. Alm, P. H. Edqvist, H. Berling, H. Tegel, J. Mulder, J. Rockberg, P. Nilsson, J. M. Schwenk, M. Hamsten, K. von Feilitzen, M. Forsberg, L. Persson, F. Johansson, M. Zwahlen, G. von Heijne, J. Nielsen, and F. Ponten, "Proteomics. tissue-based map of the human proteome," *Science*, vol. 347, no. 6220, p. 1 260 419, 2015.

[235] S. Muehlich, R. Wang, S. M. Lee, T. C. Lewis, C. Dai, and R. Prywes, "Serum-induced phosphorylation of the serum response factor coactivator mkl1 by the extracellular signal-regulated kinase 1/2 pathway inhibits its nuclear localization," *Mol Cell Biol*, vol. 28, no. 20, pp. 6302–13, 2008.

[236] H. Hirano and Y. Matsuura, "Sensing actin dynamics: Structural basis for g-actin-sensitive nuclear import of mal," *Biochem Biophys Res Commun*, vol. 414, no. 2, pp. 373–8, 2011.

[237] S. Nakamura, K. Hayashi, K. Iwasaki, T. Fujioka, H. Egusa, H. Yatani, and K. Sobue, "Nuclear import mechanism for myocardin family members and their correlation with vascular smooth muscle cell phenotype," *J Biol Chem*, vol. 285, no. 48, pp. 37 314–23, 2010.

[238] R. Pawlowski, E. K. Rajakyla, M. K. Vartiainen, and R. Treisman, "An actin-regulated importin alpha/beta-dependent extended bipartite nls directs nuclear import of mrtf-a," *EMBO J*, vol. 29, no. 20, pp. 3448–58, 2010.

[239] M. K. Vartiainen, S. Guettler, B. Larijani, and R. Treisman, "Nuclear actin regulates dynamic subcellular localization and activity of the srf cofactor mal," *Science*, vol. 316, no. 5832, pp. 1749–52, 2007.

[240] C. Baarlink, H. Wang, and R. Grosse, "Nuclear actin network assembly by formins regulates the srf coactivator mal," *Science*, vol. 340, no. 6134, pp. 864–7, 2013.

[241] M. Plessner, M. Melak, P. Chinchilla, C. Baarlink, and R. Grosse, "Nuclear f-actin formation and reorganization upon cell spreading," *J Biol Chem*, vol. 290, no. 18, pp. 11 209–16, 2015.

[242] R. Panayiotou, F. Miralles, R. Pawlowski, J. Diring, H. R. Flynn, M. Skehel, and R. Treisman, "Phosphorylation acts positively and negatively to regulate mrtf-a subcellular localisation and activity," *Elife*, vol. 5, 2016.

[243] B. Cen, A. Selvaraj, R. C. Burgess, J. K. Hitzler, Z. Ma, S. W. Morris, and R. Prywes, "Megakaryoblastic leukemia 1, a potent transcriptional coactivator for serum response factor (srf), is required for serum induction of srf target genes," *Mol Cell Biol*, vol. 23, no. 18, pp. 6597–608, 2003.

[244] B. Cen, A. Selvaraj, and R. Prywes, "Myocardin/mkl family of srf coactivators: Key regulators of immediate early and muscle specific gene expression," *J Cell Biochem*, vol. 93, no. 1, pp. 74–82, 2004.

[245] X. Shen, H. Mao, and S. Miao, "Substitution pattern of the carg element in human and mouse genomes," *Genome*, vol. 54, no. 2, pp. 144–50, 2011.

[246] M. H. Mokalled, K. J. Carroll, B. K. Cenik, B. Chen, N. Liu, E. N. Olson, and R. Bassel-Duby, "Myocardin-related transcription factors are required for cardiac development and function," *Dev Biol*, vol. 406, no. 2, pp. 109–16, 2015.

[247] C. P. Mack, M. M. Thompson, S. Lawrenz-Smith, and G. K. Owens, "Smooth muscle alpha-actin carg elements coordinate formation of a smooth muscle cell-selective, serum response factor-containing activation complex," *Circ Res*, vol. 86, no. 2, pp. 221–32, 2000.

[248] J. Wang, M. Su, J. Fan, A. Seth, and C. A. McCulloch, "Transcriptional regulation of a contractile gene by mechanical forces applied through integrins in osteoblasts," *J Biol Chem*, vol. 277, no. 25, pp. 22 889–95, 2002.

[249] B. Piersma, R. Bank, and M. Boersema, "Signaling in fibrosis: Tgf-, wnt, and yap/taz converge," vol. 2, Sep. 2015.

[250] H. W. Park and K. L. Guan, "Regulation of the hippo pathway and implications for anticancer drug development," *Trends Pharmacol Sci*, vol. 34, no. 10, pp. 581–9, 2013.

[251] S. Nasrollahi, C. Walter, A. J. Loza, G. V. Schimizzi, G. D. Longmore, and A. Pathak, "Past matrix stiffness primes epithelial cells and regulates their future collective migration through a mechanical memory," *Biomaterials*, vol. 146, pp. 146–155, 2017.

[252] M. K. Kim, J. W. Jang, and S. C. Bae, "Dna binding partners of yap/taz," *BMB Rep*, vol. 51, no. 3, pp. 126–133, 2018.

[253] C. T. Foster, F. Gualdrini, and R. Treisman, "Mutual dependence of the mrtf-srf and yap-tead pathways in cancer-associated fibroblasts is indirect and mediated by cytoskeletal dynamics," *Genes Dev*, vol. 31, no. 23-24, pp. 2361–2375, 2017.

[254] F. Calvo, N. Ege, A. Grande-Garcia, S. Hooper, R. P. Jenkins, S. I. Chaudhry, K. Harrington, P. Williamson, E. Moeendarbary, G. Charras, and E. Sahai, "Mechanotransduction and yap-dependent matrix remodelling is required for the generation and maintenance of cancer-associated fibroblasts," *Nat Cell Biol*, vol. 15, no. 6, pp. 637–46, 2013.

[255] N. A. Bhowmick, M. Ghiassi, A. Bakin, M. Aakre, C. A. Lundquist, M. E. Engel, C. L. Arteaga, and H. L. Moses, "Transforming growth factor-beta1 mediates epithelial to mesenchymal transdifferentiation through a rhoa-dependent mechanism," *Mol Biol Cell*, vol. 12, no. 1, pp. 27–36, 2001.

[256] A. Masszi, C. Di Ciano, G. Sirokmany, W. T. Arthur, O. D. Rotstein, J. Wang, C. A. McCulloch, L. Rosivall, I. Mucsi, and A. Kapus, "Central role for rho in tgf-beta1-induced alpha-smooth muscle actin expression during epithelial-mesenchymal transition," *Am J Physiol Renal Physiol*, vol. 284, no. 5, F911–24, 2003.

[257] A. Korol, A. Taiyab, and J. A. West-Mays, "Rhoa/rock signaling regulates tgfbeta-induced epithelial-mesenchymal transition of lens epithelial cells through mrtf-a," *Mol Med*, vol. 22, 2016.

[258] K. Kumawat, T. Koopmans, M. H. Menzen, A. Prins, M. Smit, A. J. Halayko, and R. Gosens, "Cooperative signaling by tgf-beta1 and wnt-11 drives sm-alpha-actin expression in smooth muscle via rho kinase-actin-mrtf-a signaling," *Am J Physiol Lung Cell Mol Physiol*, vol. 311, no. 3, pp. L529–37, 2016.

[259] J. W. O'Connor, K. Mistry, D. Detweiler, C. Wang, and E. W. Gomez, "Cell-cell contact and matrix adhesion promote alphasma expression during tgfbeta1-induced epithelial-myofibroblast transition via notch and mrtf-a," *Sci Rep*, vol. 6, p. 26 226, 2016.

[260] F. E. Johansen and R. Prywes, "Identification of transcriptional activation and inhibitory domains in serum response factor (srf) by using gal4-srf constructs," *Mol Cell Biol*, vol. 13, no. 8, pp. 4640–7, 1993.

[261] U. Arad, "Modified hirt procedure for rapid purification of extrachromosomal dna from mammalian cells," *Biotechniques*, vol. 24, no. 5, pp. 760–2, 1998.

[262] R. Aoki, A. Aoki-Yoshida, C. Suzuki, and Y. Takayama, "Protective effect of indole-3-pyruvate against ultraviolet b-induced damage to cultured hacat keratinocytes and the skin of hairless mice," *PLoS One*, vol. 9, no. 5, e96804, 2014.

[263] G. D. Stormo, Z. Zuo, and Y. K. Chang, "Spec-seq: Determining protein-dna-binding specificity by sequencing," *Brief Funct Genomics*, vol. 14, no. 1, pp. 30–8, 2015.

[264] X. Shiwen, R. Stratton, J. Nikitorowicz-Buniak, B. Ahmed-Abdi, M. Ponticos, C. Denton, D. Abraham, A. Takahashi, B. Suki, M. D. Layne, R. Lafyatis, and B. D. Smith, "A role of myocardin related transcription factor-a (mrtf-a) in scleroderma related fibrosis," *PLoS One*, vol. 10, no. 5, e0126015, 2015.

[265] V. Boeva, "Analysis of genomic sequence motifs for deciphering transcription factor binding and transcriptional regulation in eukaryotic cells," *Front Genet*, vol. 7, p. 24, 2016.

[266] H. Zhang, L. Zhu, and D. S. Huang, "Wsmd: Weakly-supervised motif discovery in transcription factor chip-seq data," *Sci Rep*, vol. 7, no. 1, p. 3217, 2017.

[267] R. Pique-Regi, J. F. Degner, A. A. Pai, D. J. Gaffney, Y. Gilad, and J. K. Pritchard, "Accurate inference of transcription factor binding from dna sequence and chromatin accessibility data," *Genome Res*, vol. 21, no. 3, pp. 447–55, 2011.

[268] A. Khan, O. Fornes, A. Stigliani, M. Gheorghe, J. A. Castro-Mondragon, R. van der Lee, A. Bessy, J. Cheneby, S. R. Kulkarni, G. Tan, D. Baranasic, D. J. Arenillas, A. Sandelin, K. Vandepoele, B. Lenhard, B. Ballester, W. W. Wasserman, F. Parcy, and A. Mathelier, "Jaspar 2018: Update of the open-access database of transcription factor binding profiles and its web framework," *Nucleic Acids Res*, vol. 46, no. D1, p. D1284, 2018.

[269] J. Hirschfeld, J. Maurer, D. Jung, M. Kwiecinski, A. K. Khimji, H. P. Dienes, J. W. Fries, and M. Odenthal, "Targeting myofibroblasts in model systems of fibrosis by an artificial alpha-smooth muscle-actin promoter hybrid," *Mol Biotechnol*, vol. 43, no. 2, pp. 121–9, 2009.

[270] Z. Kalajzic, H. Li, L. P. Wang, X. Jiang, K. Lamothe, D. J. Adams, H. L. Aguila, D. W. Rowe, and I. Kalajzic, "Use of an alpha-smooth muscle actin gfp reporter to identify an osteoprogenitor population," *Bone*, vol. 43, no. 3, pp. 501–10, 2008.

[271] M. T. Lin, C. Y. Wang, H. J. Xie, C. H. Cheung, C. H. Hsieh, H. F. Juan, B. S. Chen, and C. Lin, "Novel utilization of terminators in the design of biologically adjustable synthetic filters," *ACS Synth Biol*, vol. 5, no. 5, pp. 365–74, 2016.

[272] T. Sohka, R. A. Heins, R. M. Phelan, J. M. Greisler, C. A. Townsend, and M. Ostermeier, "An externally tunable bacterial band-pass filter," *Proc Natl Acad Sci U S A*, vol. 106, no. 25, pp. 10 135–40, 2009.

[273] D. Greber and M. Fussenegger, "An engineered mammalian band-pass network," *Nucleic Acids Res*, vol. 38, no. 18, e174, 2010.

[274] X. H. Zhao, C. Laschinger, P. Arora, K. Szaszi, A. Kapus, and C. A. McCulloch, "Force activates smooth muscle alpha-actin promoter activity through the rho signaling pathway," *J Cell Sci*, vol. 120, no. Pt 10, pp. 1801–9, 2007.

[275] S. A. Khan, J. Joyce, and T. Tsuda, "Quantification of active and total transforming growth factor-beta levels in serum and solid organ tissues by bioassay," *BMC Res Notes*, vol. 5, p. 636, 2012.

[276] S. Yonemura, M. Itoh, A. Nagafuchi, and S. Tsukita, "Cell-to-cell adherens junction formation and actin filament organization: Similarities and differences between non-polarized fibroblasts and polarized epithelial cells," *J Cell Sci*, vol. 108 (Pt 1), pp. 127–42, 1995.

[277] K. Hayashi, T. Murai, H. Oikawa, T. Masuda, K. Kimura, S. Muehlich, R. Prywes, and T. Morita, "A novel inhibitory mechanism of mrtf-a/b on the icam-1 gene expression in vascular endothelial cells," *Sci Rep*, vol. 5, p. 10 627, 2015.

[278] J. L. Balestrini, S. Chaudhry, V. Sarrazy, A. Koehler, and B. Hinz, "The mechanical memory of lung myofibroblasts," *Integr Biol (Camb)*, vol. 4, no. 4, pp. 410–21, 2012.

[279] S. M.D.S.R. P. Alyssa D. Schwartz Christopher L. Hall, "Breast cancer mechanical background controls motility and metastasis," in *Society for Biomaterials*.

[280] C. X. Li, N. P. Talele, S. Boo, A. Koehler, E. Knee-Walden, J. L. Balestrini, P. Speight, A. Kapus, and B. Hinz, "Microrna-21 preserves the fibrotic mechanical memory of mesenchymal stem cells," *Nat Mater*, vol. 16, no. 3, pp. 379–389, 2017.

[281] C. Yang, M. W. Tibbitt, L. Basta, and K. S. Anseth, "Mechanical memory and dosing influence stem cell fate," *Nat Mater*, vol. 13, no. 6, pp. 645–52, 2014.

[282] S. Xing, F. Nie, Q. Xu, Y. Deng, W. Li, Z. Yang, X. Zhao, P. Zhu, X. Wang, Y. Gao, and Z. He, "Hdac is essential for epigenetic regulation of thy-1 gene expression during lps/tlr4-mediated proliferation of lung fibroblasts," *Lab Invest*, vol. 95, no. 10, pp. 1105–16, 2015.

[283] R. C. Brewster, F. M. Weinert, H. G. Garcia, D. Song, M. Rydenfelt, and R. Phillips, "The transcription factor titration effect dictates level of gene expression," *Cell*, vol. 156, no. 6, pp. 1312–1323, 2014.

[284] L. Bintu, N. E. Buchler, H. G. Garcia, U. Gerland, T. Hwa, J. Kondev, and R. Phillips, "Transcriptional regulation by the numbers: Models," *Curr Opin Genet Dev*, vol. 15, no. 2, pp. 116–24, 2005.

[285] M. Rydenfelt, r. Cox R. S., H. Garcia, and R. Phillips, "Statistical mechanical model of coupled transcription from multiple promoters due to transcription factor titration," *Phys Rev E Stat Nonlin Soft Matter Phys*, vol. 89, no. 1, p. 012 702, 2014.

[286] V. Escriou, M. Carriere, D. Scherman, and P. Wils, "Nls bioconjugates for targeting therapeutic genes to the nucleus," *Adv Drug Deliv Rev*, vol. 55, no. 2, pp. 295–306, 2003.

[287] R. C. Carlisle, T. Bettinger, M. Ogris, S. Hale, V. Mautner, and L. W. Seymour, "Adenovirus hexon protein enhances nuclear delivery and increases transgene expression of polyethylenimine/plasmid dna vectors," *Mol Ther*, vol. 4, no. 5, pp. 473–83, 2001.

[288] Y. Wang, X. Y. Zhou, P. Y. Xiang, L. L. Wang, H. Tang, F. Xie, L. Li, and H. Wei, "The meganuclease i-scei containing nuclear localization signal (nls-i-scei) efficiently mediated mammalian germline transgenesis via embryo cytoplasmic microinjection," *PLoS One*, vol. 9, no. 9, e108347, 2014.

[289] J. Yin, X. Meng, S. Zhang, D. Zhang, L. Wang, and C. Liu, "The effect of a nuclear localization sequence on transfection efficacy of genes delivered by cobalt(ii)-polybenzimidazole complexes," *Biomaterials*, vol. 33, no. 31, pp. 7884–94, 2012.

[290] M. van der Aa, G. Koning, J. van der Gugten, C. d'Oliveira, R. Oosting, W. E. Hennink, and D. J. Crommelin, "Covalent attachment of an nls-peptide to linear dna does not enhance transfection efficiency of cationic polymer based gene delivery systems," *J Control Release*, vol. 101, no. 1-3, pp. 395–7, 2005.

[291] R. Gambari, M. Borgatti, V. Bezzerri, E. Nicolis, I. Lampronti, M. C. Dechecchi, I. Mancini, A. Tamanini, and G. Cabrini, "Decoy oligodeoxyribonucleotides and peptide nucleic acids-dna chimeras targeting nuclear factor kappa-b: Inhibition of il-8 gene expression in cystic fibrosis cells infected with pseudomonas aeruginosa," *Biochem Pharmacol*, vol. 80, no. 12, pp. 1887–94, 2010.

[292] L. Penolazzi, M. Borgatti, E. Lambertini, C. Mischiati, A. Finotti, A. Romanelli, M. Saviano, C. Pedone, R. Piva, and R. Gambari, "Peptide nucleic acid-dna decoy chimeras targeting nf-kappab transcription factors: Induction of apoptosis in human primary osteoclasts," *Int J Mol Med*, vol. 14, no. 2, pp. 145–52, 2004.

[293] E. Bertrand, P. Chartrand, M. Schaefer, S. M. Shenoy, R. H. Singer, and R. M. Long, "Localization of ash1 mrna particles in living yeast," *Mol Cell*, vol. 2, no. 4, pp. 437–45, 1998.

VITA

Dwight McCoy Chambers was born in Nashville, TN to Carol L. McCoy and Richard J. Chambers. He is the older brother to Davis Chambers. Later, Dwight would gain 4 additional step-brothers, Ethan and Justin Page and Mike and Matt Lassiter, and step-parents, Nancy Chambers and Roger Page. Dwight grew up in Nashville, TN, where he learned to love lacrosse, chemistry and Latin epics. He graduated from the University School of Nashville and matriculated at the Massachusetts Institute of Technology. At MIT, Dwight studied Course XXII - Nuclear Science and Engineering and developed an aptitude and interest in magnetic resonance as a powerful tool for biological/medical investigation without ionizing radiation. This interest led him to consider a career in medicine, and specifically, in medical science. Dwight was admitted to Emory University's Medical Scientist Training Program and moved to Atlanta, GA in 2010. After completing the first two years of medical school and the first USMLE exam, Dwight enrolled in the PhD program in Biomedical Engineering at Georgia Tech and Emory University. There, Dwight joined the lab of Tom Barker and began to study the role of genetic as a novel theraputic axis in pulmonary fibrosis. When the Barker lab left for the University of Virginia, Phil Santangelo kindly agreed to co-mentor Dwight while he completed his PhD tenure. Dwight returns to medical school with a strong interest in medical genetics, particularly in the pediatric setting.